Residence Time Distribution modeling of combustors through Chemical Reactors Network

Am Fachgebiet Maschinenbau
der Technischen Universität Darmstadt
zur Erlangung des akademischen Grades eines
Doktor-Ingenieurs (Dr.-Ing.)
eingereichte

Dissertation

vorgelegt von

Maria Angela Agizza, M.Sc.

aus Neapel (Italien)

Berichterstatter:	Prof. Dr. rer. nat. A. Dreizler
Mitberichterstatter:	Prof. Dr.-Ing. T. Faravelli
Mitberichterstatter:	Prof. Dr.-Ing. G. Sorrentino
Tag der Einreichung	16.04.2019
Tag der mündlichen Prüfung	12.06.2019

Darmstadt 2019
D17

Erklärung /Statement

Hiermit erkläre ich, dass ich die vorliegende Arbeit, abgesehen von den in ihr ausdrücklich genannten Hilfen, selbständig verfasst habe. Ich erkläre außerdem, dass ich bisher noch keinen Promotionsversuch unternommen habe.

English translation for information purposes only:

I herewith declare that I have written the submitted dissertation independently, expect for explicitly quoted sources. I furthermore declare that I have not applied for a PhD before.

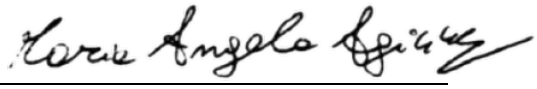

Darmstadt, 16. April 2019 Maria Angela Agizza, M.Sc.

Content

Nomenclature

Abbreviations

CARS	Coherent Anti-Stokes Raman
CM	Compartmental Model
CRN	Chemical Reactors Network
CSTR	Continuous Stirred Tank Reactor
ERZ	External Recirculation Zone
IRZ	Internal Recirculation Zone
LIF	Laser Induced Fluorescence
OFC	OxyFuel Combustor
PFR	Plug Flow Reactor
RTD	Residence Time Distribution
RZ	Recirculation Zone
SSGT	Single Sector Gas Turbine model combustor
$st.$	Staging ratio

Greek notations

φ	Equivalence ratio
σ^2	Spread of a distribution
τ	Mean residence time or space-time

Roman notations

P	Pressure
S	Swirl number
S^3	Skewness of a distribution
T	Temperature

German abstract

Schlüsselwörter: Verweilzeitverteilung, Chemical Reactors NetworkvModellierung, magere Verbrennung, Oxyfuel-Verbrennung.

Sowohl die Zunahme des Luftverkehrs als auch des Energiebedarfs erfordern eine kontinuierliche Verbesserung von Verbrennungskraftmaschinen, um die Nachhaltigkeit des Verbrennungsprozesses sicherzustellen. Um die Verbrennungseffizienz zu erhöhen und die Schadstoffemissionen zu reduzieren werden neue Verbrennungskonzepte vorgeschlagen und getestet.
Die magere Verbrennung erfüllt die Anforderungen eines effizienten und sauberen Verbrennungsprozesses für Luftfahrtgasturbinen. Sie ist oft mit einer Effusionskühlung der Brennkammerwände gekoppelt. Dabei ist die Wechselwirkung zwischen einer heißen Reaktionsumgebung und einer kalten Kühlluft noch nicht vollständig verstanden. Diese muss weiter untersucht werden, da aufgrund einer schnellen und inhomogenen Abkühlung von reagierenden Fluideinschlüssen hohe Kohlenmonoxidemissionen entstehen können.
Die Oxyfuel-Verbrennung ist stattdessen eine Strategie, die für stationäre Kraftwerke anwendbar ist. In diesem Fall erfolgt eine Substitution von Luft durch ein Gemisch aus Kohlenstoffdioxid und Sauerstoff. Dies stellt eine Neuheit in Bezug auf die Standardverbrennung in Luft dar, wodurch ein besseres Verständnis der Auswirkungen von überschüssigem CO_2 in einer Reaktionsumgebung entscheidend ist.
Zu diesem Zweck ist eine gründliche experimentelle Untersuchung in einer entsprechend realitätsnahen Konfiguration erforderlich, die idealerweise durch die Modellierung der beobachteten Phänomene ergänzt wird. Eine Modellierungsstrategie, die gut zu der Idee einer starken Synergie zwischen Experimenten und Modellierung passt, wird als “Chemical Reactors Network” (CRN) Modellierung bezeichnet. Bei dieser Vorgehensweise wird eine vereinfachte Form des Strömungsfeldes betrachtet, basierend auf zwei extremen Mischungsmöglichkeiten. Diese Modelle werden häufig gegen die Verweilzeitverteilung einer bestimmten Konfiguration bemessen, welche bereits wertvolle Informationen über die Mischcharakteristik des untersuchten Systems liefert.
In der vorliegenden Arbeit wird die CRN-Modellierung für zwei entsprechend realitätsnahe Umgebungen angewendet. Sie sind repräsentativ für die Brennkammer einer Luftfahrtgasturbine und einer Kraftwerkfeurung. Diese Konfigurationen wurden entworfen, um die zugrunde liegenden Phänomene besser zu verstehen und gleichzeitig neue Verbrennungskonzepte zu untersuchen, nämlich die magere Verbrennung bzw. die Oxyfuel-Verbrennung. Ein CRN-Modell wird jeweils für die beiden Situationen entwickelt und getestet. Diese basieren auf der zonalen Modellierung des Strömungsfeldes und der Verweilzeitverteilung der Systeme.
Für beide Fälle wird die Leistungsfähigkeit anhand zur Verfügung stehender experimenteller Daten getestet. Außerdem werden sie verwendet um die Auswirkungen der Betriebsbedingungen auf den Verbrennungsprozess besser zu verstehen. In dieser Arbeit wird die Wichtigkeit solcher einfachen und flexiblen Werkzeuge für die Verbrennungsforschung aufgezeigt.

English abstract

Keywords: Residence Time Distribution, Chemical Reactors Network, Lean Combustion, Oxyfuel Combustion.

The increase of both aviation transportation and energy demand requires a continuous improvement of combustion devices to ensure the sustainability of the combustion process. New combustion concepts are proposed and tested, to increase combustion efficiency and reduce pollutants emission.
Lean combustion fulfills the requirements of an efficient and clean combustion process, applicable to aviation gas turbines. It is often coupled with effusion cooling of the combustor liner. The interaction between a hot reaction environment and cold cooling air is not yet fully understood. It needs to be investigated further because it could lead to high carbon monoxide emissions due to rapid and inhomogeneous cooling of pockets of reacting fluid.
Oxyfuel combustion, instead, is a strategy applicable to stationary power plants. In this case, the substitution of air with a mixture comprising carbon dioxide and oxygen takes place. Such an approach represents a point of novelty with respect to standard combustion in air. Therefore, an improved understanding of the effect of excess CO_2 in a reaction environment is crucial.
To this aim, thorough experimental investigation in suitably designed close-to-reality configuration is mandatory, and ideally complemented by the modeling of the observed phenomena. A modeling strategy that well fits the idea of a strong synergy between experiments and modeling, is referred to as Chemical Reactors Network (CRN) modeling. This strategy proposes a simplified version of the flow field based on two extreme mixing possibilities. These models are often sized against the Residence Time Distribution of a certain configuration, that alone yields precious information on the mixing characteristic of the system under investigation.
In the current work, Chemical Reactors Network modeling is applied to two suitably designed close-to-reality configurations. They are representative of an aviation gas turbine combustor and a power generation furnace. These systems were designed to better understand the underlying phenomena while investigating new combustion concepts, such as lean combustion and oxyfuel combustion. CRN models are designed and tested in both situations. These models are developed based on zonal modeling of the flow field and on the Residence Time Distribution of the systems. In both cases, their performances are tested against experimental data available for both test-rigs. Additionally, they are employed to understand the impact of the operating conditions on the combustion process. This work states the importance of such simple and flexible tools in combustion research.

Italian abstract

Parole chiave: Distribuzione dei Tempi di Residenza, Modello a Compartimenti, Combustione Magra, Ossicombustione

L'aumento del trasporto aereo e della domanda energetica richiede un continuo miglioramento dei dispositivi adibiti al processo di combustione, al fine di garantirne la massima sostenibilità. A tal riguardo, nuovi processi vengono continuamente proposti e testati con l'obiettivo di aumentare l'efficienza della combustione e di ridurre le emissioni di sostanze inquinanti.
Un processo di combustione caratterizzato da condizioni magre soddisfa i requisiti di efficienza e ridotte emissioni, applicabile alle turbine a gas di tipo aeronautico. Questo processo è spesso accoppiato a un raffreddamento di tipo ad effusione del rivestimento della superficie del combustore. Tuttavia, la complessa interazione esistente tra l'ambiente di reazione estremamente caldo e la corrente di aria fredda adibita al raffreddamento non è ancora stata pienamente compresa. Per questo motivo, ulteriori studi sono necessari in quanto una tale condizione operativa potrebbe portare alla produzione di elevate emissioni di monossido di carbonio come conseguenza di un rapido e disomogeneo raffreddamento di sacche di fluido reagente.
D'altro canto, per quanto riguarda le grandi centrali elettriche, l'ossicombustione (Oxyfuel) rappresenta una valida strategia caratterizzata dalla sostituzione di aria con una miscela formata da anidride carbonica e ossigeno. Tale approccio costituisce una novità rispetto alle metodologie di combustione standard e, a tal riguardo, è quindi fondamentale ottenere una migliore comprensione degli effetti dovuti alla presenza di un eccesso di CO_2 in un ambiente reagente.
E', pertanto, fondamentale perseguire approfondite indagini di tipo sperimentale con configurazioni e apparati il più possibile realistici, le quali devono inoltre essere affiancate e completate da modellazioni di tipo numerico dei diversi fenomeni osservati. In tale contesto, una strategia che ben si adatta all'idea di questa forte sinergia tra ricerca sperimentale e investigazione numerica è rappresentata dalla cosiddetta tecnica di modellazione "Chemical Reactors Network" (CRN, detto anche "modello a compartimenti"). Questo approccio propone una versione semplificata del campo di moto, basata sulle due possibilità estreme di miscelazione. Modelli di questo genere sono spesso dimensionati rispetto alla "Residence Time Distribution" (distribuzione del tempo di residenza) di una determinata configurazione. Questa quantità consente di ottenere preziose informazioni sulle caratteristiche di miscelazione del sistema in esame.
Nel presente lavoro, la metodologia basata sul modello a compartimenti viene applicata a due configurazioni, appositamente progettate per rispecchiare condizioni di funzionamento reali, rappresentate rispettivamente da un combustore di turbina a gas per aeromobili e un forno dedicato alla produzione di potenza. Questi sistemi sono stati realizzati per comprendere al meglio i fenomeni alla base di nuovi approcci, quali la combustione in condizioni magre e l'ossicombustione. Per entrambe le condizioni, modelli di tipo CRN sono stati progettati e testati. Tali modelli sono sviluppati sulla base di una riproduzione di tipo zonale del campo di moto e della distribuzione dei tempi di residenza. I risultati ottenuti dai modelli sono confrontate con i set di dati sperimentali disponibili per entrambi gli impianti. Inoltre, i risultati ottenuti sono utilizzati per comprendere l'impatto che le condizioni operative esercitano sulla fase di combustione. Questo lavoro testimonia l'importanza che tali semplici e flessibili strumenti rivestono per un'attività di ricerca relativa ai processi di combustione.

1 Introduction

The continuous improvement of combustion-based devices is of paramount importance for environmental and economic reasons. This urgency stems from the increased usage of aviation transportation and energy demand, based on the population and economic growth. In this scenario, to keep the present pace and be able to keep up with future requirements, the growth trend needs to be backed up by the sustainability of the process [1].

The optimization of the combustion process is, nonetheless, far from trivial. It must consider two different aspects, often in opposition with each other: great enhancement of combustion efficiency and drastic reduction of pollutant emissions. The need for process efficiency is driven by economic and political reasons, linked to the availability of the fuel resources. The reduction of emissions from harmful pollutants is mandatory and strictly regulated by environmental organizations. Indeed, these regulations become more and more stringent over the years. The most important and regulated pollutants are carbon monoxide (CO), nitrogen oxides (NO, NO_2), widely known as NO_x, unburned hydrocarbons (UHC) and particulate matter. On the other hand, CO_2 is not considered a direct pollutant, but its emission must be reduced because of the role it plays on global warming [2].

Therefore, the present and well-established combustion processes must be continuously improved, whereas new combustion concepts must be as well explored [3].

There are few options to achieve the goals listed above, both for aviation engines and for stationary devices for power generation.

Lean combustion emerges as an extremely promising strategy to keep the promise of an efficient and clean combustion process, applicable to aviation gas turbines [4], [5]. The peak temperature of the process is lower with respect to the established technology, thus preventing the formation of thermal NO_x. Furthermore, lean combustion allows, in theory, to entirely consume the fuel fed to the combustor and to drastically reduce hydrocarbons and CO emission. Due to the increasingly stringent regulations on pollutant emissions, aircraft engine companies are pushing the research and development on lean technologies. However, further investigations are necessary to successfully implement this strategy. An issue that accompanies the presented technology is the higher thermal stress on the combustor walls: it stems from a lower availability of cooling air because more air is fed via the reaction airflow to achieve a leaner mixture. To adequately face this problem, smarter cooling technologies have been developed. Among others effusion cooling proves to be one of the most effective, being able to provide adequate cooling protection despite the lower available amount of air [6]. The introduction of air along the combustor walls presents, however, a drawback: it poses the problem of the interaction between a reactive flow and cold air. This chance is enhanced in small combustors, whose downsizing is driven by market requirements. In this context, carbon monoxide production becomes a pressing issue. In an ideal combustion process, CO is an intermediate species and should react further to form carbon dioxide (CO_2). This transformation is slower compared to the main combustion reactions and requires adequate residence time at high temperature. In this context, the mixing of hot combustion products with cooling air introduced along the combustor wall could indeed quench the reactions. Therefore, further studies are needed to fully understand the implications of the interaction between a high temperature reactive environment and cooling air.

A combustion process applicable to combustion devices for stationary power generation is oxyfuel combustion [7]. In this concept, a mixture of carbon dioxide (CO_2) and oxygen replaces air, leading to an exhaust gas mainly composed of water vapor and enriched in CO_2 formed by fuel combustion. The CO_2 can be separated, liquefied and stored underground to reduce the effects on the environment. This strategy is gaining increasing attention in recent years because of its suitability in the view of carbon capture and storage technologies [8]: beside the high CO_2 content of reactive mixture, it allows the existing power plants to be adapted to this process, with a lower expense that would derive to implement completely new energy production technologies. The issue here lies in the testing needed to understand the interactions and implications of a reacting environment that is different from what has been studied

so far. CO_2 has a higher calorific value with respect to nitrogen (N_2), determining a different global temperature in the system. Furthermore, CO_2 is one of the main combustion products, and its presence in the system influences the overall combustion kinetics.
As pointed out, these two new combustion concepts are proposed and explored, yet the implications and potential of those concepts are not fully understood. The development and testing of new processes, as well as the improvement of present technologies needs thorough experimental investigations on properly designed laboratory scale model combustors. To this aim, comprehensive experimental investigations on appropriate close to reality configurations are crucial to deepen the understanding of the underlying interactions occurring during the combustion process. These configurations allow considering all the complexity that characterizes real scale processes, though on a smaller scale. Ideally, the modelling of the processes involved supports the interpretation of experimental results. Although computational fluid dynamics (CFD) is nowadays a valuable tool, it is, however, computationally costly especially if detailed kinetic mechanisms are considered. Therefore, a somewhat simpler and more flexible tool is needed.
A reactive flow modelling that fits these needs is referred to as Chemical Reactors Networks (CRN). It employs a properly designed arrangement of ideal flow reactors to obtain a simplified version of the flow field inside a generic combustor. This simplification allows for the use of detailed kinetic mechanisms. A properly designed chemical reactors network enables quantitative species concentrations extraction, making parametric studies possible. This modeling strategy exploits the Residence Time Distribution (RTD) of the flow, that yields the mixing characteristics, which must be reproduced in order to properly describe the reactive flow.

1.1 Aims and Structure of the Work

In the present study, two close to reality configurations that exemplify the combustion systems mentioned above are investigated by RTD measurements followed by CRN modeling.
The aim of this work is to improve the understanding of combustion-based devices that apply the technologies mentioned earlier. This is achieved by designing a chemical reactors network of the configuration at hand and calibrating it against the measured residence time distribution of the system. In this way, an improved understanding of the interaction between mixing and chemical reaction is gained.
The chapters are arranged as follows.

- The next paragraph of this chapter is dedicated to the fundamentals of combustion and combustion features in real configurations. The last chapter is concerned about the modeling strategies applied to combustion.
- Chapter 2 introduces the basics of RTD theory and modeling. The tools and procedures employed in this work are presented, and an overview of Chemical Reactors Network modeling is provided.
- Chapter 3 contains the work carried out on the Single Sector Gas Turbine (SSGT) model combustor. This configuration allows the investigation of the interaction between a reactive flow operated in the lean combustion regime and an effusion cooling air, dealing with a pressing issue relevant for aviation gas turbines. The test rig and the RTD measurements setup are described. Follows a description of the CRNs and the comparison between the models and the experiments in terms of pollutants emission. Finally, the model is applied to several operating conditions to extract the features that characterize each one of them from a mixing and pollutants emission point of view.
- Chapter 4 is dedicated to an experimental apparatus that is conceived to mimic the most important features of power plants combustors applying the oxyfuel combustion technology, the OxyFuel Combustor (OFC). In this case, RTD data from a previous measurement campaign are exploited. Therefore, after showing the experimental apparatus, the designed networks are

introduced, and their performance evaluated. Follows a section commenting on the impact of the operating atmosphere in the case of non-reactive and reactive flow.

- Chapter 5 summarizes the work.

1.2 Combustion Fundamentals

The word "combustion" refers to the reaction between a fuel and an oxidizer that proceeds toward the oxidation of the fuel. As only gas phase combustion is addressed in this work, all the concepts reported in the following refer to combustion of gas species, i.e. single phase multicomponent reactive flow. The reaction is highly exothermic and requires a high activation energy. During the oxidation reactions, the bonds between the fuel molecules and those between oxidizer molecules are broken with release of energy released to the surrounding fluid. The formal equations to treat the evolution of a generic multicomponent reactive system, in the hypothesis of homogeneity of the system itself, are provided in the following, Equation 1-Equation 4 . The aim is to describe how such systems are approached from an analytical point of view, and a deeper description is found in [9]–[11].

Mass balance

$$\frac{\partial \rho}{\partial t} + \underline{\nabla} \cdot (\rho \underline{v}) = 0 \qquad \textit{Equation 1}$$

ρ: density, kg/m^3
$\underline{v}$: velocity, m/s
$\underline{\nabla}$: divergence

Mass balance for each species "i"

$$\frac{\partial (\rho Y_i)}{\partial t} + \underline{\nabla} \cdot (\rho \underline{v}\, Y_i) + \nabla \cdot J_{Y_i} = \dot{\rho}_i \qquad \textit{Equation 2}$$

Y_i: mass fraction of species "i"
$\dot{\rho}_i$: production of species "i"
∇: gradient

Momentum balance

$$\frac{\partial (\rho \underline{v})}{\partial t} + \underline{\nabla} \cdot (\rho \underline{v}\, \underline{v}) + \nabla \cdot J_v = -\underline{\nabla} p \qquad \textit{Equation 3}$$

∇: gradient
J_q: diffusive flux associated with quantity "q"

Energy balance

$$\frac{\partial (\rho h^s)}{\partial t} + \underline{\nabla} \cdot (\rho \underline{v}\, h^s) + \nabla \cdot J_{h^s{}_i} = \sum_i \dot{\rho}_i h_i^0 \qquad \textit{Equation 4}$$

h_i^0: enthalpy of formation of species "i"
h^s: sensible contribution to the enthalpy of the system

$$h^s = \sum_i \dot{\rho}_i \int_{T_{reference}}^{T} c_{p_i}(T) dT \qquad \textit{Equation 5}$$

c_{p_i}: sensible heat of the system

1.2.1 Turbulent flow fields

The main characteristic of a turbulent flow field is the irregularity of its evolution over time. Beside this strong irregularity, these flow fields show high diffusivity of extensive quantities and are intrinsically three dimensional. Furthermore, they are highly dissipative, meaning that the kinetic energy of the flow is converted, through an energy cascade from large scale of motion to smallest eddies, responsible for viscous dissipation, into internal energy. The mentioned high diffusivity of extensive quantities makes this flow attractive for practical applications: when turbulent flows are applied to combustion, mixing is enhanced. However, given the complexity of the situation, the coupling between the equations

Equation 1-Equation 4 makes it impossible to achieve an analytical solution of the system of equations for such flows.
A flow is classified turbulent or laminar based on its Reynolds number [12]:

$$\Re = \frac{\rho v D}{\mu} \qquad \textit{Equation 6}$$

ρ: density, kg/m^3
v: characteristic velocity, m/s
D: characteristic length, m
μ: dynamic viscosity, Pa · s

For $\Re > 4000$, turbulent flows are identified.
Eddies of different size compose turbulent flows, according to [13]. The maximum size of these eddies coincides with the integral length scale of the problem, called also integral length scale, D. The big eddies undergo a break-up process, forming smaller eddies distributed among several different length scales. Energy is transferred from the bigger to the smaller length scales, until the dissipation region, where the energy is dissipated and not transferred further [14]. Based on this concept, two characteristic domains of scales are identified: the integral time and length scales (τ_0 and l_0 respectively, that are highly dependent on the flow), and the Kolmogorov time scales (τ_k and l_k). The latter are the smallest identified scales before viscous dissipation occurs instead of energy transfer.

1.2.2 Chemical kinetics

Considering a generic fuel reacting with an oxidizer to form combustion products, the reaction is written as follows:

$$f Fuel + o Oxidizer \rightarrow p Products \qquad \textit{Reaction 1}$$

Reaction 1 indicates that f moles of fuels react o moles of oxidizer to form p moles of products. In this work, the fuel considered is methane, CH_4, and Reaction 1 is written in a more specific way as Reaction 2:

$$CH_4 + 2O_2 \rightarrow CO_2 + H_2O \qquad \textit{Reaction 2}$$

Reaction 2 is a global reaction: it describes a process; but behind it there is a huge number of elementary reactions [15]. The ensemble of elementary reactions behind a combustion process defines the kinetic mechanisms. For each elementary reaction, a rate coefficient is following an Arrehnius approach:

$$k = k_0 T^{\beta} e^{\left(\frac{-E}{RT}\right)} \qquad \textit{Reaction 3}$$

k_0: pre-exponential factor
E: activation energy
R: universal gas constant
β: temperature exponent

A crucial quantity in combustion processes is the amount of available oxidizer with respect to the fuel defines the stoichiometric conditions of the mixture. If the amount of oxidizer is less than the one necessary to achieve complete fuel burnout, the combustion process is said to be rich. If the amount of oxidizer is more than the one necessary to achieve complete fuel burnout, lean conditions are established. When the amount of oxidizer is exactly the one required to ensure complete consumption of the fuel, the reactive mixture is in stoichiometric conditions. To describe the conditions of a reactive system in terms of stoichiometry, a parameter is used, called equivalence ratio, φ:

$$\varphi = \frac{m_{fuel}/m_{oxidizer}}{(m_{fuel}/m_{oxidizer})_{\text{stoichiometric}}} = \frac{n_{fuel}/n_{oxidizer}}{(n_{fuel}/n_{oxidizer})_{\text{stoichiometric}}} \qquad \textit{Equation 7}$$

m: mass of a certain species, fuel or oxidizer
n: number of moles of a certain species

1.2.3 Swirl combustion

Combustion stabilization in practical configurations is realized by imparting a spiraling motion to the flow entering the combustor. The implementation of this feature shortens the flame length (higher mixing rated), limits flame impingement on the combustor and enhances stability by triggering the formation of recirculation zones by means of vortex breakdown. The recirculation zones recirculate heat and chemical species sustaining the combustion process of the incoming fresh mixture [16], [17]. The degree of a tangential component impressed on the flow, referred to as degree of swirl, S, is defined as the axial flux of tangential momentum divided by axial flux of axial momentum times equivalent nozzle radius, Equation 8 [18].

$$S = \frac{G_{tan}}{RG_{ax}} \qquad \textit{Equation 8}$$

Peculiar features characterize swirling flows in confined configurations, as schematized in Figure 1.

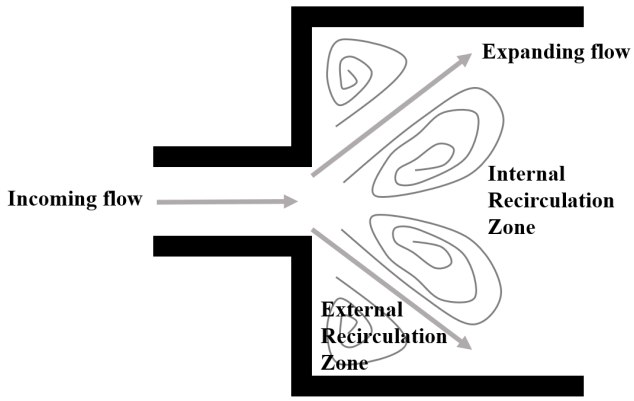

Figure 1: schematization of the main features of a swirling flow in a generic confined configuration. The configuration itself is sketched in black, the features of the swirling flow in grey.

The swirl imparted to the incoming flow is responsible for the formation of the recirculation zones indicated in Figure 1. These are responsible for flame stabilization by recirculating heat and reactive species. Swirling flows are therefore crucial while adopting lean combustion strategies, where the risk of instabilities is high.

1.2.4 Pollutants formation

Several harmful pollutants are formed during the combustion process. The most important, and the ones that will be addressed in the following, are nitrogen oxides, carbon monoxide and soot. However, the latter will not be directly addressed, but rather a precursor, acetylene, will be discussed in the following work.

1.2.4.1 Nitrogen oxides

Several reaction pathways lead to the formation and emission of nitrogen oxides [19], NO_x.

- Thermal NO_x: oxygen radicals attack the atmospheric nitrogen, forming NO [20]. Relevant reactions are the following Reaction 4-Reaction 7:

$$O_2 + M \rightarrow O\cdot + O\cdot + M \qquad \textit{Reaction 4}$$
$$O\cdot + N_2 \rightarrow NO + N\cdot \qquad \textit{Reaction 5}$$
$$N\cdot + O_2 \rightarrow NO + O\cdot \qquad \textit{Reaction 6}$$
$$N\cdot + OH\cdot \rightarrow NO + H\cdot \qquad \textit{Reaction 7}$$

  Reaction 7 is clearly an important one because consumes the hydroxyl radical, that has a crucial role in CO oxidation to CO_2 (more details below).

- Prompt NO_x: the formation of HCN is triggered by the attack from hydrocarbon radicals to atmospheric nitrogen. Relevant reaction listed below:

$$CH_2\cdot + N_2 \rightarrow HCN + NH\cdot \qquad \textit{Reaction 8}$$

$$CH\cdot + N_2 \rightarrow HCN + N\cdot \qquad \textit{Reaction 9}$$

$$C\cdot + N_2 \rightarrow CN\cdot + N\cdot \qquad \textit{Reaction 10}$$

HCN and $CN\cdot$ are easily oxidized to NO.

- Fuel NO_x: the nitrogen contained in the fuel is converted to nitrogen oxides.
- NO_2 formation. This transformation is a relatively slow one, and favoured below 1200 K.

$$NO + \frac{1}{2}O_2 \rightarrow NO_2 \qquad \textit{Reaction 11}$$

$$NO + HO_2\cdot \rightarrow NO_2 + OH\cdot \qquad \textit{Reaction 12}$$

Reaction 9 produces a highly reactive radical ($OH\cdot$) starting from a weaker one ($HO_2\cdot$). For this reason, this reaction might be crucial for CO oxidation to CO_2 in post-flame conditions [21].

- N_2O formation. The reactions listed below acquire importance below 1500 K.

$$NH\cdot + NO \rightarrow N_2O + H\cdot \qquad \textit{Reaction 13}$$

$$O\cdot + N_2 + M \rightarrow N_2O + M \qquad \textit{Reaction 14}$$

1.2.4.2 Carbon Monoxide

Carbon monoxide is an intermediate species in the oxidation of hydrocarbon fuels to CO_2 and H_2O. Therefore, besides being a pollutant, it is also an indicator of fuel burnout. It is obviously present in fuel-rich combustion but should be in theory absent while adopting lean combustion. However, rapid cooling of reactive flow pockets or poor mixing cause high levels of CO to be produced also in overall lean applications. The significant reaction leading to CO_2 from CO is:

$$OH\cdot + CO \rightarrow CO_2 + H\cdot \qquad \textit{Reaction 15}$$

This reaction is strongly affected by the temperature of the system, attribute to the temperature effect on equilibrium OH concentration [19].

1.2.4.3 Soot

Soot is a harmful pollutant produced in the form of carbonaceous nanoparticles. Soot precursors are formed Polycyclic Aromatic Hydrocarbons (PAH) and C_2H_2. The latter is believed to be the dominant mass growth species, according to [22]. C_2H_2 comes from dehydrogenation of hydrocarbon fuels, its formation starts from the recombination of two methyl radicals [23].and is therefore formed in the first react an intermediate towards complete oxidation. It is also directly involved in CO formation through the global process:

$$OH\cdot + C_2H_2 \rightarrow CO + CH_3\cdot \qquad \textit{Reaction 16}$$

Because of its involvement in soot formation, C_2H_2 formation will be consider later in this work.

1.3 Combustion Modeling

As outlined before, the understanding of combustion in technically-relevant configuration is crucial. However, this task is far from being trivial. Direct observation of the phenomena by means of thorough experimental investigations would be ideal, though not always possible in real configurations because of the costs and the large variety of processes involved. For this reason, close to reality configurations are designed, to allow considering features of real combustion-based devices in a controlled environment. An overview of experimental work carried out so far in close to reality configurations is given by [24]. Experimental work is ideally accompanied by numerical modeling of the processes involved: the modeling of the phenomena improves the understanding of the experimental results. Moreover, a strong interaction between experiments and modeling is crucial, because experiments provide evidence to validate models, and predictive, robust and accurate models speed up the design phases of experiments, testing of new concepts and design of optimized real devices. Two numerical modeling strategies are briefly introduced in the following, widely employed nowadays: Computational Fluid Dynamics (CFD) and Chemical Reactors Network (CRN) modeling. Their strengths and weaknesses are highlighted, and the reasons why, in certain situations, one is chosen over the other is given.

1.3.1 Computational Fluid Dynamics

The basic concept of CFD is to solve a set of partial differential equations. The governing equations are the Navier–Stokes and continuity equations. According to [25], three different strategies are employed to carry out CFD simulations of combustion phenomena:

- Reynolds Averaged Navier Stokes (RANS);
- Large Eddy Simulations (LES);
- Direct Numerical Simulations (DNS).

These methods are listed in increasing complexity/computation cost order. They are based on a discretization of the domain (by applying a grid to the domain) in smaller control volumes, and the balance equations are applied and solved in each control volume. The difference among the named methods concerns the different treatment of turbulent motions.
RANS models average in time the equations, and all the turbulence scales are modeled. This reduces the time required for a computation with respect to the other two (see below). When dealing with reactive flows in combustion, heavily simplified models are applied to incorporate chemical kinetics in the computation.
A turbulent flow field is separated in two scales while carrying out LES: a cut-off length is defined and referred to as filter size. Scales smaller than the length of the filter size are modeled using subgrid closure rules, whereas larger scales are calculated explicitly. Detailed chemical kinetics is not incorporated in this strategy because of the huge computational effort that it would imply, and several modeling strategies are applied. LES is more expensive than RANS from a computational point of view.
DNS models explicitly calculate all the instantaneous heat and mass transport equations. In other words, all the turbulence scales of the flow are considered and solved. Detailed kinetics is incorporated in the model. This approach is the most expensive, among the three presented, from a computational point of view, making it impossible to employ it to model practical applications. This chance might be realized in the future, because of the upcoming increase in computational power.
These strategies deliver more detailed insights into the flow field characteristics and the combustion process itself. However, the only two methods that can be exploited to model complex configurations use a heavy simplification of the chemistry. Still, the most important features, namely combustion efficiency and pollutant emissions of combustion-based devices are determined by the complex interaction between turbulence and chemical reactions [26], [27]. Therefore, a somewhat simpler and more flexible tool is needed to incorporate chemical kinetics in the analysis of complex combustion devices.

1.3.2 Chemical Reactors Network modeling

The modeling of turbulent combustion makes an extensive use of Chemical Reactors Networks (CRNs). Such models are based on dividing the combustor into multiple zones according to the identified mixing feature in the specific zone. The mixing characteristics are extremely simplified, and a combustor zone can be regarded as a perfectly mixed or completely segregated one. The identified zones are then properly arranged in series or in parallel to yield a simplified description of the flow field. In each reactor of the network, the chemistry is solved with detailed kinetics. Compared to CFD models, the simplification of the fluid dynamic by adopting zone models with a well-defined mixing pattern lowers the computational demand by several orders of magnitude. The inclusion of detailed chemistry enables the understanding of the species formation pathways even in a complex system. The possibility to include detailed kinetic mechanisms into the analysis, still yielding severely lower computational effort with respect to CFD models, constitutes the main strength of this modelling strategy. On the other hand, the flow field is implemented indirectly, by inferring to a certain region inside the system a specific mixing behaviour rather than the other, and by connecting the zones in a certain way.
Nonetheless, CRN models provide insight into the principal macroscopic mixing and reactive features of a generic complex system. They are indeed widely employed at the design stage of combustion based

devices, to quickly estimate the response of a generic combustor to changes in design details or boundary conditions [28], [29]. The simplification of the flow field in zones with a defined mixing pattern allows a more direct link between setup modification and response of the system, linking it to macromixing pattern. Besides, reliable and validated CFD simulations of real and close to reality configurations are not easy to achieve. When this is the case, modelling the configuration under investigation using a CRN deepens the understanding of said configuration, helping to identify the crucial parameters influencing combustor performance. For this reason, this modelling strategy is extensively employed in this work to study the mixing and reactive characteristics of two close to reality configurations that simplify two pressing topics of combustion research: lean combustion coupled with effusion cooling for aviation gas turbines and oxyfuel combustion for stationary power plants. The different strategies that lead to the design of a CRN are described in chapter 2, together with a literature review about the results achieved by the various research groups adopting this methodology.

2 Chemical Reactors Network modeling

Chemical Reactors Network (CRN) modeling is employed in the following chapters to gain knowledge into the fundamental features that characterize combustion in technologically-relevant experimental test rigs. There are several ways to apply this modeling strategy, outlined in 2.2.2 and 2.4. In the present work, CRN modeling is achieved exploiting Residence Time Distribution (RTD) data of the flow in the enclosed environments under investigation. Therefore, a theoretical background on ideal flow reactors and basics on non-ideal flows is provided in the first part of this chapter, 2.1 and 2.2. After, an explanation of the methodology the tools employed is given. Follows a review of the application of the CRN modeling and the different ways to achieve it.

2.1 Ideal flow reactors

Before a brief description of the basic components employed to design a CRN, quantities relevant to chemical reaction engineering analysis are introduced.

A chemical reactor is a system where a chemical reaction takes place, transforming reactants into products. They are, in the first place, classified based on the type of process they fit in: batch or continuous. In this work, only continuous flow reactors are considered: reactants are fed into the process unit and emerge as continuous stream of product. This kind of process is usually run at steady-state.

The mass balance equation to calculate the conversion of a reactant feed stream in such a system is the generic:

$$output = input - reacted\ quantity \qquad \textit{Equation 9}$$

The term referring to the accumulated quantity, to be subtracted to the input, was omitted because only steady-state systems are treated.

The space-time [30] of a generic stream flowing through a reactor is defined as:

$$\tau = \ time\ the\ system\ needs\ to\ process\ one\ unity\ of\ feed\ stream\ at\ the\ specified\ operating\ condition$$

This quantity measures the advancement of a given reaction, given operating conditions and type of reactor. Thus, it depends on the reactor volume and the characteristics of the feed stream. In a generic situation, where

$$A = generic\ reactant,$$

$$C_{A_0} = concentration\ of\ the\ generic\ reactant\ \mathrm{A}\ in\ the\ feed\ stream, \left[{}^{mol}/_{m^3}\right]$$

$$V = volume\ of\ the\ reactor, [m^3]$$

$$F_{A_0} = molar\ flow\ rate\ of\ reactant\ A\ entering\ the\ system, \left[{}^{mol}/_{s}\right]$$

$$\dot{v} = volumetric\ flow\ rate\ entering\ the\ system, \left[{}^{m^3}/_{s}\right]$$

$$X_A = degree\ of\ conversion\ of\ reactant\ A, [-]$$

$$r_A = volumetric\ reaction\ rate\ of\ reactant\ A, [unit\ depends\ on\ the\ reaction\ order]$$

the space time is calculated as:

$$\tau = {}^{C_{A_0} V}\Big/_{F_{A_0}} = {}^{V}/_{\dot{v}} \qquad \textit{Equation 10}$$

2.1.1 Continuous Stirred Tank Reactor

The Continuous Stirred Tank Reactor (CSTR), schematized in Figure 2, is the simplest flow reactor because it provides a 0D description of the flow and reaction pattern. The hypothesis behind it is that, as soon as the reactants enter the system, the mixing is so efficient that the concentration inside the system is spatially uniform and equals the concentration of the outgoing stream.

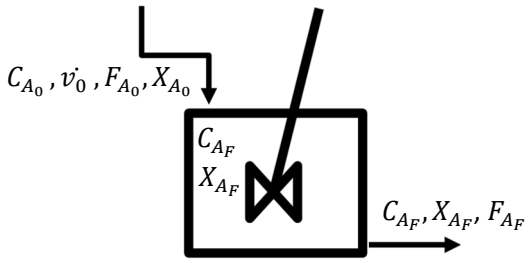

Figure 2: schematic of a Continuous Stirred Tank Reactor.

Because of the specific assumption of perfect mixing that is the foundation of this reactor, the terms of the general equation, Equation 9, is written as follows:

$$F_{A_0}(1 - X_{A_0}) = input \quad \textit{Equation 11}$$

$$F_{A_0}(1 - X_A) = output \quad \textit{Equation 12}$$

$$(-r_A)V = consumed\ quantity \quad \textit{Equation 13}$$

And the space-time of the reactor is given by:

$$\tau = {C_{A_0} V}/{F_{A_0}} = {V}/{\dot{v}} = {C_{A_0} X_A}/{(-r_A)} \quad \textit{Equation 14}$$

2.1.2 Plug Flow Reactor

The Plug Flow Reactor, or PFR (Figure 3), introduces complexities with respect to the previously presented reactor. It provides a 1-D description of the flow inside a system, and in this case the conversion of the reactants proceeds along the spatial coordinate, which is therefore also a reaction coordinate. This means that the concentration of each species varies along the length of the reactor. A plug flow is assumed, such that there is no back mixing of reactants and no possibility that a reaction product mixes with the unreacted, entering stream. However, along each cross section, perfect mixing on the radial coordinate is assumed.

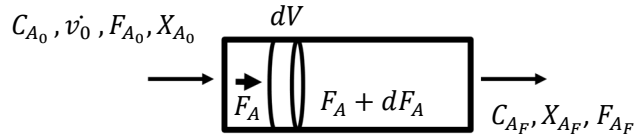

Figure 3: schematic of a Plug Flow Reactor.

Because of the basic hypothesis behind a PFR, Equation 9 should be solved for each control volume inside the system, dV. Therefore, for each dV:

$$F_A = input \quad \textit{Equation 15}$$

$$F_A + dF_A = output \quad \textit{Equation 16}$$

$$(-r_A)dV = consumed\ quantity \quad \textit{Equation 17}$$

And the space-time of the reactor is given by:

$$\tau = C_{A_0} \int_{X_{A_0}}^{X_{A_f}} {dX_A}/{(-r_A)} \quad \textit{Equation 18}$$

As stated before, and as proved by the absence of the accumulation term in Equation 9, the equation written up to now describe a steady state system, and no evolution over time is taken into account.

2.2 Residence time distribution

The two ideal flow reactors presented characterize two extreme mixing possibilities. To simplify the study of a certain system, a flow may be approximated either as fully mixed (CSTR) or completely segregated (PFR). Beyond a first simplification, real systems behavior is in between these two: there might be regions where complete mixing is an acceptable approximation, together with regions better

described by plug flow. In addition, flow peculiarities such as dead volumes (stagnant regions that trap part of the flow inhibiting good mixing, Figure 4.a), or channeling of the flow (part of the flow that is accelerated to the exit of the rector without having the chance to properly react, Figure 4.b) might as well take place, complicating the fluid dynamics of the system. In most cases, systems whose behavior can at a first glance be traced back to ideal systems, might undergo complex non-idealities, as shown in Figure 4.

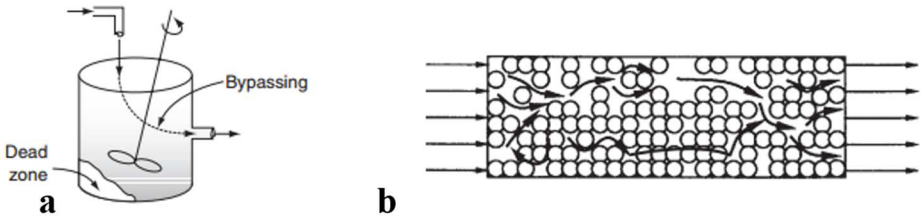

Figure 4: example of non-ideal flow in configurations that can be, in a first approximation, treated as ideal flow reactors, [30]. ***a**, non-ideal CSTR; **b**, non-ideal PFR.*

The study of real flow configurations gets more and more complicated the more information is needed for a good characterization. To approach this problem, it is necessary to focus on the basic information that allows reconstructing the fluid history inside a generic system. This is the distribution of residence times of the flowing fluid, i.e., the time the individual flow pockets spend inside the system. This distribution arises from the different lengths of time that different pockets of fluid take to pass in a flowing system where non-idealities of the flow occur: fluid particles that entered at the same time might not leave the reactor at the same time. For this reason, it is crucial to determine the Residence Time Distribution (RTD) of the flow [30]–[32], also represented by the notation $E(t)$, as for Exit Age Distribution. $E(t)$ has units s^{-1}, and it is normally presented in its normalized form:

$$\int_0^\infty E(t)dt = 1 \qquad \textit{Equation 19}$$

In the following paragraph, the relevant aspects of Residence Time Distribution Theory will be briefly reviewed, according to [30]–[34].

The RTD of a system is determined experimentally, adopting the stimulus-response experiment: a certain amount of an inert tracer is introduced in one or all feed streams entering the reactor under investigation, with a defined input function. The temporal evolution of the concentration of this tracer in the stream exiting the reactor yields, directly or after mathematical treatment, the RTD of the reactor itself. In this way, the investigated system is treated as a black box: it is nothing more than a vessel with continuous fluid flow, as exemplified in Figure 5.

Figure 5: black box-treatment of a generic real system. An input is introduced in the system, and the output yilds information on the intrinsic behavior of the system itself.

Adopting the described procedure, a perturbation, also referred to as disturbance, in the steady-state concentration of the system is introduced with a certain function over time. This perturbation propagates through the system experiencing its mixing features. The time-dependent concentration of the tracer at the exit of the reactor differs from the one at the input. This difference is due to the peculiarities of the flow and mixing characteristics of the vessel: it is the result of the mixing pattern that occurs and enables to retrieve the transfer function of the system concerning its mixing behaviour. For the RTD to be a meaningful quantity to give insight into the global fluid dynamic of a generic reactor, it should respect the "closed-closed" vessel boundary condition: the flow can pass the boundaries, ideally conceived as detection stages as well, just once. In other words, there must be no risk of detecting the same pocket of fluid twice.

Several input schemes to inject the tracer can be considered [30], [33], but only two of them are detailed in the following because the other possibilities can be regarded as combination of the described two.

- Pulse input function: while adopting this injection strategy, a given amount of tracer is introduced at $t = 0$ in the designated stream in a short time, ideally employing a Dirac-delta function, $\delta(t)$. As such a function is difficult to achieve in real experiments, while dealing with practical problems it is enough that the input pulse is significantly shorter than the mean residence time of the system under study. As the tracer passes through the system experiencing its mixing features, the peak of the concentration curve gets lower and its shape gets stretched: the resulting curve is referred to as the C_{pulse} curve. If a quantity M, expressed in kilograms or moles, of a tracer have been fed to a stream whose flow rate is $\dot{v}$, and the concentration over time exiting the system is C_{pulse}, the RTD is obtained from:

$$E(t) = {C_{pulse}(t)}/{M/\dot{v}} \qquad \textit{Equation 20}$$

  As illustrated in Equation 20, the response of any system to a pulse input readily yields its RTD. For this reason, a pulse input is preferred, though its practical implementation is far from trivial. From the $E(t)$, the following global quantities are deduced:

$$\tau^m = \int_0^\infty t\, E(t)\, dt \qquad \textit{Equation 21}$$

$$\sigma^2 = \int_0^\infty (t - \bar{\tau})^2 E(t)\, dt \qquad \textit{Equation 22}$$

$$S^3 = \int_0^\infty (t - \bar{\tau})^3 E(t)\, dt \qquad \textit{Equation 23}$$

  Equation 21 defines the mean residence time of a system. It indicates the mean of the distribution, and the time a pocket of fluid spends on average in the configuration. In an ideal situation it is the same as the space-time τ, otherwise the two values differ due to flow non-idealities. Equation 22 calculates the variance of the distribution, a measure of the spread of the curve. The skewness of the curve is obtained by Equation 23. It quantifies the asymmetry of a distribution: $S^3 < 0$ indicates a left skew distribution, right skew otherwise.

- Step input function: at $t = 0$, the concentration of the tracer in the inlet stream is suddenly increased to its final value and kept constant indefinitely. The transition from 0 to the final concentration value should be as fast as possible, ideally reproducing a Heaviside function. As the disturbance propagates through the system, the peak concentration gets lowered because of the mixing of the tracer. The outlet curve C_{step} is, in this case, a Cumulative Distribution Function (CDF), normalized according to its maximum value. It is referred to as $F(t)$. If $\dot{m}$ is the mass or molar flow rate of tracer injected in a stream whose flow rate is $\dot{v}$, the peak concentration in the outlet stream is given by:

$$C_{max} = {\dot{m}}/{\dot{v}} \qquad \textit{Equation 24}$$

  And the CDF normalized accordingly:

$$F(t) = {C_{step}}/{C_{max}} \qquad \textit{Equation 25}$$

  The probability density function $E(t)$, and the CDF are linked by

$$E(t) = {dF(t)}/{dt} \qquad \textit{Equation 26}$$

  The positive step input has just been described, but in practical experiments, it might be more convenient to use a negative step input. While adopting this procedure, the investigated system is continuously fed with a known amount of tracer, until the concentration of the tracer at the exit (at the measurement location) reaches its steady-state value. at $t = 0$, the concentration of the tracer in the inlet stream is suddenly stopped to its final value and kept constant indefinitely.

As the RTD is the response of a system to a known disturbance, the distribution of residence times for the ideal systems introduced in 2.1 can be analytically retrieved [35]. To this aim, the concept of transfer

function is applied. A transfer function is a function that models the output of a system for each possible input. The mathematical model of systems with regards to the investigated quantity must be written to obtain the transfer function. Considering a CSTR, where $\dot{v}_{in}$ and $\dot{v}_{out}$ are the incoming and exiting flow rates in m^3/s, and C_{in} and C_{out} the inlet and outlet tracer concentration, the mass balance on the tracer concentration in a reactor whose volume is V, is written as follows:

$$V\frac{dC_{out}}{dt} = \dot{v}_{in}\,C_{in} - \dot{v}_{out}\,C_{out} \qquad \textit{Equation 27}$$

Transforming the previous balance equation to solve it in the Laplace domain (variable s), and solving for C_{out}, one obtains:

$$C_{out} = \frac{\left(\dot{v}_{in}/\dot{v}_{out}\right)}{\left(\left(V/\dot{v}_{out}\right)s+1\right)}C_{in} = \frac{(K_P)}{(\tau\, s+1)}C_{in} \qquad \textit{Equation 28}$$

Equation 28 is a specific case of the more general Equation 29, describing the evolution of a linear system:

$$\frac{Output}{Input} = G(s) \qquad \textit{Equation 29}$$

$G(s)$ is the transfer function of a generic system. K_P is referred to as the Gain, and τ is the Time Constant [35] of the transfer function of the CSTR: $G(s) = \frac{(K_P)}{(\tau\, s+1)}$. Using the transfer function, it is possible to retrieve the effect of variations of C_{in} on C_{out}. The analytical form of the RTD of a stirred reactor is obtained by returning into the time domain. For an isothermal system:

$$E(t) = e^{-t/\tau}/\tau \qquad \textit{Equation 30}$$

For a PFR, the discussion is even easier. According to the basic hypothesis behind the PFR, there is no back mixing of products and piston flow is ensured. Therefore, the exit of the system shows the same behavior as the entrance but delayed. The delay time between the injection of the tracer and its appearance in the outlet concentration is the physical time the flow takes to reach the outlet, τ. Therefore, for a PFR:

$$E(t) = \delta(t-\tau) \qquad \textit{Equation 31}$$

The $E(t)$ obtained for the two systems is shown in Figure 6. It is to be noted that, differently from the characteristic equations, Equation 11-Equation 18,written for ideal flow reactors in the previous paragraph, the equations needed to describe the tracer evolution inside the system are time-dependent. RTD analysis studies the response of steady-state systems to non-steady disturbances and check whether new steady states are reached and how.

The analytical expressions for the RTD of the ideal flow reactors are the starting point to approach the analysis of real systems, characterized by more complicated RTDs. When dealing with such complex mixing patterns, simple flow models comprising a given number of tuning parameters can be fit to the RTD to understand the behaviour of the system under investigation, retrieve the impact of different operating conditions on the chosen parameters and estimate the performance of the reactor. These flow models are sorted as follows:

- one-parameter models,
- multi-parameters models.

The one-parameter models category comprises two main approaches to RTD modelling, briefly presented in the following.

- The dispersion model. This strategy superimposes a certain amount of dispersion [36] to the plug flow of a generical stream: in this way, it is possible to explain the peak broadening that follows the sharp injection of a tracer in a flowing fluid via a pulse-like input function. The dispersion parameter D is therefore the parameter that accounts for the non-idealities of the system considered.

- The tanks-in-series model. In this case, the treatment stems from the basic statement that a PFR can be regarded as an infinite number of CSTRs (referred to as "tanks") in series. Being the CSTR model able to describe two opposite flow behaviours, a suitable number of CSTRs in series between 0 and infinite can reasonably describe the mixing properties of a general system. The tuning parameter, in this case, is the number of tanks to put in series.

One-parameter models are practical, flexible and applicable to a wide range of situations. However, they provide a one-dimensional description of the flow, making it not possible to account for large scale non-ideal flow phenomena, like recirculation or bypassing. For a more elaborate modelling, multi-parameters models are applied.
In these models, the ideal systems introduced in 2.1 act as basic construction blocks to setup a network of interconnected ideal flow reactors whose dynamic behaviour is as close as possible to the one of the investigated real configurations. In other words, the RTD that characterizes a non-ideal case is regarded as the response of a system consisting of ideal flow reactors arranged in a proper way, assuming the superposition principle. Therefore, the real reactor under investigation is assumed as the combination of ideal reactors arranged in a suitable way, whose mathematical description is well-known. This approach is exemplified in Figure 6.

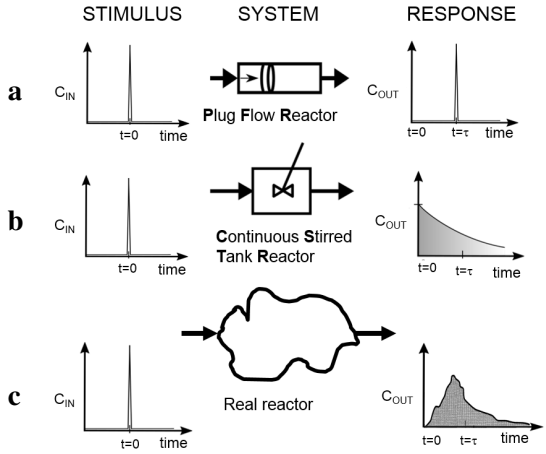

*Figure 6: pulse responses of ideal system and generic response of a real system. **a**: PFR; **b**: CSTR; **c**: exemplified real reactor.*

The great strength of these models lies in the chance to achieve an analytical model of a complex, non-ideal flow, where sensitivity analysis and basic understanding of the phenomena is, generally, difficult. They are addressed as Compartmental Models (CM) or Chemical Reactors Network (CRN) models. By applying such a modelling strategy, the flow is decomposed in ideal elements, enabling the study of troubleshooting, reactor performance and sensitivity analysis. Once a model is designed, it needs to be properly sized by matching the RTD of the system. This methodology is explained in the next chapter.

2.2.1 Chemicals Reactors Network fit

The problem that drives the present work, and more generally, the setup of suitable CM to reproduce the RTD of a system, can be stated as follows: given a Residence Time Distribution from a generic system, determine a Chemical Reactors Network whose RTD is the closest possible to the measured one. Generally, to design a CRN of a given configuration, the guidelines set by [37]–[39] are applied. In short, the listed steps are followed:

1. Establish the reactor unit representation. In this work, the reactors employed as base unit of the network are the ones introduced in 2.1: the CSTR and the PFR.
2. Design the reactor network superstructure: a superstructure is postulated that considers different feeding, recycling, etc., strategies for the reactor units. In this step, a network arrangement is designed, and is should comprise all the flow features that might occur in the process under

investigation. These features comprise, as an example, recycling of part of the flow, or trapping of flow in dead zones. The chosen superstructures used in this work, and the criteria behind them, are explained in the following sections, 3.3.1 and 3.3.2, 4.2.1 and 4.2.2.

3. The designed superstructure is formulated as an optimization problem.
4. The optimization problem is solved.

More details are provided about 3 and 4.
Once a CM layout is designed, the values of several network parameters, or network variables, be determined. These parameters are, usually:

- zones volumes,
- flow rates exchanged among the identified zones,
- temperatures or heat exchange coefficients if non-isothermal processes are considered.

For the mathematical treatment of the problem, the introduction of the tracer in a steady-state system is regarded as a disturbance of the system state. From a phenomenological point a view, it is necessary to describe the propagation of a generic disturbance, introduced with a generic input function, in a system [35]. The problem is therefore approached assuming a linear lumped-parameter system, a good approximation for single input-single output cases (SISO): it is defined by ordinary differential equations, describing the evolution of the concentration of the tracer in the network over time. Spatial gradients are not considered. In this scenario, a first-order linear system accounts for the CSTR, as in Equation 28, and a delay time accounts for the PFR, Equation 31.
A mathematical model is written for each base unit of the network, considering interconnections and flow splitting. It provides the equations to calculate the space-time of the adopted reactors (τ), and the gain parameters (Kp) for the mixing of multiple streams, starting from the zone volumes and exchanged flow rate. For the generic reactor unit, the following equations are written:

Mass balance $$\dot{m}_{in} = \dot{m}_{out}$$ *Equation 32*

Space-time calculation $$\tau = V / \left(\frac{\dot{m}_{out}}{\rho}\right)$$ *Equation 33*

Where

$\dot{m}_{in}$	Incoming mass flow, kg
$\dot{m}_{out}$	Outgoing mass flow, kg
V	Reactor volume, m^3
ρ	Density of the stream, kg/m^3

Beside the reactors units, other components constitute the network: splitters and mixers. A splitter allows a generic stream to feed more than one unit, as long as the mass balance is respected. It is characterized by the splitting ratio α, that quantifies the ratio of splitter feed stream in all the splitter exit streams. A mixer merges two feed streams, coming from different reactors, and usually with a different tracer concentration. Their treatment is exemplified in FIGURE.

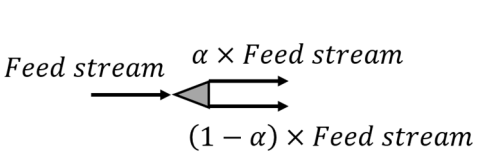

Figure 7: schematization of a splitting element.

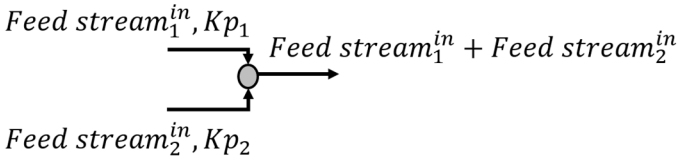

Figure 8: schematization of a mixing element.

Equation 32 must be fulfilled in both cases. The evolution of the concentration of a generic species, in this case the one of the inert tracer that has been introduced, is treated as follows:

- Splitter: the concentration of the outgoing streams equals the one of the stream entering the splitter.
- Mixers: the equations are written following Equation 27, Equation 28 and Equation 29, and the K_P coefficients for each stream are retrieved.

The equations above are written for every component of the network: for each reactor, mixer and splitter, constituting the mathematical model of the system. This model is implemented in Matlab®, and allows the calculation of the τ and Kp. It is linked to a Simulink® flow chart that calculates the dynamic response of a given system: the network superstructure is reproduced in the Simulink® environment. In this environment, the dynamic response is calculated by stimulating the system with an int signal that acts as "disturbance signal". It is propagated through the system, according to the dynamic behaviour of the base units and their arrangement. In the following chapters, the input function fed to the Simulink® model is the inlet signal measured during the RTD experiments. The Simulink® model comprises several components:

- the base units: either a first-order transfer function (CSTR) or a delay time (PFR);
- splitters: a stream exiting a certain zone can be distributed to more than one subsequent zone;
- mixers: if more than one feed stream enters a reactor, the streams are assumed to perfectly mix in advance;
- source components: source of a signal, usually the inputs to a model;
- sink components: to collect and export signals, usually the outputs of a model.

The output of the simulation is a curve over time (the RTD in this case) describing the dynamic response of the system to the disturbance introduced and is a function of the parameters identified for a given network in terms of volumes and flow splits. This curve is then compared to the experimental curve in terms of sum of the squared residuals: this is the objective function that must be minimized in order to retrieve the value of the network variables. To this aim the mathematical model coupled with the Simulink® flow chart is implemented in an optimization routine. The basic steps of the CRN-fitting routine are clarified in Figure 9. The Matlab Global Optimization Toolbox® and its built-in functions are employed.

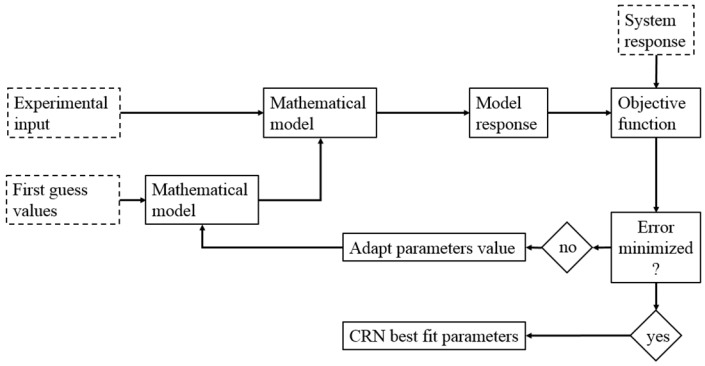

Figure 9: CRN-fitting procedure.

2.2.2 Chemical Reactors Network solver

Once the network has been calibrated against the RTD of the system, the chemical kinetics inside each reactor unit is solved by using a newly developed solver for CRN kinetic evaluation: NetSMOKE [40], a C++ code to solve reactor networks models. An input file is written, comprising all the units, reactors and mixing/splitting devices, and is read by the program, that applies the required kinetic mechanism. All kinetic mechanisms can be used together with this solver.

2.3 Residence Time Distribution and Chemical Reactors Network

In the previous paragraph, the basics of RTD theory have been presented, and the importance of such quantity clarified. The response of a system to a stimulation with a known disturbance gives macroscopic

information about the fluid dynamic behavior of the system itself. RTD data can be exploited in several different ways, each one crucial for the understanding of the facility under investigation.
As explained earlier, combustion in practical situations is a highly complex phenomenon: the transformation of the fuel often takes place in a highly turbulent environment, with peculiar features generated by the existence of a swirling flow, 1.2. Therefore, for a good understanding of the processes involved, description of both mixing and chemical reactions is needed. One way to deal with such a complex task is to start from the global response of the combustor, regarded as a generical system. This strategy approaches the complexity stemming from the intimate connection between mixing and chemical reaction from a macroscopic point of view. A direct exploitation of the RTD lies in the calculation of the global flow quantities from the distribution curve: in this way the overall mixing behaviour of the system is quantified by the calculation of few crucial quantities, as in Equation 21, Equation 22 and Equation 23. Moreover, a complex reacting system can be modelled based on RTD data. This option is widely used, as it allows the comparison between ideal responses and the real response at hand by involving one or more parameters, that encase all the sources of non-ideality that apply to real systems. These models, called Chemical Reactors Network (CRN) models, or Compartmental Models (CM), match the requirements set by the need for a description of the mixing features together with a detailed description of the chemical kinetics. RTD-derived CRNs involve usually few zones, exemplifying the macro mixing features of a process. This coarse description encases also the strength of this modelling strategies: a low number of zones describing the gross flow structures allow the identification of the main mixing and reacting properties of the flow, enabling trend identification and guiding reactor design [29], [41], [42].
Among the first studies to lay the foundation of RTD notion, [31], [32], approach the RTD study from a theoretical point of view, linking it to the ideal flow reactors and deducing the analytical RTD for ideal systems. [30] extends these works, adding further suggestion on the use of RTD. The field is further explored in [43], dealing with the connection between RTD and micro mixing, while [44] summarizes the analytical ways to interpret the distribution of residence times in a system. Following these pioneering studies, RTD data have been used, and are still widely employed in the chemical industry, for design and troubleshooting purposes. More important, these data are actively used to gain insight on the effect of design variables on the performance of the system under investigation [45]–[47]. A review is provided about RTD in the industrial area, although limited to the use of radiotracers [48]. In general, these CRNs are rather simple and designed considering the features that are most likely relevant to the process. Therefore, although information about the output are obtained with this technique, a general compartment model does not make it possible to relate its base units to defined zones inside the reactor as pointed out in [44]. In combustion research, a good description of the mixing pattern is crucial. Therefore, the interpretation of RTD data is given in terms of main flow structures inside the system, as proposed by [41], [49]: in these works, it is already proposed to choose and connect the base units retrieving a correspondence between the ideal flow reactors and the flow features in the different zones inside the combustor. According to this strategy, the identification of zones with a preferred mixing pattern based on the local flow characteristics and their subsequent representation by means of a base unit is referred to as “zonal modelling”. A CSTR is used to describe volume that has been identified inside a system if no preferential flow direction is present, whereas a PFR is preferred when a preferential flow direction is identified, as stated in [50]. According to this strategy, [51] presents a simple schematization of a gas turbine combustor employing a CSTR to model the first part of their facility, also referred to as primary zone, where reactants and fuel are mixed and the flame is stabilized, and a PFR to model the final part. It was proven that this reactor arrangement was indeed the one yielding the best performance. After this sensitivity study, they measure RTD in a water model of a furnace, and in the real furnace under reactive conditions. The tests proved that, indeed, a real combustion device can be approximated with the series of ideal reactors mentioned above. It was also noted that a different swirl number yielded a different value of the ratio between the stirred part and the segregated part. It was furthermore proved that the results achieved in the cold prototype model and those achieved in the

furnace showed a good agreement if the swirl number was kept the same for both cases. This kind of study was proposed again by [52]. Building on the previous work, the authors carried out RTD measurements at the outlet of a model gas turbine combustor, varying the inlet position. In their opinion, measuring the output tracer response between various locations within the combustor was crucial in order to overcome the risk of non-uniqueness of the arrangement of ideal reactors in a network. The aim of the experiment was twofold, as it was carried out also to validate an algorithm to calculate the distribution of residence times starting from CFD data. The volume obtained for the primary, stirred zone in the combustor was used to determine the lean blowout limit for the investigated combustor. RTD data enabled the estimation of the primary combustion zone volume also in [53], where the tracer response with and without combustion is compared and commented in terms of entrainment of the tracer and frequency of the tracer peaks detected. [54], [55] faced the problem of the optimization of municipal waste incinerators. They dealt with it calculating the RTD from CFD results and analyzing it in terms of desired macromixing inside the system. Because of these studies, [54], [55], modifications for the improvement of the system were proposed, proving once again the relevance of the distribution of residence time for system design and optimization. The studies also highlighted that the geometry of the system itself plays a crucial role in the mixing process. The latter finding was supported by CFD and subsequent RTD calculation of the chamber with a modified geometry, that enhanced the mixing in the system under investigation. [56] carried out a similar work, developing their model based on the RTD obtained from CFD data of two pulverized coal flames furnaces. They proposed three simple CRN models of interconnected reactors based on the knowledge of main flow and mixing zones. The models were tested against the CFD- calculated tracer response for both ovens, which had different thermal output. These models presented few optimization parameters, obtained via optimization of the network response to the distribution of residence times. The developed network was optimized against experimental data as well, proving capable of adapting to several practical situation, and was exploited in a subsequent work [57]. Here, detailed kinetics is applied to the reactors model in order to gain knowledge on the combustion of pulverized coal in a confined swirling furnace.
[41] exploited the finding from [51] about the swirl number in a cold or reactive case to carry out a RTD analysis in a scaled down version of a furnace. This work presents RTD measurements in a cold swirling flow, focusing on the effects of the swirl number. The measurements were carried out at three different locations inside the system: at the exit of the chamber, both at the centerline and off-centerline, and inside the internal recirculation zone formed by the vortex breakdown of the swirling flow, on the centerline. Based on the results obtained from these three measurements locations, the flow features were reconstructed, and a CRN was accordingly designed. It allowed a deeper insight in the mixing characteristics of the system with respect to [51], because few network parameters were identified and optimized based on the RTD data. The extreme simplicity of the network [51], though correctly reproducing the effect of the different operating conditions on the gross schematization of the flow pattern, does not properly highlight the different routes the flow might take inside such a system. Real combustion devices have complex flow patterns comprising zones with different mixing characteristics parallel to each other, and a simplified version of the flow should consider them. This is what the networks [41], [56] try to include in their works. Referring to the Figure 10, they identify the recirculation zones and a jet zone, and arrange networks that consider their presence.

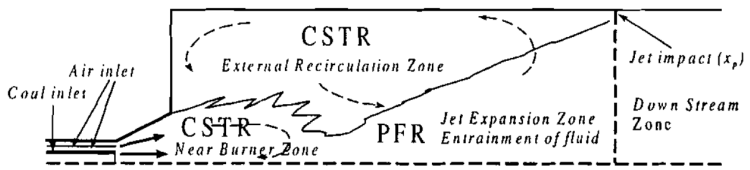

Figure 10: simplification of the fluid dynamics of a confined swirling flame, from [57].

Usually, a recirculation zone is represented by a CSTR, because there is no preferential direction of the flow and they can be considered as perfectly mixed volumes. A PFR is preferred when a preferential

flow direction can be identified, and jets and the shear regions between the recirculation zones are usually represented as plug flow systems.
[58], [59] acknowledge and exploit the power of RTD data for combustion chamber design purposes. More in detail, the authors measured the distribution of residence times in a secondary combustion chamber of a rotary kiln, together with temperature profiles. These data, together with the knowledge of the flow pattern the combustion facility, were used to fit a network of interconnected flow reactors able to reproduce the response of the system. The simplified system highlighted issues in the mixing process, and modification of the system were proposed. Detailed kinetics is applied to the network of reactors in [58]. The emission trends were correctly predicted, although the overall agreement with experimental data was poor. Nonetheless, the correct identification of the trends confirmed the validity of the identified network: it was then employed to identify the sensitivity of these trends to the parameters of the CRN model.
Further works exploiting residence time distribution data to deepen the understanding of phenomena in gas turbine model combustors are [60]–[62]. [60] measures RTD in a gas turbine combustor with the aim of testing different injector arrangements. The differences between an injector arrangement comprising a central jet and one without the central jet were highlighted and explained by means of the tracer decay curves. RTD measurement have been carried out in [61] as well, and the RTD analysis was complemented by the design of a CRN to explain the observed phenomena in a scaled model of a combustor. This work is extended in [62], exploring reactive conditions and exploiting RTD-modeling to assess the effect on the flow field of steam diluted conditions. Here lies the strength of such an analysis: when investigating new combustion concepts, RTD-analysis is a powerful candidate for a first examination on the impact of the operating conditions with respect to the benchmark combustion process. In [62], the different mixing characteristics among cold flow, as well as reactive flow at dry and steam diluted conditions are highlighted and discussed, once again by means of a CRN analysis. The network proposed is a very simple one, showing a jet zone, two recirculation zones (internal, IRZ, and external, ERZ) receiving flow from it and a segregated zone downstream of the jet. The jet zone, having high flow velocity and a preferential direction, was modeled as a PFR, whereas a CSTR for each zone represented the recirculated flow regions. The zones were established based on zonal modeling of the flow; therefore, the volumes of the zones were deduced from the available PIV measurements in the different situations investigated. What emerged from the study, was that the volumes that refer to the different zones are indeed different when the operating conditions change, pointing out the importance of the zones volumes determination. [63], [64] investigated oxyfuel combustion atmospheres for both gas and coal flames exploiting RTD measurements. The results of the measurements were linked to the different flow and reactive behavior while investigating oxyfuel combustion by analyzing the principal moments of the distributions. A simple CRN, similar to the one in [51], was fitted to the data. The aim of this simple CRN-fitting was twofold. The first was to obtain smooth distribution curves out of noisy ones, without applying severe signal-filtering of the data. From these smooth distributions, the principal moments (Equation 21-Equation 23) were retrieved. In this case, a CRN-fitting was also employed as a suitable RTD signal-postprocessing strategy. Beside this application of the CRN, it proved once again a valuable tool to understand the impact of the operating conditions on the mixing pattern by allowing the calculation of the ratio between the stirred and segregated region while moving from air-fed combustion environments to oxyfuel combustion, varying the ratio $CO_2/O2$.

2.4 Other Chemical Reactors Network strategies

Given the complexity of practical combustion systems, the chance of a simple, yet effective, schematization of the process employing ideal flow reactors is attractive. CRN strategies independent from RTD data have been developed and applied over the years.
A network of interconnected ideal flow reactors was recognized as the best option to model combustion in a practical environment [65] against the turbulent flame speed models and the microvolume burning

models. What makes this analytical modelling appealing is that in each reactor a detailed kinetic mechanism is applied to model the combustion reaction. Furthermore, choose and connect the base units retrieving a correspondence between the ideal flow reactors and the flow features in the different zones inside the combustor aids the identification of underlying process. The authors [49], [65], [66] identified the critical features and the corresponding zones in a combustion chamber in terms of mixing characteristics and modeled them accordingly using ideal flow reactors. The flow splits were grossly established based on the subdivision of the quantity of air required for reaction and available for secondary inlet and were refined using a program for flow pattern prediction and the available experimental data. The inclusion of the principal characteristics of the flow field in the model had the aim of enabling the investigation of flame stability characteristics as well, i.e. blow off. The model was used in the first place to get performance and emission trends and showed a good prediction capability in a later work [66], where the results were compared to experiments. In the latter work, the usage and strengths of a CRN are emphasized and framed referring to the need of emission reduction and new technology development. [67] designs a CRN to be employed as a hybrid combustion design strategy. It is based on based on turbulent mixing concepts applied to partially stirred reactors, which takes as its starting point the geometrical shape for a given design and predicts the performance variables (like blow-off, combustion efficiency etc.). The primary zone, in which combustion starts and occurs in a recirculation zone, where combustion products are recirculated to the root of the flame and stabilize it, was described using two parallel CSTRs in a recycle loop. This strategy had been first adopted by [68], where this arrangement was employed to explore flame sensitives while changing operation parameters. These first works state the extreme importance of being able to predict stability issues, crucial for gas turbine operation. The possibility of gaining blowout information from this zonal modelling of the combustor makes it appealing while in the designing stage. Several studies have been published with the precise aim of exploiting a simplified version of a combustor as a simple tool to gain stability information [26], [69]–[72]. In [26], [69] blowout conditions are investigated first using one CSTR to represent the primary combustion zones, and then retrieving a more complex network from CFD calculation, postprocessing the numerical results using a supra-grid approach that took into account several characteristics of the different zones. [70] used the same approach to achieve the reactors network, and applied it to vitiated combustion, proving the suitability of the CRN modelling to aid the study, design and development of novel combustion processes.

The usage of a reactors network to predict stability, and therefore the chance to gain information inside the combustor and not only at the exhaust suggest another strength of this tool: the possibility to estimate species formation and combustion performance in the different zones inside the combustor itself, though a really gross network (i.e., two or three reactors as in [51]) proved insufficient to this aim, as pointed out by [41]. Based on this consideration [73] put effort in designing a reactors schematization to include air staging and entrainment of flow in the near wall region. Based on their results from the model, they propose empirical correlations to predict pollutant formation in the different zones of a generic combustor. Following this path, the capability of the CRN modelling was successfully applied by [74], whose authors summarize the findings from previous works to design effective CRNs to include in a global plant simulation code. They strongly state the necessity of being able to describe the different combustion modes that take place in a combustion chamber, namely premixed or diffusive. These different possibilities of combustion operation pose the necessity of being able to consider diffusive processes while employing ideal reactors, that expect instead a homogenous mixture. To this aim, they rely on previous works [73], [75] and move from them to propose two different networks applicable to premixed and diffusive combustion. In this way, a premixed combustion and a Rich-Quench-Lean combustor are modeled. The works [76]–[78] deal as well with the representation of a diffusive combustion chamber, starting from the calculated fluid dynamic solution. The diffusion process is taken into modeled using parallel reactors, and their operating network parameters are determined by the calculated mixture fraction.

[79] take advantage of a reactor approach to investigate the importance of the nitrous oxide pathway in lean premixed gas turbine combustion. They employ the simplicity already set by [51] and carry out a sensitivity analysis by varying the volumes of the main reactor-zones identified. This work was ampliated later [80], [81] where the model was applied, respectively, to a lab scale GT combustor to identify the main mechanisms of NO_x and CO formation while changing the inlet parameters, and to investigate the role of unmixedness on the formation of those same pollutants in an industrial lean-premixed gas turbine engine combustor. In both cases, the CRN strategy gave insights into the main mechanisms responsible for pollutant formation in lean premixed operation. Further investigations about lean premixed operation for gas turbines are carried out by [82], [83], which retrieve a network based on the different zones that are identified in a combustor from both flow pattern and temperatures gained from CFD. In [83], and more in details in [82], the identified zones were located and explained on a phenomenological basis, and their volumes and the interconnections determined by the numerical results. The modelling approach was applied to several gas turbine applications, showing that the method had the ability to accurately predict NO_x and CO emissions for lean premixed gas turbine combustion applications.

The works [26], [69]–[72], [76]–[78] and [82], [83] already demonstrate the relevance of CFD as the starting point to achieve a CRN. Differently from [54]–[56], where CFD results have been employed to calculate the RTD of a given configuration in order to fit a network of reactors, it is shown that the results from a numerical simulation can be directly exploited to achieve an intelligently designed CRN. Furthermore, the possibility to apply detailed kinetics to CFD results is appealing because it makes computational fluid dynamics of combustors a prediction tool, overcoming the unfeasibility of the application of detailed mechanisms to numerical modeling. According to this strategy, the results of a generic numerical simulation are then the first step toward a CRN. An automated hybrid approach where a network is retrieved as a next step after numerical modelling is proposed [5], [27], where a network of interconnected ideal flow reactors represented an industrial boiler taking as starting point its calculated flow field. In this case, a CRN with the same number of reactors as the grid cells is generated, and then the isothermal reactors are solved with detailed chemistry. It is therefore clear that a huge number of reactors is achieved in this case. Clustering of the reactors-cells can be done starting from the CFD-retrieved network, to enable the analysis of the behavior of the combustor in terms of main macro zones. Turbulent temperature fluctuations were afterwards taken into account with the development of a Kinetic Post-Processor (KPP) [85]. The code was further improved in a successive work [86], which proposed a fully coupled and parallel algorithm. The improvements concerned the performance of the code, made more flexible and efficient using external libraries and distributing data and tasks among several processors.

The idea behind the hybrid CFD-CRN approach is that a validated numerical simulation run with a reduced kinetic model contains all the relevant information, namely flow field, temperature and main species. Minor species like nitric oxides and carbon monoxide, which are the most harmful and therefore regulated and thoroughly investigated pollutants, need a detailed kinetic approach. Numerous research groups have so far followed this idea, achieving a CRN analysis of the system as a postprocessing step of their numerical simulations. These networks are attained either by the user based on some criteria (i.e. temperature field/flow pattern) or can be automated. In the latter case, the number of interconnected reactors might be huge, differently from the former case, where a user retrieves a network based on observation of the calculated flow field. As a huge improvement with respect to [74], the same research group continued the work on the development and optimization of the hybrid modelling approach, developing their own CFD-CRN algorithm [87], [88]. These works propose innovative ways to deal with heat exchange as well: in [52] the thermal fluxes coming from radiation were included in the network construction via a correlative 1-D approach; in [53], the diffusive turbulent flux was also incorporated in the reactors equations, to correctly model the interaction between the idealized reactor zone and its surroundings. The CRN is inferred via a two-step approach, which considers first the flow pattern, and then refines the network considering the chemical condition of the identified reactors. [89]

extract the network features from their CFD calculation using a fluid tracer and referring to the fluid age. The addressed quantity refers to the time the fluid has been in the domain and is exploited when determining recirculation flows. This methodology uses to a certain level the link between the Residence Time Distribution of the system and the network of reactors.

Though the proven effectiveness of an automated CFD-CRN approach, simpler approaches ([28], [90]–[92]) are preferred while investigating industrial applications and practical systems. The preference has several reasons. Among others, the possibility to relate a specific reactor to a region inside a combustor and understanding how the behavior associated with that zone changes while exploring a range of operating conditions. This aspect is particularly relevant, making a simple CRN the preferred tool for combustors design [28], [91]. In particular, [28] enlightens on the importance of the reactors network strategy, that is indeed incorporated into the design strategy of gas turbines combustors. The work shows that a network is obtained from the combined experimental and numerical investigation of a small-scale combustor, using the Siemens in-house 1D reactor network code. The zonal decomposition of the simplified combustor serves as starting point to design a simple reactor network of a full-scale combustor, the SGT-400. It is of course a complex configuration, as it features the introduction of cooling air along the combustor wall, and a more sophisticated model is required. This model, though more complex than the previous one, keeps a small number of base units, easily relatable to different regions inside the system. [91] has the double aim to investigate LBO and NO_x formation for H_2 enriched fuels. Both experimental and numerical investigations, which were previously carried out on the combustor under study, support the setup of a 4-elements CRN. The authors strongly state the necessity of such a simple and flexible tool to aid the design and optimization of combustion-based devices. Understanding NO_x formation under gas turbine-relevant conditions concerns as well the works [92]–[94]. The network parameters are derived from CFD simulations, and they compare a basic network, comprising four units, with a more elaborate one, including up to seventeen units. Though the complexity of the model is increased, the zones are easily relatable to well defined regions inside the investigated combustor. The two models did not yield significant differences in the prediction of pollutant emissions.

As already showed in the initial part of this section, close to reality configurations are successfully model using a CRN also without including the aid of CFD. According to previous works like [49], [65], [67], component modeling is often used to retrieve a network. This strategy relies on relationships applied in smaller control volumes and local phenomena (i.e., liquid fuel evaporation) identified inside the system. From these relationships the relevant information for the setup of a network of interconnected reactors is obtained, as proved in [95]. A specific review about hybrid emission modelling methods applied so far is given in the first part of [96]. These hybrid emission models are applied to gas turbines in [97]–[99], and to an industrial furnace in [100]. The authors [101]–[104] rely on zonal modeling of the flow to interconnect the base units. To size the network, optimization routines are employed, defining an objective function based on available emission and performance data. As a correct determination of the volumes of each reactor is crucial, both volumes and the flow rates of each zone are retrieved by the calibration of the network. Such technique has the advantage of being faster than a CFD-based one and to give insight into the macroscopic features controlling combustion phenomena.

An interesting suggestion on the unexplored potential and future use of the CRN modeling strategy comes from [105]–[107]. The idea behind it is to prevent lean blowout in gas turbines setting up an on-line CRN modeling, during combustor operation. The network is kept simple, retaining the description of the main flow and flame zones, and boundary conditions (feed stream mass flows, inlet temperatures, etc.) the necessary parameters are live-taken from the monitoring system of the facility. In this case, the simplicity of the network was crucial to gain knowledge on the impact of the operating parameters on the identified macro-mixing zones. The proof-of-concepts of a Real-Time CRN was successfully demonstrated. The CRN monitored species and radical formation and proved a valuable tool to control methodology to prevent incipient lean blowout.

2.5 Summary

Combustion in practical configurations is a highly complex phenomenon: the transformation of the fuel takes place in a highly turbulent environment, with peculiar overall features generated, for example, by the existence of a swirling flow. Therefore, for a good overall understanding of the processes involved, a good description of both mixing and chemical reactions is crucial. The huge complexity of this task requires the development and use of simple and flexible analysis tools, whose aim is to give insights into the mechanisms of the process considering, both the fundamental aspects of gas turbine combustion. Chemical Reactors Network (CRN) models, or Compartmental Models (CM), match the requirements set by the need for a description of the mixing features together with a detailed description of the chemical kinetics. In this chapter, the different strategies to achieve a CRN have been briefly reviewed, together with a review about the results achieved by the various research groups. A CRN is designed by applying different methodologies:

- regard the RTD as the transfer function of the system under investigation, and design and size the network to reproduce it;
- fit the network of ideal reactors to know emission data or rely on fluid dynamic and design equations;
- exploit CFD to retrieve the network. This process can be:
    - automated,
    - user defined.

RTD-driven CRN-modelling of the system is employed in this work. The first reason behind the choice is that RTD data yields important information about the mixing properties of a non-ideal flow. Also, before the application of the CRN modelling methodology, those data are exploitable to gain knowledge about a given configuration and the impact of boundary conditions on its behaviour. Furthermore, RTD-driven CRN are generally kept simple, allowing the recognition of the fundamental mixing zones that characterize a system. this is once again important for sensitivity analysis, because it makes possible to practically understand the effect of a change in the process on the specific zone behaviour.

3 Gas Turbine Model Combustor

The modelling strategy introduced earlier, section 2, is applied to a Single Sector Gas Turbine (SSGT) model combustor designed at Technische Universität Darmstadt, and presented in [18], [108]. RTD measurements have been carried out in this apparatus, with the aim of exploiting the data to design and size a network of ideal flow reactors able to reproduce the mixing and reactive characteristics of the experimental configuration. The model has then been used to gain knowledge on the effect of the operating conditions on the mixing and reactive features of gas turbine combustion. In the following, the SSGT and the measurement setup for RTD data collection are presented. Afterwards, the CRN models are designed and fit to the data. A discussion on the results follows, for both non-reactive and reactive operating conditions.

3.1 Experimental apparatus

The investigated apparatus is shown in Figure 11. It consists of a pressurized Single Sector Gas Turbine model combustor (SSGT). To create engine like boundary conditions, the test rig is housed in a pressurized vessel, shown in grey. A movable block swirl generator (TECFLAM), shown in orange and in Figure 12, generates a swirl flow with central recirculation to stabilize the flame. This component allows changing the geometrical swirl number, ranging from 0 to 1.7, to generate flow patterns typical of technically relevant combustion systems. The operating fuel is natural gas. This choice follows the trend developed in the last years, that aims at increasing the use of natural gas as operation fuel, for its large availability and the chance to reduce CO_2 emissions. To answer the questions related to the optimization and improvement of natural gas-fuelled facilities, more studies on close to reality configurations based on this fuel are needed. Natural gas is fed either before the movable block, with the main air feed or directly into the combustion chamber via a central pilot jet. There is, therefore, the chance to investigate purely premixed as well as partially premixed flame, reachig also purely diffusion flames. For premixed operation, six inlet nozzles arranged radially around the main air plenum bring the fuel directly in the main air flow entering the swirler. For fuel-staged operation, the natural gas is additionally issued by the central pilot, yellow colour in Figure 12. A detail of the swirl generator, together with the bluff body/pilot tube, the main air intake and the fuel inlet nozzles for premixed operation is shown in Figure 12. A subsonic exit nozzle guides the flue gas outside the combustion chamber (red colour in Figure 11), where they are mixed with the pressure vessel cooling air. Three sides of the flame tube are optically accessible over the whole size. On the bottom side, there is an effusion-cooled wall (shown in green), whose cooling geometry can be changed to study the effect of different cooling geometries on the flow and reacting field. The presence of the effusion cooling liner is a crucial feature of the combustor, allowing to study the interaction between a combustion and cooling air. A hot air wind tunnel feeds the effusion cooling liner, to ensure the homogeneity of the cooling air flow pattern inside the combustion chamber. Figure 11 shows in blue the H_2 torch that is used in an initial stage, to ignite the reacting mixture. The current reference operation point, also referred to as "standard operation point", is summarized in Table 1.

Table 1: Relevant parameters of the standard operation point and flame tube dimensions.

Operation point, units			**Flame tube dimensions, m**	
Preheating temperature	623	K	Height	0.1
System pressure, P	0.25	MPa	Width	0.1
Main air mass flow, m_{in_main}	0.030	kg/s	Length	0.18
Equivalence ratio, $\varphi_{\text{lean premixed}}$	0.75	[-]	Effusion cooling length	0.152
Swirl number, S	0.7	[-]		
Effusion cooling mass flow, m_{cool}	0.015	kg/s		

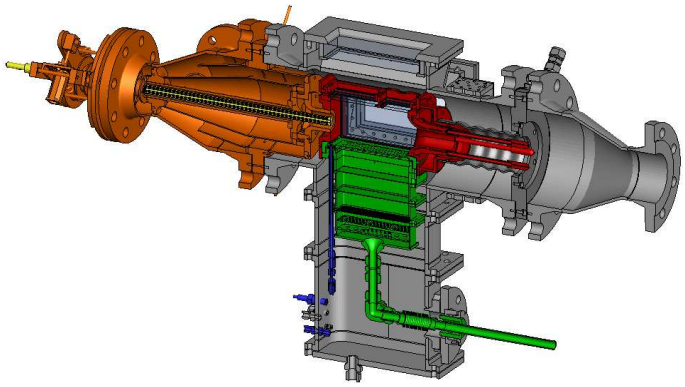

Figure 11: Main components of the SSGT test rig. Grey, pressure vessel; red; flame tube; orange, movable block radial swirler; blue, ignition torch; green; effusion cooling liner.

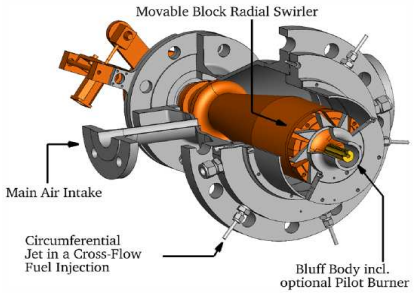

Figure 12: Detail of the movable block radial swirler and nozzles for fuel injection [18].

3.2 Residence Time Distribution measurements

Residence Time Distribution measurements have been carried out in the SSGT. The aim of this experimental campaign was twofold: get insight on the influence of the operating conditions on the global mean residence time and mixing pattern inside the combustion chamber and get the relevant parameters for to size a chemical reactors network representative of the flow and mixing field inside the test facility.

The basic principle behind the measurements of RTD is simple: an inert tracer is injected in the system under investigation, its input function as close as possible to dirac pulse, and its temporal outlet profile is monitored at the exit of the system. Its implementation is, however, far from trivial. Problems might arise from the flow non-idealities, the difficulties in injecting the tracer “close enough” to the entrance of the investigated reactor, and the choice of the detection strategy. In the following, a brief review of the strategies applied to deal with the task in close to reality combustion configurations is proposed.

Beèr and Lee, 1965, [51] measured RTD in strongly swirling flow, in a water model of a furnace, and in the real furnace under reactive conditions. Among the input function possibilities, the authors fed the tracer into the system using a negative step input function. This is the best choice if experimental issues prevent a pulse function [34], though this is stated because it was found that a negative step generated a less noisy signal compared to this positive one. This was observed in [63]. However, [64] investigates this aspect further, and it was proven that a negative step induces a bigger error on the initial part of the signal, whereas a positive one has a worse effect on the final part, stating once again the importance of a well-implemented input strategy. The tracer used in [51] was a salt solution, probed by means of conductivity cells, in the cold prototype and Argon, detected by means of the chromatographic method, in the furnace. [52] carried out RTD measurements at the outlet of a model GT combustor, varying the inlet position. In their opinion, measuring the output tracer response between various locations within the combustor was crucial in order to overcome the risk of non-uniqueness of the arrangement of ideal reactors in a network. The measurements themselves were carried out using a previously proposed by [53], that injected a pulse of mercury vapor into the test rig to measure the RTD of a flow past a V-gutter flame holder. The tracer was detected by measuring the absorption of radiation from a 254 nm mercury-neon hollow cathode lamp. Both works realized a pulse input. RTD measurements in a scaled down version of a furnace were also carried out by [41]. This work presents RTD measurements in a cold swirling flow, focusing on the effects of the swirl number. Helium was fed into the combustion chamber with a negative step input function and detected by a fast response probe. Following the example set by [52], the point wise measurements were carried out at three different locations inside the system: at the exit of the chamber, both at the centerline and off-centerline, and inside the internal recirculation zone formed by the vortex breakdown of the swirling flow, on the centerline. A secondary combustion

chamber of a rotary kiln is studied via RTD analysis in [59]. The tracer, SO_2, was step-fed and sampled to be analyzed in a gas analyzer. [109] explored the use of alkali atoms as tracer, to probe by means of Tunable Diode Laser Absorption Spectroscopy (TDLAS). Different injection strategies were proposed, and a pulse-like input was identified to yield the best results. [60] measured RTD via Planar Laser-Induced Fluorescence (PLIF) of a dye tracer in a water model of a gas turbine combustor. The dye was used to simulate the fuel flow. It was injected until it reached a steady state, and the rapidly cut off. Simultaneous PIV measurements were taken to ensure that the flow cut did not change the flow pattern inside the test facility. The mass flows were adjusted by matching the momentum flux ratio of a combusting flow. PLIF of a dye tracer in a water model was employed by [61], realizing a pulse-injection in a water model of a gas turbine combustor. This work is extended in [62], exploring reactive conditions, as well as steam diluted conditions. The measurement technique is different in this case, and the Quantitative Laser Sheet [110] (QLS) was instead applied. A step input was chosen because it was considered more robust with respect to the highly turbulent combustion environment. [63], [64] deal with RTD measurements by means of TDLAS. Cold- and reactive-flow measurements were carried out in a scaled down version of a furnace to investigate oxyfuel combustion [111], [112]. The tracer was methane for non-reactive conditions, and HCl for the reacting case. Several injection strategies were tested (positive and negative step, and pulse) and compared. As clarified before, the pulse input yielded the best results.

In the present work, to measure the distribution of residence times in the SSGT ([18], [108] and Figure 11), the Light Extinction Measurement (LEM) technique was employed. This technique uses a laser beam passing across a control volume, and the residual laser light after the control volume is measured. It is a good strategy to follow the dynamics of fluids and embedded particles, and it is vastly employed for soot measurements [113], [114]. The continuous monitoring of the light passing a certain control volume makes it suitable for time-resolved measurements and, more specifically, for non-stationary processes, like those involved during RTD measurements. Alumina (Al_2O_3, diameter ~ 1 µm) particles were chosen as process tracer. Solid tracers applied to RTD measurements have been successfully applied in combustion environments while burning gaseous fuels [62]. It is as well a good light-blocking tracer, while gaseous tracers would require different measurements techniques [53], [63].

3.2.1 Measurement setup

As mentioned in section 3.2, RTD was measured by means of the LEM technique, using Alumina (Al_2O_3, diameter ~ 1 µm) particles as process tracer. The Stokes number, Equation 34, that measures the flow tracer fidelity, was calculated to ensure the suitability of the tracer.

$$Stk = \frac{t_0 u_0}{l_0} \qquad \textit{Equation 34}$$

u_0: fluid velocity;

l_0: characteristic length;

t_0: relaxation time of the particle, Equation 35.

$$t_0 = \frac{d_p^2 \rho_p}{18 \mu_g} \qquad \textit{Equation 35}$$

d_p: tracer particle diameter;

ρ_p: particle density;

μ_g: viscosity of the fluid.

For $Stk < 1$, the particles fully follow the flow streamlines. $Stk < 0.1$ is a threshold below which tracing accuracy errors are below 1%. In this work, the order of magnitude for Stk during non-reactive measurements is 5×10^{-4}. Particles are therefore assumed to properly follow the flow streamlines, and the RTD measured employing solid particles equals that of the gaseous flow.

The particles were fed to the system using a pulse input function. To achieve it, a flow bypass was designed and installed on one of the fuel inlets, Figure 13. While carrying out RTD measurements, the

fuel flow was distributed among five inlet nozzles instead of six. Part of the main air flow (m_t, 0.002 kg/s out of 0.03 kg/s) was diverted to the bypass and used to entrain the seeding in the combustion chamber. While the extinction signal was not recorded, the diverted air flow was flowing in the upper part of the bypass system, Figure 13. The Al_2O_3 was batch-fed from the valve v_1, while v_2 and v_3 were closed to maintain the system pressurized. The valve v_f is a fast-switching valve (FESTO, switching time 2 ms) connected to a switch. After the tracer is fed, the valve v_1 is closed, while v_2 and v_3 are opened again. The valve v_f is triggered by the switch and diverts the flow path of m_t, so that its passage in the lower path of the bypass entrains the seeding to the combustion chamber. The experimental apparatus produces a pulse input, as is shown later. The switch triggers also the data acquisition program (sampling frequency 500 MHz, sampling time 1 s).

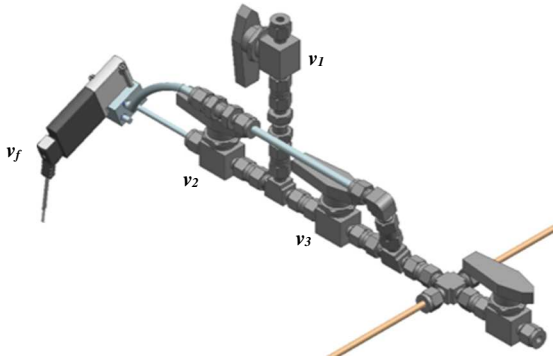

Figure 13: sketch of the bypass device. Unseeded flow m_t flows in the upper path, v_f switches the flow to the lower path to entrain the seeding for the measurements.

The light from a 1527 nm diode laser (Thorlabs) was used as probing light. The laser was connected to a 1:4 custom made fiber splitter, and the light was guided by means of laser fibers to four different detection positions, described in the following and shown in Figure 14 and Figure 15.

- 1: right after the entrainment of the tracer. The first extinction signal is collected outside the combustion chamber, in the bypass system. This is achieved by housing the laser fiber in a steel pipe, highlighted in orange in Figure 13 so that it fits in the cross connector. A lens is fixed at the end of the first part of the pipe, to focus the laser light on a photodiode (extended InGas, Hamamatsu), which is fixed on the other half of the pipe. The aim of this measurement is to collect the extinction profile as close as possible to the seeding-collection location.
- 2: at the entrance of the combustion chamber. Here, a line lens apparatus (Thorlabs) generates a laser sheet to collect the extinction signal over part of the inlet annulus cross-section. The light is focused on a photodiode by means of a spherical lens (Thorlabs). Before the photodiode, a 1530 nm filter (Thorlabs) blocks the light emitted from the flame in the detection range of the photodiode.
- 3, 4: at the exit of the combustion chamber. Here, the signal is simultaneously recorded in two positions: one at the centerline (referred to as Out_1) and one ~ 10 mm below the centerline (referred to as Out_2). The aim of the latter probing position is to check for any non-uniformity of the exit tracer concentration along the cross-section as a consequence of the cooling air, issuing from the lower side of the combustion chamber. The laser fibers are equipped with GRIN lenses. The light is directed on the recording photodiodes by means of gold coated 90° off-axis parabolic mirrors (Thorlabs). Undesired light from flame luminosity is filtered as for the previous case.

The photodiodes are linked to current-to-voltage converters amplifiers (Femto), which are connected to a four-channel oscilloscope (Tektronix) for on-line monitoring. The signal is recorded to a personal computer with a DAQ acquisition system (National Instruments), triggered by the same switch that triggers the fast-switching valve, v_f.

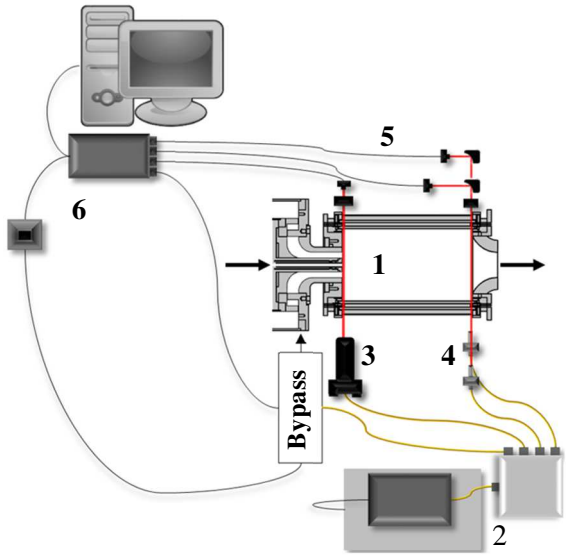

Figure 14: schematic of the measurement setup
1. Combustor and bypass system (more in Figure 13)
2. Laser apparatus, comprising a 1→4 fiber splitter to split the signal to the measurements channels
3. Line lens – entrance nozzle signal (Figure 15)
4. Laser beams – combustor exit (Figure 15)
5. Detection side photodiodes
6. Trigger switch and signal acquisition system

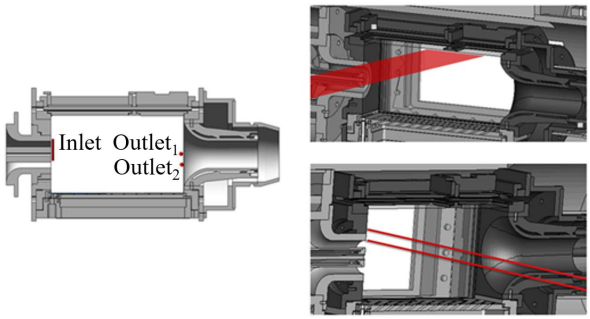

Figure 15: explanation of the measurements locations inside the combustion chamber.

A sketch of the measurement setup is proposed in Figure 14, where a schematic representation of all the main components is given. The black lines represent electrical connections, while the lines drawn in yellow represent the laser fibers issuing from the 1:4 fiber splitter. The bold black arrow indicates the direction of the flow of reactants entering the combustion chamber. Figure 15 shows a detail of the output probing points, not distinguishable from the perspective in figure 13. The top view in Figure 14 does not make clear the output probing points, which are further clarified in Figure 15. As mentioned earlier, the feeding of the tracer is a batch operation. For each one of the explored operation points, the following steps, in the presented order, are followed:

1. Establishment of the desired operating condition and wait for the steady state to be reached.
2. While the bypass flow rate is flowing in the upper part of the bypass, close v_2 and v_3, and feed the tracer through v_1.
3. Close v_1 and open v_2 and v_3.
4. Use the trigger switch to change the flow path of m_t. In this way, the tracer fed during step 2 is entrained and trasported to the combustion chamber. The extinction signal for all the channels is automatically recorded.
5. Repeat steps 2-4.

Due to the batch nature of the process, for each operating condition tested the tracer measurements were carried out 10 times, i.e., step 5. was repeated 9 times. The single-injection results are then averaged to obtain a single extinction signal representative of the investigated point of operation. The choice to measure each operating condition ten times is based on a signal-to-noise (S/N) ratio analysis, shown in Figure 16: here, the variation of the signal-to-noise ratio with the number of injection used to compute the average signal is reported for the non-reactive (upper row) and reactive (lower row) case. Two different boundary conditions were considered: $m_{cool} = 15\ g/s$ (corresponding to the set of boundary conditions identified as "standard operation point") and $m_{cool} = 7.5\ g/s$. All the images show that the ratio has reached a flat level, and further gain that might come from an increased number of measurements would not be crucial for the average signal. To prove this point, one set of measurement, correspondig to reactive $m_{cool} = 15\ g/s$ (lower row, left), has been taken twice, and the effect of a higher number of tracer injections evaluated in terms of S/N: it is clear that the ratio does not bring a substantial improvement to the investigated parameter, and ten measurements was taken as the suitable number of measurements. The choice to refer to the specific boundary conditions reported in Figure 16 is linked to the availability of CO measurements for these operating conditions: as these measurements are employed in the following paragraphs to validate the reactive CRN, the same set of boundary

conditions has been taken as reference. For this reason, sensitivity analysis and error estimation are applied to these two situations, taken as benchmark both for non-reactive and reactive operation.

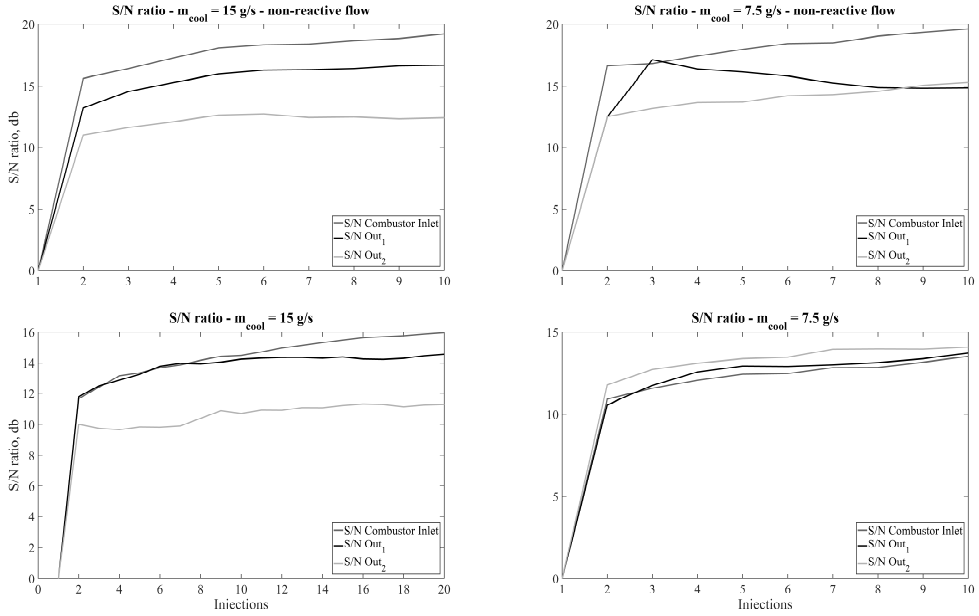

Figure 16: signal to noise ratio for $m_{cool} = 15\ g/s$ and $m_{cool} = 7.5\ g/s$, non-reactive flow (upper row) and reactive flow (lower row). The Inlet Pulse has not been considered for S/N analysis.

The boundary conditions were varied according to Table 2, where the differences with respect to the reference point of operation are highlighted.

Table 2: explored operation points.

Parameters that are varied	Explored values, units	
Equivalence ratio - φ	0.65, 0.75 and 0.85	[-]
Pressure - P	2.5 and 3	bar
Cooling mass flow - m_{cool}	15 and 7.5	g/s
Swirl number - S	0.7 and 1.3	[-]
Combustion mode – St.	0%, 10%, 30 % and 50% fuel staging	[-]

3.2.2 Experimental data treatment

In order to derive residence time distributions from raw data, several processing steps were implemented:

- Baseline correction. This step was necessary because of the progressing fouling of the optical windows, due to the deposition of the tracer. To this aim, an estimation of the start and end time of the extinction signal was required.
  The start time was calculated as the time required for each channel to reach a threshold percentage of the maximum extinction value. The value of 2% was found to be suitable to properly catch the start of the signal. The end time was taken as four times the time corresponding to the maximum extinction reached. This estimation is based on a rule of thumb proposed by [33], though concerning the adequate observation time and not the end time: it was proposed that the observation time should be taken as three or four times the mean residence time in the investigated system.
  Once this information was obtained, the fouling was assumed to be a linear function of the sampling time, and therefore, the light intensity to decrease linearly to the final value. The extinction was then calculated using the Lambert-Beer equation:

$$E_l = log_{10}(I/I_0) \qquad \textit{Equation 36}$$

E_l	Extinction, absorbance of the material for light with a wavelength $l = \lambda$.
I	Intensity of transmitted light
I_0	Intensity of incident light

- Smoothing of the data using a moving average filter. To remove part of the background noise, the signals were filtered using a moving average filter, with a 400-points interrogation window. This simple smoothing has been applied in a similar situation [62] and proved sufficient to prepare the data to the subsequent fitting via CRN modelling.
- Area normalization. The resulting signals were normalized by their area to obtain the corresponding distributions. These results, although not strictly corresponding to the RTD of the investigated combustion chamber (see 3.3.1.2 and 3.3.2.2), are referred in the following as "$E(t)$".
- Averaging of the single-injection measurements.

An additional step was required for the inlet pulse signal, before the post-processing steps, in order to use the signal for the CRN modelling. As explained earlier, this signal was taken immediately after the entrainment of the tracer by the bypass air, namely the highest concentration of tracer in the system. This led to saturation of the light extinction, making the recorded signal not exploitable for further use without an additional step: the inlet pulse injection signals have been fitted by a curve comprising a sum of Gaussian curves before proceeding with the processing.

The post-processed distributions for the four acquisition channels, after treatment and area normalization, are shown in Figure 17, non-reactive flow, and Figure 18, reactive flow. Behind each curve, the single-injection results are superimposed to each other, as an indication of the experimental variation. The standard deviation for the sample channel is also reported. For both reactive and non-reactive flow, two operating conditions are reported: $m_{cool} = 15\, g/s$ (corresponding to the set of boundary conditions identified as "standard operation point") and $m_{cool} = 7.5\, g/s$.

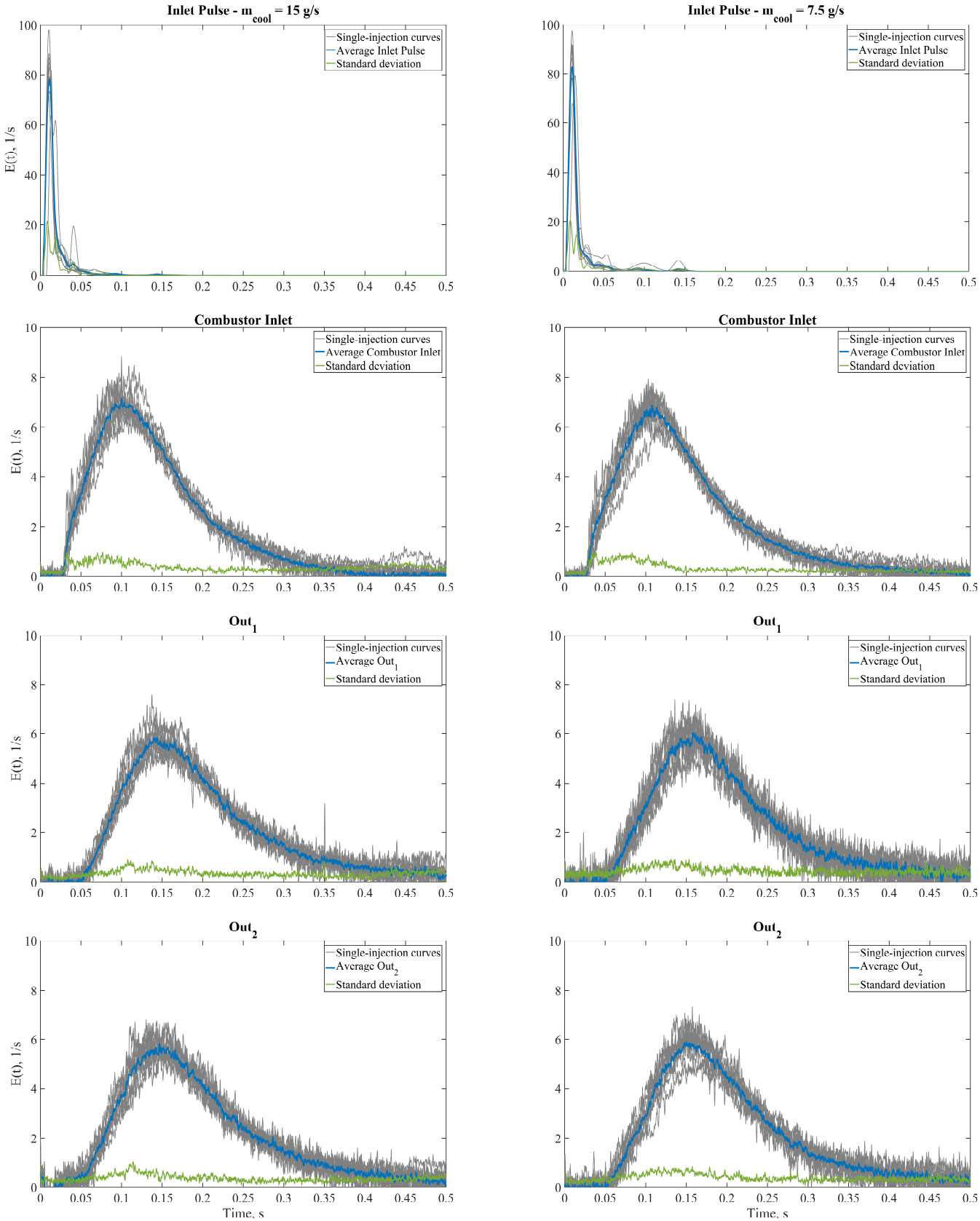

Figure 17: average RTD, superimposed to the single injection curves for $m_{cool} = 15\ g/s$ and $m_{cool} = 7.5\ g/s$, non-reactive flow. The standard deviation is also reported.

-

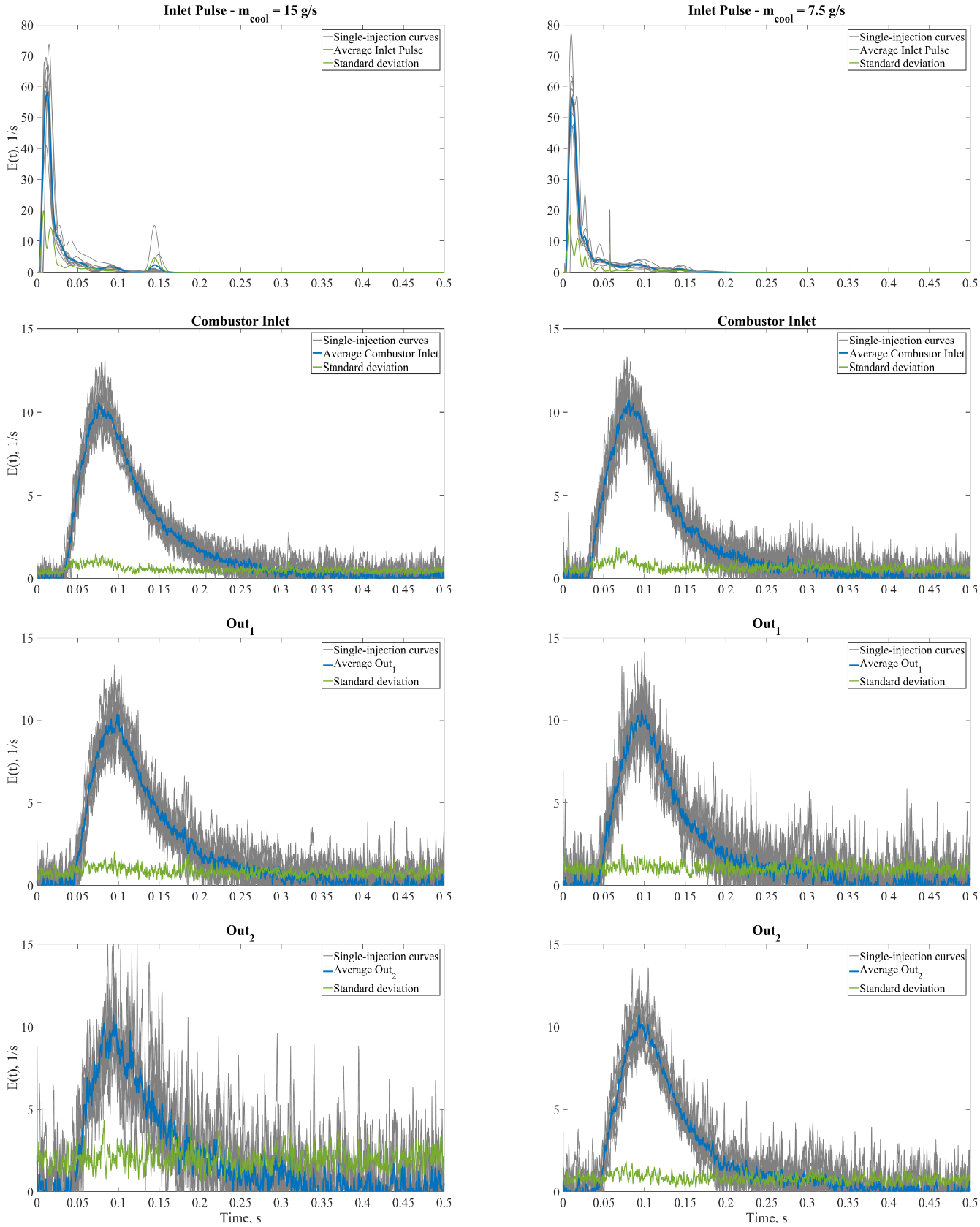

Figure 18: average RTD, superimposed to the single injection curves for $m_{cool} = 15\ g/s$ and $m_{cool} = 7.5\ g/s$. The standard deviation is also reported.

3.3 Chemical Reactors Network

The Chemical Reactors Networks (CRNs) applied to the combustion chamber have been designed exploiting the available experimental data on the test rig [18], [108] and testing modelling strategies proposed in the literature, applied in similar situations. At first, a CRN for the cold flow field was designed, based on the mixing characteristics of the different zones identified in the system, as shown in 3.3.1. A slight modification of the model, motivated and explained in 3.3.2, was applied to make the CM suitable to describe both reactive and mixing features of the configuration.
In this paragraph, the procedure and the tools exploited to size the CRN model is briefly described. The models are then introduced and explained. The experimental fit is presented for the two benchmark cases introduced before: $\mathrm{m_{cool}} = 15\ \mathrm{g/s}$ and $\mathrm{m_{cool}} = 7.5\ \mathrm{g/s}$.

3.3.1 Cold flow Chemical Reactors Network

The CRN ,developed to describe the flow features, is shown in Figure 20 (separated parts) and Figure 21 (entire network) for the non-reactive operation. The simple layout is mainly inspired by [61], [62], where a simple network is proposed, that takes the fundamental macro-mixing zones in a model gas turbine combustor into account. Below, Figure 19 depicts the non-reactive flow field of the combustor as a result of PIV measurements from [18]. A high velocity jet-region giving rise to two main recirculation zone (central or Internal Recirculation Zone (IRZ) and a corner or External Recirculation Zone, ERZ) is present, as a typical flow field of a swirling confined configuration, see 1.2.

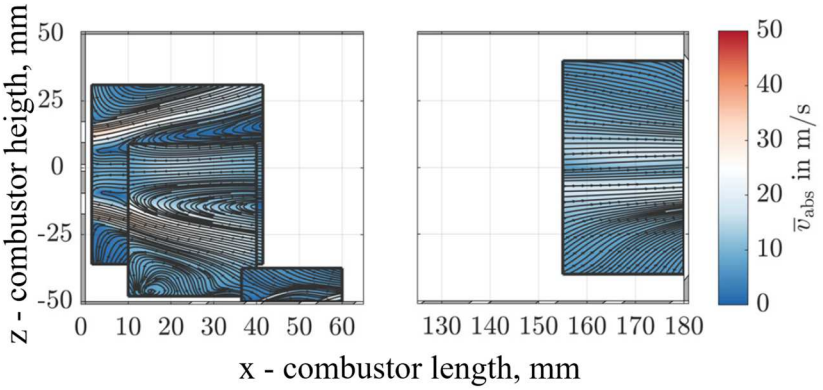

Figure 19: non-reactive flow field of the SSGT, [18].

Taking Figure 19 as a reference of the non-reactive flow field, three main paths form the CRN, see Figure 20 and entirely shown in Figure 21. As shown in Figure 20.a, a PSR is used to represent the IRZ and the ERZ. The jet-like region that occupies the volume between these two recirculation zones is schematized by a series of two PFRs, since a preferential flow direction can be identified. In this region, the recirculated flow merges with the fresh mixture and can either be recirculated or bypass the recirculation zones. Two parallel PFRs are employed to simplify the fluid dynamics of the exit region of the combustion chamber. Here, the flow streamlines mostly follow linear trajectories, which justifies the use of the PFR. The small, upper PFR in the segregated exit region (Figure 20) represents the central part of the mass flowing towards the exit, and the bigger, lower one represents the rest of the volume around it, leaving out just the volume attributed to the lower effusion path. In this way, the designed network is a 2D schematization of the flow in the combustor, with the addition of the effusion cooling path. This path, as illustrated in Figure 20.b, is represented by a series of PFRs, as suggested also in [28], whose volume is estimated from [108]. Three reactors are employed because three zones are identified to exchange flow with the effusion cooling region. This is schematized in Figure 21, where the entire network is shown. As stated earlier, the injection of the seeding to measure the RTD of the system occurs before the combustion chamber. More precisely, the seeding is entrained in the bypass tube, and then mixes with the main air flow rate in the plenum before the swirler.

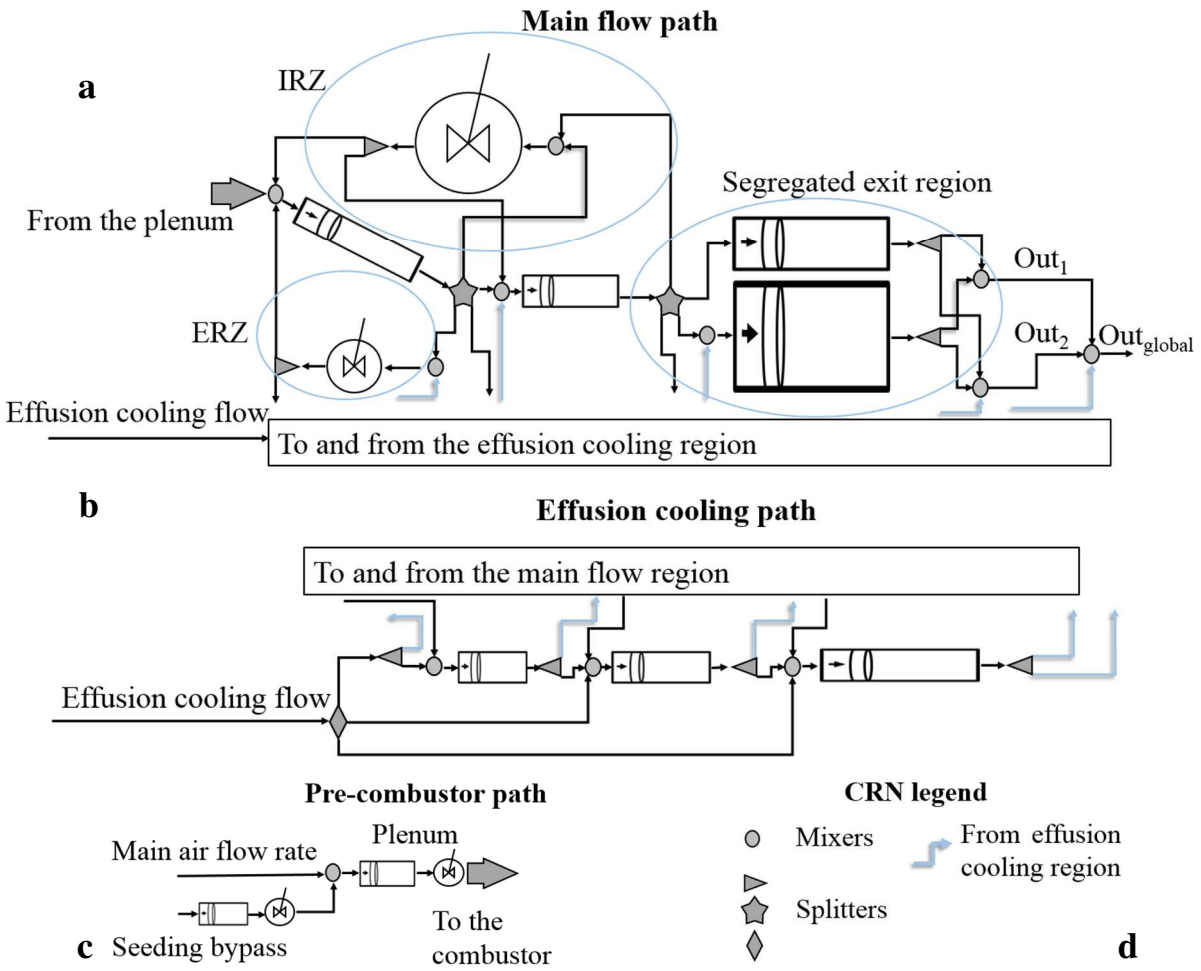

*Figure 20: non-reactive flow CRN, represented in terms of main flow paths. **a**, main flow path; **b**, effusion cooling path; **c**, pre-combustor path; **d**, symbols used.*

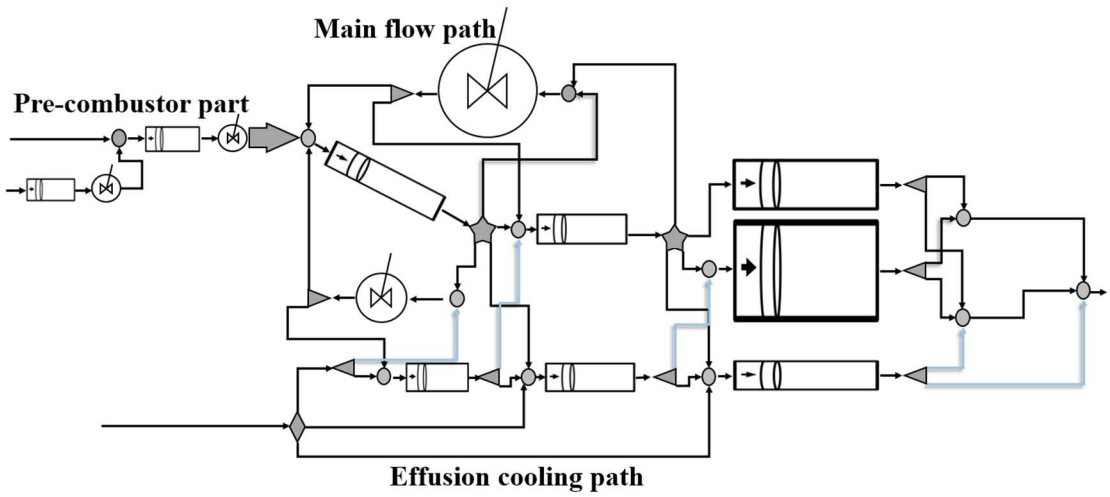

Figure 21: non-reactive flow CRN, entire representation.

This path of the seeding is taken into account in the CRN structure in the following manner: the flow of the fluid in this pre-combustor part translates to a severe broadening of the initial pulse (detailed description in 3.3.1.2 and 3.3.2.2), and it is incorrect to still assume a pulse-like input function at the entrance of the combustor. This is indeed clear from the extinction signal collected at the entrance of the combustor (Figure 17 and Figure 18) and makes it necessary to introduce a section of the network

for the pre-combustor path. Therefore, a delay time and an exponential decay time were considered both for the bypass path and for the plenum/swirler part (refer to Figure 11). These characteristic times were part of the optimization procedure for $\dot{m}_{cool} = 15\ g/s$ and $\dot{m}_{cool} = 7.5\ g/s$, both reactive and non-reactive. They are not part of the optimization procedure for the other investigated cases Table 2: an average value between the optimized ones was used instead, in order to reduce the number of parameters. The network parameters to be optimized to size the network are the splitting ratio at each illustrated splitter in Figure 20 and Figure 21, obtained by fitting the network response to that of the investigated system. More detailed, the mathematical model of the CRN is implemented in Matlab Simulink® [115] and the dynamic response of the model to the experimental input is fit to the experimental response of the system. An optimization routine from the Matlab Optimization Toolbox is employed. The routine (Figure 9) compares the response of the CRN-system implemented in Simulink®, calculated using the first guess parameters to the experimental one. The objective function, that must be minimized in order to find the suitable network parameters, is written taking into account the sum of the squared residuals, as in Equation 31:

$$Objective\ function = \sum_{i=1}^{n} (response_{calculated}(i) - response_{measured}(i))^2 \qquad \textit{Equation 37}$$

i = sample count. It refers to each time sample that constitutes the experimental curves and the numerical ones.

Both Out_1 and Out_2, Figure 20, are included in the objective function. Ideally, these two responses combined give the global tracer response of the system, referred in the following as Out_{tot}. It represents the response ideally measured after the exit nozzle of the combustion chamber. This measurement is not available, and this quantity has been obtained as a result of a weighted mean between the distribution Out_1 and Out_2. It is not involved in the optimization procedure, and the agreement of the fit is shown in the following for completeness. Indeed, this distribution is the one employed in 3.4 to comment on the impact of the operating conditions on the mixing behavior of the combustor.

Once the flow rate entering the reactors is known, it is possible to calculate the mean residence time for each component of the network and the gain parameters for each mixer, 2.2.1. these parameters make it possible to calculate the dynamic response of the system.

3.3.1.1 Experimental fit

The agreement between the results of the CRN fit and the experimental data for the standard operating point and for the case with lower effusion cooling mass flow is presented in Figure 22. In each plot, the tracer response detected shortly after the entrainment of the seeding is also reported, as a visual comparison of the broadening of the signal. The Experimental Inlet Pulse is normalized in each plot to the maximum of the distribution involved, for graphical reasons.

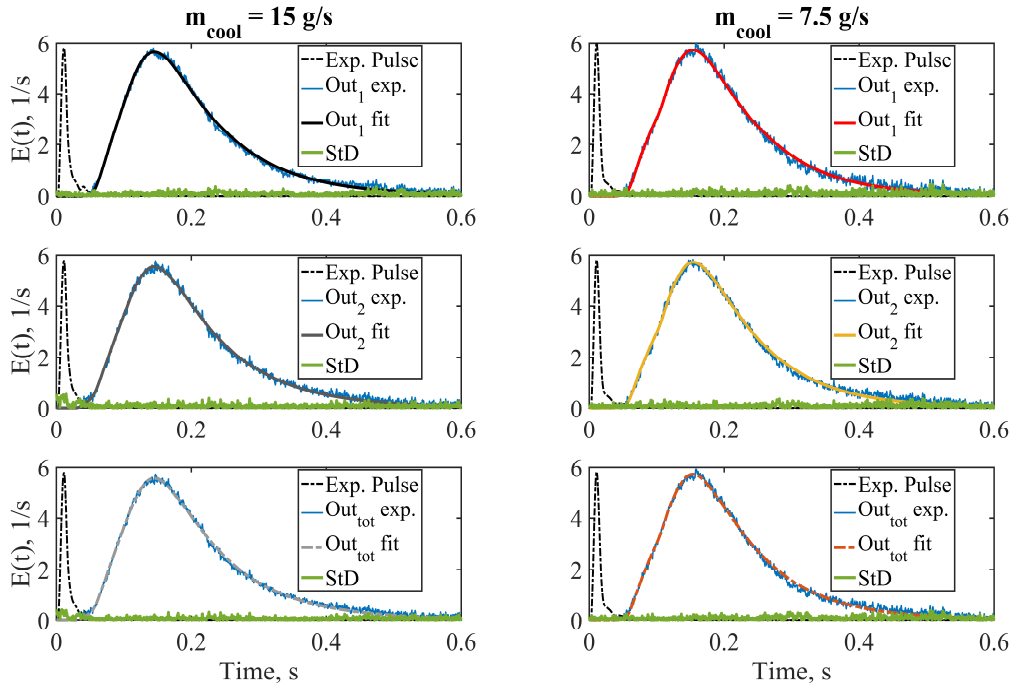

Figure 22: experimental tracer response with superimposed CRN fit, for $m_{cool} = 15\ g/s$ and $m_{cool} = 7.5\ g/s$, non-reactive operation. The Inlet Pulse is reported for comparison.

To quantify the uncertainty of the network variables and, accordingly, the one of the quantities chosen to describe the differences among the tested cases, the optimization has been carried out for the standard operating point (Table 1) on a single-injection basis. For this task, the single-injection Inlet Pulse was fed to the Simulink® program, and the model fitted to the corresponding single-injection Out_1 and Out_2. The set of optimization values obtained with this procedure have been employed to calculate network-specific parameters (see Table 4) that will be later exploited to describe the effect of the boundary conditions on the RTD. The deviation around the tracer response curves is shown in Figure 23, and the uncertainty on selected parameters is reported in Table 4. The column "Average fit" contains the values extracted from the fit of the average distribution, while "Mean single injection" contains the mean of the values calculated for each injection. The calculated standard deviations will be applied to in the following to all the non-reactive CRN fits. Each parameter is explained in Table 3.

Table 3: model parameters.

$\tau^m_{i\_response}$	Mean residence time calculated according to the tracer response.	τ_i^c	Convective time delay, calculated as the time instant at which the derivative of the distribution becomes higher than a certain threshold.
τ_i^m	Mean residence time calculated according to the extracted RTD (more in 3.3.1.2)	$\tau_i^{0.95}, \tau_i^{0.99}$	Time at which the area below the RTD reaches 95% or 99% of its value. Both characteristic times are reported to comment on the slow characteristic of the distributions.
σ_i^2	Variance of the distribution, calculated according to the extracted RTD (3.3.1.2)	$\frac{m_{IRZ}}{m_{in\_main}}$	Mass flow recirculated in the IRZ with respect to the mass flow issuing from the inlet nozzle.

S_i^3	Skewness of the distribution, calculated according to the extracted RTD (3.3.1.2)	$\frac{m_{ERZ}}{m_{in\_main}}$	Mass flow recirculated in the ERZ with respect to the mass flow issuing from the inlet nozzle.
τ_{IRZ}	Residence time in the IRZ.	$\frac{m_{cooling\rightarrow main}}{m_{total\_feed}}$	Global amount of mass flow mixing into the main flow path from the cooling region.
τ_{ERZ}	Residence time in the ERZ.	$\frac{m_{main\rightarrow cooling}}{m_{total\_feed}}$	Global amount of mass flow mixing into the cooling region from the main flow path.

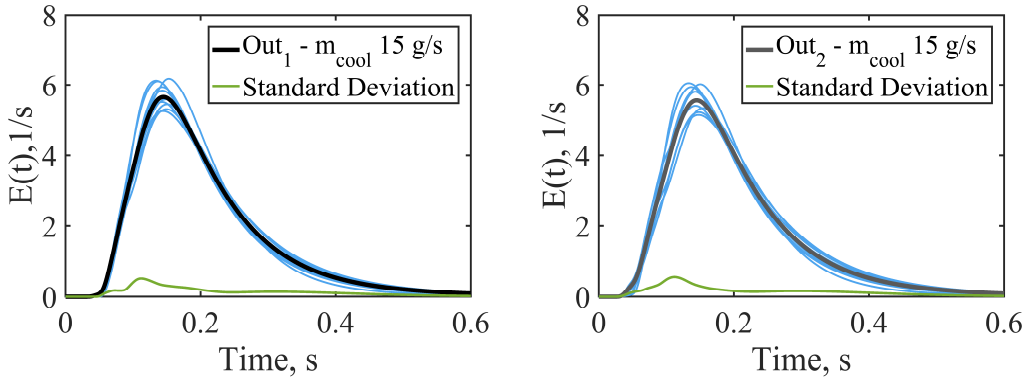

Figure 23: single-injection CRN-fit for non-reactive measurements, in blue, and superimposed average fit. The single-injection optimization is applied on $m_{cool} = 15\ g/s$.

Table 4: uncertainties associated with the CRN fit, non-reactive flow, $m_{cool} = 15\ g/s$.

	Average fit	Mean single injection		Average fit	Mean single injection
$\tau^m_{1\_response}$	0.209±0.008	0.208	τ_1^c	0.029±0.002	0.031
$\tau^m_{2\_response}$	0.207±0.009	0.206	τ_2^c	0.011±0.002	0.011
$\tau^m_{tot\_response}$	0.207±0.009	0.197	τ_{tot}^c	0.011±0.002	0.011
τ_1^m	0.081±0.004	0.081	$\tau_1^{0.95}$	0.16±0.02	0.16
τ_2^m	0.079±0.004	0.079	$\tau_2^{0.95}$	0.16±0.03	0.16
			$\tau_{tot}^{0.95}$	±0.02	0.15
τ_{tot}^m	0.072±0.002	0.070	$\tau_1^{0.99}$	0.44±0.02	0.44
			$\tau_2^{0.99}$	0.44±0.02	0.43
σ_1^2	0.0054±0.0004	0.0052	$\tau_{tot}^{0.99}$	0.43±0.02	0.43
			$\frac{m_{IRZ}}{m_{in\_main}}$	1.3±0.3	1.1
σ_2^2	0.0055±0.0003	0.0054	$\frac{m_{ERZ}}{m_{in\_main}}$	0.08±0.03	0.07
σ_{tot}^2	0.0057±0.0003	0.0055	$\frac{m_{cooling\rightarrow main}}{m_{total\_feed}}$	0.30±0.06	0.28
S_1^3	5±1	6	τ_{IRZ}	0.011±0.004	0.014
S_2^3	5±1	5	$\frac{m_{main\rightarrow cooling}}{m_{total\_feed}}$	0.27±0.05	0.3
S_{tot}^3	5±1	5	τ_{ERZ}	0.17±0.09	

In addition to the error analysis, a sensitivity analysis is also carried out, to assess the relevancy of selected fit parameters and comment on their effect on the overall fit quality. This study is conducted on both reference conditions, $\mathrm{m_{cool}} = 15\ \mathrm{g/s}$ and $\mathrm{m_{cool}} = 7.5\ \mathrm{g/s}$, and the different behaviour is commented based on the specific operating condition.

- Mixing characteristics of the reactors of the network.
  Compartmental Models analysis proved useful in many practical situations, combustion-related and not [41], [46], [62]. Despite its power to simplify complex phenomena, this modelling strategy requires caution, in that more than one reactor arrangements might be able to reproduce the response of a given system. A first precaution against this possibility is to measure the by determining the RTD between various locations within the investigated reactors [52],in order to be able to match more than one experimental curves. Another strategy, largely employed in combustion studies, makes a joint use of CM and Zonal Modelling of the flow. In other words, a basic knowledge of the flow features guides the reactors arrangement [41], [50], [57], [61]. In the current work, the response measured at two different locations on the exit plane of the combustion chamber has been used as objective to deduce the CRN parameters. However, the effect of a different choice of the reactor characteristics has then been tested. That is, in one case the model was run on a network comprising just PFR reactor, and in the other case, on a network comprising CSTR reactors only. The results are reported in Figure 24. Swapping segregated zones for mixed ones has a more severe effect then swapping mixed zones for segregated ones. Precisely, when all the PFRs are replaced with CSTRs, the curve rises earlier (except for Out_2, $m_{cool} = 15\ g/s$) and is slightly broader, determining a lower distribution. Replacing plug flow zones translates into removing those zones that are responsible for a delay in the response of the system, explaining the earlier onset of the curves. In particular, the replacement of the main flow reactors in the segregated exit region has the main effect on the shape and features of the distributions. This is confirmed by several factors. The first, is the lower impact of the modification of the network on the rising edge of Out_2, $m_{cool} = 15\ g/s$: as discussed in a later chapter, this distribution is more affected by the mixing of cooling air in the system, determining a “fast-track” path along the combustor due to tracer entrained in the effusion flow. Replacing PFRs with CSTRs does not change the properties of this flow regarding the onset of the curve. This discussion does not apply to Out_2, $m_{cool} = 7.5\ g/s$, because the interaction between the main and effusion cooling flow is not as pronounced as in the previous operating point. Exchanging mixing zones for segregated ones shows instead a closer resemblance to the optimized one, that confirms the faithfulness to reality of a segregated exit regions and its major impact on a “CSTR” model. Nevertheless, introducing a delay in some areas of the combustor translated to a later rise of the response curve and to a higher mean residence time, τ^m. The close similarity between the two curves also points out the major impact that the mixing tube has on the broadening of the distribution: the presence of zones that are schematized as perfectly mixed, though correct both from a phenological and an optimization point of view, does not significantly contribute to the further broadening of the response curves.

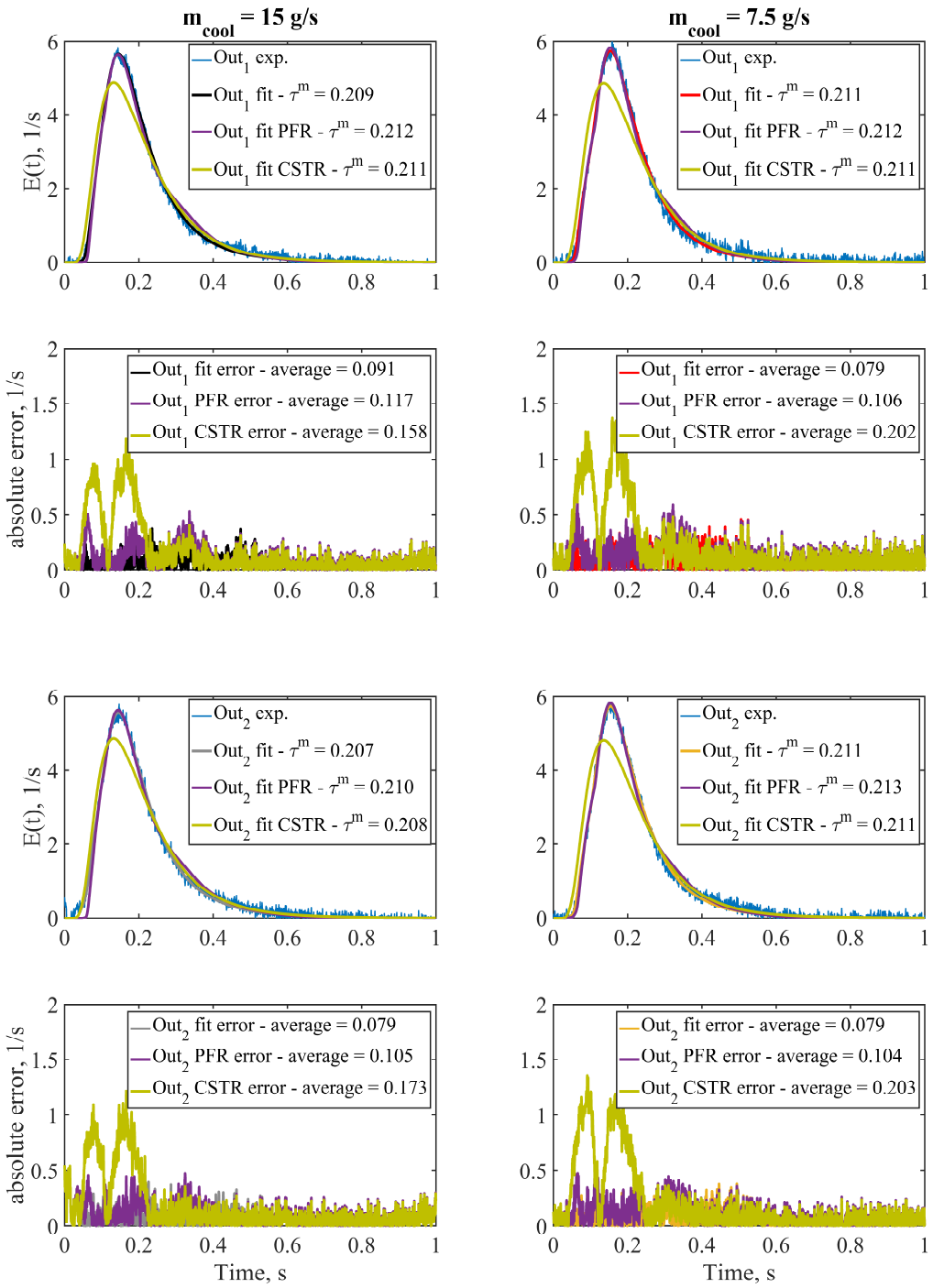

Figure 24: effect of reactors type.

- Effect of the global mass flow from the effusion cooling region to the main flow region.
  In the following, the parameters regulating the flow exchange between the effusion cooling region to the main flow region are altered to check their effect on the global response of the system. More precisely, the effect of a reduction of the parameters (minus 25%, 50% and 90%) is investigated. The reason why only a reduction was investigated for these parameters lies in the need to respect the mass balance at each splitter of the network (2.2.1): in this case, an increase in the parameters value was not possible without altering it. From Figure 25, a heavier reduction implies a larger deviation, as clear both from the shape of the distributions (and respective τ^m) and from the deviation between the experimental and calculated response. The

overall effect is a progressive delay of the main features like position of the maximum and falling edge, that in turn stems into higher calculated τ^m. It is interesting to notice that the rising edge in $Out_1$is not significantly altered, as the onset is anyway mainly determined by the main flow. There is instead an effect on the rising edge of Out_2, $m_{cool} = 15\ g/s$. As stated earlier, the involvement of the cooling air flow on this curve is the strongest among the four presented curves: it is therefore the case that exhibits the highest sensitivity to a change in the parameters regulating the entrainment of cooling air in the main flow. Indeed, both Out_1 and Out_2, $m_{cool} = 7.5\ g/s$, show a weaker responsiveness to this factor, clear from the calculated τ^m and deviation.

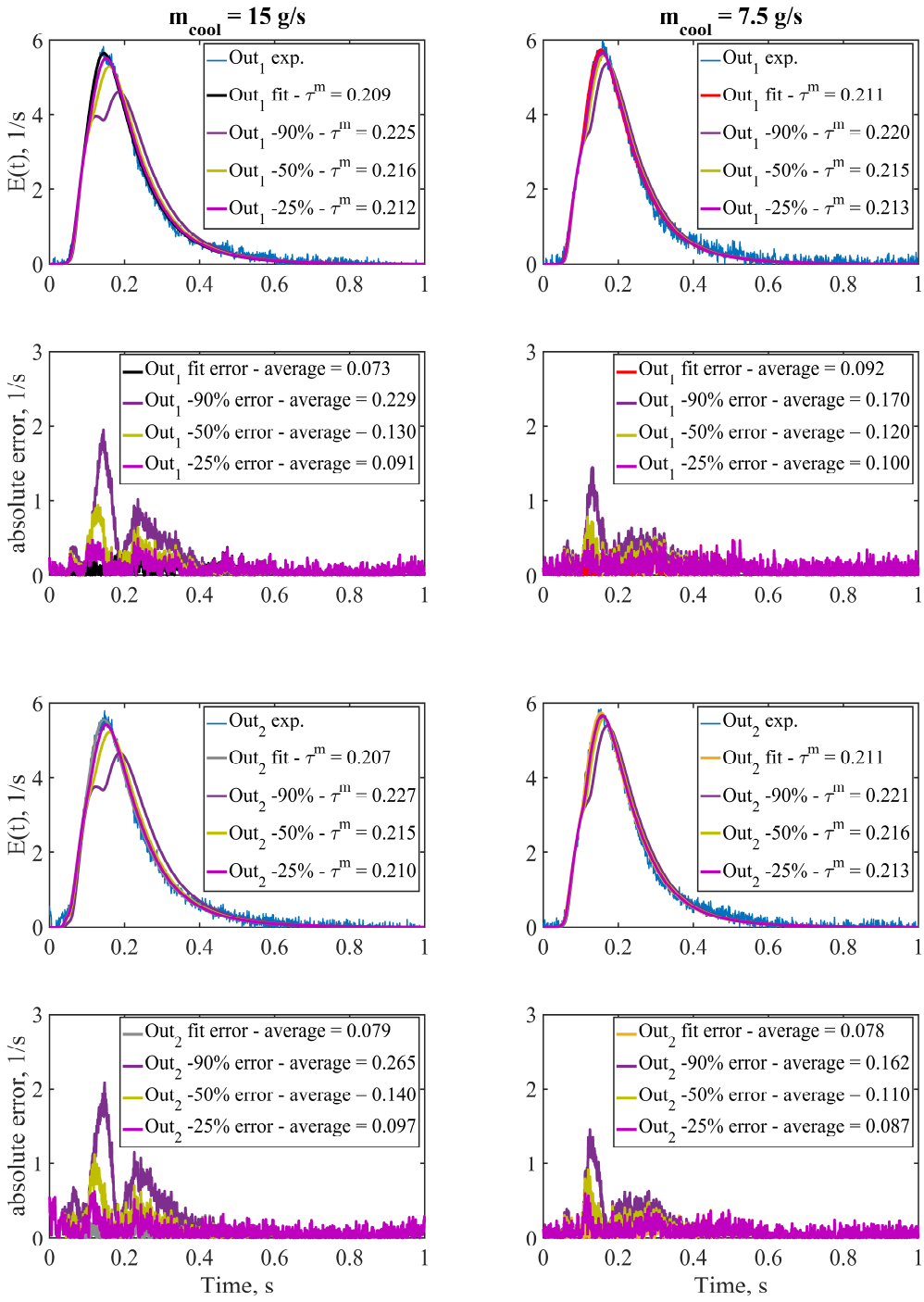

Figure 25: effect of the global mass flow from the effusion cooling region to the main flow region.

- Effect of the global mass flow from the main flow region to the effusion cooling region.
  The sensitivity analysis carried out now shows the effect of a reduction of the parameters involved in the entrainment of the flow from the main path to the effusion cooling on the calculated tracer response. The consequence is a faster distribution, in that a higher flow rate yields a lower τ^m.

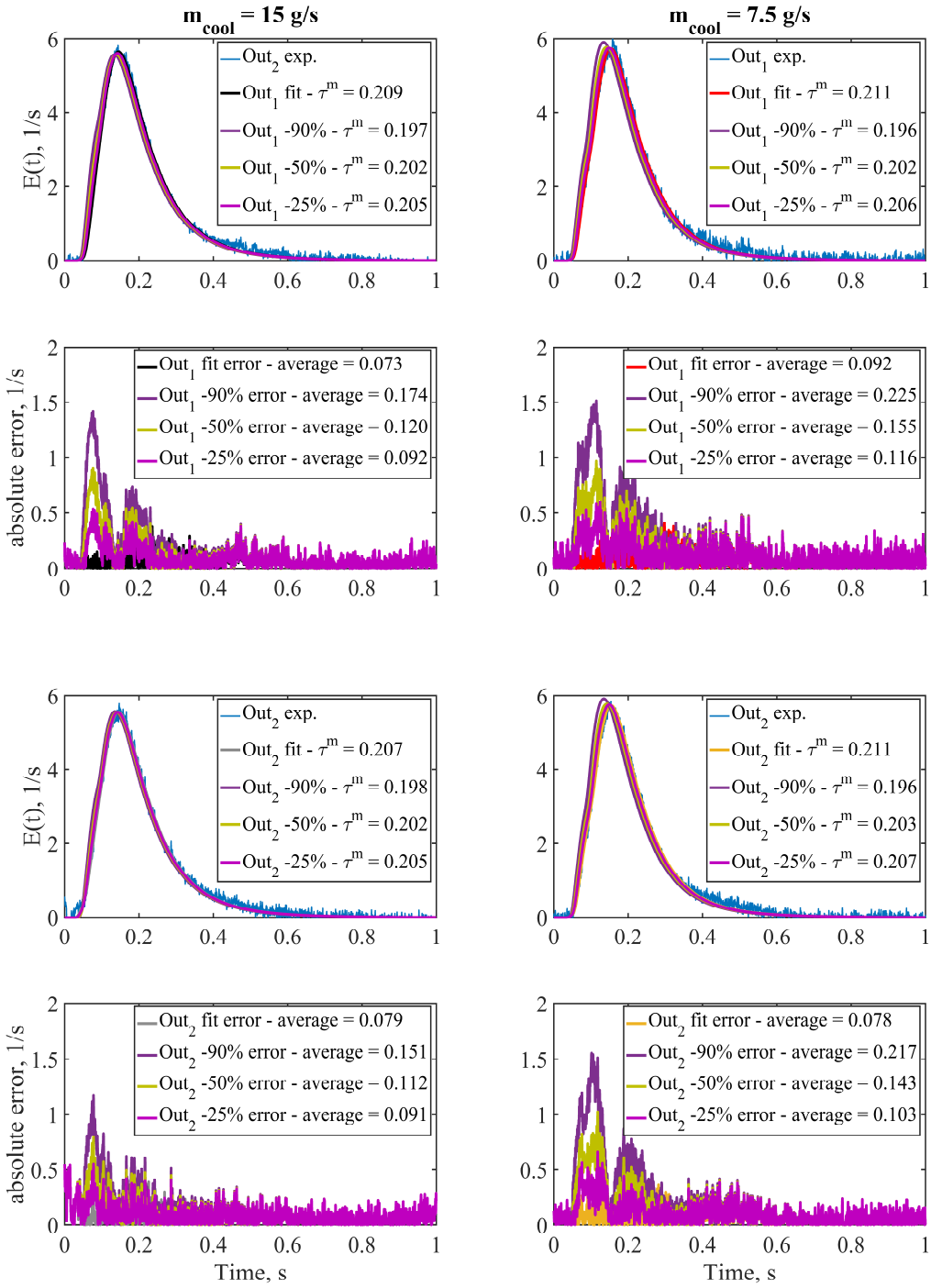

Figure 26: effect of the global mass flow from the main flow region to the effusion cooling region.

- Effect of the mass flow recirculated in the ERZ.
  The results of this analysis are shown in Figure 27. The network parameter responsible for the flow entrained in the ERZ was increased by 10% and decreased by 50% and 90%. The 10% increase has no appreciable effect on the shape of the distribution, or on the parameters chosen

to carry out the comparison (τ^m and the deviation between the experimental and the calculated curves). A decrease in the recirculated mass flow leads to faster distributions, because more flow is heading towards the exit of the combustor, reducing the passing time along its length.

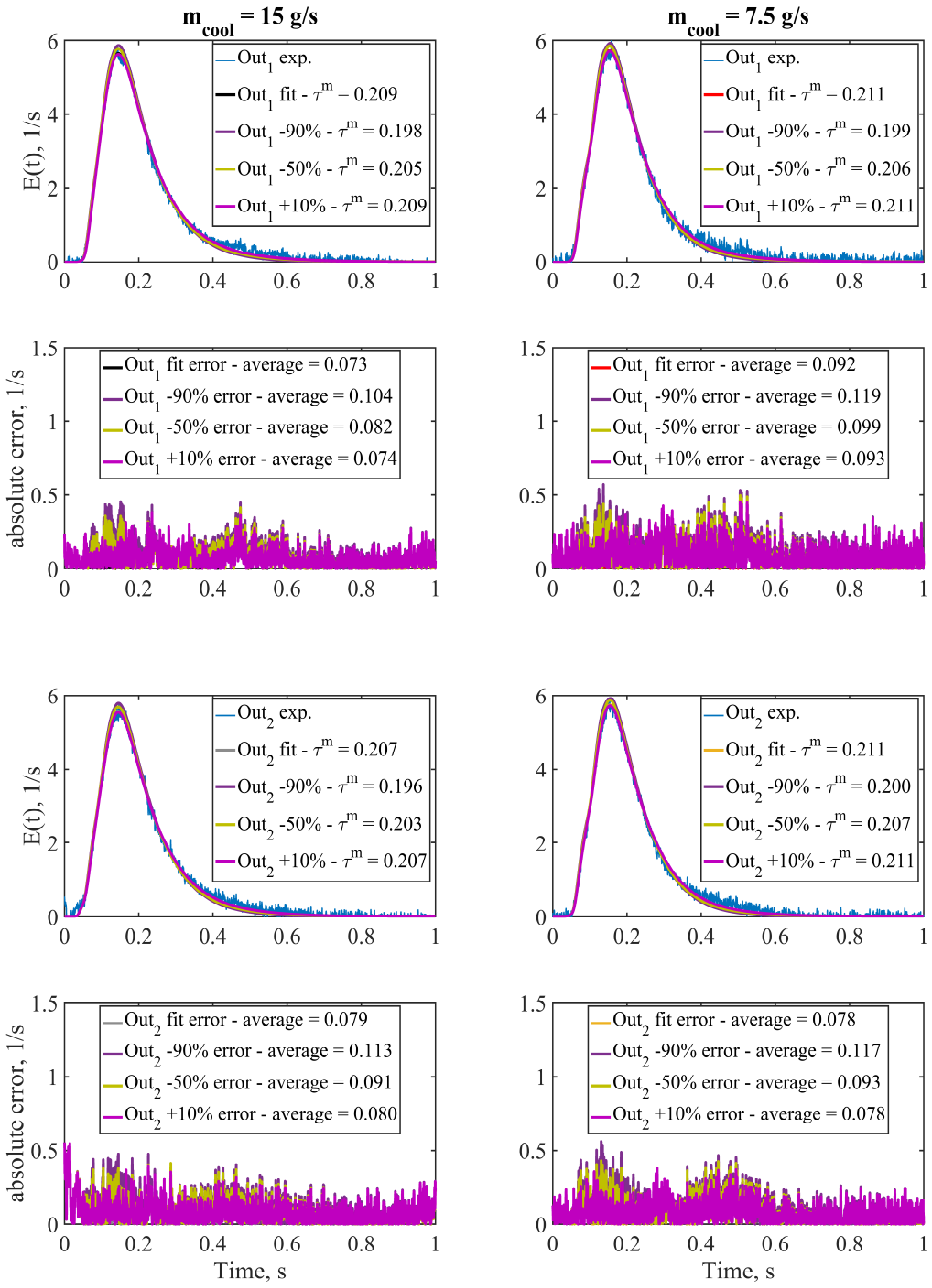

Figure 27: effect of the global mass flow recirculated in the ERZ.

- Effect of the global mass flow recirculated in the IRZ.
  To carry out this last comparison, the network parameters regulating the flow entrained in the ERZ were increased by 10% and decreased by 50% and 90%. The results of this analysis are shown in Figure 28. The 10% increase has a minor effect on the shape of the distribution and

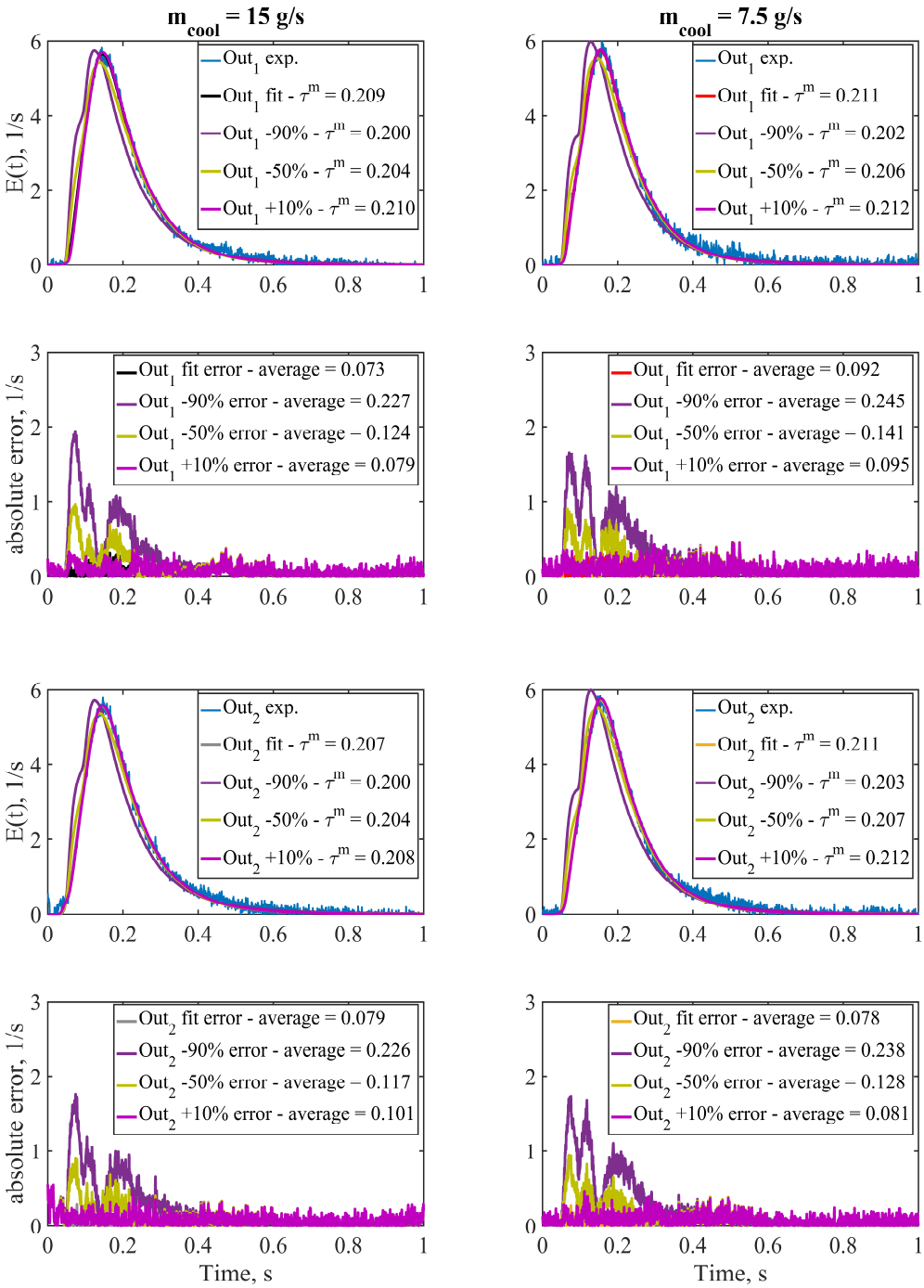

Figure 28: effect of the global mass flow recirculated in the IRZ.

on the τ^m, though clear from the higher deviation between experiments and calculations. A decrease in the recirculated mass flow leads to faster distributions, because more flow is heading towards the exit of the combustor, reducing the passing time along its length. There is no appreciable difference between the two operation points examined, or between the two measurement locations for a given point of operation. The clearer consequence for a reduction of the IRZ flow compared to a reduction of the ERZ flow is attributed to the different value of the characteristic times in these two areas. ERZ residence times are usually larger than IRZ residence times (shown also in [62]). A higher mixing residence time implies a lower peak concentration and an RTD distributed over longer periods, making it less straightforward to appreciate the differences. For the same reason, the situation is clearer if the τ calculated for a certain reactor has a lower value. Furthermore, a change in the ERZ flow directly alters the

dynamic of the system only in the first part of the combustor, whereas changing the IRZ flow directly affects both initial part and exit zone of the combustion chamber. This is an additional explanation for the stronger impact that the IRZ flow has on the overall flow behaviour.

3.3.1.2 RTD extraction from tracer responses

According to RTD theory [30], [34], [42], only the response to a pulse input function can, strictly, be called RTD or $E(t)$. In the hypothesis that the experimental pulse fed to the system during the experiments is a close-to-ideality input function, it still yields the RTD of a system that comprises both the combustion chamber and the pre-combustor path. As already pointed out, this path plays a major role on the broadening of the pulse input, making it unfeasible to invoke the closed-vessel-boundary condition that would make it possible to claim that the tracer response is indeed the $E(t)$ of the system [30].

Therefore, in the following, the RTD, of the system is deduced. The calibrated CRN is initialized with an idealized pulse and the outcome is, strictly, the RTD of the combustor. A comparison between the tracer responses and the RTDs is reported in Figure 29. In the figure, both the simulated pulse impulse and the resulting RTD are shifted in a way that the pulse and the dump plane tracer response (combustor Inlet, Figure 17 and Figure 18) start at the same time. These two signals are both representative of the state at the entrance of the system, and the difference between a response that has already a history and a pulse input is better visualised in the hypothesis that they start at the same time. The experimental, as well as the numerical pulse are normalized to the maximum of the mixing tube signal, whereas the RTD is normalized on the maximum of the corresponding Out_i fit. This is necessary for representation purpose: each calculated $E(t)$ is significantly shorter than the respective tracer evolution. This feature results in higher $E(t)$ values due to the area normalization of the distribution, preventing a qualitative comparison, as the one shown in Figure 29. The pre-combustor path has clearly a strong impact on the dynamics of the system. The non-ideal entrainment of the seeding in the bypass tube (long tail of the experimental pulse) and the mixing in the plenum before the burner outlet make it possible for a broader signal to enter the combustor, severely stretching the exit distributions and the characteristic times.

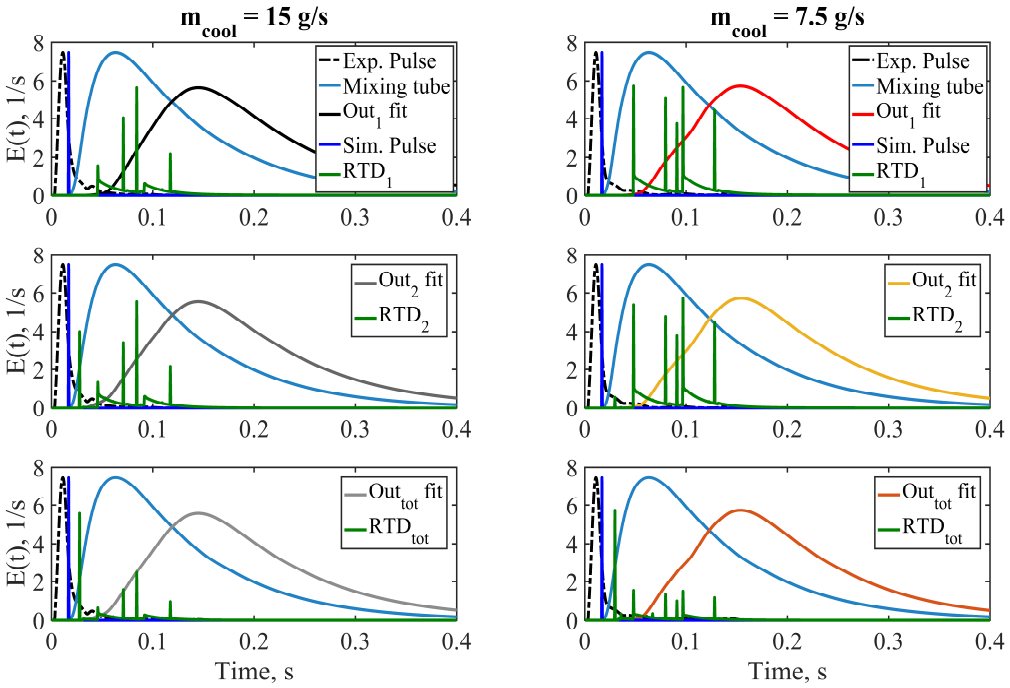

Figure 29: comparison between tracer response and RTD.

Owing to the significant difference between the tracer response and the $E(t)$ calculated from a numerical pulse, the effect of the operating condition on the RTD of the combustor presented in the next chapters (3.4.1) are addressed referring to the calculated closed-vessel RTD $_{tot}$ as shown in Figure 29.

3.3.2 Reactive flow Chemical Reactors Network

The model applied to the fluid dynamic and kinetic modelling of the gas turbine combustor is shown in Figure 30 and Figure 31. Figure 30 shows the different sections of the CRN, while Figure 31 shows the global model. A slight modification to the non-reactive model was made, with the aim highlight macro-mixing zones, taking into account the effect that combustion has on the overall flow field. In this way, it has been possible to consider the zones with a similar mixing behaviour triggered by the presence of a reaction zone. As for the cold flow, three main paths, Figure 30, form the CRN, entirely shown Figure 31.

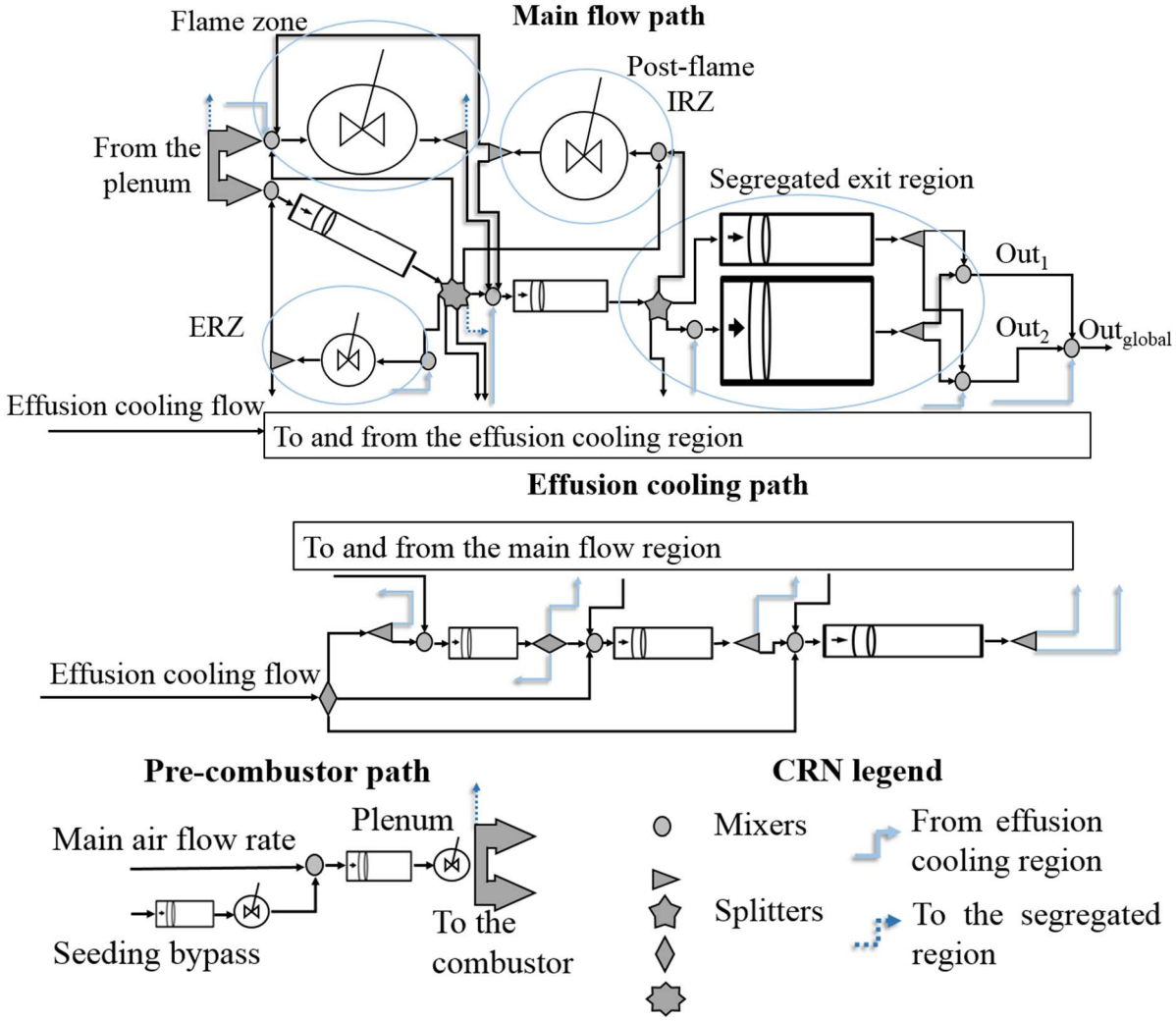

Figure 30: sketch of the CRN employed to fit the reactive flow measurements. ***a****, main path;* ***b****, effusion cooling path;* ***c****, pre-combustor path;* ***d****, explanation of the symbols used.*

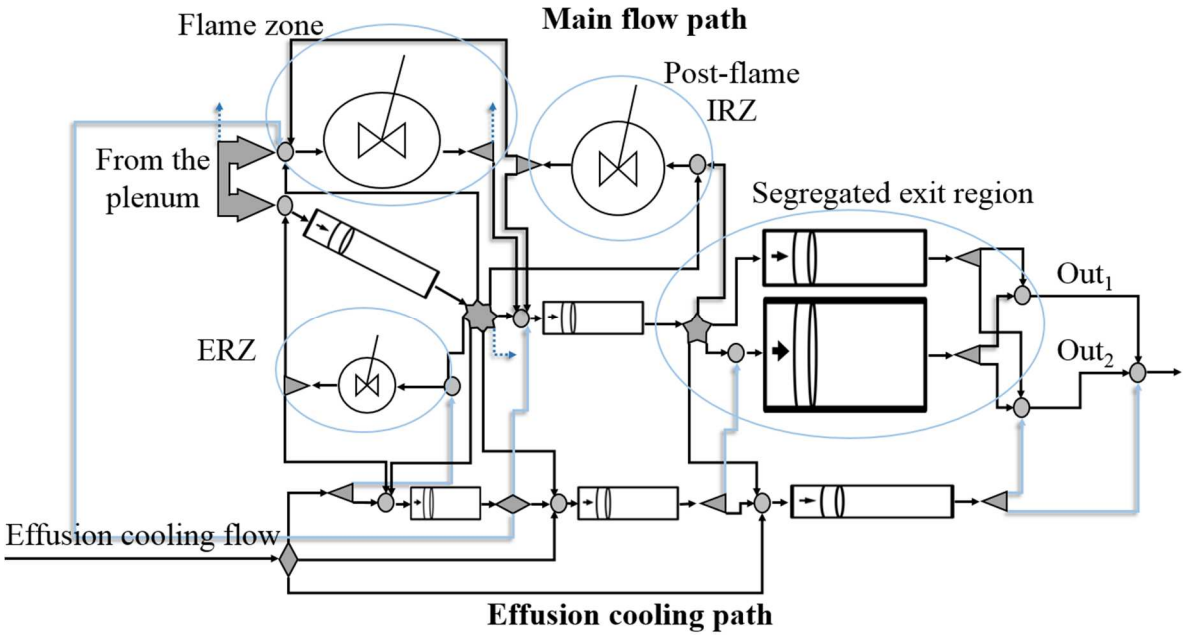

Figure 31: complete sketch of the CRN employed to fit the reactive flow measurements.

Guided by experimental data [18], [108], also reported in Figure 32 and Figure 33, the flame zone was taken as the zone indicated in Figure 33. Therefore, one single zone describes both the flame that stabilizes in the shear layer between the recirculation zones and the first part of the inner recirculation zone. This simple modelling is encouraged by several works [51], [53], [79], [116], where the first part of a swirling-flow combustor is simplified by using one stirred reactor to represent it, due to the high turbulence intensity and strong mixing. After the flame, another CSTR represents the remaining part of the combustor that can be regarded as a stirred region, called Post-flame IRZ. A corner recirculation zone develops in the first part of the combustor, called ERZ, and is as well schematized by a CSTR.

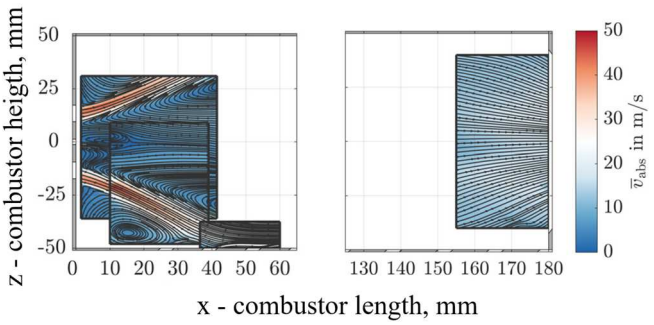

Figure 32: Velocity magnitude and streamlines at partially premixed operation. Reacting flow field, image from [18].

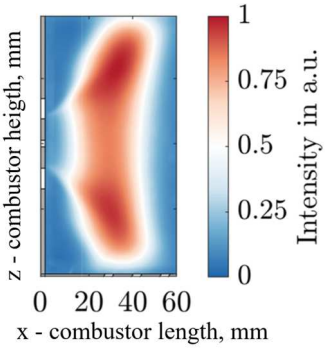

Figure 33: Time averaged chemiluminescence of the partially-premixed and fully-premixed flame, image from [18].

A jet-like region, schematized by a series of two PFRs, occupies the volume between these two recirculation zones. In this region jet region, the recirculated flow merges with the fresh mixture and can either be recirculated or bypass the recirculation zones. Two parallel PFRs are employed to simplify the fluid dynamics of the exit region of the combustion chamber. Here, the flow streamlines mostly follow linear trajectories [18] which justifies the use of the PFR. The effusion cooling path, as in Figure 20.b, is represented by a series of PFRs, as suggested also in [28]. As for the cold flow CRN, the pre-combustor path is also accounted for.

3.3.2.1 Experimental fit – Residence Time Distribution

The agreement between the fit and the experimental data is shown in Figure 34, while Table 5 quantifies the uncertainty of the network variables and, accordingly, the one of the quantities chosen to describe the differences among the tested cases.

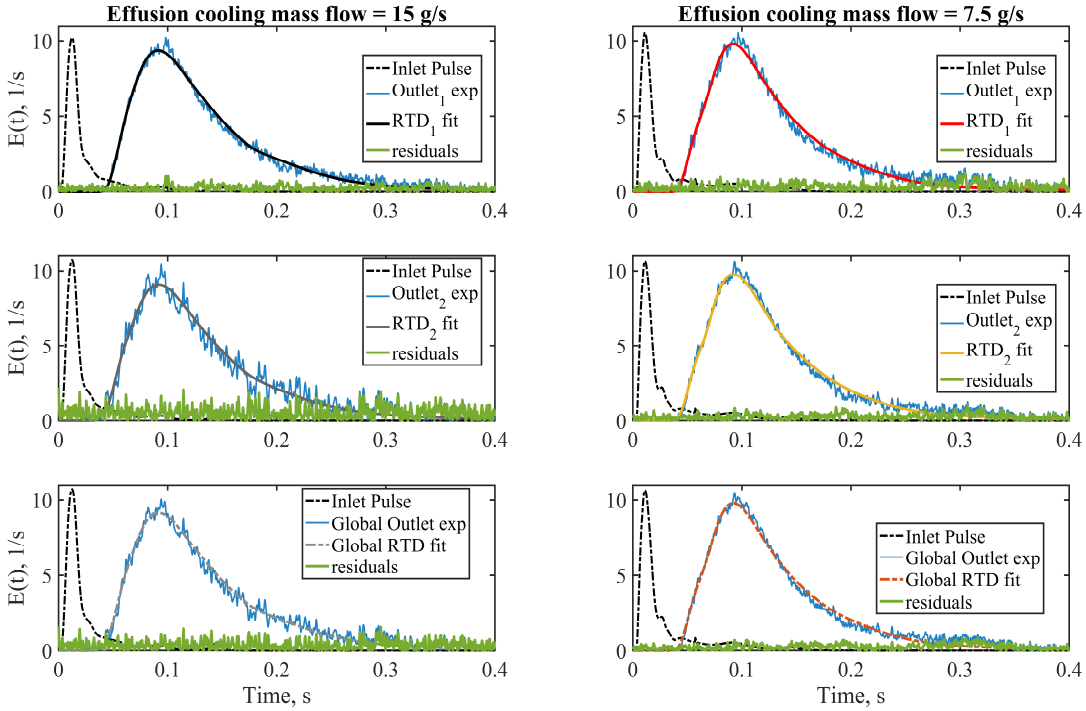

Figure 34: experimental tracer response with superimposed CRN fit, for $m_{cool} = 15\ g/s$ and $m_{cool} = 7.5\ g/s$, reactive flow. The Inlet Pulse is reported for comparison.

As in the 3.3.1.1, the single-injection Inlet Pulse was fed to the Simulink® program, and the model fitted to the corresponding single-injection Out_1 and Out_2. The parameters are explained in Table 3.

Table 5: uncertainties associated with the CRN fit, reactive flow, $m_{cool} = 15\ g/s$.

	Average fit	Mean single injection		Average fit	Mean single injection
$\tau^m_{1\_response}$	0.13 ± 0.05	0.11	τ^c_1	0.010 ± 0.002	0.012
$\tau^m_{2\_response}$	0.14 ± 0.05	0.12	τ^c_2	0.001 ± 0.002	0.003
$\tau^m_{tot\_response}$	0.13 ± 0.05	0.10	τ^c_2	0.001 ± 0.002	0.003
τ^m_1	0.0260 ± 0.006	0.026	$\tau^{0.95}_1$	0.05 ± 0.03	0.06
τ^m_2	0.026 ± 0.005	0.027	$\tau^{0.95}_2$	0.05 ± 0.03	0.07
τ^m_{tot}	0.018 ± 0.003	0.017	$\tau^{0.95}_{tot}$	0.041 ± 0.005	0.043
σ^2_1	$0.0013 \pm 8 \times 10^{-4}$	0.0011	$\tau^{0.99}_1$	0.20 ± 0.09	0.16
σ^2_2	$0.0016 \pm 9 \times 10^{-4}$	0.0017	$\tau^{0.99}_2$	0.22 ± 0.08	0.20
σ^2_{tot}	$0.0010 \pm 1 \times 10^{-4}$	8×10^{-4}	$\tau^{0.99}_{tot}$	0.13 ± 0.03	0.12
S^3_1	8 ± 4	10	$\frac{m_{IRZ}}{m_{in\_main}}$	6.5 ± 0.7	7
S^3_2	8 ± 3	8	$\frac{m_{ERZ}}{m_{in\_main}}$	0.15 ± 0.05	0.15
S^3_{tot}	10 ± 2	10	$\frac{m_{flame}}{m_{in\_main}}$	0.97 ± 0.03	0.98
$\frac{m_{main\to cooling}}{m_{total\_feed}}$	0.43 ± 0.05	0.47	$\frac{m_{cooling\to ma}}{m_{total\_feed}}$	0.18 ± 0.03	0.2
τ_{ERZ}	0.03 ± 0.01	0.03	τ_{IRZ}	$5.8 \times 10^{-4} \pm 7 \times 10^{-5}$	5.5×10^{-4}
			τ_{flame}	$0.0031 \pm 1 \times 10^{-4}$	0.0031

The single-injection variation of the fits is shown in Figure 35.

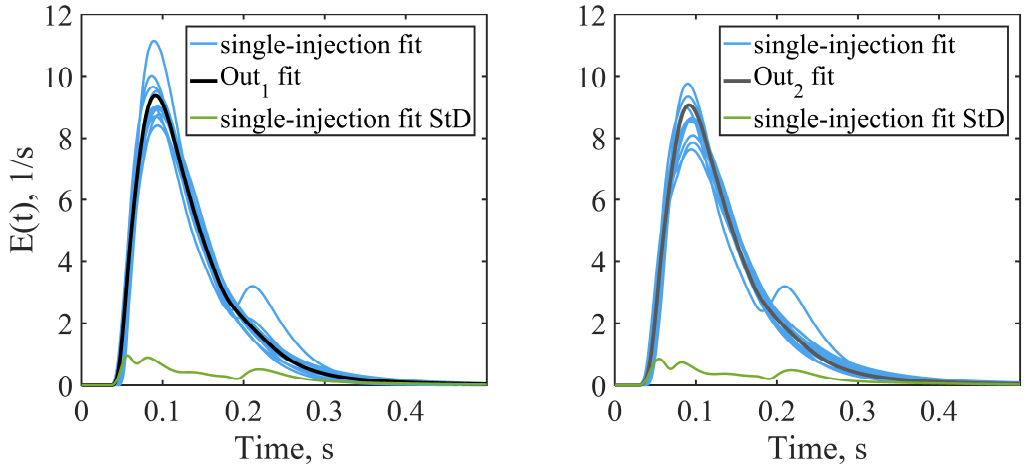

Figure 35: single-injection CRN-fit for reactive measurements, in blue, and superimposed average fit. The single-injection optimization is applied on $m_{cool} = 15\ g/s$.

3.3.2.2 RTD extraction from tracer responses

The RTD, or $E(t)$, during reactive operation is deduced as already done in the previous chapter. The calibrated CRN is initialized with an idealized pulse and the outcome is, strictly, the RTD of the combustor [30]. A comparison between the tracer responses and the RTDs is reported in Figure 36. In the figure, both the simulated pulse impulse and the resulting RTD are shifted in a way that the pulse and the dump plane tracer response start at the same time. These two signals are both representative of the state at the entrance of the system, and the difference between a response that has already a history and a pulse input is better visualised in the hypothesis that they start at the same time. The experimental, as well as the simulated pulse are normalized to the maximum of the mixing tube signal, whereas the RTD is normalized on the maximum of the corresponding Out_i fit. This is necessary for representation purpose: each calculated $E(t)$ is significantly shorter than the respective tracer evolution. This feature results in higher $E(t)$ values due to the area normalization of the distribution, preventing a qualitative comparison, as the one shown in Figure 33. The strong impact of the pre-combustor path on the dynamics of the system is once again confirmed.

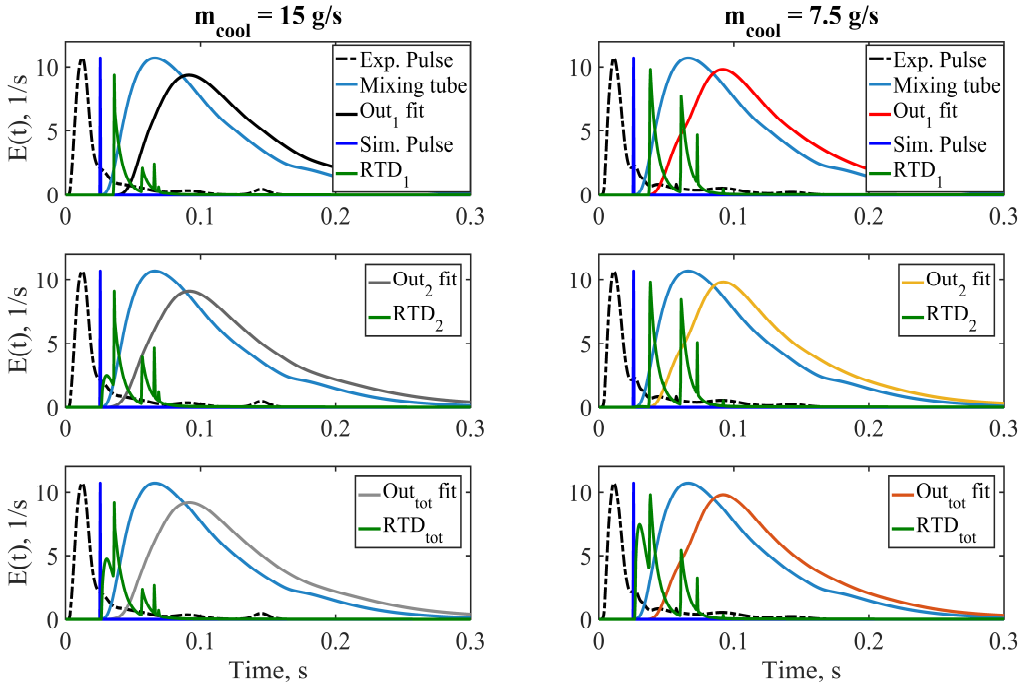

Figure 36: comparison between calculated RTDs and tracer responses for the reactive flow with variyng effusion cooling massflow.

As established for the analysis of the cold flow results, the calculated RTDs will be employed in the following to comment on the different flow behaviour under different operating conditions. Except for the two reference cases, $m_{cool} = 15\ g/s$ and $m_{cool} = 7.5\ g/s$, only the global RTD is considered for comparison.

3.3.2.3 Experimental fit – carbon monoxide prediction

The following figures, Figure 38 and Figure 39, illustrate the comparison between the kinetic results of the CRN in terms of CO concentration and experimental measurements. The comparison is carried out comparing measured and calculated profiles inside the combustor, whose location is better highlighted in Figure 37. A clarification before going further into the comparison: zones represented by CSTRs give as result a single value of species concentration, in virtue of the basic hypothesis behind this reactor, 2.1.1; whereas a PFR returns an evolution along its reaction coordinate, that can be regarded as a spatial coordinate, and as an evolution over time, 2.1.2.

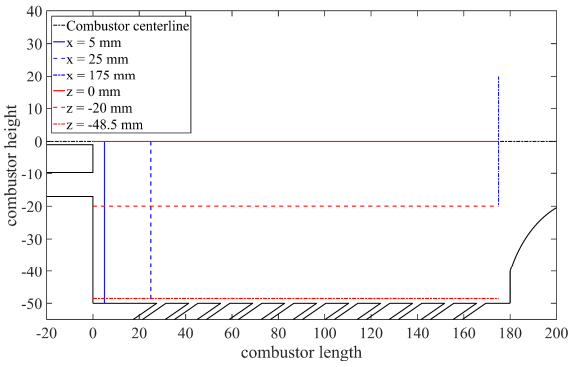

Figure 37: sketch of the lower half of the flame tube. Radial (blue) and axial (red) location used for the following comparison are highlighted.

The overall agreement is good for both investigated operating conditions. Several kinetic mechanisms are tested: the two-step combustion mechanism from Ansys Fluent®[117], the $GRI\ 3$ [118], the $C1 - C4$ kinetic mechanism with NO_x formation [119]–[122] and the Aramco mechanism [123]. Except for the two-step mechanism, which fails to correctly reproduce the trends, the other mechanisms do not show severe discrepancies among each other. The following discussion refers to the results obtained with the $C1 - C4$ mechanism, and it also employed for the kinetic calculations in 3.4.2. The choice is based on its overall better agreement to the data with respect to the $GRI\ 3$, and its ability to reach converge faster compared to the Aramco mechanism (approximately 5 times faster). Nonetheless, in some cases the RNA software failed to reach convergence in a reasonable time employing the $C1 - C4$ mechanism. The GRI was therefore employed to cover those cases, in virtue of the similar prediction between the two mechanisms.

For the following discussion on the comparison between experiments and kinetic calculations, Figure 30Figure 33 are taken as reference for the zonal modelling. Referring to Figure 37, Figure 38 and Figure 39, starting from the left side for $z = 0\ mm$, and proceeding along the combustor length, there is the CO amount produced in the zone that accounts for the flame and the first part of the IRZ. The calculated mole fraction value appears higher in the flame zone with respect to experiments. This slight discrepancy stems from the employment of a single macro-zone to outline this region, where formation from the flame stabilizing in the shear layer between the recirculation zones, recirculation and further reaction of the combustion intermediates take place. Because of the intense mixing characteristic and the coupled mixing evolution, several researchers recognize this zone to be representable by one sole CSTR [51], [53], [80], [116]. This possibility also supports the need to employ, if possible, macro-mixing zones, when approaching the problem using RTD-driven compartmental models. Macro zones chosen for their fluid dynamic characteristic reduce the number of parameters necessary for the optimization, making it more reliable and able to mirror the underlying phenomena inside the system under investigation. These

two reasons are behind the choice of a unique reactor for the flame and the first part of the IRZ. Nonetheless, this choice translates in a value of CO mole fraction that is average between those that characterize this region (0.004 in the flame region and 0.001 in the early IRZ, for $\mathrm{m_{cool}} = 15\ \mathrm{g/s}$). To support what just stated, the profile $z = -20\ mm$ shows a better agreement between experiments and modelling, differently from $z = 0\ mm$ and $x = 5\ mm$ (where the first zone extends until $-10\ mm$). Going back to the centreline plot, $z = 0\ mm$, after the flame length (approximately $50\ mm$ [18]) there is the post-flame IRZ, where the additional time available for reaction and the intense mixing lower the CO concentration. Its value increases again reaching segregated exit region of the combustor: here flow bypasses from the burner, flame and jet region bring unreacted CO and CH_4 that react further. The profiles $x = 5\ mm$ and $x = 25\ mm$ further clarify the CO formation in the jet region and in the ERZ. The jet region has, until $x = 25\ mm$, an increasing CO amount forming along its length due to the proceeding reaction: it represents the interval $-20 < z < -10$ in $x = 5\ mm$, and $-32.5 < z < -25$ in $x = 25\ mm$, with a CO mole fraction increasing with x coordinate. The extreme left part of both x profiles shows the CO consumption in the ERZ. The profile $z = -48.5\ mm$ is chosen to compare the CRN performance against experimental data in the vicinity of the effusion cooling region. Until $x = 27.5\ mm$ the amount of CO corresponds to the ERZ. After $x = 27.5\ mm$, the effusion cooling region starts. At the beginning of this zone there is a high value of CO concentration coming from the jet flow with high CO content, that reacts with the additional air entering in this area and lowers its concentration. It rises again because of the flow entrained in the second near-effusion reactor, since more flow containing CO and fuel is entrained in this part of the system. The mole fraction decrease is slower than before: the trend is correctly caught by the CRN near-wall reactor, although the exact value is not reproduced. This zone is followed by a last exit-region near-wall PFR: although the temperature is way lower than the average combustor temperature, the CO concentration decreases fast due to mixing and further reaction, reaching the lowest measured value (in the order of ~ 10 ppm). This is attributed to the entrainment of completely reacted flow pockets and continuous mixing with the effusion air entering the system along its length. The vertical profile $x = 175\ mm$ compares the results on a vertical line almost at the exit of the combustion chamber, where average values are correctly reproduced.

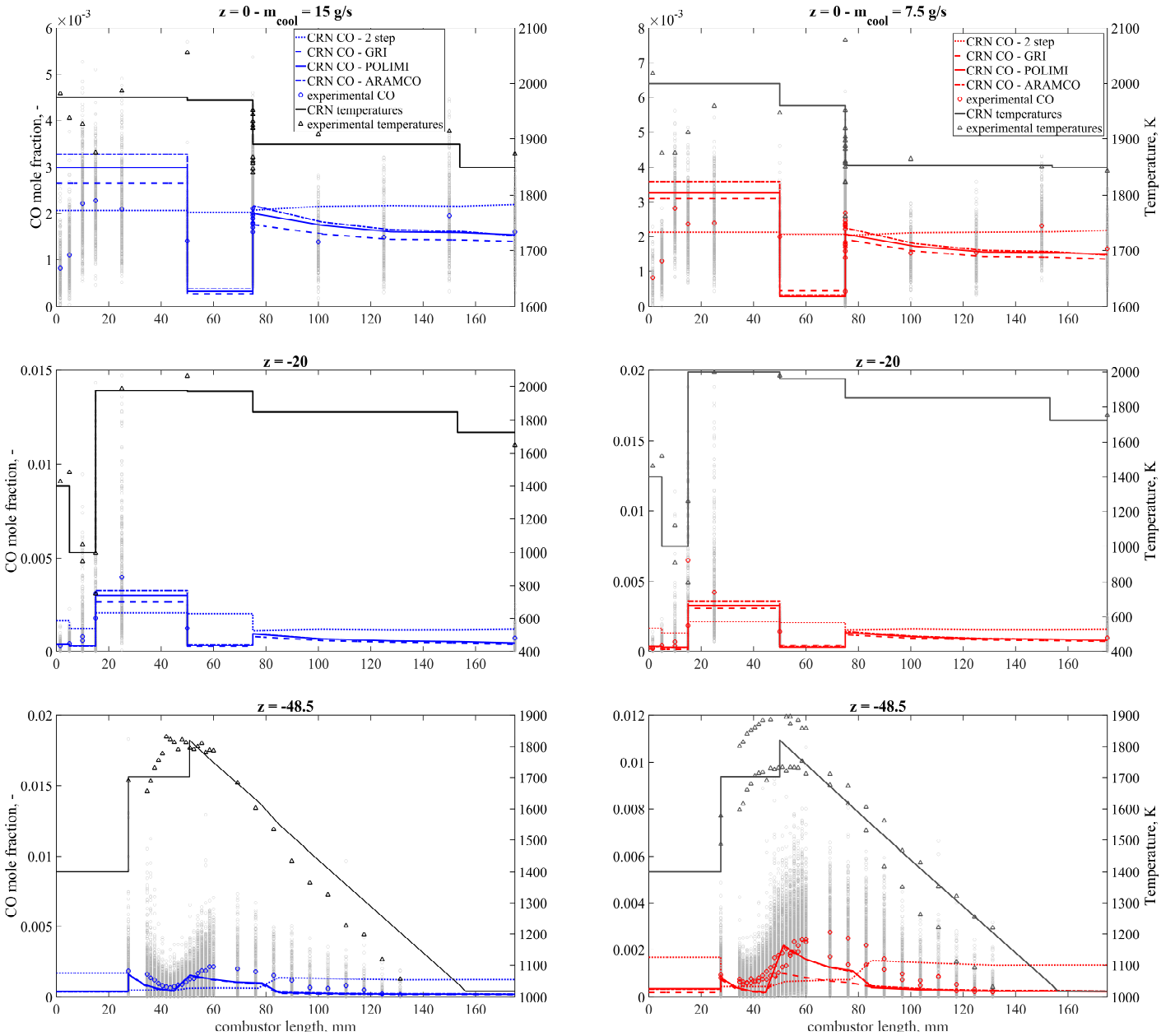

Figure 38: comparison between experimental data and CRN-predicted CO concentration values along horizontal profiles, $m_{cool} = 15\ g/s$ and $m_{cool} = 7.5\ g/s$. Several kinetic mechanisms are applied. The grey circles are experimental CO single-shot concentration values.

-

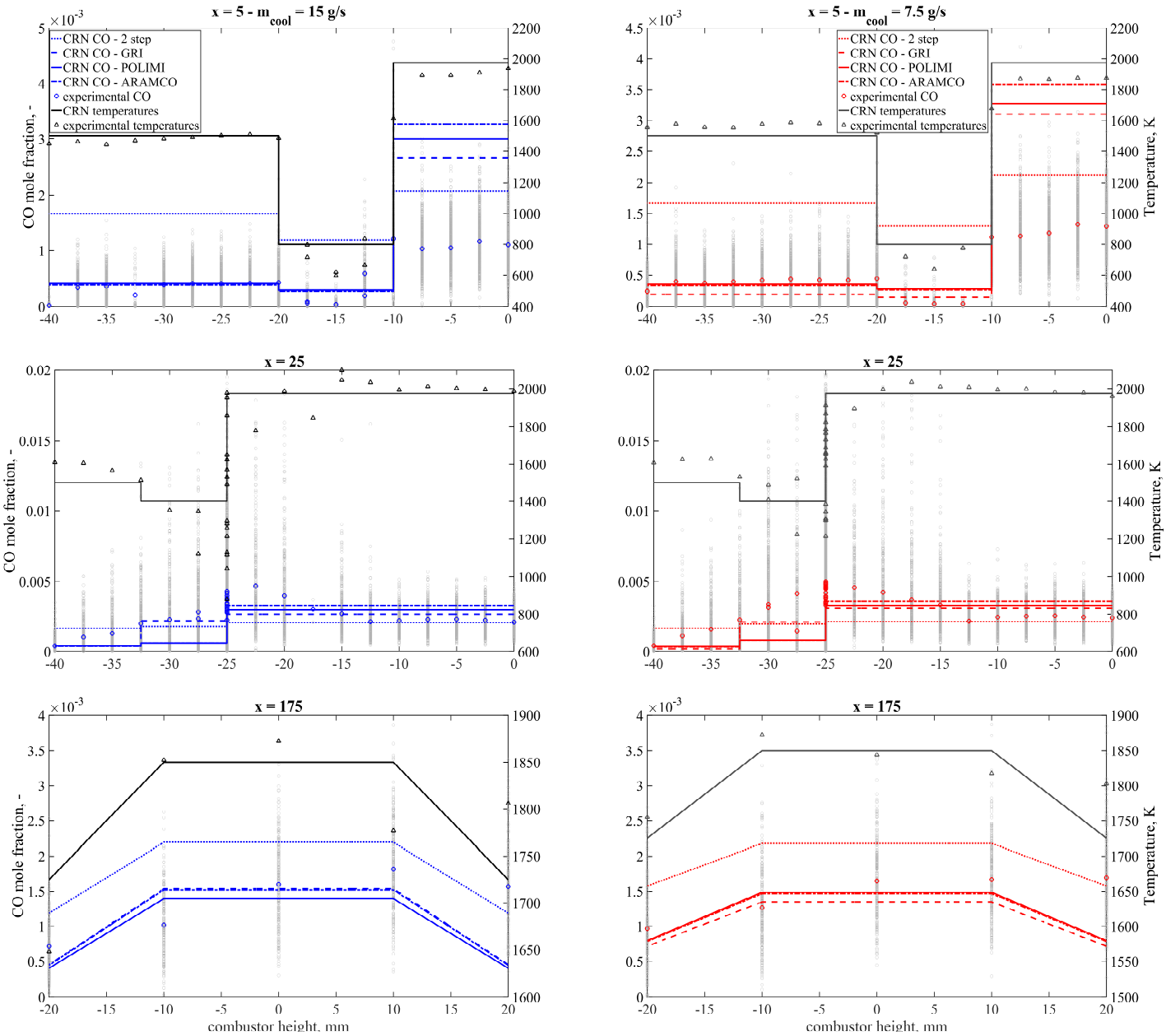

Figure 39: comparison between experimental data and CRN-predicted CO concentration values along vertical profiles, $m_{cool} = 15\ g/s$ and $m_{cool} = 7.5\ g/s$. Several kinetic mechanisms are applied. The grey circles are experimental CO single-shot concentration values.

As shown in the comparison carried out, the CRN model reproduces the CO evolution trends throughout the combustor with reasonable agreement, along several selected profiles. It is therefore employed in the following paragraphs to evaluate the influence of the different operating parameters on CO and other pollutants formation in the gas turbine model combustor under realistic boundary conditions.

3.4 Results and discussion

In this section, the results obtained from the CRN fit applied to the investigated operating conditions are shown and discussed. First, the isothermal flow fits are studied in terms of characteristic times and shapes of the global distributions. Each operating condition shown is compared to the standard operation point, which is summarized in Table 6.

Table 6: relevant boundary conditions of the standard operation point.

	Operation point, units	
Preheating temperature	623	K
System pressure, P	2.5	bar
Main air mass flow, m_{in_main}	30	g/s
Equivalence ratio, $\varphi_{\text{lean premixed}}$	0.75	[-]
Swirl number, S	0.7	[-]
Effusion cooling mass flow, m_{cool}	15	g/s
Fuel staging ratio, st.	0%,	[-]

The RTDs for the reactive measurements follow the section on the cold flow results. In this case, a discussion about the impact on the operating condition on the species formation in the SSGT accompanies the discussion about the global RTD quantities.

3.4.1 Cold flow results

The impact of the boundary conditions on the RTD of the system is described. With respect to Table 6, the following variations on the parameters were explored.

Table 7: explored parameters for the cold-flow measurements.

	Operation point, units	
System pressure, P	2.5 and 3	bar
Swirl number, S	0.7 and 1.3	[-]
Effusion cooling mass flow, m_{cool}	15 and 7.5	g/s
Fuel staging ratio, st.	0% and 50%	[-]

The results are presented in the following order:

- effect of effusion cooling mass flow, m_{cool},
- effect of the fuel-staging ratio, $st.$,
- effect of the operating pressure, P,
- effect of the swirl number, S.

3.4.1.1 Effect of effusion cooling mass flow

The CRN-fit tracer responses are proposed in Figure 40. The main conclusion is already clear: a lower effusion cooling mass flow has a lower impact on the mixing field inside the combustion chamber. For $m_{cool} = 15\ g/s$ there is a visible distinction between Out_1 and Out_2 (quantified in Table 8), as the latter shows an earlier rise. This feature is not visible for $m_{cool} = 7.5\ g/s$, where the distributions overlap. On the lower row, for a given measurement position, the decrease in coolant flow seems to have a similar delaying effect, even though the effect is more pronounced on Out_2.

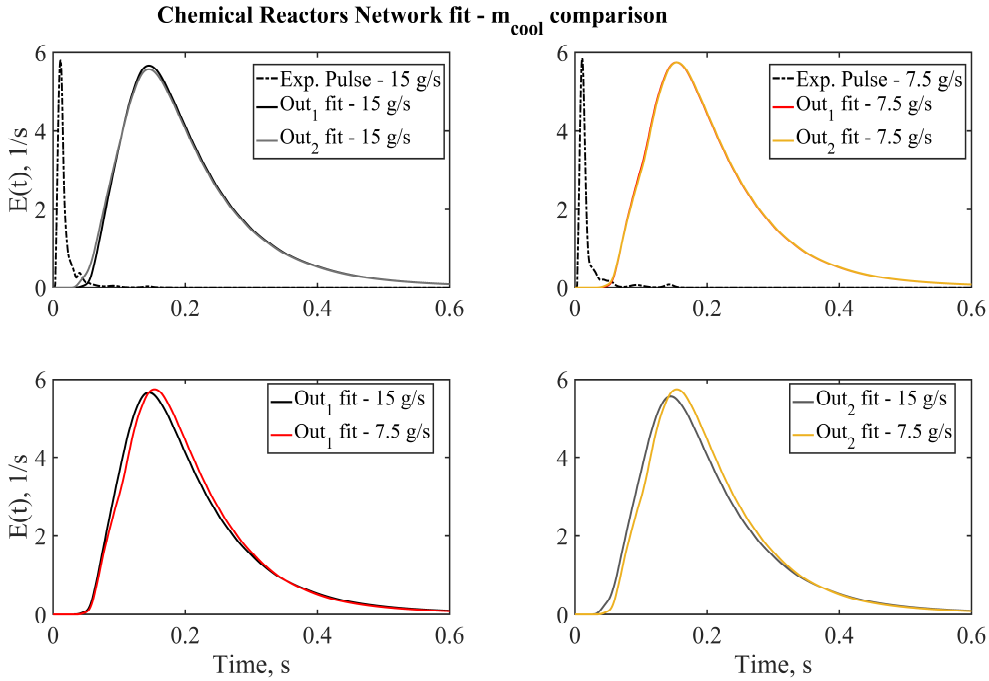

Figure 40: CRN-fit experimental tracer responses, $m_{cool} = 15\ g/s$ and $m_{cool} = 7.5\ g/s$. Upper row:Out_1 and Out_2 for the two investigated operating conditions; lower row: comparison between the same measurement location for different operating conditions.

Figure 41 shows the extracted RTDs. For the two operating conditions under investigation, which are also the reference ones as explained in paragraph 3.2.2, the comparison is carried out showing the RTDs relative to both measurements locations as well. They show several huge peaks, out of scale with respect to the mean of the distributions, which are associated with the entrainment of the tracer in the effusion cooling region.

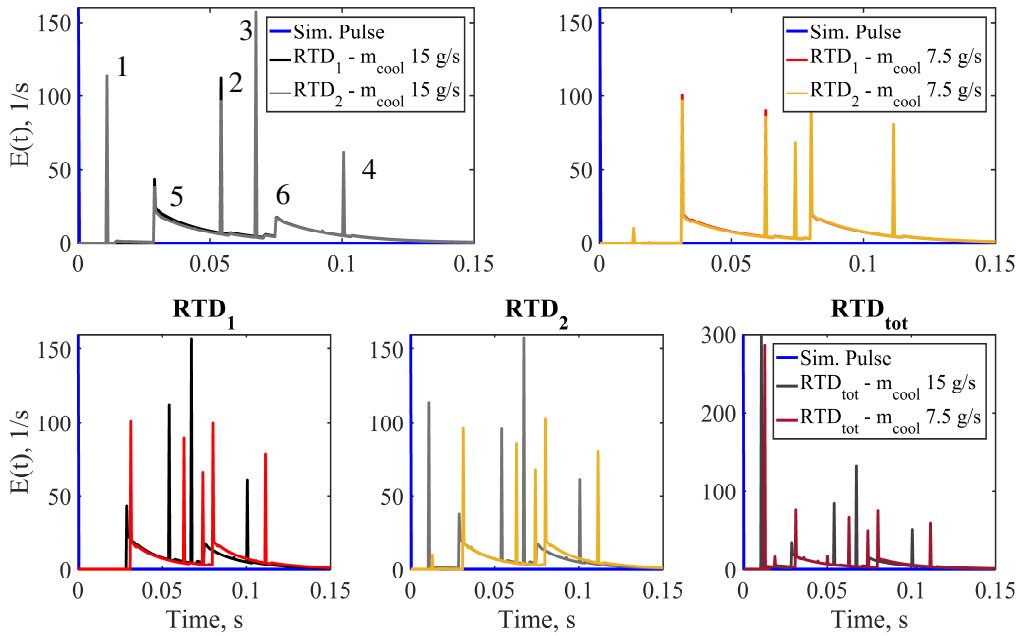

Figure 41: RTDs extract ed from the calibrated CRN, $m_{cool} = 15\ g/s$ and $m_{cool} = 7.5\ g/s$. Upper row:Out_1 and Out_2 for the two investigated operating conditions; lower row: comparison between different operating conditions for the same measurement location.

Multiple peaks are present, exemplifying the different entrainment opportunities in the PFR-zones. The association between a phenomenon and a given peak is based on the analysis of the residence times in

each zone. This value is one of the output of a model whose parameters have been optimized against the response of the system. The following features are distinguished:

- immediate entrainment in the effusion cooling region (peak "1", Figure 41),
- first entrainment in the effusion cooling region and later mixing in the main flow ("2", "3" and "4", Figure 41).

These flow paths are better explained in Figure 42. In this figure, the identified pathways have been sketched and linked to the peaks shown in Figure 41.

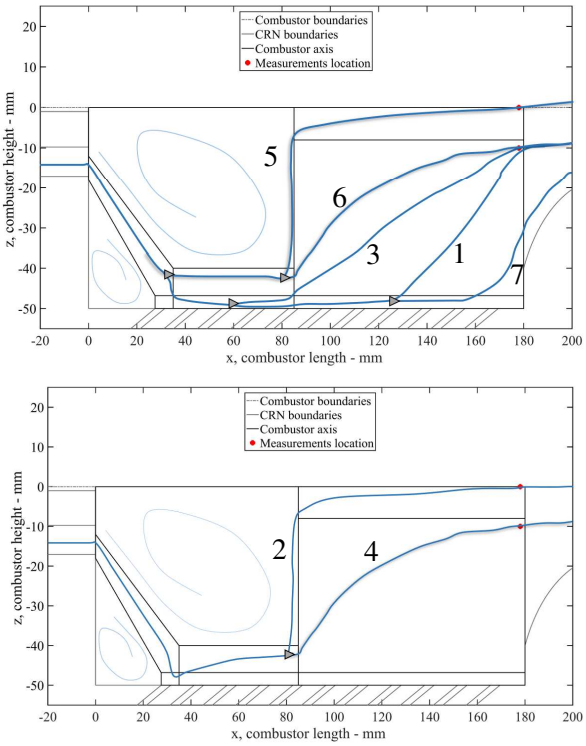

Figure 42: basic sketch of the identified flow paths responsible for the appearance of the ensemble of peaks differently delayed with respect to each other. A grey triangle symbolizes a splitting element, in accordance with the CRN legend, introduced in Figure 20 and Figure 30. The lighter curves indicate the position of the RZs. Besides the paths found in Figure 41 and described here, another path, number 7, is possible: part of the flow is entrained in the effusion cooling region and exits undetected. This part of the flow is accounted for only in the RTD_{tot}.

Instead, the local maxima at $t{\sim}0.03\ s$ and $t{\sim}0.07\ s$, "5" and "6", are attributed to the portion of tracer that follows the main flow paths. These two peaks show an exponential decay after a sharp rise in virtue of the parallel mixing in the recirculation zones. More specifically, "5" represent the portion of the flow following the jet-like region and then mixing in the central PFR at the exit. The peak "6" represents the portion of the flow that mixes in the side PFR after passing the jet region. From the coupled analysis of Figure 41 and Figure 42 emerges that the flow entrained from the main path in the cooling path reaches the exit later if it entrained since the start of the liner, peaks "2" and "3".

The bypass-effect of the effusion path is nonetheless present in $m_{cool} = 7.5\ g/s$ as well, as evident from Figure 41. However, its contribution to RTD_2 with respect to RTD_1 is negligible, especially if compared to $m_{cool} = 15\ g/s$: it was indeed not possible to discern it by judging the tracer responses alone. This is confirmed by the τ_i^c values reported in Table 8. Here, the parameter $\frac{m_{cooling \rightarrow main}}{m_{total\_feed}}$ is reported, as an attempt to quantify the involvement of the near-wall path on the global mixing characteristics. As reported, its value is approximately half while feeding half the effusion cooling mass flow.

Besides the clear differences attributed to the main flow - effusion cooling interaction, the RTDs present a similar behaviour, exemplified by the global moments of the three distributions, Table 8. The parameters shown in Table 8, and in the other comparison tables, are explained in Table 3. The τ_i^m are similar, slightly higher in the case of $m_{cool} = 7.5\ g/s$ because of the lower flow rate introduced in the system. The $\tau_i^{0.95}$ and $\tau_i^{0.99}$ highlight the same tendency, as well as the higher moments of the distributions. It is interesting to notice the time range between these two characteristic times: 95% of the tracer gets outside of the system before 0.2 s, while additional 0.3 s, and thus approximately 1.5

times the $\tau_i^{0.95}$, are required to reach the point where 99% has left the system. This phenomenon is attributed to the continuous entrainment in the recirculation zones, indicated in Table 8 as $\frac{m_{IRZ}}{m_{in\_main}}$ and $\frac{m_{ERZ}}{m_{in\_main}}$: a great amount of flow is entrained and recirculated, especially in the IRZ.

Table 8: global properties of the RTDs and CRN-fit parameters, $m_{cool} = 15\ g/s$ and $m_{cool} = 7.5\ g/s$.

	$m_{cool} = 15\ g/s$	$m_{cool} = 7.5\ g/s$		$m_{cool} = 15\ g/s$	$m_{cool} = 7.5\ g/s$
τ_1^m	0.081	0.089	τ_1^c	0.029	0.031
τ_2^m	0.080	0.090	τ_2^c	0.011	0.013
τ_{tot}^m	0.072	0.077	τ_{tot}^c	0.011	0.013
σ_1^2	0.0054	0.0054	$\tau_1^{0.95}$	0.16	0.18
σ_2^2	0.0055	0.0054	$\tau_2^{0.95}$	0.16	0.18
σ_{tot}^2	0.0057	0.0058	$\tau_{tot}^{0.95}$	0.16	0.17
S_1^3	5	5	$\tau_1^{0.99}$	0.443	0.446
S_2^3	5	5	$\tau_1^{0.99}$	0.441	0.447
S_{tot}^3	5	4	$\tau_{tot}^{0.99}$	0.43	0.43
τ_{IRZ}	0.011	0.012	$\frac{m_{cooling\rightarrow main}}{m_{total\_feed}}$	0.30	0.14
τ_{ERZ}	0.17	0.17	$\frac{m_{main\rightarrow cooling}}{m_{total\_feed}}$	0.27	0.32
$\frac{m_{IRZ}}{m_{in\_main}}$	1.3	1.2	$\frac{m_{ERZ}}{m_{in\_main}}$	0.08	0.08

3.4.1.2 Effect of fuel staging

To properly describe the flow phenomena while altering a certain amount of fuel staging, a slight modification of the network was necessary to consider the extra feed-stream and the different mixing phenomena it might induce. Referring to Figure 20 and Figure 21 for the basic CRN (no fuel staging), the modified near-nozzle region is shown in Figure 43. It follows the model proposed by [75], adopted and adjusted by [74], [100]. The model in Figure 43 has one more mixed zone that receives flow from the pilot tube, and entrains flow emerging from the plenum and from the IRZ: in this way, the main features linked to the presence of an additional flow are addressed. The flow from this pilot zone is then entirely entrained into the IRZ.

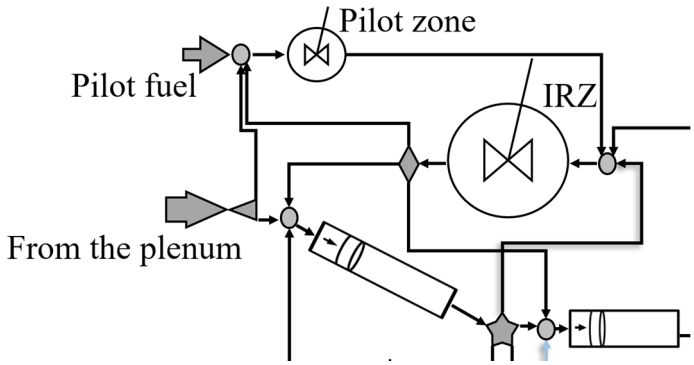

Figure 43: modified network to describe the near-nozzle region for fuel-staging operation. A CSTR reactor to exemplify the injection of the pilot-fuel has been added in the IRZ.

The CRN-fits for the case without fuel staging, $st. = 0\%$, and for the case with 50% fuel staging, $st. = 50\%$, are displayed in Figure 44. In these cases, as m_{cool} was kept constant, the behaviors of the tracer responses with respect to different measurement locations are is similar: Out_2 shows the exit of tracer earlier than the higher measurement location. The near-effusion liner zone serves as a bypass zone also in this case. In the latter case, this effect is more pronounced.

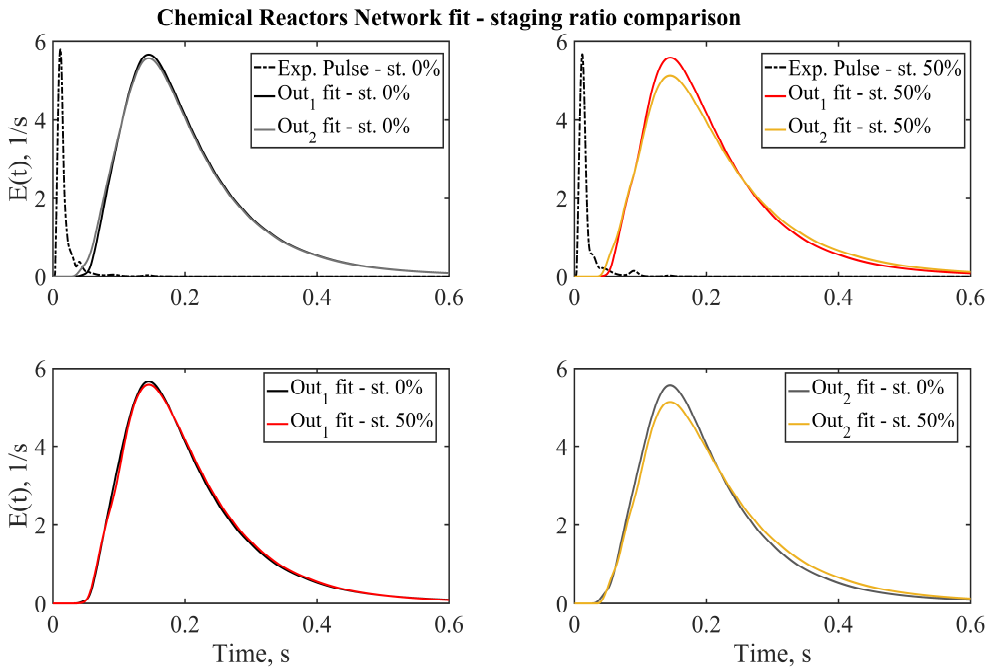

Figure 44: CRN-fit experimental tracer responses. Upper row:Out_1 and Out_2 for the two investigated operating conditions; lower row: comparison between the same measurement location for different operating conditions.

RTDs are illustrated in Figure 45. Although the bypass-feature of the effusion cooling is evident for $st. = 50\%$ from peak "3", it appears delayed with respect to the same feature in $st. = 0\%$. As indicated by $\frac{m_{main \rightarrow cooling}}{m_{total\_feed}}$, reported in Table 9, there is a lower amount of mass flow involved in the mixing with cooling air.

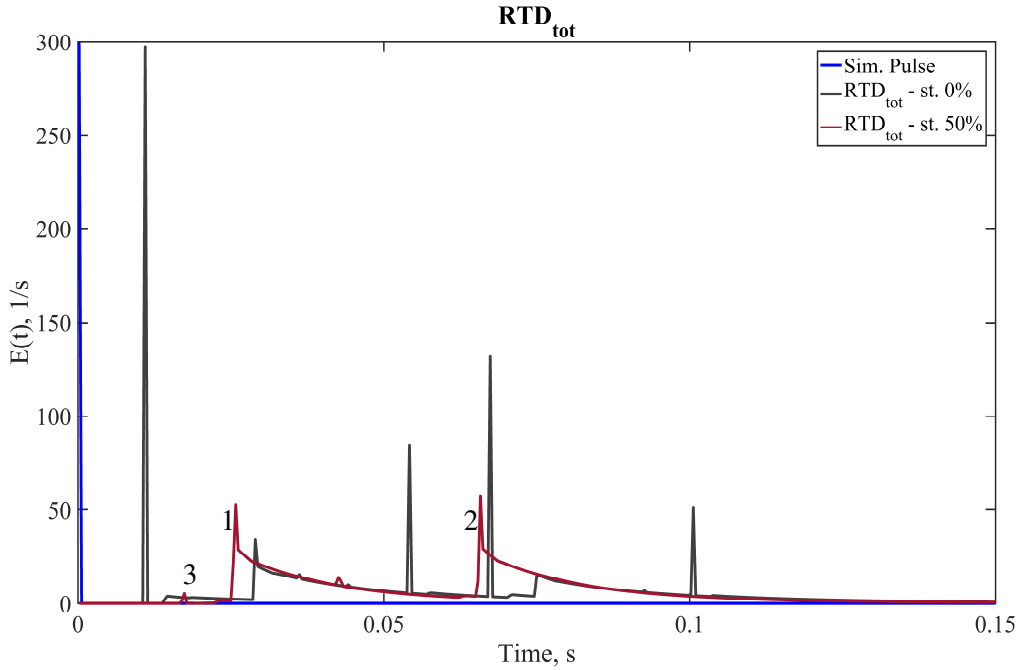

Figure 45: Global RTD of the combustion chamber $st. = 0\%$ and $st. = 50\%$.

This is attributed to the presence of an additional mixing volume (Figure 43) that entrains flow and alters the mixing time in the IRZ. The first, direct effect of this additional volume is a reduction of the IRZ-size. Furthermore, it causes a higher share of mass flow to mix in this region, presumably due to additional entrainment by the Pilot zone: more mass flow is entrained in the IRZ ($\frac{m_{IRZ}}{m_{in\_main}}$), and less is

available to take the effusion path. The entrainment in the ERZ is also enhanced, $\frac{m_{ERZ}}{m_{in\_main}}$. The seeding passing through the jet regions and then entrained in the central exit zone, "1" in Figure 45, exits the combustion chamber earlier for $st. = 50\%$ compared to the absence of pilot fuel. This is attributed to two factors. The first has been addressed before and concerns the higher amount of mass flow available in the main flow, inducing lower characteristic times. In addition to that, there is direct entrainment of tracer in the IRZ via the Pilot zone CSTR (Figure 43), and therefore, a certain amount of tracer available for mixing before the delay time induced by the jet region. The two maxima, "1" and "2", are associated to the passing time necessary to complete one of the two available PFR flow paths: the centerline or the lateral zone. The rearrangement of the flow caused by the presence of the pilot-fuel region generates a distribution with a longer τ_{tot}^{m}, attributed to a reduced residence time and lower overall mass flow in the cooling region. Instead, σ_{tot}^{2} is lower, due to the reduced residence time in each recirculation zone. The same conclusion can be drawn by looking at the $\tau_{tot}^{0.95}$ and $\tau_{tot}^{0.99}$: $\tau_{tot}^{0.95}$ is longer for $st. = 50\%$, as an effect of the higher share of mass flow recirculated and the influence of a lower mass flow in the effusion path. However, $\tau_{tot}^{0.99}$ is shorter for staged operation, because a higher recirculated mass flow reduces the residence time as well.

Table 9: global properties of the RTDs and CRN-fit parameters

	$st. = 0\%$:	$st. = 50\%$:		$st. = 0\%$:	$st. = 50\%$:
τ_{tot}^{m}	0.072	0.074	τ_{tot}^{c}	0.0286	0.0250
σ_{tot}^{2}	0.0057	0.0042	$\tau_{tot}^{0.95}$	0.16	0.17
S_{tot}^{3}	5	5	$\tau_{tot}^{0.99}$	0.44	0.38
τ_{IRZ}	0.011	0.009	m_{IRZ}/m_{in_main}	1.3	1.7
τ_{ERZ}	0.17	0.12	m_{ERZ}/m_{in_main}	0.08	0.12
$\frac{m_{cooling\rightarrow main}}{m_{total\_feed}}$	0.30	0.29	$\frac{m_{main\rightarrow cooling}}{m_{total\_feed}}$	0.27	0.01

3.4.1.3 *Effect of operating pressure*

The tracer responses obtained by fitting the cold flow CRN to the RTD measured at increased pressure is shown in Figure 46. What clearly emerges is the almost perfect overlap of the two distributions measured at different positions at $P = 3$ bar.

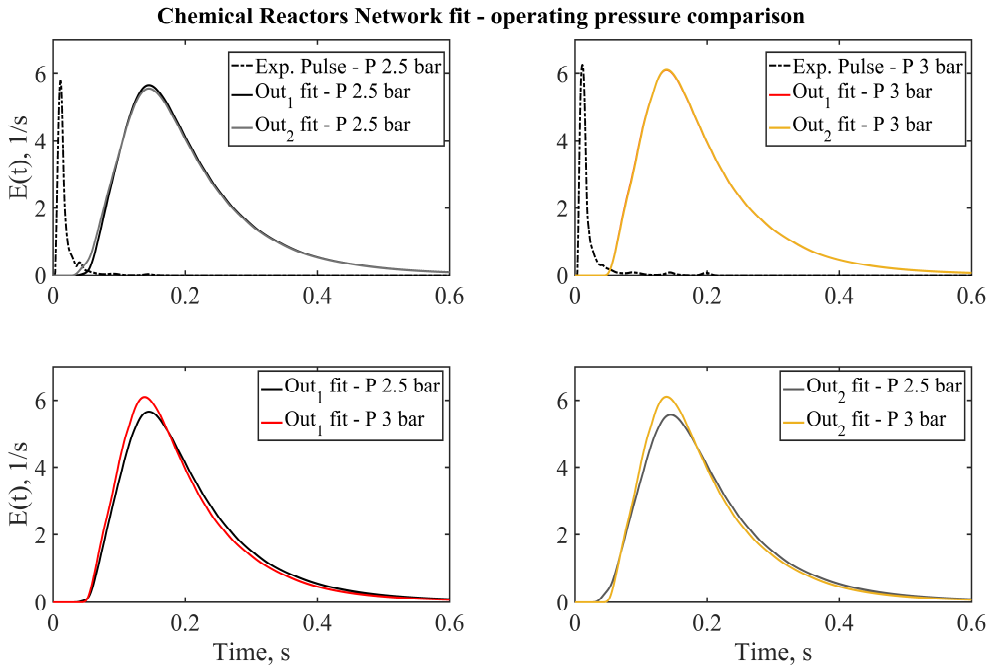

Figure 46: CRN-fit experimental tracer responses. Upper row:Out_1 and Out_2 for $P = 2.5\ bar$ and $P = 3\ bar$; lower row: comparison between the same measurement location for different operating conditions.

In Figure 47 the global exit RTD for the two operating conditions with different pressure are compared, while RTD-based parameters are calculated and compared in Table 10. The explanation to the spatially coupled evolution of the tracer concentration over time, shown in Figure 46 and evident also by the lack of sharp peak preceding the whole RTD in Figure 47, experienced by both probing locations, lies in the altered interaction with the cooling region as the pressure increases. The amount of mass flow from the cooling area to the main area (expressed by $\frac{m_{cooling \rightarrow main}}{m_{total\_feed}}$) is approximately the same for both investigated operating condition. However, a drastic decrease (one order of magnitude) is experienced by the reverse flow, as evident from $\frac{m_{main \rightarrow cooling}}{m_{total\_feed}}$. The lack of flow entrained in the effusion cooling region from the main flow is responsible for the increased passing times in the lower path, making them comparable to those of the main path. Referring to Figure 47, "1" denotes the time of arrival of the tracer from the centreline path, followed by the rest of the tracer in "2", where the flow in the outer region reaches the exit. Because of the already mentioned dramatically decreased mixing from the main flow to the effusion cooling flow, the contribution from the amount of flow entrained in the lower path to the global RTD is negligible, and barely distinguishable in form of negligible peaks in the global distribution. An exception is presented by "3". Its time of appearance corresponds to entrainment of the tracer in the effusion cooling flow from the beginning of the effusion cooling liner. As pointed out in paragraph 3.4.1.1, the flow that experiences mixing with cooling air from the beginning of the liner takes a longer time to pass through the combustor (refer to the lower image in Figure 42).

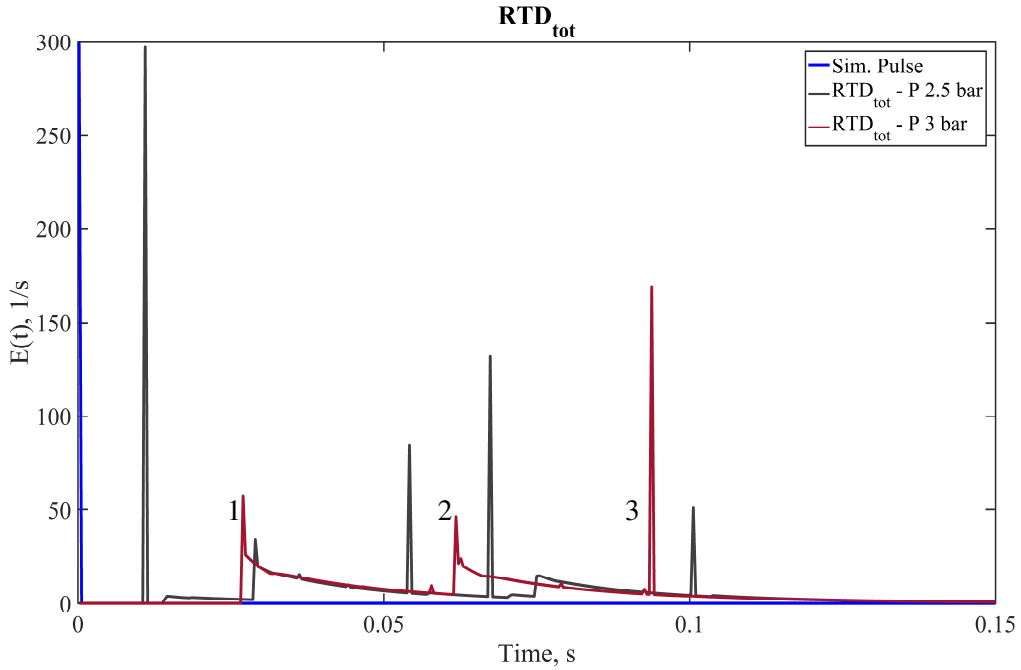

Figure 47: Global RTD of the combustion chamber $P = 2.5\ bar$ and $P = 3\ bar$.

The distribution calculated for $P = 3$ bar exhibits a longer mean residence time, but both $\tau_{tot}^{0.95}$ and $\tau_{tot}^{0.99}$ take similar values, Table 10. More mass flow is entrained in both RZs, in virtue of the lower momentum of the flow caused by the higher pressure, and the residence times in those zones are therefore lower.

Table 10: global properties of the RTDs and CRN-fit parameters, $P = 2.5\ bar$ and $P = 3\ bar$

	$P = 2.5\ bar$	$P = 3\ bar$		$P = 2.5\ bar$	$P = 3\ bar$
τ_{tot}^{m}	0.072	0.082	τ_{tot}^{c}	0.011	0.027
σ_{tot}^{2}	0.0057	0.0056	$\tau_{tot}^{0.95}$	0.16	0.19
S_{tot}^{3}	5	5	$\tau_{tot}^{0.99}$	0.43	0.44
τ_{ERZ}	0.17	0.14	$\frac{m_{IRZ}}{m_{in\_main}}$	1.3	1.9
τ_{IRZ}	0.011	0.008	$\frac{m_{ERZ}}{m_{in\_main}}$	0.08	0.12
$\frac{m_{cooling\rightarrow main}}{m_{total\_feed}}$	0.30	0.38	$\frac{m_{main\rightarrow cooling}}{m_{total\_feed}}$	0.27	0.06

3.4.1.4 Effect of swirl number

In Figure 48 the tracer responses that result from the CRN-fitting of the data for S = 0.7 and S = 1.3 are presented. They show broader distributions going from S = 0.7 to S = 1.3, in virtue of the higher amount of recirculated mass flow. The accelerating effect of the lower path in the combustor is evident in Figure 48 also for a higher value of S. It is even more evident while comparing the Out_1- measurement position of both operating conditions: the rising edge of Out_1 generated with S = 1.3 is delayed with respect to Out_1 for S = 0.7 (more evident for the RTD in Figure 49). In the former case, the tangential momentum flux is increased and the axial momentum flux lower, slightly delaying the appearance of the seeding at the centreline probing location. At the lower location, however, two effects result in an earlier appearance of tracer: higher mass flow pushed towards the boundaries following the swirl motion (as quantified by an additional parameter considered in this case, the ratio $\frac{m_{outer\_region\ S=1.3}}{m_{outer\_region\ S=0.7}}$, Table 11) and subsequent entrainment in the effusion cooling region.

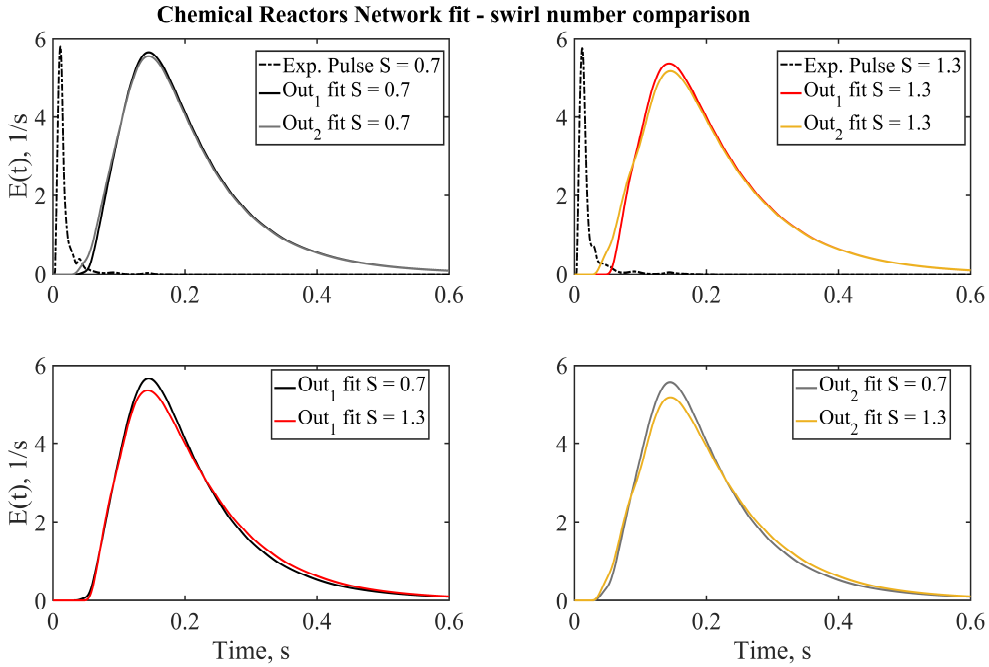

Figure 48: CRN-fit experimental tracer responses. Upper row:Out_1 and Out_2 for $S = 0.7$ and $S = 1.3$ the two investigated operating conditions; lower row: comparison between the same measurement location for different operating conditions.

In Figure 49 the global exit RTD for the two operating conditions with different S are compared, while RTD-based parameters are given and compared in Table 11.

Table 11: global properties of the RTDs and CRN-fit parameters – swirl number (S) variation

	$S = 0.7$	$S = 1.3$		$S = 0.7$	$S = 1.3$
τ_{tot}^{m}	0.072	0.072	τ_{tot}^{c}	0.011	0.010
σ_{tot}^{2}	0.0057	0.0045	$\tau_{tot}^{0.95}$	0.16	0.16
S_{tot}^{3}	5	4	$\tau_{tot}^{0.99}$	0.43	0.38
τ_{ERZ}	0.17	0.13	$m_{cooling \to main}/m_{total\_feed}$	0.30	0.38
τ_{IRZ}	0.011	0.010	$m_{main \to cooling}/m_{total\_feed}$	0.27	0.20
m_{IRZ}/m_{in_main}	1.3	1.5	$\frac{m_{outer\_region\ S=1.3}}{m_{outer\_region\ S=0.7}}$	1.1	
m_{ERZ}/m_{in_main}	0.08	0.10			

Identical to the standard operating condition, there is a first peak associated with entrainment in the effusion cooling path and immediate transport to the exit of the combustion chamber, "1". Subsequently, "2" contains the flow recirculated in the recirculation zone and additionally in the effusion cooling region. Afterward, "3", the flow following the main path reaches the outlet plane and exhibits the CSTR-decay to the catch-up of the flow trapped in the RZs. The peak "4" corresponds to the tracer first entrained by the cooling air and entrained by the main flow once again, as shown in the path number 3 in Figure 42. Instead, "5" corresponds to the path 6 in Figure 42: part of the flow following the jet region and exiting through the side segregated PFR.

As expected, the amount of recirculated mass flow is higher for a higher swirl number, both in the ERZ and in the IRZ. The higher share of recirculated flow causes a lower mean residence time in both recirculated zones. In the ERZ, a higher flow rate is accompanied by a reduction of the volume, because of a higher aperture angle of the flow issuing from the inlet nozzle. Concerning the IRZ, the higher angle increases the volume of the zone; nonetheless, this increase in the zone volume does not compensate the higher mass flow passing in the zone, and the residence time is therefore smaller with respect to $S = 0.7$. The interaction between main flow and cooling flow changes: there is more mass flow entrained from the effusion path, and less entrained in the lower path from the main flow region.

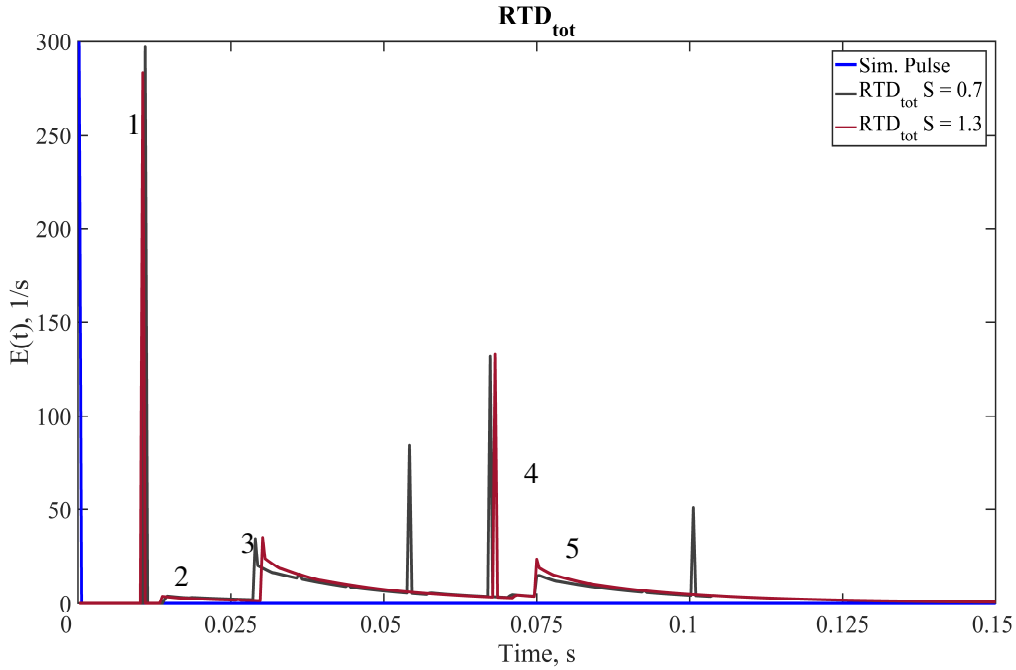

Figure 49: Global RTD of the combustion chamber, $S = 0.7$ and $S = 1.3$.

3.4.1.5 Summary

In this chapter, the impact of the operating conditions on the RTD of the SSGT has been described referring to the standard operation point. In Table 12, some relevant parameters are given to provide a comparison among the investigated sets of boundary conditions. Beside the global mean residence time inside the combustor, τ_{tot}^{m}, $\frac{m_{recirculation}}{m_{in\_main}}$ represents the total share of the flow entrained in the recirculated regions and $\frac{m_{main\_cooling}}{m_{total\_feed}}$ calculates the ratio of the total mass flow exchanged between the two flow paths (main and cooling) with respect to total mass flow fed to the system.

Table 12: comparison among the different investigated operating points.

	Basic operating point (Table 6)	$m_{cool} = 7.5$ g/s	st. $= 50\%$	P $= 3$ bar	S $= 1.3$
τ_{tot}^{m}	0.074	0.077	0.074	0.082	0.072
$\frac{m_{main\_cooling}}{m_{total\_feed}}$	0.57	0.38	0.30	0.44	0.58
$\frac{m_{recirculation}}{m_{in\_main}}$	1.4	1.3	1.8	2.0	1.6

From Table 12 it can be concluded that that a lower cooling mass flow yields a higher global mean residence time in the combustor, presumably linked to the lower mass flow in the system. The overall mixing between the two identified paths is lower, and the entrainment in the RZs is approximately in the same order of magnitude for as operating with a higher cooling mass flow.

The presence of a pilot-flow has no appreciable effect on τ_{tot}^{m}, but clearly alters the mixing behaviour of the system increasing the entrainment in the recirculation zones. The interaction between the main and cooling paths in terms of exchanged mass flow appears lowered.

A higher P greatly enhances the mixing in the recirculation zones, presumably because of the lower momentum of the flow. The slower distribution is also attributed to the pressure increase. The global amount of mass flow exchanged between the main paths is decreased.

Finally, a higher swirling ratio *S* does not affect the mean residence time in the system, but does increase the entrainment in the RZs, that is higher. Overall, the mixing between near-wall region and central region has the same value.

3.4.2 Reactive flow results

The impact of the boundary conditions on the system RTD during combustion is described. With respect to table 6, the following variation on the parameters were explored:

Table 13: explored parameters for the cold-flow measurements.

	Operation point, units	
System pressure, *P*	2.5 and 3	bar
Swirl number, *S*	0.7 and 1.3	[-]
Effusion cooling mass flow, m_{cool}	15 and 7.5	g/s
Fuel staging ratio, st.	0%, 10%, 30% and 50%	[-]
Equivalence ratio, φ	0.65, 0.75 and 0.85	[-]

Beside the description of the RTDs, aided by the discussion of selected network-derived parameters (explained in Table 3), the impact of the operating conditions on species production is also shown and discussed along selected profiles, shown in the schematic in Figure 50.

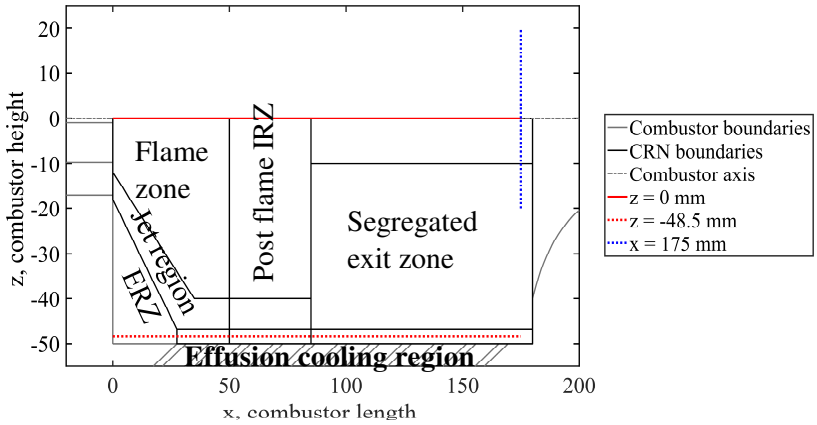

Figure 50: sketch of the lower half of the flame tube, with superimposed CRN boundaries. Radial (blue) and axial (red) location used to show species formation under different operating conditions are highlighted.

Following the interest on pollutant formation in gas turbine combustion, the following species were selected for comparison: CO, C_2H_2 and NO_x, the latter considered as the sum of the concentration of NO, N_2O and NO_2. Beside the polluting aspect of the listed species, CO and C_2H_2 are directly linked to the incomplete combustion of the fuel, addressing the need for combustion device optimization. C_2H_2 is also a soot precursor. As specified before, while dealing with CSTRs (flame, IRZ and ERZ) only one concentration value is displayed, namely the one referring to the concentration at the exit (see 2.1.1). A PFR shows instead a continuous evolution of the concentration along its axial coordinate, that serves also as a reaction time.
The results are presented in the following order:

- effect of effusion cooling mass flow, m_{cool},
- effect of the fuel-staging ratio, $st.$,
- effect of the operating pressure, P,
- effect of the swirl number, S,
- effect of the equivalence ratio, φ.

3.4.2.1 Effect of effusion cooling mass flow

Figure 51 shows the comparison among the different tracer responses recorded at the exit of the combustor. The upper row of images shows the two responses for a given mass flow, while the lower row compares the results at the same measurement location for different amounts of effusion air. Figure 51 confirms the effect of a lower quantity of cooling air on the measured responses, though less clear than in the non-reactive case, presumably due to the higher velocities associated to thermal expansion through combustion inside the chamber. A lower amount of effusion air introduced in the system corresponds to tracer responses that almost overlap, whereas there is a clear difference while feeding a higher mass flow of cooling air.

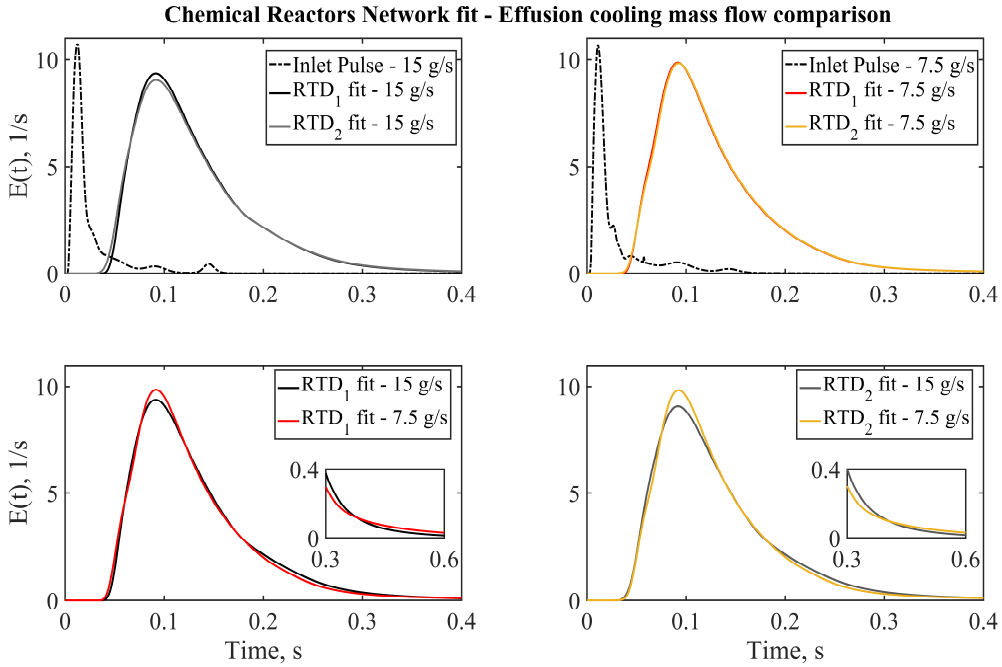

Figure 51: CRN-fit experimental tracer responses for $m_{cool} = 15\ g/s$ and $m_{cool} = 7.5\ g/s$. Upper row: Out_1 and Out_2 for the two investigated operating conditions; lower row: comparison between the same measurement location for different operating conditions.

Figure 52, comparing the RTDs for both different measurements positions as well as the same measurement position for a different amount of cooling air, confirms the main phenomena already observed for the temporal evolution of the tracer: the impact of the cooling on the flow homogeneity is reduced for a lower amount of effusion cooling air introduced in the system.

Table 14: global properties of the RTDs and CRN-fit parameters, $m_{cool} = 15\ g/s$ and $m_{cool} = 7.5\ g/s$.

	$m_{cool} = 15\ g/s$	$m_{cool} = 7.5\ g/s$		$m_{cool} = 15\ g/s$	$m_{cool} = 7.5\ g/s$
τ_1^m	0.026	0.032	τ_1^c	0.010	0.012
τ_2^m	0.026	0.032	τ_2^c	0.001	0.012
τ_{tot}^m	0.018	0.020	τ_{tot}^c	0.001	0.001
σ_1^2	0.0013	0.0013	$\tau_1^{0.95}$	0.05	0.05
σ_2^2	0.0016	0.0013	$\tau_2^{0.95}$	0.05	0.05
σ_{tot}^2	0.001	0.001	$\tau_{tot}^{0.95}$	0.041	0.052
S_1^3	8	10	$\tau_1^{0.99}$	0.2	0.17
S_2^3	8	10	$\tau_2^{0.99}$	0.22	0.17
S_{tot}^3	10	12	$\tau_{tot}^{0.99}$	0.13	0.13
τ_{flame}	0.0031	0.0028	$\frac{m_{IRZ}}{m_{in\_main}}$	6.5	5
$\frac{m_{main \to cooling}}{m_{total\_feed}}$	0.43	0.49	$\frac{m_{ERZ}}{m_{in\_main}}$	0.15	0.16
τ_{ERZ}	0.03	0.03	m_{flame}/m_{in_main}	0.97	1.00
τ_{IRZ}	5.8×10^{-4}	8.0×10^{-4}	$\frac{m_{cooling \to main}}{m_{total\_feed}}$	0.28	0.09

In more details, seeding is present at the exit of the combustor almost immediately (~ 1 ms, see Table 14) after the pulse input for $m_{cool} = 15\ g/s$. This portion of seeding is entrained in the flame zone, and then immediately in the near-cooling air region. Because of the flow rates involved, this part of the combustor can be regarded as a fast-bypass one, causing the fluid pockets entrained here to reach the

exit plane of the combustion chamber faster than the others. This holds true also for $m_{cool} = 7.5\ g/s$ (see magnified area in Figure 52 and RTD_{tot}). However, the flow entrained in the near wall path mainly continues towards the exit without significantly influencing the main flow, and it exits the combustor without being detected by either of the measurement location (except for the small amount, shown in the inset) and its presence is clear only looking at the RTD_{tot} (weighted mean of the RTDs obtained from the measured tracer response). This lower impact is also quantified in Table 14: the parameter $\frac{m_{cooling \to main}}{m_{total\_feed}}$ is one order of magnitude lower for $\mathrm{m_{cool}} = 7.5\ \mathrm{g/s}$, confirming the lower involvement of the effusion cooling air in the global evolution of the main flow path. Mixing from the main path, $\frac{m_{main \to cooling}}{m_{total\_feed}}$, shows instead the same order of magnitude, as it is not altered. Entrainment in the ERZ and in the flame zone is favoured for a lower amount of liner air introduced in the system, but entrainment in the IRZ is lower. Globally, the RTD_{tot} shows a higher τ_{tot}^{m} for $\mathrm{m_{cool}} = 7.5\ \mathrm{g/s}$, in accordance to the lower global flowrate introduced in the system. The calculated $\tau_{tot}^{0.99}$ is the same for both distributions, as it mostly depends on the mixing in the recirculation zones, which are not significantly altered by the reduction of the effusion cooling rate.

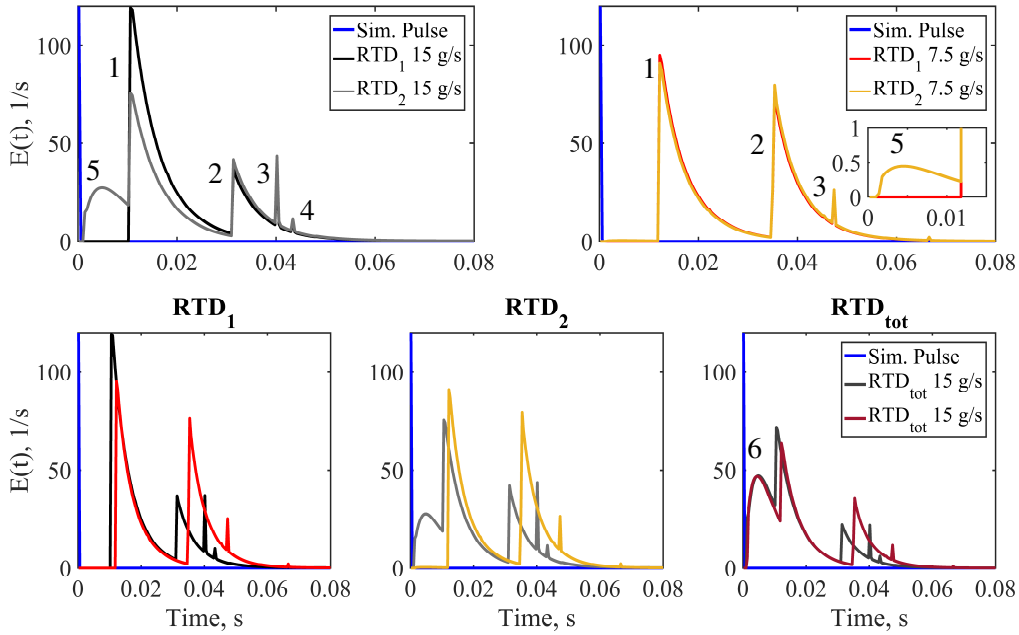

Figure 52: RTDs calculated from the CRN calibrated against the experimental tracer response, $m_{cool} = 15\ g/s$ and $m_{cool} = 7.5\ g/s$. Upper row: comparison between RTD_1 and RTD_2 for the same value of the effusion cooling mass flow. Lower row: comparison between the RTD_i for different values of effusion cooling mass flow.

According to Figure 52, besides the initial part of the distribution, "5", the identifiable peaks mainly stem from the mixing in the main flow path. Figure 53 helps the visualization of the possible flow paths by means of a basic sketch of the combustor and the possible routes. Each peak has been associated to a certain event based on the analysis of the residence time in each zone. After the initial mixing in the flame region, the flow entrained in the post-flame and central segregated-region PFR gives rise to the first peak, "1" in Figure 52. The portion of flow entrained in the post-flame and outer segregated-region PFR gives rise to the second one. The smaller, subsequent peaks derive from the exchange of flow between the main path and the effusion cooling path. Respectively, the third peak exemplifies the event of entrainment of flow from the main path at a later stage (~ second or third near wall reactor), whereas "4", comes from an earlier entrainment in the effusion region (already in the first liner-reactor).

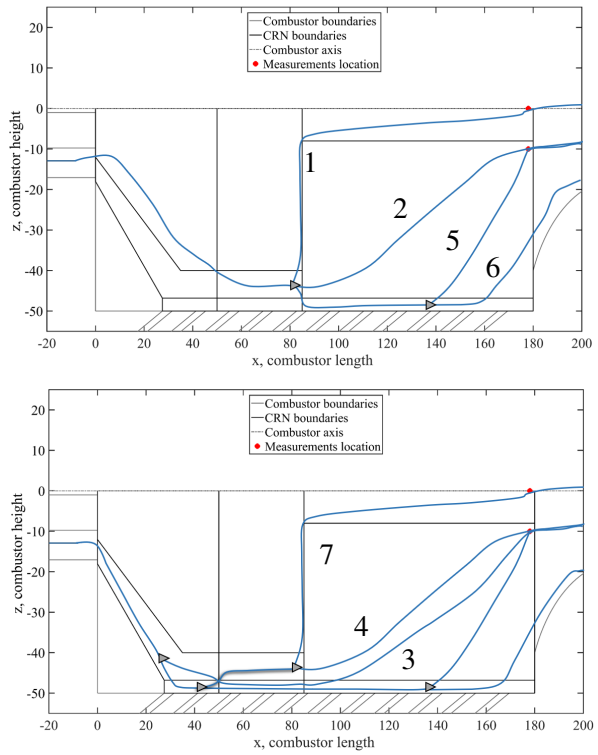

Figure 53: basic sketch of the identified flow paths for reactive flow. The grey triangle symbolizes a splitting element, in accordance with the CRN legend, introduced in Figure 20 and Figure 30. 6 represents the part of the flow that is not detected during the measurements, and is accounted for in RTD_{tot} only. Additional numbers, like number 7, are added in the figure to highlight the different existing paths, that might acquire importance for different operating conditions.

Figure 54 reports on the influence of m_{cool} on species formation. As remarked in section 3.4.2, the following species were selected for comparison: CO, C_2H_2 and NO_x.

The CO evolution along the centreline of the combustor ($z = 0$, Figure 54) presents only minor differences in the flame region. $m_{cool} = 7.5\ g/s$ shows a higher in-flame CO production, in agreement with experimental data. This behaviour is attributed to both the slightly higher mass flow that is entrained into the flame zone from the main inlet stream for this boundary condition (m_{flame}/m_{in_main}, Table 14) and to the higher temperature fit in this zone by the CRN optimization. These two factors point in the direction of a lower residence time in the flame zone, causing a lower conversion of CO. Along the effusion cooling liner ($z = -48.5$) two CO formation peaks are identified, corresponding to the areas of higher flow exchange between the main path and the effusion cooling path (Figure 31). The operating condition of $m_{cool} = 15\ g/s$ exhibits the highest CO concentration at the start of the cooling liner, because of the higher amount of reactive mixture entrained in this zone. The trend changes while looking at the second maximum in the CO concentration: higher CO levels are found for $m_{cool} = 7.5\ g/s$. In this case, the mixing features that characterize the two different operating conditions are strongly linked with this result: a higher m_{cool} entrains a higher quantity of reactive mixture from the surroundings, while being less prone to be entrained in the main flow. Therefore, the CO mole fraction is lowered by mixture that has already reacted in the previous near-wall reactor and by the higher mass flow entering the boundaries. On the other hand, for a lower m_{cool}, a higher share of the mixture exiting the first near-wall zone is entrained into the main path, and an overall lower mass flow is accessing the specific reactor. These differences soften until they disappear along the liner-zone, in virtue of the higher homogeneity reached in this zone from a mixing point of view and the almost complete CO conversion.

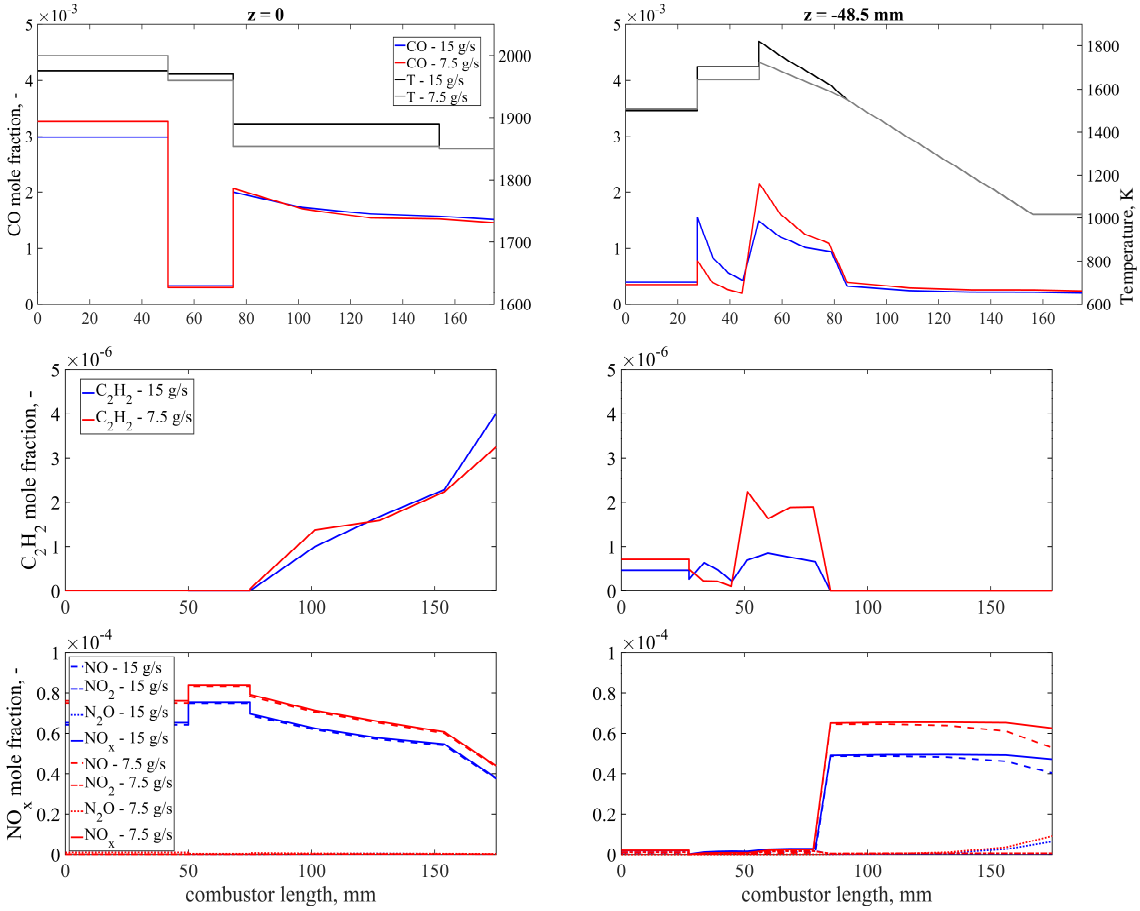

Figure 54: influence of m_{cool} on species formation. Upper row: CO along selected profiles, middle row: C_2H_2, lower row: NO_x.

Along the vertical profile at the exit of the combustor, Figure 55, shows a slightly higher CO concentration in the side reactor for $m_{cool} = 7.5\ g/s$, stemming from the lower mass flow rate passing in this region for this specific operating condition and the higher temperature of the side reactor.

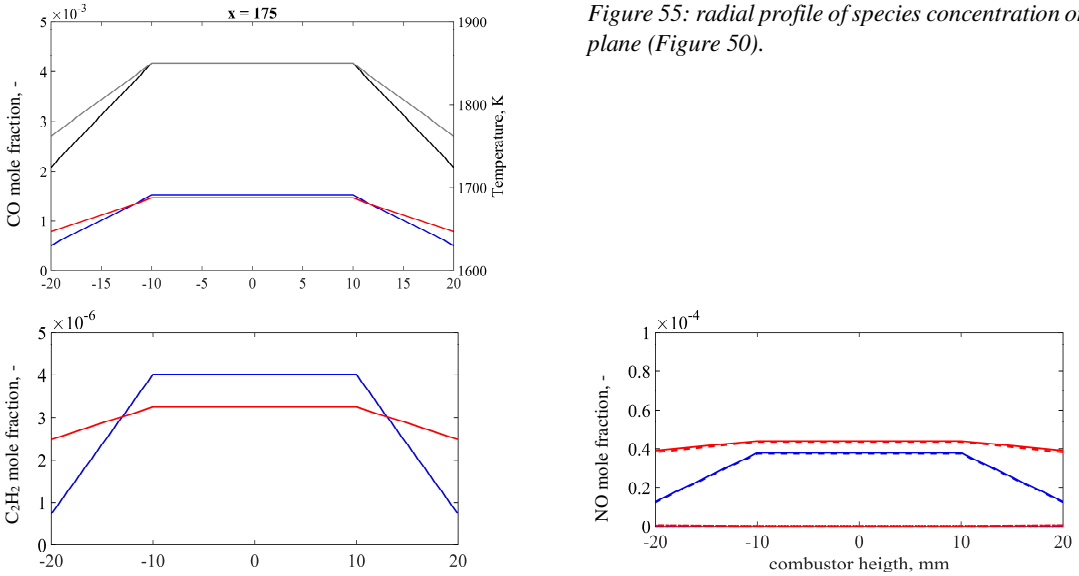

Figure 55: radial profile of species concentration on the exit plane (Figure 50).

The second row in Figure 54 is dedicated to C_2H_2, whose overall amount is lower (three orders of magnitude or less) compared to CO. There is no acetylene in the flame and in the recirculation zone at their exit conditions. Few ppm of the species are formed in the last PFR, because the small amount of

fuel bypass reaching this zone. Near the effusion cooling liner, C_2H_2 shows the same trend as CO. C_2H_2 is a dehydrogenated combustion intermediate, therefore, in an ideal situation, it should in the end be all converted into CO, that is then ideally completely converted to CO_2. Furthermore, C_2H_2 reaction with OH radical plays a significant role in the CO formation, because of the following reaction path, Reaction 17, that involves $C_2H_3\cdot$ and $C_2H\cdot$ as intermediates [23]:

$$C_2H_2 + OH\cdot \rightarrow CH_3\cdot + CO \qquad \textit{Reaction 17}$$

The C_2H_2 behaviour responds promptly to the arrival of partially reacted mixture, showing the maximum production in the second effusion cooling reactor. As commented before, partially reacted mixture reaches this point, and the further mixing with air at high temperature (though lower than flame temperature) encourages the formation of acetylene. Proceeding further along the liner, the species is no more produced, because the mixture here contains almost no fuel anymore, and the combustion reactions are basically done. In addition, mixing with flue gas coming from the main path further lowers its concentration. On the exit plane, the C_2H_2 behaviour still closely resembles the one of CO.

The evolution of NO_xformation along the centreline shows, at first, that NO is the dominant species along the oxidized nitrogen products. represents the most amount of nitrogen oxidized products, while NO_2 and N_2O are present in much lower amount. The differences seen until the IRZ are attributable to both temperature effect and CO concentration: in the IRZ there is a low level of CO, therefore NO is not reduced again to N_2 by CO. Instead, because of the additional time at high temperature, its concentration rises with respect to flame concentration. The NO concentration slowly decreases towards the exit, with a higher concentration for $m_{cool} = 7.5\ g/s$. Along the cooling liner, the NO_x mole fraction is in the sub-ppm region until approximately half of the combustor length. At this point, at the stage of the third cooling reactor, the sharp rise (to ~ 70 ppm) is attributed to the flow coming from the second reactor of the jet region, Figure 31. This reactor has an intermediate temperature between that of the flame and the one of the second effusion cooling reactor (Figure 54, upper row) and reacted or partially reacted mixture is entrained in this zone. Owing to the high temperature of the reactor and to the residence time that the mixture flowing through it has already experienced in the system, the NO_x content is higher compared to the first part of the effusion cooling liner. Therefore, the entrainment in the third near-wall reactor of part of the flow exiting this second jet-reactor causes an increase in the NO_x concentration along the liner zone. This zone is the coldest in the reactor, and the formation N_2O from NO is visible. This process is exemplified by Reaction 18, favoured below 1500 K:

$$NO + NH\cdot \rightarrow N_2O + H\cdot \qquad \textit{Reaction 18}$$

The NO_x amount on the vertical profile shows higher NO_x emission for $m_{cool} = 7.5\ g/s$. This is attributed to the higher temperatures and the lower dilution, due to the lower amount of cooling air fed to the combustor.

3.4.2.2 Effect of staging ratio

The results of the CRN fit to tracer response measured at different fuel-staging ratio are shown in Figure 57. Beside the standard operating conditions, where the fully premixed combustion is investigated, the explored staging ratios were $10\%, 30\%$ and 50%. From Figure 57 it is evident that the distribution becomes broader with increasing fuel splitting ratio, symptom of an alteration of the mixing residence times inside the combustor. The effect appears more evident on Out_2.

To describe the combustion phenomena while operating with a certain amount of fuel splitting, the network was modified, according to the explanation provided in 3.4.1.2. The image of the modified near-burner region is shown again below, in Figure 56.

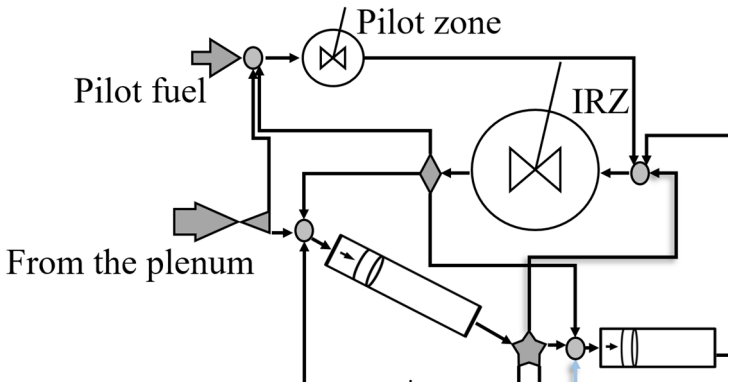

Figure 56: modified network to describe the near-nozzle region for fuel-staging operation. A CSTR reactor to exemplify the injection of the pilot-fuel has been added in the IRZ.

The mass flow entrained in the pilot reactor, as well as its volume, increases with increasing ratio of pilot fuel to main premixed fuel, Table 15. The global RTDs, Figure 58, show the early rising edge due to the entrainment from the lower path. This feature corresponds to the ensemble of peaks "1" in Figure 58. It is clearly sharper in the case of $st. = 50\%$, attributed to the different interaction between main flow and the effusion cooling flow at different staging ratios. The mass flow from the main zone into the cooling zone, expressed by $\frac{m_{main \rightarrow cooling}}{m_{total\_feed}}$, decreases for $st. = 10\%$ and then increases again until $st. = 50\%$, which exhibits an even higher value of the parameter. The staging flow creates an additional mixing volume in the combustion chamber, altering mixing times and mixing pattern. Initially, this different mixing attitude rearranges the flow such that the exchange with the effusion cooling air is lowered. While increasing the staging ratio, the additional mixing volume increases and influences the opening angle of the jet flow, possibly the cause of the increment of $\frac{m_{main \rightarrow cooling}}{m_{total\_feed}}$ with the staging ratio. It is additionally likely to be also responsible for the higher amount of flow recirculated through the ERZ. On the other hand, recirculation through the IRZ is discouraged with higher staging ratio because of the higher axial momentum of the flow, induced by the axial fuel injection and the locally higher temperatures with respect to fully premixed combustion, which cause thermal expansion. The effect on the global residence time τ^m follows the observations from above: a small amount of pilot fuel increases the global mean residence time because of the alteration of mixing times in the flame zone, whereas a larger amount of pilot fuel above $st. = 20\%$ increases the axial momentum and leads to a reduction of global residence times. According to σ_{tot}^2, in Table 15, the spread of the distribution increases with increasing pilot fuel amount, with the exception of $st. = 30\%$.

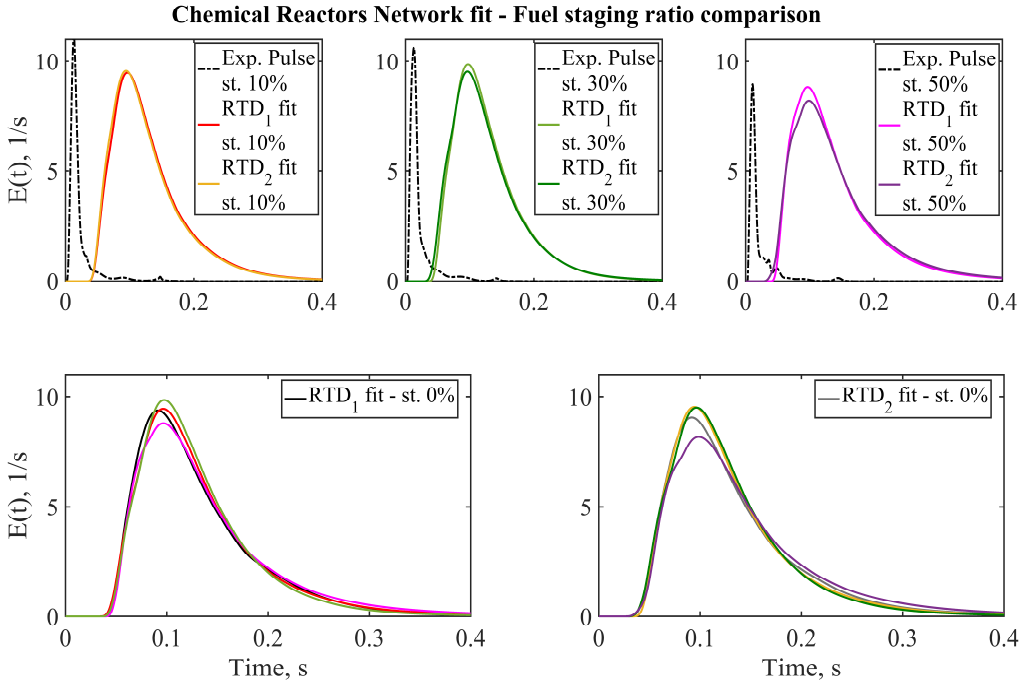

Figure 57: CRN-fit experimental tracer responses for $staging\ ratio = 0\%, 10\%, 30\%$ *and* 50%*. Upper row:* Out_1 *and* Out_2 *for the two investigated operating conditions; lower row: comparison between the same measurement location for different operating conditions.*

The general evolution of the distributions, Figure 58, is analogous to what explained before: there is a first increase in the $E(t)$ due to direct entrainment in the effusion cooling region, ensemble of peaks "1". As explained, the highest is reached for $st = 50\%$. The peaks "2" concern the flow evolving first in the two jet regions, and then mixing in the central exit zone, associated with higher flow velocities, see "path 1" in Figure 53. Follows the flow that is entrained in the side reactor in the exit zone, peaks "3" in Figure 58, corresponding to "path 2" in Figure 53.

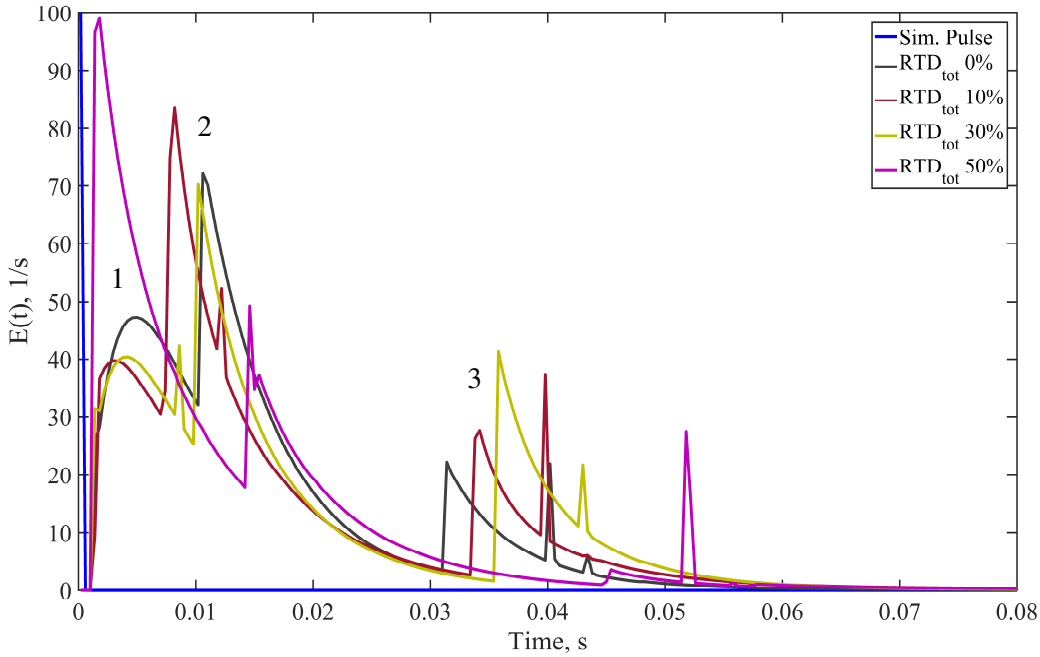

Figure 58: global RTD of the combustion chamber, $staging\ ratio = 0\%, 10\%, 30\%$ *and* 50%*.*

Figure 60 shows the influence of the pilot-splitting ratio on species formation. Before commenting on the results, an issue already mentioned in paragraph 3.3.2.3 should be addressed. In paragraph 3.3.2.3, it was stated that the kinetic model chosen to carry out the kinetic analysis was the $C1-C4$ mechanism, but that the RNA software (introduced in 2.2.2) could not always reach convergence in a reasonable time. That was the case for the boundary condition $st.=50\%$. Therefore, in this case, the profiles reported in Figure 60 for this case have been calculated using the $GRI\ 3$ mechanism. In addition to the sensitivity analysis to the employed kinetic mechanism carried out in 3.3.2.3, the suitability $GRI\ 3$ is tested here once again, providing a comparison between the results obtained with the $C1-C4$ mechanism and the $GRI\ 3$ in the case of $st.=30\%$. This comparison is shown in Figure 59.

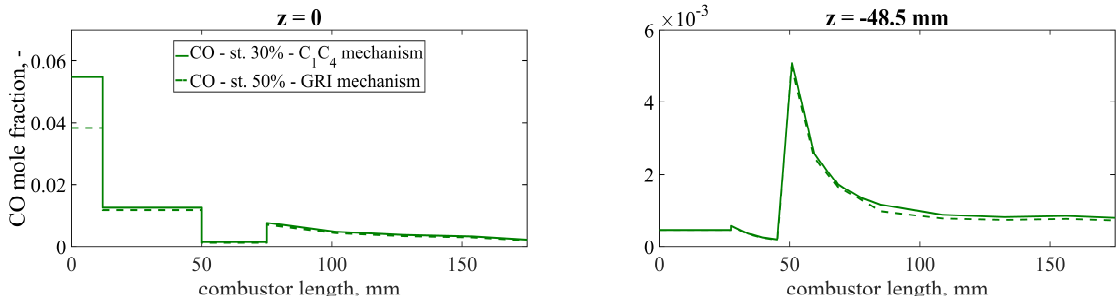

Figure 59: comparison between the $C1-C4$ mechanism and the GRI 3 mechanism. This additional comparison has the aim of determining whether it is correct or not to use the GRI 3 mechanism to evaluate the kinetics in those cases where the $C1-C4$ mechanism was not applicable.

The agreement between the profiles calculated with the two different kinetic mechanisms is good along the selected profiles yielding an error below 10%. An exception is evident in the first part of the centreline plot, when comparing the calculation carried out in the pilot reactor. Here the error is 40%, and the $GRI\ 3$ heavily underpredicts CO formation in this case. However, as stated earlier, this discrepancy disappears with further mixing and reaction inside the system. Therefore, keeping in mind the chance of this discrepancy happening in the first pilot reactor, where fuel-rich conditions are established, the $GRI\ 3$ is employed in the following discussion for the kinetic evaluation of the CRN for $st.=50\%$.

Going to Figure 60, the amount of CO clearly increases while increasing the staging ratio. While, for st.$=$ 10% and st.$=$ 30%, the concentrations remain at values whose order of magnitude is comparable with those found for premixed combustion, those predicted for st.$=$ 50% remain higher along the whole coordinate, though showing the same trend as for the other cases. In the cooling region, z $=$ $-$ 48.5 mm in Figure 60, a high staging ratio of st.$=$ 50% is also responsible for the largest CO production. An only marginally increased staging ratio (st.$=$ 10%) compared to the standard operating condition follows the trend seen for premixed combustion. st.$=$ 30% shows a lower amount of CO in the first liner reactor - analogous to st.$=$ 50% - but then the species mole fraction increases up to ~7000 ppm in the second liner reactor. The CO quantity gets lowered moving along the last part of the liner zone, being consumed with the advancement of mixing and chemical reaction. st.$=$ 50% presents the same trend as st.$=$ 30% in the initial part of the near wall region. Once the final cooling-zone is reached, its behaviour is completely different from the other cases: CO concentration increases to 0.02 on a mole fraction basis, and then decreases only to 0.01 along the combustion length. This is attributed to two factors: the first is the ratio of $\frac{m_{main\rightarrow cooling}}{m_{total\_feed}}$, discussed earlier, the second is a different mixing behavior whose importance grows with increasing splitting ratio. Besides a higher share of the main flow mixing in the cooling path (higher $\frac{m_{main\rightarrow cooling}}{m_{total\_feed}}$) in the case st.$=$ 50%, a clear trend emerges from CO data regarding the axial position at which the significant exchange of mass flow between main and liner path occurs,. With increasing amount of fuel fed to the pilot, the flow from the main flow zone to the initial part of the near wall reactors gets lower, resulting in less CO in an early stage with increasing staging ratio. In the second cooling reactor, st.$=$ 30% and st.$=$ 50% show approximately

the same increase in CO mole fraction, because there is a more intense mixing between the parallel paths. At the final stage, CO formation for $\mathrm{st.} = 50\%$ increases dramatically because in this case there is the highest entrainment of reacting flow into the cooling region. In other words, the splitting ratio shifts the axial coordinate at which the higher share of reacting flow mixes with fresh cooling air. Beside the amount of entrained flow, it is necessary to consider its CO content as well, which for $\mathrm{st.} = 50\%$ is high at the centreline $z = 0$. These factors define the different behaviour: there is a higher share of reacting mixture, containing a great amount of CO, entrained into the coldest zone of the near wall region and most likely of the reactor itself. While the cooling does not seem to pose a severe inhibition to CO oxidation in the other cases, the reaction does not significantly lower the species concentration for such high quantities of CO. On the other hand, $\mathrm{st.} = 30\%$ shows the same behaviour as the other two compared operating conditions in the third part of the near-wall region: to comment in a similar way as before, a lower share of reacting flow mixes in this zone, whose CO content is easily oxidized. This tendency is as well clear on the exit plane.

Table 15: global properties of the RTDs and CRN-fit parameters, $st. = 0\%, 10\%, 30\%$ and 50%

	$st. = 0\%$	$st. = 10\%$	$st. = 30\%$	$st. = 50\%$		$st. = 0\%$	$st. = 10\%$	$st. = 30\%$	$st. = 50\%$
τ_{tot}^{m}	0.018	0.021	0.022	0.018	τ_{tot}^{c}	0.001	0.001	0.001	0.001
σ_{tot}^{2}	0.0013	0.0042	0.0037	0.0057	$\tau_{tot}^{0.95}$	0.041	0.052	0.049	0.053
S_{tot}^{3}	10	7	8	7	$\tau_{tot}^{0.99}$	0.13	0.16	0.12	0.17
$\frac{m_{pilot\ reactor}}{m_{total\_feed}}$	-	0.01	0.0224	0.139	$\frac{m_{IRZ}}{m_{in\_main}}$	6.5	3.3	4.4	1.7
$\frac{V_{pilot}}{V_{flame}}$	-	2.4×10^{-4}	0.0051	0.0086	$\frac{m_{ERZ}}{m_{in\_main}}$	0.15	0.28	0.23	0.19
$\frac{m_{flame}}{m_{in\_main}}$	0.98	1.30	1.32	1.38	$\frac{m_{cooling \rightarrow main}}{m_{total\_feed}}$	0.18	0.06	0.21	0.09
$\frac{m_{main \rightarrow cooling}}{m_{total\_feed}}$	0.43	0.35	0.40	0.58	τ_{IRZ}	5.8 $\times 10^{-4}$	1.13 $\times 10^{-3}$	8.7 $\times 10^{-4}$	2.40 $\times 10^{-3}$
τ_{ERZ}	0.03	0.01	0.02	0.02	τ_{flame}	0.0031	0.0023	0.0027	0.0022

The levels of C_2H_2 formation on the centreline of the combustor show the same behaviour seen before for a variation in the cooling mass flow (see Figure 54), except for the pilot reactor. Here, rich combustion conditions are established, leading to high acetylene mole fraction. This high amount of the species is consumed in the downstream section of the combustor, though still showing higher levels for $\mathrm{st.} = 50\%$ at the exit plane. The C_2H_2 evolution at $z = -48.5$ shows the same trend as the carbon monoxide. A higher concentration is detected for the case $\mathrm{st.} = 30\%$ in the second effusion cooling region (Figure 31 as a reference).

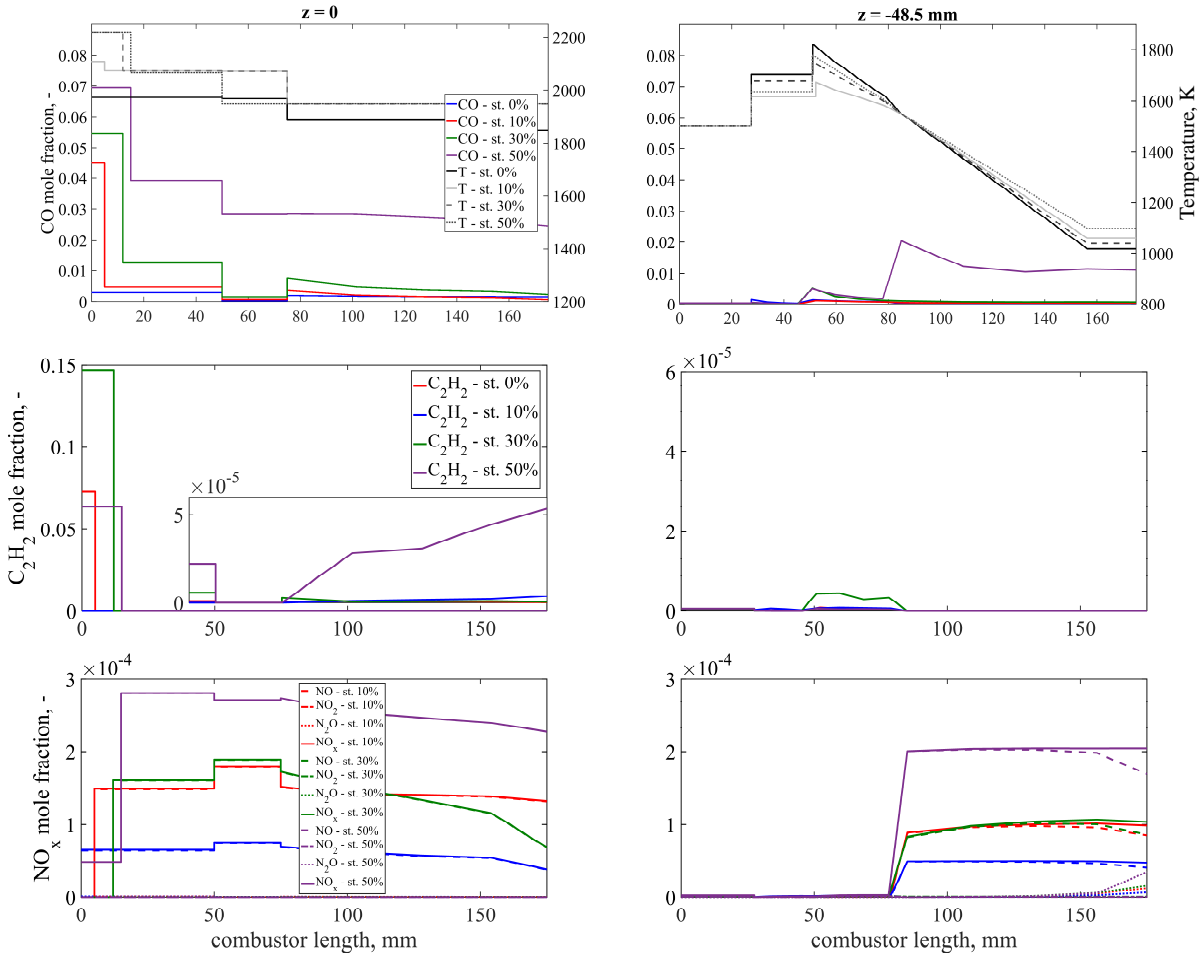

Figure 60: influence of staging ratio on species formation. Upper row: CO along selected profiles, middle row: C_2H_2, lower row: NO_x.

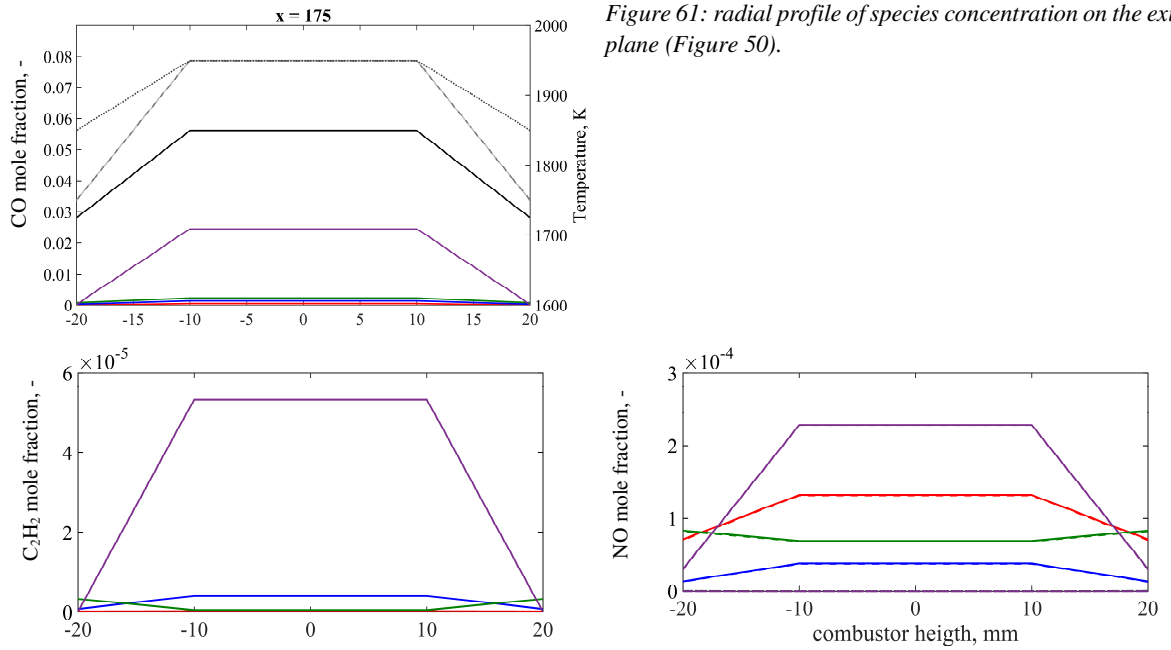

Figure 61: radial profile of species concentration on the exit plane (Figure 50).

NO_x concentration as a function of staging ratio is given in the last row of Figure 60. The calculated species concentration equals zero in the core reactor for $st. = 10\%$ and $st. = 30\%$, most likely due to the low residence times in this zone for the mentioned staging ratios. In the flame zone, the nitrogen oxides concentration rises sharply, reaching a larger value for the higher the staging ratios. $st. = 50\%$

exhibits nonetheless a notably increased amount of these species compared to the other two cases. The NO_x concentration in the IRZ shows the slight increase seen also in Figure 54, except for the case with the highest splitting ratio: here the IRZ concentration of NO_x experiences a slight decrease instead, because of the higher τ_{IRZ}. In the segregated exit zone, the concentration slowly decreases. The concentration of NO_x is neglectable in the effusion cooling region until the most downstream part. This part exchanges flow with the bypass around the IRZ, whose temperature is high enough to trigger NO_x production. The flow with a low nitrogen oxides content mixes in the first part of the liner zone. On the exit plane, shown in Figure 61, the NO_x concentration increases with increasing staging ratio, with the exception of the side reactor for $st. = 50\%$, whose concentration is comparable to the premixed case. This is attributed to the higher residence time in this zone for this condition: the passing time in this zone was found larger with increasing fuel splitting ratio. The 30% fuel splitting ratio results as the optimal operating condition for yielding the lowest NO_x concentration.

3.4.2.3 Effect of operating pressure

The CRN-fit for the measurements carried out at a higher pressure, $P = 3$ bar, is shown in Figure 62. The length of the flame zone, l_{flame}, was an additional parameter of the optimization. The earlier rise of the distribution for the lower measurement location is present also for the higher-pressure case. Both high-pressure distributions appear broader than the low-pressure ones, owing to the lower flowrate in the system, though partially balanced by the higher CRN-fit temperatures. The significantly different shape of the two measurements positions for $P = 3$ bar, evident also in peak "3" in Figure 63, is attributed to the lower mass flow exchanged from the effusion cooling path to the main path, quantified in Table 16.

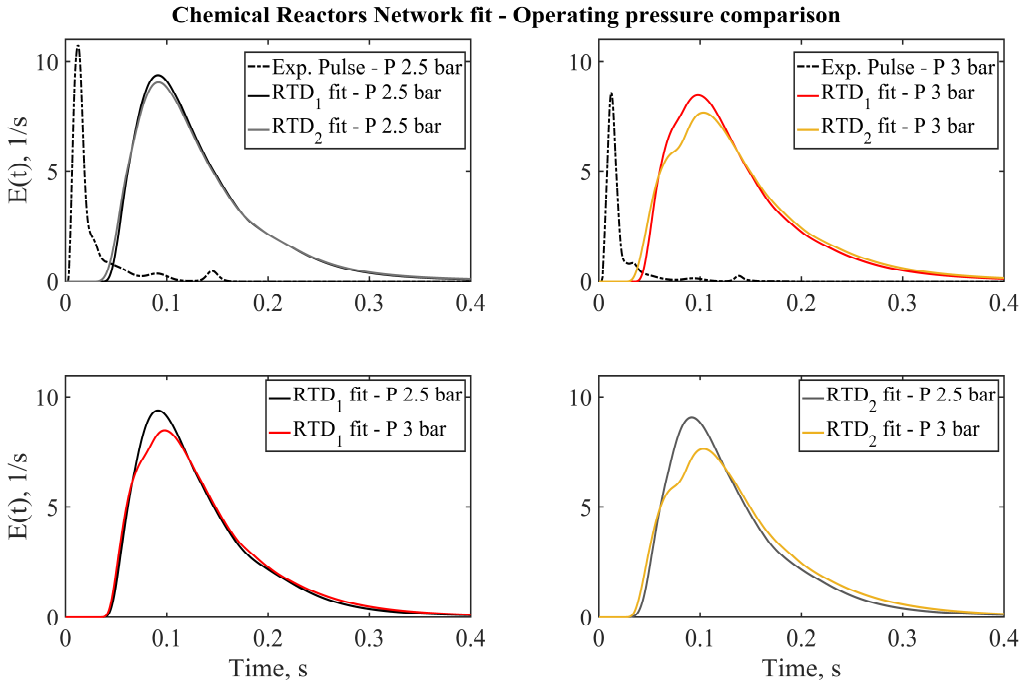

Figure 62: CRN-fit experimental tracer responses for $P = 2.5$ bar and $P = 3$ bar. Upper row: Out_1 and Out_2 for the two investigated operating conditions; lower row: comparison between the same measurement location for different operating conditions.

The global RTD for $P = 3$ bar is shown in Figure 63, while Table 16 proposes the values of selected parameters to carry out the comparison. The distribution rises sharply after approximately 2 ms, due to the tracer entrained from the cooling flow. This event takes place earlier for $P = 2.5$ bar than for the increased pressure, attributed to the pressure effect on the flow field. Consequently, the mean residence times $\tau^m$and the spreads σ^2, as well as $\tau_{tot}^{0.95}$ and $\tau_{tot}^{0.99}$ (Table 16) show increased values for a higher operating pressure. The sharper rise, and, accordingly, the sharper falling edge that characterizes the

RTD for $P = 3$ bar is attributed to the lower τ_{flame}, due to the concurrent effect of a lower l_{flame} and a higher mass flow into the flame region, characterized by $\frac{m_{flame}}{m_{in\_main}}$. Referring to the model schematization, Figure 31, the fastest path to the exit foresees entrainment in the flame zone and then in the cooling path. A lower τ_{flame} translates to a sharper falling edge because of the lower mixing time experienced by the fluid.

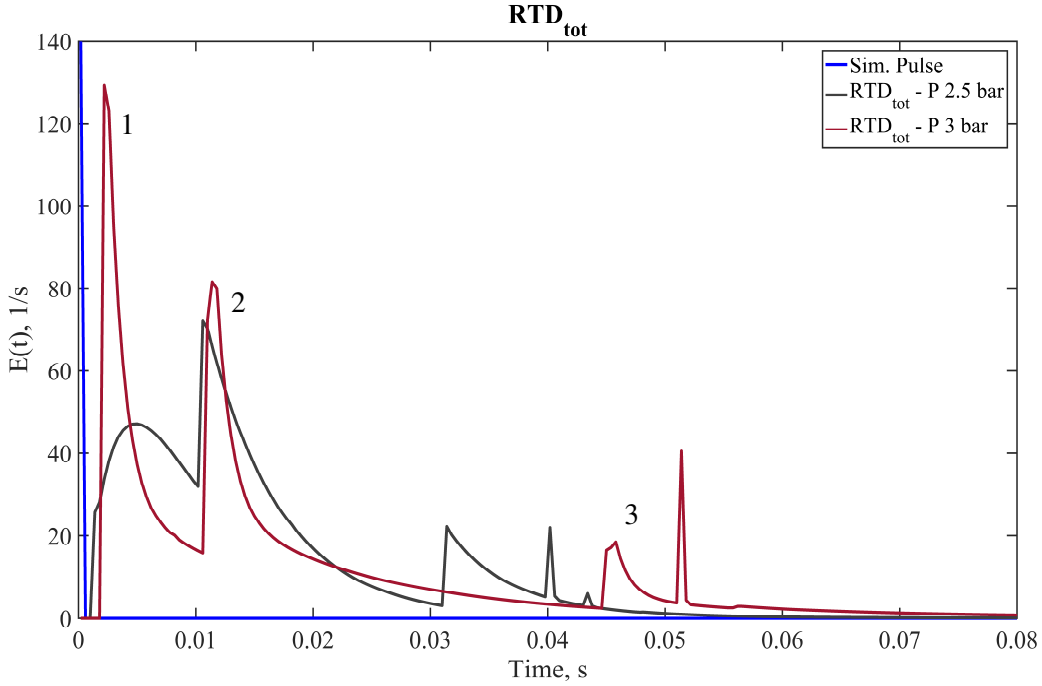

Figure 63: global RTD of the combustion chamber, $P = 2.5$ bar and $P = 3$ bar.

The local maximum in the RTD after $t = 0.01\ s$ corresponds to the tracer carried by the part of the flow following the two jet-PFRs, and then being entrained in the central PFR in the exit region, "path 1" in Figure 53. It exhibits exhibit a sharp rise followed by a similarly sharp decay until after $t = 0.02\ s$: here the slope of the falling edge of the distribution calculated for $P = 3$ bar lowers, possibly due to the τ_{IRZ}, which is one order of magnitude higher for the higher pressure. Instead, the τ_{ERZ} is slightly lower because of the higher recirculated mass flow in this region, as indicated by $\frac{m_{ERZ}}{m_{in\_main}}$. The peak "3" corresponds to the passage of the fluid in the jet-region and then in the side exit-PFR, and is followed by the sharp peak that characterizes entrainment of the flow in the effusion cooling region and, at a later stage, in the side exit-PFR. The interaction with the effusion cooling air path does not significantly change when considering the mass flow from the main to the cooling zone $\frac{m_{main \to cooling}}{m_{total\_feed}}$, but a significant decrease by approximately a factor of three is calculated for the reverse flow $\frac{m_{cooling \to main}}{m_{total\_feed}}$. The lower mixing of mass from the liner path to the bulk flow is likely responsible for the delay of the peak "3": besides the pressure effect on the flowrate, a lower amount of mass flow in the zone determines a higher passing time.

Table 16: global properties of the RTDs and CRN-fit parameters, $P = 2.5$ bar and $P = 3$ bar

	$P = 2.5$ bar	$P = 3$ bar		$P = 2.5$ bar	$P = 3$ bar
τ_{tot}^{m}	0.018	0.023	τ_{tot}^{c}	0.001	0.002
σ_{tot}^{2}	0.0013	0.0011	$\tau_{tot}^{0.95}$	0.041	0.067
S_{tot}^{3}	10	5	$\tau_{tot}^{0.99}$	0.13	0.17
$\frac{m_{flame}}{m_{in\_main}}$	0.97	1.46	$\frac{m_{IRZ}}{m_{in\_main}}$	6.5	1.2
$\frac{m_{main\rightarrow cooling}}{m_{total\_feed}}$	0.43	0.46	$\frac{m_{ERZ}}{m_{in\_main}}$	0.15	0.31
$\frac{m_{cooling\rightarrow main}}{m_{total\_feed}}$	0.18	0.06	τ_{IRZ}	5.8×10^{-4}	0.0051
$\frac{m_{flame}}{m_{in\_main}}$	0.97	1.46	τ_{ERZ}	0.03	0.02
l_{flame}	50	40	τ_{flame}	0.0031	0.0014

The impact of the operating pressure is now discussed in terms of pollutants formation, Figure 64. Carbon monoxide along the symmetry axis of the combustor does not show significant changes, and neither does the acetylene concentration. As seen in the previous chapters, the latter species is usually zero in the regions of CO formation schematized with a CSTR. The reason lies in C_2H_2 being an intermediate, directly linked to CO by Reaction 17, and indicating the progress of the reaction towards oxidized species. In a CSTR, the evolution of the reactions is not shown, and the temperatures and residence times in these CSTRs zones are such that there is no acetylene left in their product streams. The axial coordinate showing the major variation is $z = -48.5$ mm: after similar amount of CO in the ERZ, the CO concentration drops significantly while operating with a higher pressure. Proceeding along the axial coordinate, the opposite trend is observed, with a high peak of the CO concentration for $P = 3$ bar. The species is consumed to levels below ~500 ppm while approaching the exit plane. C_2H_2 clearly shows the same tendency. For both species, the observed profiles are caused by the different mixing behaviour attributable to the different boundary condition applied: the higher $\frac{m_{flame}}{m_{in\_main}}$, Table 16, causes a lower mass flow to mix with effusion cooling in an early stage. This situation changes in a later stage, where reacting mixture reaches the liner zone and mixes with fresh air. There is no significant difference in the species concentration at the exit plane, $x = 175$ mm, see Figure 65.

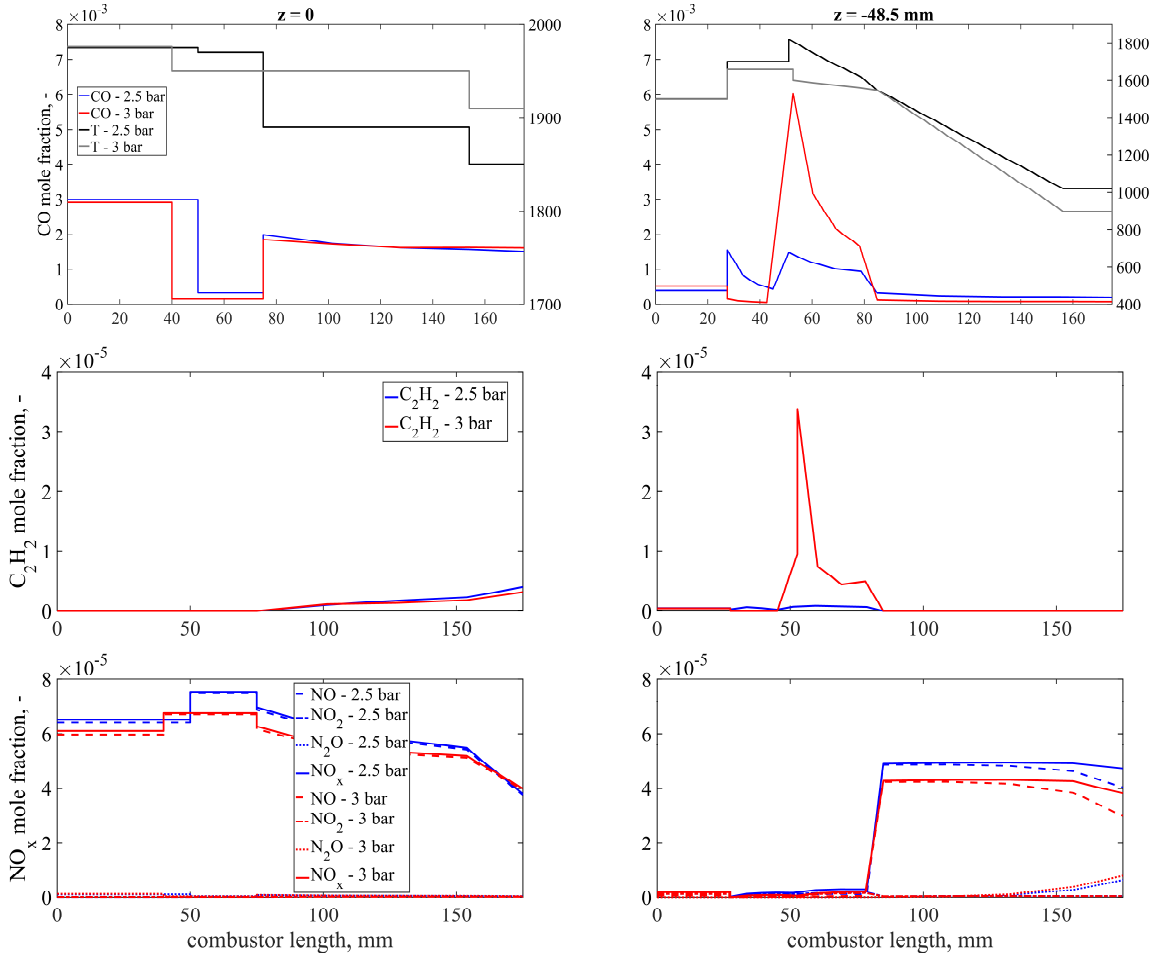

Figure 64: influence of P on species formation. Upper row: CO along selected profiles, middle row: C_2H_2, lower row: NO_x.

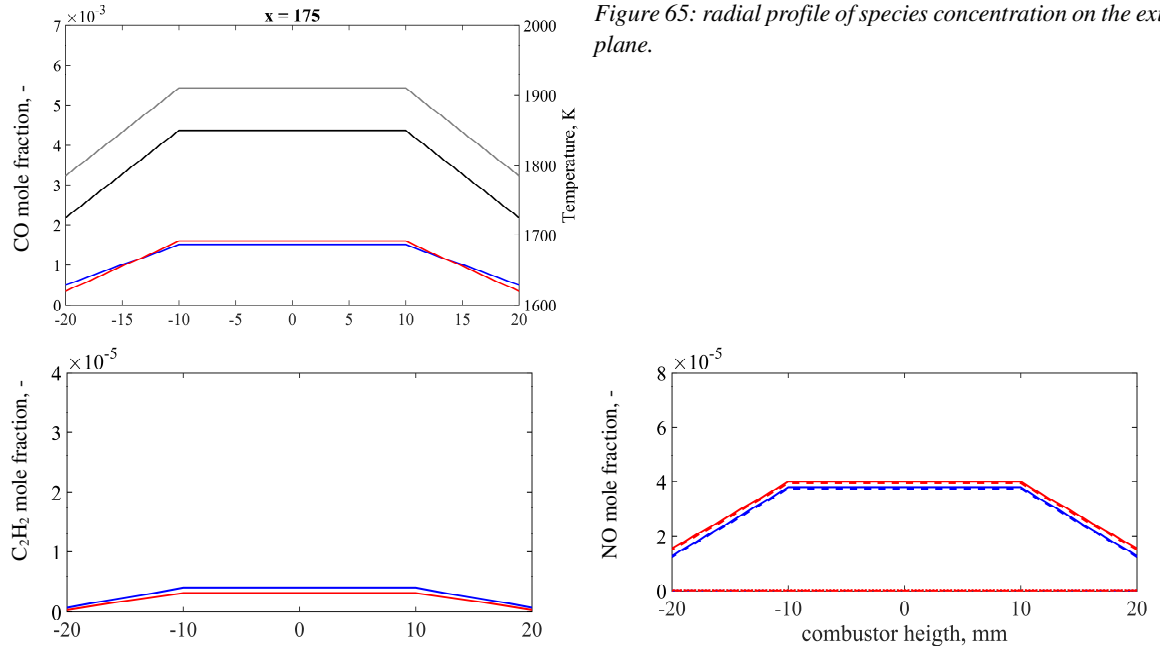

Figure 65: radial profile of species concentration on the exit plane.

Nitrogen oxides concentrations are shown in the last row of Figure 64. Starting from the combustor centreline plot, a lower in-flame NO formation is found for P = 3 bar, presumably caused by a lower residence time at high temperature. Its concentration remains lower than the one at a lower pressure along the whole combustor length, though reaching the same value at the exit, as shown also for

x = 175 mm. The lower NO concentration in the IRZ is believed to come from the interaction between NO and CO to form CO_2 and molecular nitrogen: indeed, to the lower concentration of NO in the IRZ corresponds also a lower CO concentration. Along the cooling liner, no significant amount of NO_x is calculated until the last part of the liner zone. The higher concentration in this part is attributed to mixing of flow from the main path that has experienced a sufficiently long time at high temperatures, as explained in 3.4.2.1. The NO_x amount is, in this case, lower because of the lower flow from the cooling to the main region, $\frac{m_{cooling \rightarrow main}}{m_{total\_feed}}$ that dilutes the species concentration. As seen in the z = 0 mm plot, the NO exit concentration is almost overlapping for the two cases considered.

3.4.2.4 Effect of swirl number

Figure 66 compares the CRN-fit distributions for a different swirl number, S. To consider the effect of a different swirl number on the flow field, two additional parameters were added to the optimization: the reattachment length, l_1 and the length of the post-flame IRZ, l_2. An estimation of these parameters was obtained in the designe phase of the network based on flow field visualization data, as described in 3.3.2 and Figure 32. In accordance to [124], a lower reattachment length is found and a longer IRZ are found. The higher swirling ratio S influences the spread of the curves, as evident from Figure 66, and the effect is clearer on Out_2. The earlier rise of the Out_2 curve is present in this set of measurements as well, confirming the impact of the effusion cooling air on the overall mixing characteristics.

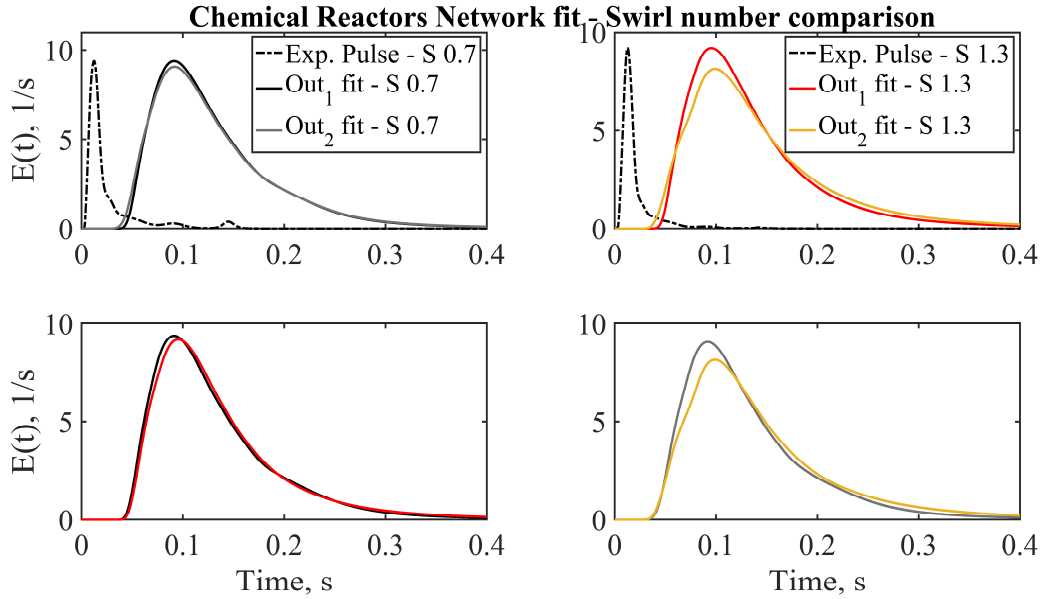

Figure 66: CRN-fit experimental tracer responses for $S = 0.7$ and $S = 1.3$ bar. Upper row:Out_1 and Out_2 for the two investigated operating conditions; lower row: comparison between the same measurement location for different operating conditions.

The effect of the different boundary condition on the RTD is given in Figure 67, and quantified in Table 17. As evident, all the parameters related to the duration of the distribution as well as the σ_{tot}^2 yield higher values. The general behaviour, as already seen in other cases, shows a first peak pushing a part of the tracer towards the exit of the combustor after entrainment in the effusion cooling air. The sharpest shape observed for $S = 1.3$ is attributed to the lower residence time within the flame, due to a higher mass flow involved in this zone. Referring to the model schematization, Figure 31, the fastest path to the exit foresees entrainment in the flame zone and then in the cooling path. A lower τ_{flame} leads to sharper falling edges because of the lower mixing time experienced by the fluid. The reduced τ_{flame} calculated for $S = 1.3$ lies in the higher flowrate passing through this zone: a greater $\frac{m_{flame}}{m_{in\_main}}$ is identified in virtue of the more intense mixing. Afterwards, the features stemming from both mixing in the main and liner flow path reach the exit, as described in earlier paragraphs. For a higher swirl number,

there is a larger share of mass flow entrained in the flame zone, in virtue of the more intense mixing. A higher percentage of the flow in the main path mixes with cooling air, but less cooling air is entrained to mix with the main reactive mixture. This is attributed to a larger part of the flow being pushed toward the boundaries with increasing S. The residence times in the recirculation zones is higher while operating with a higher swirl number, determining a longer distribution, as observed earlier.

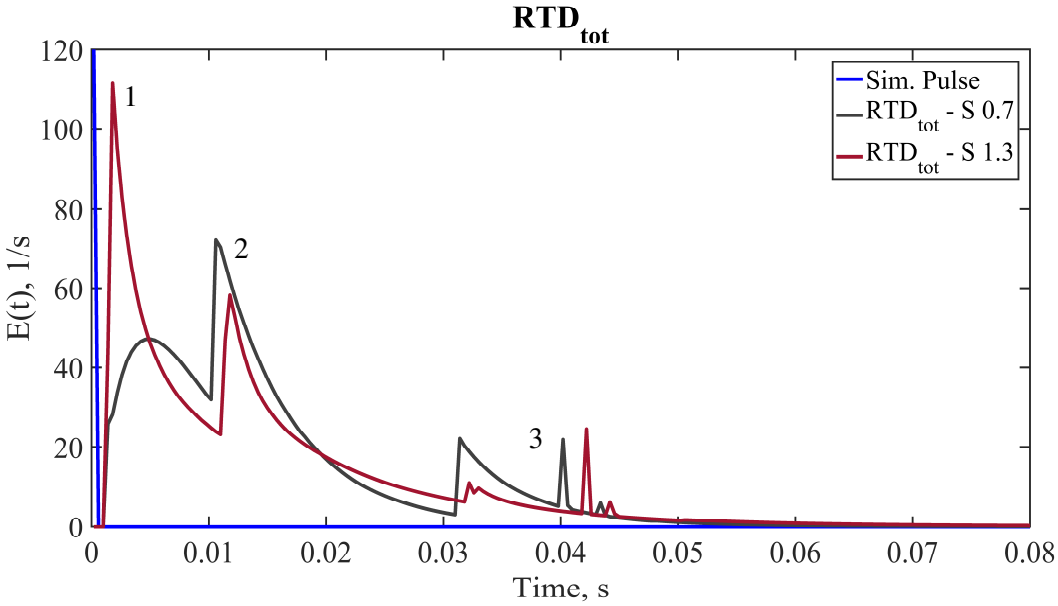

Figure 67: global RTD of the combustion chamber, $S = 0.7$ and $S = 1.3$.

Table 17: global properties of the RTDs and CRN-fit parameters – swirl number S variation

	$S = 0.7$	$S = 1.3$		$S = 0.7$	$S = 1.3$
τ_{tot}^{m}	0.018	0.019	τ_{tot}^{c}	0.001	0.001
σ_{tot}^{2}	9.069×10^{-4}	0.00104	$\tau_{tot}^{0.95}$	0.041	0.049
S_{tot}^{3}	10.26	8.201	$\tau_{tot}^{0.99}$	0.13	0.16
$\frac{m_{main \to cooling}}{m_{total\_feed}}$	0.430	0.5289	$\frac{m_{IRZ}}{m_{in\_main}}$	6.5	1.6
$\frac{m_{cooling \to main}}{m_{total\_feed}}$	0.278	0.1951	$\frac{m_{ERZ}}{m_{in\_main}}$	0.148	0.1045
$\frac{m_{flame}}{m_{in\_main}}$	0.976	1.78	τ_{ERZ}	0.0296	0.041
τ_{IRZ}	0.000582	0.0032	τ_{flame}	0.0031	0.0020
l_1, mm	35	32	l_2, mm	75	85

Figure 68 shows the impact of the swirl number on species formation.

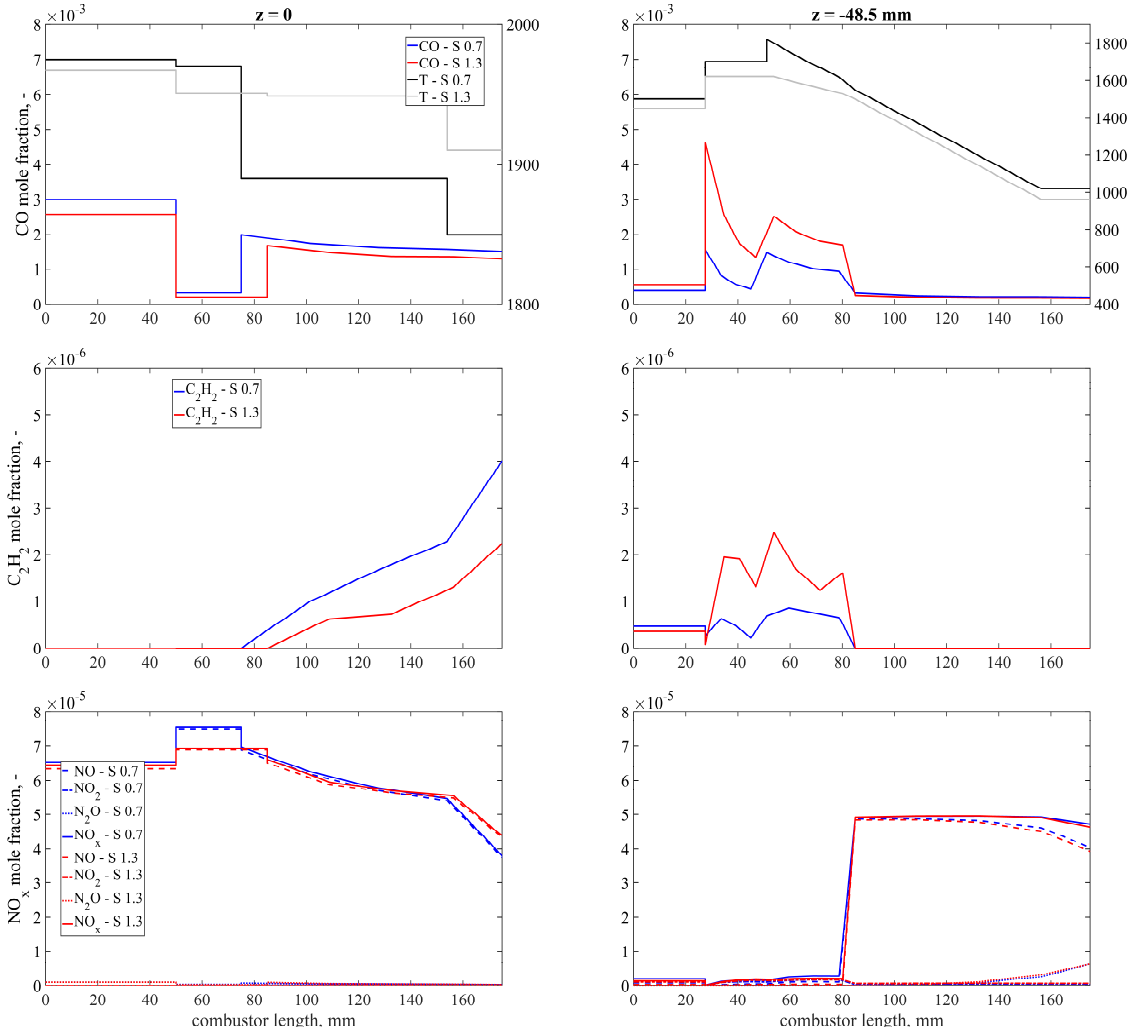

Figure 68: influence of S on species formation. Upper row: CO along selected profiles, middle row: C_2H_2, lower row: NO_x.

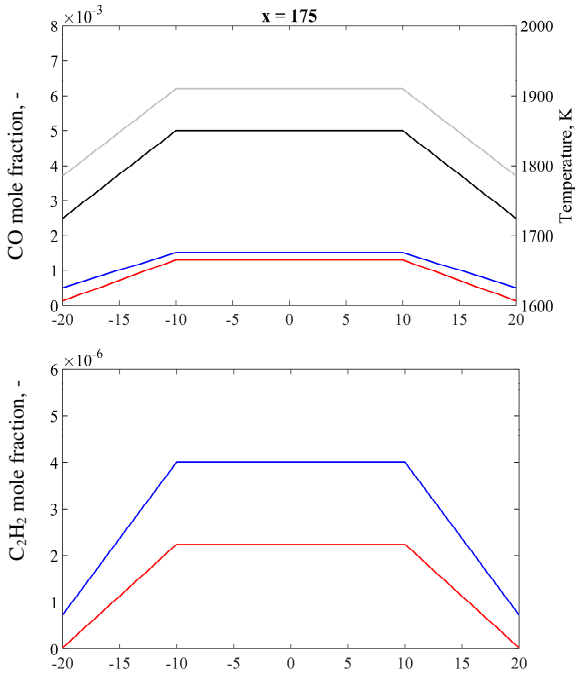

Figure 69: radial profile of species concentration on the exit plane.

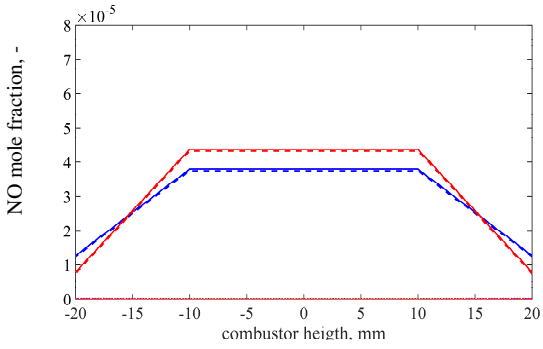

Starting from the CO formation at the central axis of the combustor, it is clear is that a higher S yields a lower amount of carbon monoxide along the whole combustor length, though the difference is not pronounced. The result is attributed to the more intense mixing in the near-burner region that encourages entrainment of a higher share of mass flow in the high temperature reaction zone, as quantified by $\frac{m_{flame}}{m_{in\_main}}$, Table 17. Instead, the parameter quantifying the amount of mass flow entrained in the post-flame IRZ is lower for $S = 1.3$, but it determines a higher τ_{IRZ} (approximately one order of magnitude) with respect to the lower swirl number: therefore, less CO is calculated in this region. The CO evolution in the segregated exit region is the same for both investigated cases, and its value is slightly lower for the high-swirl case, because of the higher CO consumption highlighted before. The scenario changes when looking at the profiles in the near-effusion cooling region. Here, a higher amount of CO is formed in the first part of the liner for $S = 1.3$, approximately doubled with respect to $S = 0.7$. The reason is the higher share of reactive mixture that mixes in the near wall region, as highlighted before and as clear from the ratio $\frac{m_{main \rightarrow cooling}}{m_{total\_feed}}$: the more intense mixing causes high carbon monoxide levels in the first part of the liner wall. However, the carbon monoxide content in the last part of the effusion cooling is low and approximately the same as the one observed in the case of $S = 0.7$. The reason lies in the high average temperature of the middle part of the plot, encouraging CO reduction, and in the mixing with the bulk flow: this flow has a low CO content. As anticipated before, the CO content at the exit of the combustor is lower while adopting a higher swirl number, and the difference is more pronounced in the lateral part of the combustor.

Just a few ppm of C_2H_2 is present, and its evolution follows that of CO, though the order of magnitude is significantly lower. This species is absent in the CSTR zones, where it completely reacted to form combustion products. Its formation is appreciable in the exit-zone central PFR, where bypasses from the near nozzle region bring unreacted mixture. In the near-wall reactors, a few ppm are formed as a consequence of the flow mixing from the main flow region. C_2H_2 on the exit plane, in Figure 69, is significantly lower for a higher swirl number, presumably because of the lower amount of fuel bypass that reaches this zone. This parameter has not been selected to carry out the comparison among the different operating conditions, but it is, in this case, an explanation to the lower amount of C_2H_2 at the exit of the combustor: the bypass fuel for $S = 1.3$ is approximately half with respect to the same quantity for $S = 0.7$. This is likely to cause the difference in the concentration of C_2H_2 on the exit plane. Therefore, a higher swirl enhances the conversion limiting the amount of bypass fuel.

The NO_x concentrations present a rather identical evolution along the central axis of the combustor, except in the IRZ, where a lower swirl number yields a higher amount of pollutant species. The trend changes in the central PFR of the exit region, where the NO_x amount becomes slightly larger for a higher swirl number. The scenario at $z = -48.5\ mm$ is the same encountered up to now: the NO_x level is low (sub-ppm) until the last part of the effusion cooling liner, then it rapidly reaches ~50 ppm. This is attributed to the longer residence time of the mixture in a high temperature environment before mixing in this region. The flue gases reaching this point have spent more time in the system with respect to that mixing earlier in the liner-zone. Therefore, its NO_x content is higher, and it mixes in a cold region, freezing the reaction, until the nitrous oxide reaction starts, consuming NO and producing N_2O. On the exit plane, a higher NO_x mole fraction is associated with a higher swirl number, while observing the central exit PFR, but is lower at the side, which is the zone that experiences the more intense mixing due to the high swirl motion.

3.4.2.5 Effect of equivalence ratio

The effect of stoichiometry on the tracer response of the system is reported in Figure 70. Three different equivalence ratios were investigated (Table 2 and Table 6) : $\varphi = 0.65$, $\varphi = 0.75$ and $\varphi = 0.85$. As shown in the magnification, the rising edges of the distributions follow the trend of the average temperature in the combustion chamber: the higher the equivalence ratio (hence, higher average temperature) the earlier the tracer response starts. This phenomenon is more pronounced while

comparing $\varphi = 0.65$ and $\varphi = 0.75$. The impact of cooling air entraining part of the tracer and transporting it towards the exit earlier than the main flow is clear for all investigated equivalence ratios. An additional parameter was considered for the optimization in this case: the length of the flame zone, l_{flame}, Table 18.

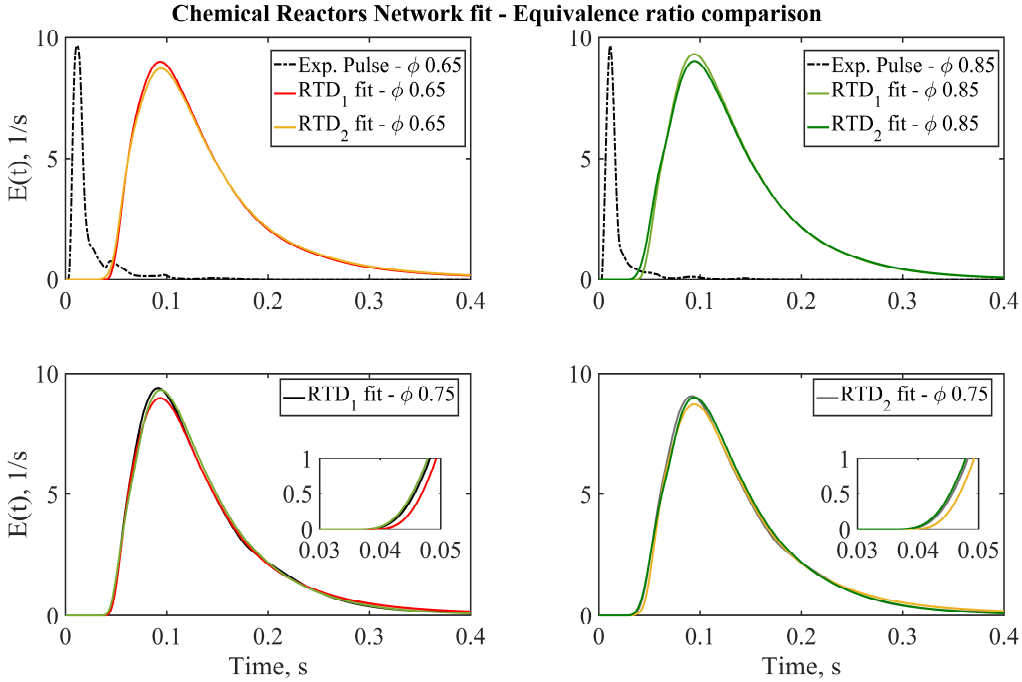

Figure 70: CRN-fit experimental tracer responses for $\varphi = 0.65$, $\varphi = 0.75$ and $\varphi = 0.85$. Upper row:Out_1 and Out_2 for $\varphi = 0.65$ and $\varphi = 0.85$; lower row: comparison between the same measurement location for different φ.

The RTD calculated using a mathematically generated pulse is presented in Figure 71. A higher initial peak is associated with entraining of the tracer in the effusion cooling path, consistent with the larger amount of $\frac{m_{main \to cooling}}{m_{total\_feed}}$. $\varphi = 0.85$ exhibits a sharpest shape for its peak "1", compared to the other two cases: it is attributed to the lower residence time in the flame (Table 18), due to a higher mass flow involved in this zone. Referring to Figure 30 and Figure 31, the fastest path to the exit foresees entrainment in the flame zone and then in the cooling path. A lower τ_{flame} translates to a lower mixing time experienced by the fluid, hence a sharper falling edge. A reduced τ_{flame} calculated for $\varphi = 0.85$ - despite a larger flame zone - has been identified, which lies in the higher flowrate passing through this zone: a greater $\frac{m_{flame}}{m_{in\_main}}$ is identified, and a higher temperature is experienced within this zone in virtue of the increased fuel quantity in the system. These two factors are not balanced by the increased l_{flame}, resulting anyway in a lower τ_{flame}. After the first fast arrival of part of the tracer at the exit of the combustor, the evolution of the fluid history continues following the other possible routes inside the combustor: the ensemble of peaks "2" concerns the fluid whose evolution in the main path ends following the faster region identified on the centreline of the combustor (Figure 30 and Figure 31), whereas the remaining flow is entrained in the side zone of the segregated region of the combustor. The ratio $\frac{m_{cooling \to main}}{m_{total\_feed}}$ increases from $\varphi = 0.65$ to $\varphi = 0.75$, most likely because of the increased impulse towards the wall-zone imputable to the higher temperatures linked to the equivalence ratio. The mentioned parameter slightly decreases while increasing φ further. This phenomenon is attributed once again to the increased impulse due to the higher temperatures and thus thermal expansion: it is indeed responsible for a certain share of mass flow mixing in the cooling region. However, the higher flow inertia caused by the combustion-induced acceleration pushes forward a higher share of the flow in the case of $\varphi = 0.85$ with respect to $\varphi = 0.75$.

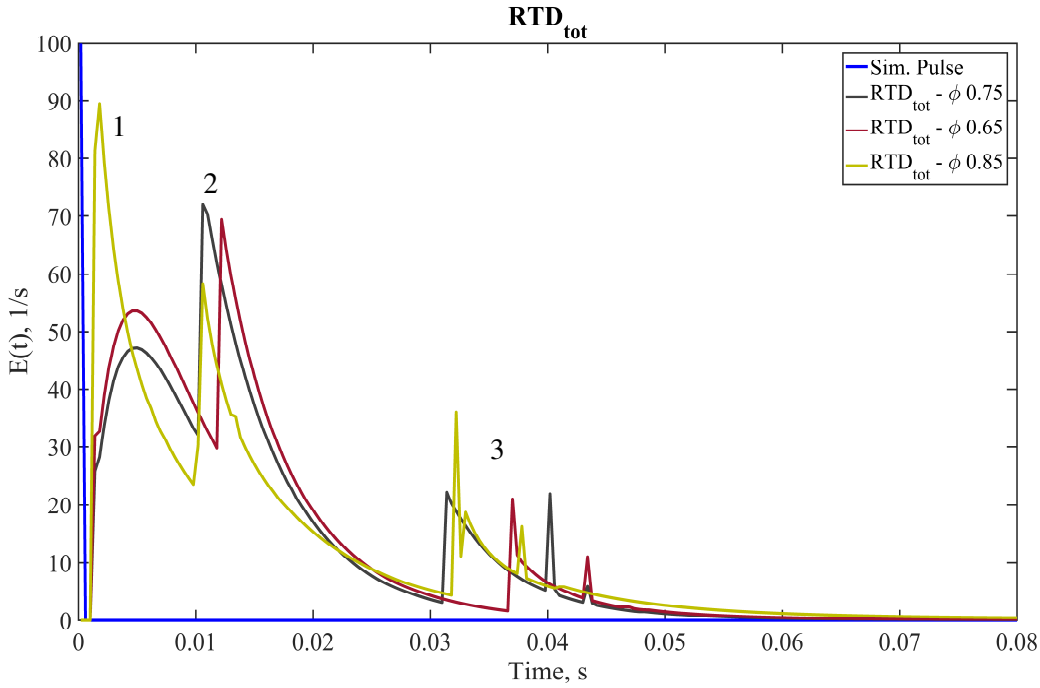

Figure 71: global RTD of the combustion chamber, $\varphi = 0.65$, $\varphi = 0.75$ and $\varphi = 0.85$.

The flow acceleration caused by combustion is also responsible for the trend identified for the parameter $\frac{m_{IRZ}}{m_{in\_main}}$: the higher the flow inertia, the lower the relative centrifugal forces that cause the flow recirculation in the IRZ [116]. Therefore, τ_{IRZ} increases with the equivalence ratio. The mass entrained in the ERZ decreases going from $\varphi = 0.65$ to $\varphi = 0.75$, in accordance to the increased velocities that push the flow forward. However, this parameter increases for $\varphi = 0.85$. This is most likely due to the higher intensity of the ERZ with increasing equivalence ratio, due to the higher temperatures and more intense gas expansion [125]. A higher τ_{tot}^{m} characterizes the richer operating condition, directly linked to the higher τ_{IRZ}. The σ_{tot}^{2} takes its higher value in the leaner case, in accordance the longer distributions generated by lower temperatures in the system.

Table 18: global properties of the RTDs and CRN-fit parameters – equivalence ratio φ variation

	$\varphi = 0.65$	$\varphi = 0.75$	$\varphi = 0.85$		$\varphi = 0.65$	$\varphi = 0.75$	$\varphi = 0.85$
τ_{tot}^{m}	0.018	0.018	0.019	τ_{tot}^{c}	0.001	0.001	0.001
σ_{tot}^{2}	0.001	9×10^{-4}	7×10^{-4}	$\tau_{tot}^{0.95}$	0.044	0.041	0.053
S_{tot}^{3}	9	10	5	$\tau_{tot}^{0.99}$	0.15	0.13	0.14
$\frac{m_{main\rightarrow cooling}}{m_{total\_feed}}$	0.49	0.43	0.51	$\frac{m_{IRZ}}{m_{in\_main}}$	7.5	6.5	1.7
$\frac{m_{cooling\rightarrow main}}{m_{total\_feed}}$	0.17	0.28	0.24	$\frac{m_{ERZ}}{m_{in\_main}}$	0.30	0.15	0.35
$\frac{m_{flame}}{m_{in\_main}}$	0.97	0.98	1.5	τ_{flame}	0.0029	0.0031	0.0021
τ_{IRZ}	0.00058	0.00058	0.0025	τ_{ERZ}	0.02	0.03	0.01
l_{flame}, mm	47	50	54				

The profiles of selected species along representative coordinates inside the combustor are shown in Figure 72. The upper row is dedicated to CO. Along the combustor centreline, $z = 0\,mm$, the flame zone is the first one starting from the left side. Here, the CO concentration follows the equivalence ratio, increasing as the mixture becomes richer. In the IRZ, $\varphi = 0.75$ and $\varphi = 0.85$ show the same CO mole fraction; while $\varphi = 0.65$ has a lower CO content. $\varphi = 0.65$ and $\varphi = 0.75$ exhibit the same behaviour

in the exit zone PFR: more CO is formed due to flow bypasses from the near burner region, and its concentration lowers towards the exit due to mixing and reaction. $\varphi = 0.85$ presents an increasing concentration of carbon monoxide in the beginning of the zone, that stays almost constant until the exit.

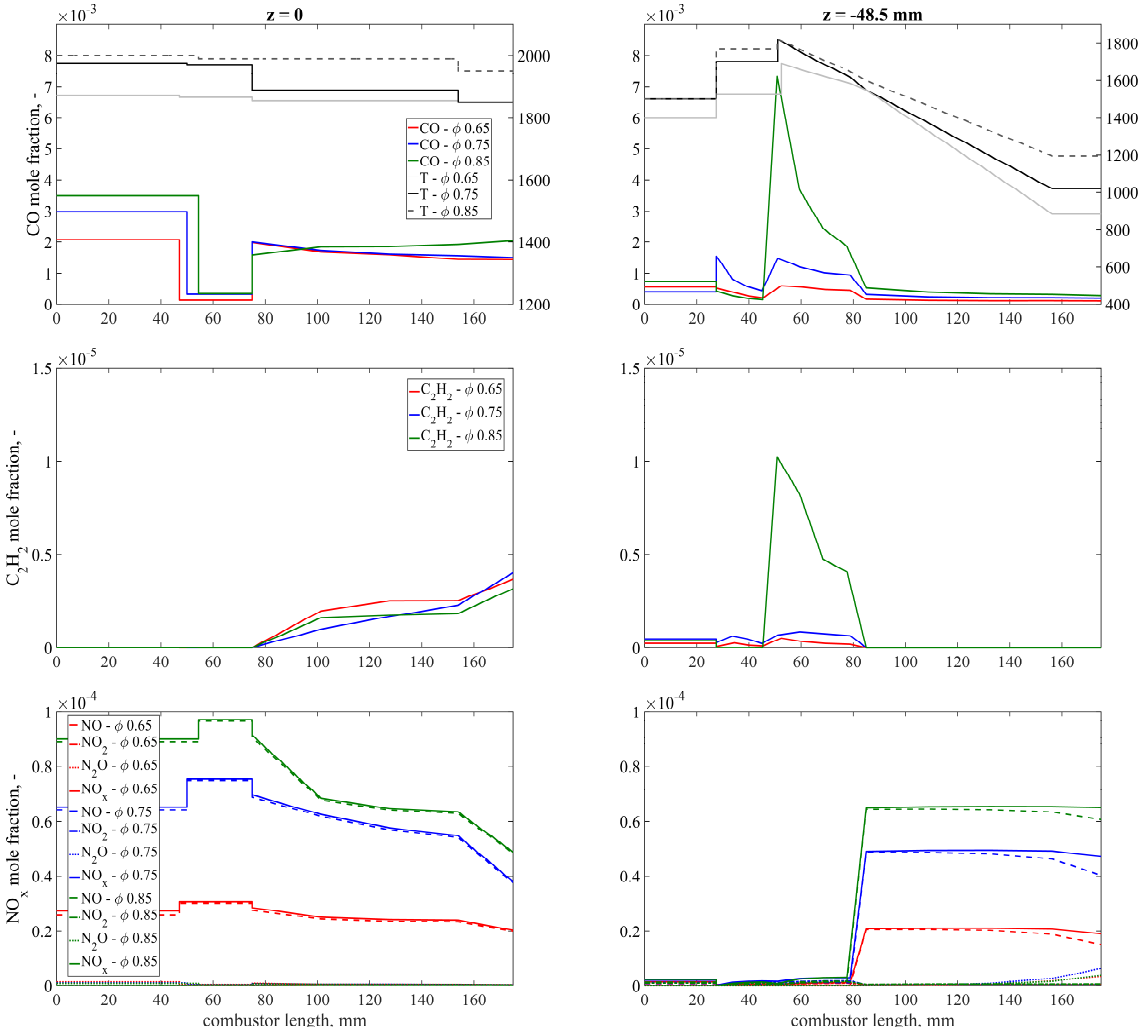

Figure 72: influence of φ on species formation. Upper row: CO along selected profiles, middle row: C_2H_2, lower row: NO_x.

For $z = -48.5\ mm$, the CO concentration along the ERZ and the effusion cooling liner is given. The ERZ shows a higher carbon monoxide content with increasing φ, independently from the different τ_{ERZ}. The start of the effusion cooling liner at $x = 27.5\ mm$ is characterized by a CO increase for the mid-equivalence ratio value, but both richer and leaner conditions exhibit a decrease in the species concentration, due to the different interaction with cooling air at this stage: clearly a lower amount of mixture carrying reactive species is entrained at this stage. The trend changes moving along the combustor length. In the second near wall region, $\varphi = 0.65$ and $\varphi = 0.75$ show the same trend, though with a lower intensity for the leaner case: reactive mixture is transported from the bulk flow region and reacts with incoming air to slowly consume the CO, dropping its concentration. The richer condition instead shows a noticeably higher CO concentration, due to the higher mixing of main flow in this region of the combustor. Nevertheless, the carbon monoxide formed in this zone is oxidized, reaching the same concentration level as the other two operating conditions at the end of the liner. The concentrations calculated on the vertical exit plane reproduce those already seen in the last part of the centreline profile. Acetylene shows the same behaviour seen in other cases. The species is not present in the flame and IRZ zones of the combustor owing to the high temperatures and suitable residence times to consume the available C_2H_2. Traces of the compound are produced in the last PFR as a result of flow bypasses

carrying fuel from the inlet nozzle. The acetylene evolution along the effusion cooling liner follows the one explained for carbon monoxide.
The NO_x concentration along the selected profiles is shown in the last row. The in-flame content increases with the equivalence ratio, and, therefore, the temperature. This trend is kept in all the presented plots.

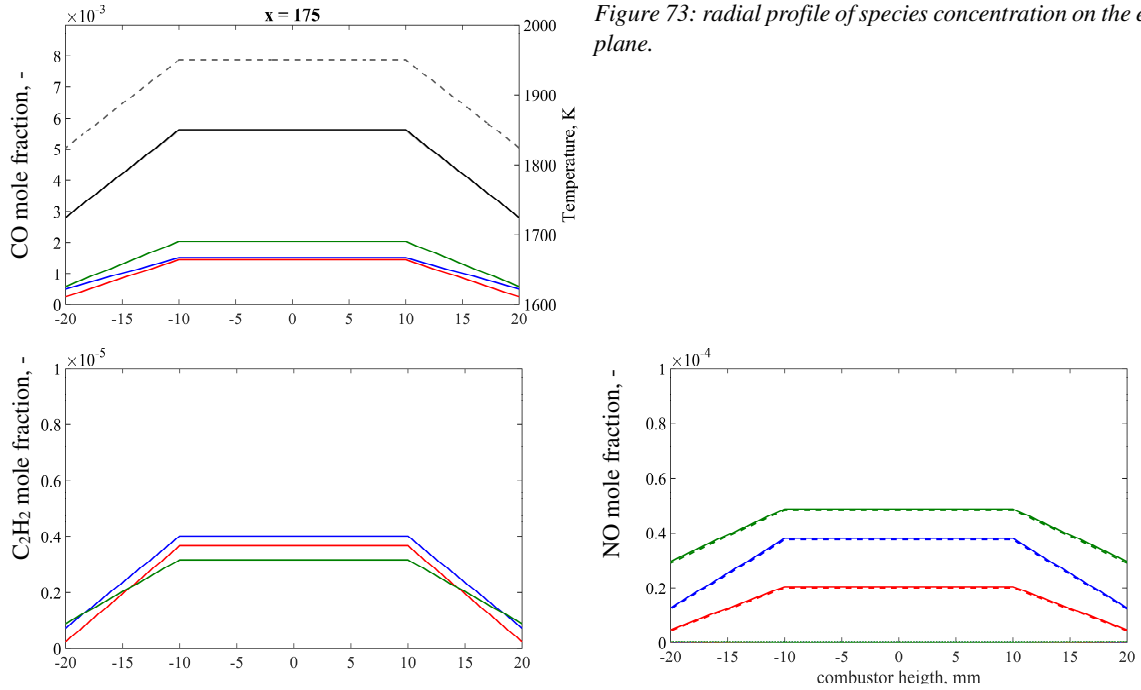

Figure 73: radial profile of species concentration on the exit plane.

3.4.2.6 Summary

In this chapter, the impact of the operating conditions on the RTD and species formation in the SSGT has been described referring to the standard operation point. The relevant parameters that characterize this point are proposed again below, in Table 19.

Table 19: relevant parameters of the standard operation point.

	Operation point, units	
Preheating temperature	623	K
System pressure, P	2.5	bar
Main air mass flow, m_{in_main}	30	g/s
Equivalence ratio, $\varphi_{\text{lean premixed}}$	0.75	[-]
Swirl number, S	0.7	[-]
Effusion cooling mass flow, m_{cool}	15	g/s
Fuel staging ratio, st.	0%	[-]

In Table 20, some relevant parameters are proposed to provide a last comparison among the investigated sets of boundary conditions. Besides the global mean residence time inside the combustor, τ_{tot}^{m}, $\frac{m_{recirculation}}{m_{in\_main}}$ represents the total share of entrained flow in the recirculated regions with respect to the total air mass flow introduced at the entrance nozzle, and $\frac{m_{main\_cooling}}{m_{total\_feed}}$ calculates the ratio of the total mass flow exchanged between the two flow paths (main and cooling) with respect to total air mass flow (main and effusion cooling) fed to the system. A final overview is given also in terms of pollutants emission. The quantities CO_{global}, $C_2H_{2_{global}}$ and NO_{global} in Table 20 are calculated as the weighted mean of the concentration of the species at the exit plane, $x = 175\ mm$. The equilibrium value for the same species is reported. This equilibrium value has been calculated in an isothermal PFR at $T =$

1800 K. This temperature was chosen as mean reactive temperature, indicating an average thermal state of the mixture in the bulk flow. Furthermore, using the same temperature for all computations enables recognizing trends depending on the specific operating condition.

Table 20: comparison among the different investigated operating points – part one

	Basic operating point (Table 19)	$\mathrm{m_{cool}} = 7.5\ \mathrm{g/s}$	$\mathrm{P} = 3\ \mathrm{bar}$	$\varphi = 0.65$	$\varphi = 0.85$
τ_{tot}^{m}	0.018	0.020	0.023	0.018	0.019
τ_{flame}	0.0031	0.0028	0.0014	0.0029	0.0021
$\frac{m_{main\_cooling}}{m_{total\_feed}}$	0.71	0.60	0.52	0.67	0.75
$\frac{m_{recirculation}}{m_{in\_main}}$	6.7	5.2	1.5	7.8	2
$\mathrm{CO_{global}}$	7.6×10^{-4}	8.7×10^{-4}	7×10^{-4}	6.3×10^{-4}	0.001
$\mathrm{C_2H_{2global}}$	1.5×10^{-6}	2.0×10^{-6}	1.2×10^{-6}	1.2×10^{-6}	1.3×10^{-6}
$\mathrm{NO_{global}}$	3.7×10^{-5}	7×10^{-5}	3.1×10^{-5}	1.6×10^{-5}	6.8×10^{-5}
$\mathrm{CO_{equilibrium}}$	2.1×10^{-5}	2.8×10^{-5}	1.9×10^{-5}	1.7×10^{-5}	2.8×10^{-5}
$\mathrm{C_2H_{2equilibrium}}$	0	0	0	0	0
$\mathrm{NO_{equilibrium}}$	0.0028	0.0013	0.0028	0.0030	0.0025

Table 21: comparison among the different investigated operating points – part two

	Basic operating point (Table 19)	$\mathrm{S} = 1.3$	$\mathrm{st.} = 10\%$	$\mathrm{st.} = 30\%$	$\mathrm{st.} = 50\%$
τ_{tot}^{m}	0.018	0.019	0.021	0.022	0.017
τ_{flame}	0.0031	0.0020	0.0023	0.0027	0.0022
$\frac{m_{main\_cooling}}{m_{total\_feed}}$	0.71	0.72	0.40	0.61	0.68
$\frac{m_{recirculation}}{m_{in\_main}}$	6.7	1.7	3.6	4.6	1.8
$\mathrm{CO_{global}}$	7.6×10^{-4}	5.6×10^{-4}	4.7×10^{-4}	0.0015	0.011
$\mathrm{C_2H_{2global}}$	1.5×10^{-6}	7.0×10^{-7}	1.1×10^{-7}	1.3×10^{-6}	1.6×10^{-5}
$\mathrm{NO_{global}}$	3.7×10^{-5}	4.1×10^{-5}	1.0×10^{-4}	9.8×10^{-5}	9.8×10^{-5}

The highest τ_{tot}^{m} is attributed to $\mathrm{P} = 3\ \mathrm{bar}$, most likely due to the pressure effect on the flow rate of the system and to the large value of τ_{IRZ} (see Table 10). This agrees with the value of the parameter $\frac{m_{recirculation}}{m_{in\_main}}$ being the lowest in the system, accompanied by an increased value of the IRZ volume in view of a smaller flame. The global mass flow exchanged between the effusion cooling path and the main path is lower with respect to the standard operation point. $\mathrm{P} = 3\ \mathrm{bar}$ shows a lower global concentration of pollutants reaching the exit plane. The CO value agrees with the pressure effect on the equilibrium concentration, while the result for NO is attributed to the lower τ_{flame}.

Decreasing $\mathrm{m_{cool}}$ increases the τ_{tot}^{m} species spend in the system, because of the lower flow rate globally fed to the combustor and because of a slightly lower $\frac{m_{recirculation}}{m_{in\_main}}$, that increases residence times in recirculation zones. The lower $\frac{m_{recirculation}}{m_{in\_main}}$ stems from the higher temperatures of the system, due to a lower amount of cooling air. As expected, introducing a lower amount of air along the effusion liner lowers the interaction between the bulk flow and flow in the lower part of the combustor. The

concentration of pollutants at $x = 175\,mm$ is higher, partly for a global concentration effect, as indicated by the equilibrium value. The amount of NO_{global} is indeed noticeably higher. Referring to Figure 54, this increase might come from the higher in-flame concentration, attributed to the higher temperature.

A higher equivalence ratio shows a larger value of τ_{tot}^{m}, likely because of the lower entrainment of flow in the IRZ, which causes a higher residence time in this perfectly mixed zone. Accordingly, the parameter $\frac{m_{recirculation}}{m_{in\_main}}$ decreases if the φ is increased. τ_{flame} shows its lower value while adopting $\varphi = 0.85$, because more mass flow is entrained in this zone and the flame temperature is higher. The interaction between the two flow paths inside the combustor, quantified by the parameter $\frac{m_{main\_cooling}}{m_{total\_feed}}$, becomes larger going from $\varphi = 0.65$ to $\varphi = 0.85$. The species concentration follows the same trend.

A higher swirl number increases the mixing times resulting in broader distributions. The swirl entrains more mass flow in the flame zone, resulting in a lower τ_{flame}. The tendency of the flow to be entrained in recirculation zones is reduced, and $\frac{m_{main\_cooling}}{m_{total\_feed}}$ is similar for the low and high swirl number. Carbon-based pollutants are drastically reduced for $S = 1.3$, in virtue of the high mixing and the lower amount of fuel bypass, explained in 3.4.2.4. The slightly higher value of NO_{global} is attributed to a temperature effect: $S = 1.3$ shows a higher post-flame temperature with respect to $S = 0.7$.

An increasing staging ratio increases τ_{tot}^{m} until $st. = 30\%$, then the mean residence time in the combustor experiences a decrease, attributed to the higher average temperature in the system. The in-flame residence time is globally lower with respect to premixed combustion, though exhibiting a maximum for $st. = 30\%$. For staged operation, the mass flow entrained in the flame increases with increasing staging ratio. Besides, there is an additional volume, the pilot reactor, that increases with increasing staging ratio. Therefore, τ_{flame} stems from the concurrent effects of a different flame volume and an increased in-flame mass flow. $\frac{m_{recirculation}}{m_{in\_main}}$ is lower for partially premixed combustion with respect to purely premixed, and exhibits a maximum, once again, in the case of $st. = 30\%$. The interaction between the main flow path and the cooling air is lower for all staging cases with respect to the absence of staging. Nevertheless, the global amount of mass flow exchanged between the two paths, $\frac{m_{main\_cooling}}{m_{total\_feed}}$, increases together with the staging ratio. The same trend is followed by the species concentration. However, $st. = 10\%$ exhibits a lower amount of CO_{global}.

A final overview is additionally given in terms of exit temperature profile. The interest towards the temperature profile at the exit of the gas turbine combustor is high, because this parameter is crucial for the durability of the turbine. A uniform temperature profile would be ideal, whereas a high level of non-homogeneity is harmful for the turbine because it causes local hot spots that decrease the life of the turbine. Non-uniform temperature profiles at the exit of the combustor are referred as hot streaks [126], [127] and efforts to improve the mixing inside the combustor in order to reduce the non-homogeneity of the temperature profile have been made [128]. Given the technological relevance of this topic, the temperature profile at $x = 175\,mm$, showing the behaviour along the lower half of the combustor, is given in Figure 74.a. Figure 74.b shows the difference between the maximum and the minimum temperature at the same location as, to give an idea of the inhomogeity for each tested operation point. The temperatures presented are those fitted by the optimization procedure while fitting the CRN to the tracer response. The description “standard” refers to the boundary conditions that characterize the standard operation point.

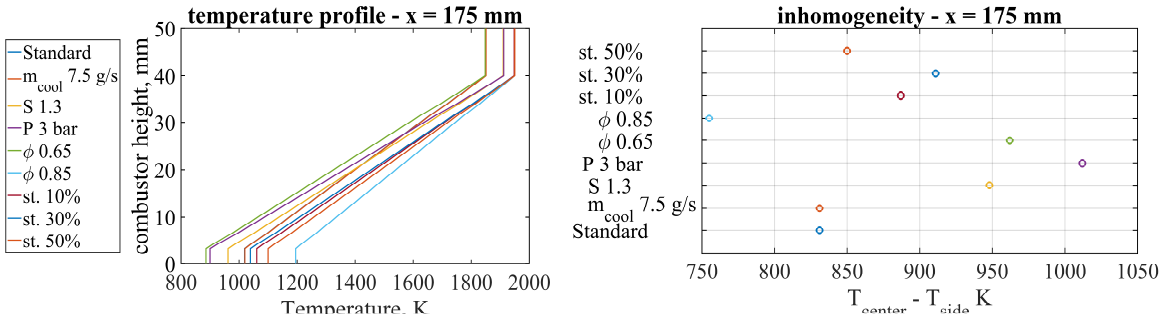

*Figure 74: **a**, temperature along a vertical profile at $x = 175\ mm$; **b**: difference between the maximum and minimum temperature along the vertical profile at $x = 175\ mm$.*

From Figure 74.b, it emerges that the higher equivalence ratio that was tested exhibits the lowest value of the temperature difference. The highest value of the parameter chosen to quantify the inhomogeneity occurs while operating the system with a higher pressure. The standard operation point and the lower m_{cool} operation point show the same value, almost 100 K higher with respect to the same difference at $\varphi = 0.85$.

4 Oxyfuel Combustor

As already outlined in the introduction chapter, combustion of fossil fuels dominates the global energy market, and will continue to dominate it in the future, as just a slight decrease is forecasted in the next decades [1]. The use of fossil fuels to feed combustion-based devices has a strong environmental impact that now more than ever must be minimized. The challenge of combustion research is to explore new ways to reduce pollutant emissions along with high process efficiency. One option lies in a continuous improvement of the combustion system or the application of new combustion concepts [3], such as oxyfuel combustion. In this concept, air is replaced by a mixture of carbon dioxide (CO_2) and oxygen as oxidizer, leading to an exhaust gas mainly composed of CO_2 and water vapor. The CO_2 can be separated, liquefied and stored underground to reduce the effects on the environment [3]. This chapter is dedicated to the CRN modelling of intermediate-scale (20 kW) combustor designed at Technische Universität Darmstadt, suitable for operating gas flames as well as gas-assisted coal flames, exploring both air and oxyfuel atmospheres. The modelling exploits the available RTD measurements in the mentioned test rig. As highlighted in paragraph 2.3, such a modelling proves its strength when investigating new combustion concepts: RTD-derived CRN models are a powerful candidate for a first examination on the impact of the operating conditions with respect to the benchmark combustion process in terms of simple mixing and reaction zones.
After the description of the experimental apparatus, the CRNs are introduced and their fit to experimental data discussed. Finally, the CRNs are employed to draw conclusions on the effect of the oxidizer (namely air or oxyfuel) on the mixing and reactive features of the flow.

4.1 Experimental apparatus

The test rig under investigation is an intermediate-scale combustor, suitable for operating gas flames as well as gas-assisted coal flames. It is designed to close the gap between unconfined laboratory-scale coal burners and confined industrial-scale coal combustors and allows the exploration of both air and oxyfuel atmospheres. In the following, it is referred to as OFC (OxyFuel Combustor). Thorough experimental investigations have been carried out in this apparatus [64], [111], [112], [129], supported as well by numerical simulations [130], [131]. Figure 75 shows the geometry. Dimensions are provided in Table 22. The burner down-fires into the combustion chamber. Walls are made of wedged fused silica to enable optical access. Inside the burner quarl, two inlet orifices surround a bluff body (magnification in Figure 75.b): a partially premixed mixture of fuel and oxidizer (air or oxyfuel, details in Table 22) is exiting the inner orifice (primary flow, FI), whereas swirled oxidizer issues through the outer orifice (secondary flow, FII). A tertiary flow, FIII, of oxidizer is injected close to the windows (Figure 75.a). In the following, the cases employing air as diluent of the system are addressed as NRair (non-reactive) and Rair (reactive), whereas, when using an oxyfuel mixture, the cases are added as NR30 and R30. Details about the characteristics of the two operating points explored are reported in Table 22.

RTD measurements have been carried out both in non-reactive and reactive conditions [63], [64]. The operating points are listed in Table 22. For non-reactive measurements, CH_4 was injected as a gaseous tracer in the primary flow orifice (see Figure 75) and was detected in-situ by means of direct Tunable Diode Laser Absorption Spectroscopy (TDLAS). The gas phase RTD was measured probing the concentration of CH_4 injected in the primary flow at the inlet and representative positions at the combustor exit simultaneously, using a diode laser. It was shown, that the choice of the tracer had a negligible impact on the flow and the measured

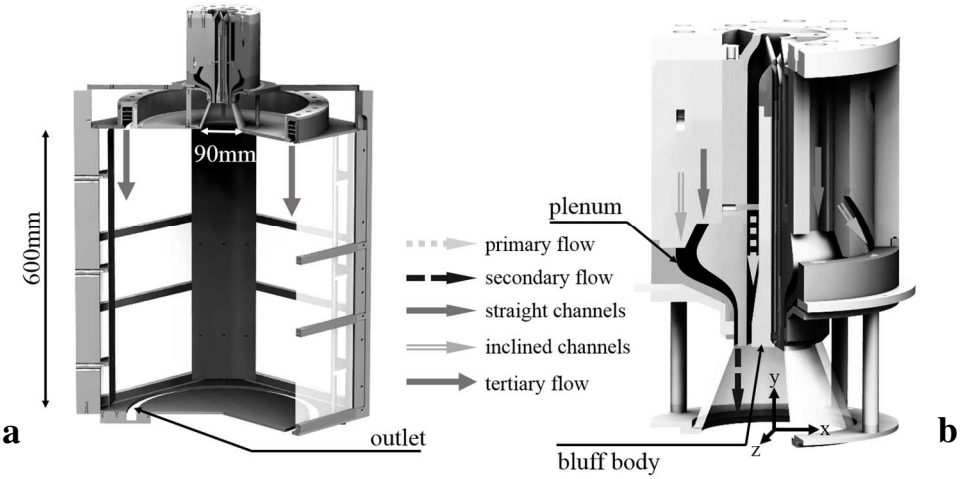

Figure 75: Sectional view of the oxyfuel combustor. ***(a)*** *Complete combustion chamber;* ***(b)*** *magnification of the burner region.*

tracer response. HCl was instead chosen as a tracer to measure the RTD during combustion.

Table 22 : relevant dimensions of the combustion chamber and details of the points of operation [111].

Quarl dimensions	[mm]	**Operation points**	**NRair / Rair**	**NR30 / R30**
Larger diameter, D	90	Oxidizer Air/O_2/CO_2 (vol%)	100/0/0	0/30/70
Smaller diameter, d	49.2	I CH_4 (m^3/h)	2.01 (only for **Rair**)	2.01 (only for **R30**)
Height	53	I Oxidizer (m^3/h)	13.55	8.16
Combustion chamber dimensions	[mm]	II Straight Oxidizer (m^3/h)	5.97	3.76
Length	600	II Inclined Oxidizer (m^3/h)	12.02	7.27
Width	420	III Oxidizer (m^3/h)	69.95	42.60
Depth	420			

4.2 Chemical Reactors Network

The data from the RTD measurements carried out in [64] are employed to fit a network of interconnected ideal flow reactors. Two operating conditions, concerning different operating atmospheres, are explored, both for non-reactive and reactive flow, Table 22. The reactors arrangements are presented, together with evidence from previous experiments or numerical simulations to support the CRN choice. The experimental fit is shown, together with a quantification of the numerical error. For the reactive case, a comparison between the kinetic output of the network and experimental data [129] is also carried out.

4.2.1 Non-reactive flow

Figure 76 guides the design of the CRN, shown in Figure 77 and Figure 78, based on zonal modelling of the flow. Figure 76.a shows the flow field of the non-reactive operation points [111], considering the quarl region (upper row), and a small part of the combustor at the exit of the quarl; while Figure 76.b shows flow streamlines of the entire combustor flow field, calculated for NRair [130], comprising a schematization that highlights the main mixing zones [130]. In the quarl zone, Figure 76.a, a small corner recirculation is present at the entrance of the inlet streams, not reproduced in Figure 76.b. The flow continues its path forming a lateral jet-like region, where segregated flow streamlines can be assumed, and a central IRZ, that recirculates flow from the jet region. Both identified flow features, the jet region

and the IRZ, continue further downstream the dump plane of the quarl. According to Figure 76.b, after the ensemble "jet-IRZ", follows a segregated region, that serves as post-flame zone under reactive conditions. After the quarl zone, there is introduction of oxidizer by means of the lateral inlets. They define a "dilution region", creating lateral recirculation zones. A mixed exit region is identified before the exit of the combustor. Given the symmetry of the system, a 2D model is adopted. Figure 77 and Figure 78 propose a simple schematization of the flow field.

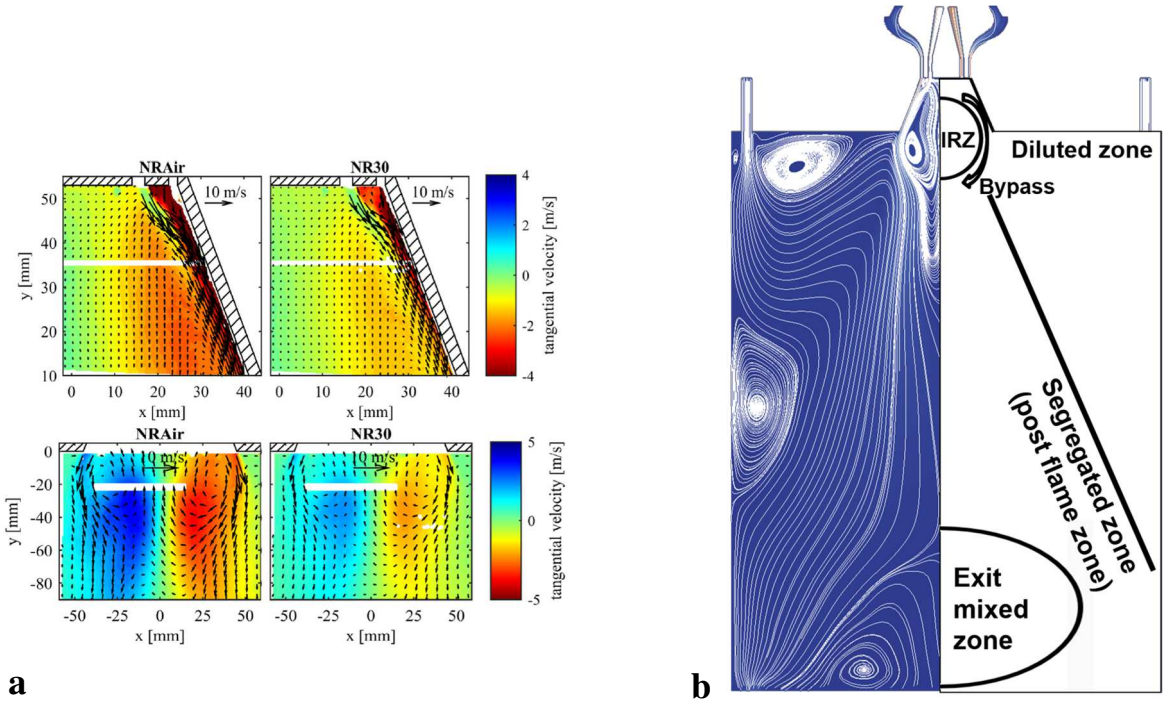

*Figure 76: **a**, flow field of non-reactive operation points* [111]*; **b**, CFD calculation of the mean flow field for NRair, comprising a schematization highlighting the main mixing zones* [130].

Figure 77 shows the CRN of the near-burner region of the OFC. It comprises the portion shown in Figure 76.a, equivalent to the bypass-IRZ part in Figure 76.b. As in the previous case 3.3.1, a PFR exemplifies the bypass region, where a preferential flow direction is identified. The corner RZ and the IRZ are regarded as mixed zones. After this entrance zone, a plug flow zone is identified until a final mixing zone. The dilution region is modelled as a series of PFRs in parallel with CSTRs, exemplifying the vortex-zones clear from Figure 76.b.

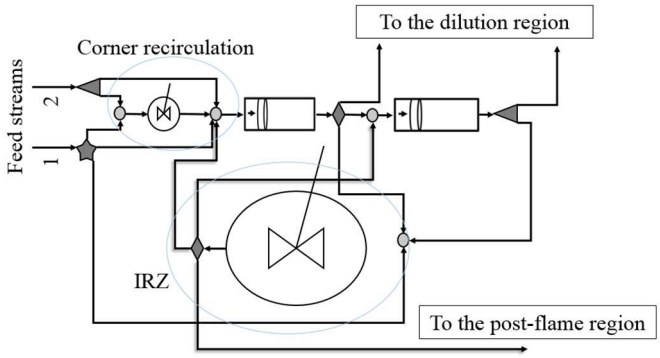

Figure 77: CRN of the near-burner region of the OFC. It comprises the portion shown in Figure 76.a, equivalent to the bypass-IRZ part in Figure 76.b.

The parameters to be optimized are the splitting ratios and the volumes of the mixing zones identified in the dilution region. As explained in 2.2.1, the mathematical model describing the mixing behaviour of the network is implemented in Matlab®, and the network superstructure reproduced in Simulink®. An

optimization routine is applied to retrieve the network parameters by means of the minimization of an objective function (more in 2.2.1).

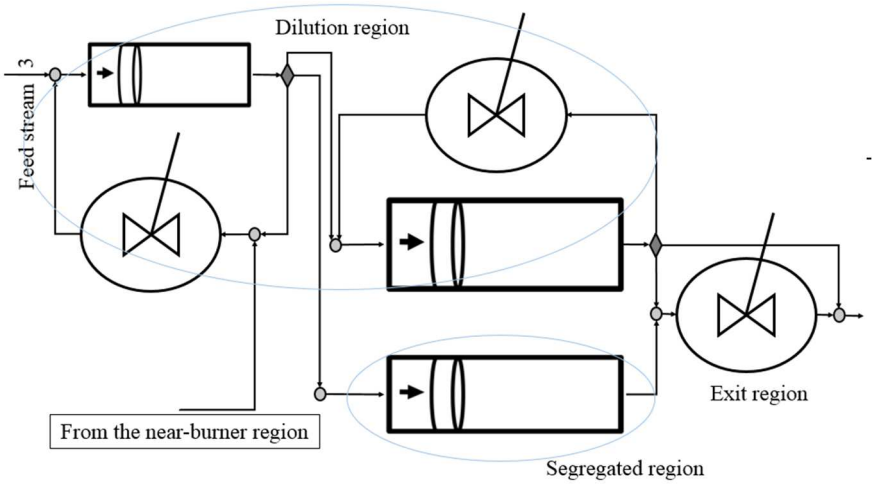

Figure 78: schematization of the combustor without the near burner region, Figure 77. The CM shown here comprises the segregated zone, the dilution zone and the exit zone in Figure 76.b.

4.2.1.1 Experimental fit

Figure 79 shows the dynamic response of the CRN after the parameter estimation via the optimization routine. It is superimposed to the experimental curve, and the residuals between the experimental tracer response and the CRN optimized response are reported. The Inlet Pulse is shown for graphical comparison, though scaled to the maximum of the plots for graphical reasons.

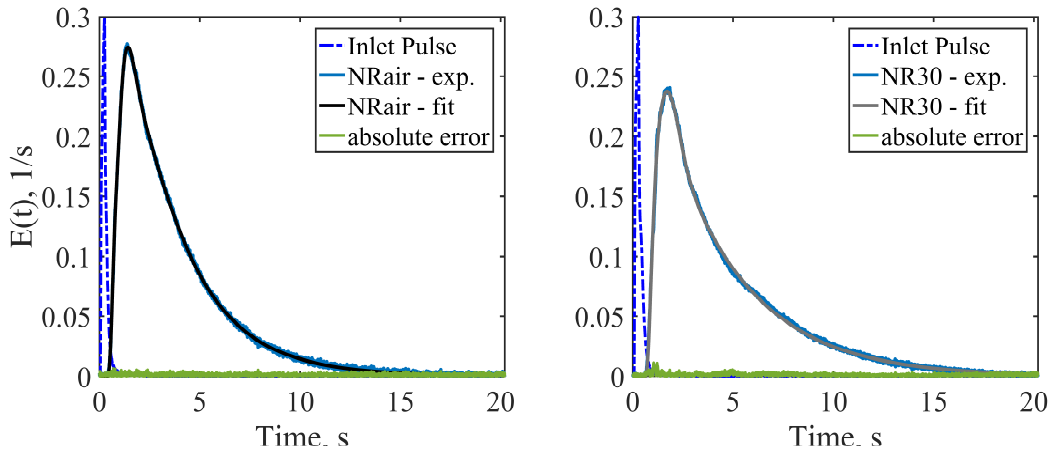

Figure 79: experimental RTD with superimposed CRN fit, NRair and NR30.

Figure 80 and Table 24 quantify the uncertainty of selected RTD parameters. The parameters used to carry out the comparison are defined below, in Table 23.

Table 23: parameters used to carry out the comparison between the operating atmospheres.

Parameter	Explanation		NRair – average fit
τ_1^m	Mean residence time inside the system.	τ_1^c	Convective time delay, time before the first arrival of the tracer.
σ_1^2	Variance of the distribution.	$\tau_i^{0.95}$, $\tau_i^{0.99}$	Time necessary for the 95% or the 99% of the tracer to exit the system.
S_1^3	Skewness of the distribution	$\frac{m_{IRZ}}{m_{in\_quarl}}$	Mass flow entrained into the IRZ, related to the mass flow fed to the quarl.

$\frac{m_{main\rightarrow dilution}}{m_{total\_feed}}$	Amount of mass flow from the main flow region to the dilution region, related to the total mass flow fed to the system	τ_{IRZ}	Mean residence time in the IRZ
$\frac{m_{dilution\rightarrow main}}{m_{total\_feed}}$	Amount of mass flow from the dilution region to the main flow region, related to the total mass flow fed to the system	$\frac{\tau_{dead}}{\tau^m}$	Residence time associated to dead zones in the system, related to the mean residence time inside the system.
$\frac{V_{dead}}{V_{tot}}$	Volume associated to dead zones in the system, related to the total volume of the system.		

Beside the main moments of the distribution (explained in 2.2), few network-derived parameters are proposed that are chosen to carry out the comparison between the different operating conditions in the following paragraph 4.3.1.

As in 3.3.1.1, the uncertainty was calculated fitting the network to the single-injection data. In this case, the experimental RTD was averaged from 50 single-injection curves. The proposed calculation considers only ten curves from this dataset, and NRair was chosen to carry out the analysis. Therefore, Figure 80 compares the fit of the average RTD, the one shown in Figure 79, with the single-injection fits. The standard deviation among the ten fits of the single injections is included.

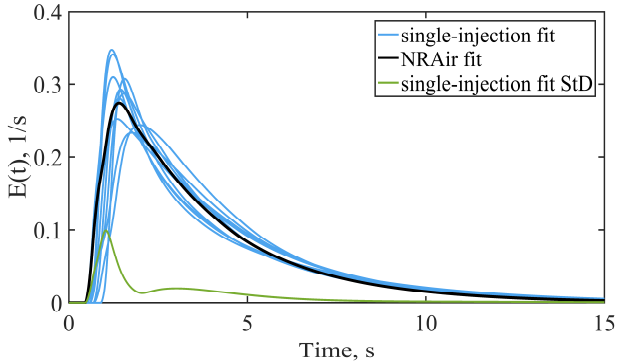

Figure 80: comparison among the fit of the average RTD and the fits of the single injection curves. The standard deviation among the ten single-injection fits is also proposed.

Table 24 reports the standard deviation among the ten single-injection fits. The parameters obtained from the fit of the average RTD (NRair in Figure 79) and the mean of the values of the same parameters calculated for each single injection (column "Mean values") is also compared. Globally, the mean value of the parameter coincides or close (in the calculated error) to the one calculated for the average fit. Larger errors are attributed to the use of 10 single-injections instead of 50.

Table 24: uncertainties associated with the CRN fit, NRair

	NRair – average fit	Mean values		NRair – average fit	Mean values
τ_1^m	3.8 ± 0.2	4.0	τ_1^c	0.4 ± 0.1	0.6
σ_1^2	8.09 ± 1	9	$\tau_1^{0.95}$	9.6 ± 0.5	10.3
S_1^3	1.75 ± 0.09	1.71	$\tau_1^{0.99}$	14.1 ± 0.7	14.8
$\frac{m_{main\rightarrow dilution}}{m_{total\_feed}}$	0.21 ± 0.04	0.22	$\frac{m_{IRZ}}{m_{in\_quarl}}$	1.4 ± 0.2	1.6
$\frac{m_{dilution\rightarrow main}}{m_{total\_feed}}$	0.79 ± 0.07	0.84	τ_{IRZ}	0.076 ± 0.006	0.067
$\frac{V_{dead}}{V_{tot}}$	0.33 ± 0.03	0.35	$\frac{\tau_{dead}}{\tau^m}$	0.5 ± 0.1	0.6

Once the network was calibrated against the measured tracer response, the response of the system was calculated using as input signal an ideal numerical pulse, instead of the experimental one. As in 3.3.1.1, the aim was to check whether it was more appropriate to employ distributions generated by an ideal signal in order to properly describe the observed phenomena. As shown in Figure 81, the experimental pulse gives rise to a distribution that is very close to the one generated by an ideal pulse. Differently from the SSGT, the tracer response and the RTD coincide in this case. As shown in both Figure 79 and Figure 81, the experimental pulse is sharp compared to the subsequent distribution, fulfilling the condition for an appropriate pulse input to be far shorter than the mean residence time in the system. Furthermore, the amount of dispersion between injection point and reactor entrance must be negligible. These conditions are satisfied by the present experiment [64]. Therefore, the tracer response directly yields the $E(t)$ of the combustor. For this reason, it will be employed in the following discussion without further processing.

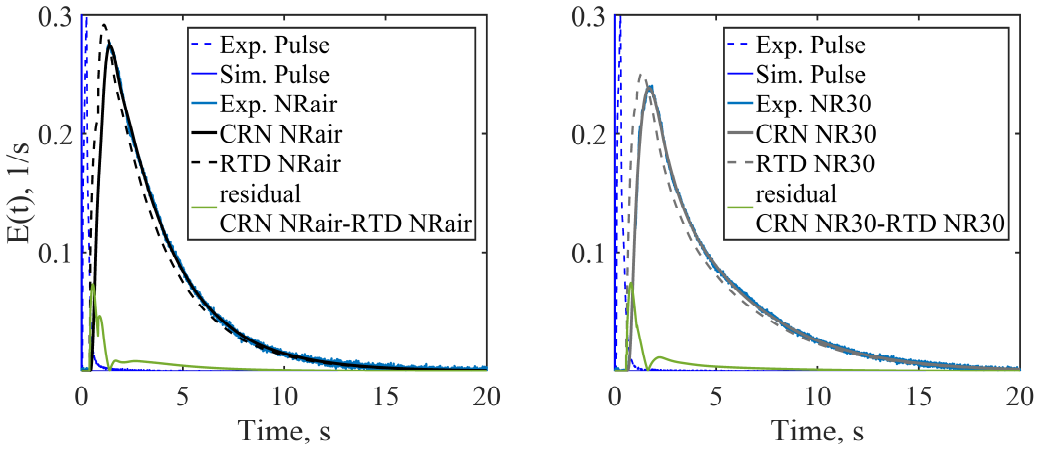

Figure 81: experimental RTD with superimposed CRN fit, NRair and NR30.

4.2.2 Reactive flow

The CRN designed to model the reactive flow exhibits a slight modification with respect to the one presented in 4.2.1. As for the SSGT case, par. 3.3.2, an additional zone was added, splitting the IRZ volume. This additional zone has the aim of representing, even if by means of a gross schematization, a high temperature region approximately schematizing the flame zone, Figure 82. Only the modified near-burner region is shown.

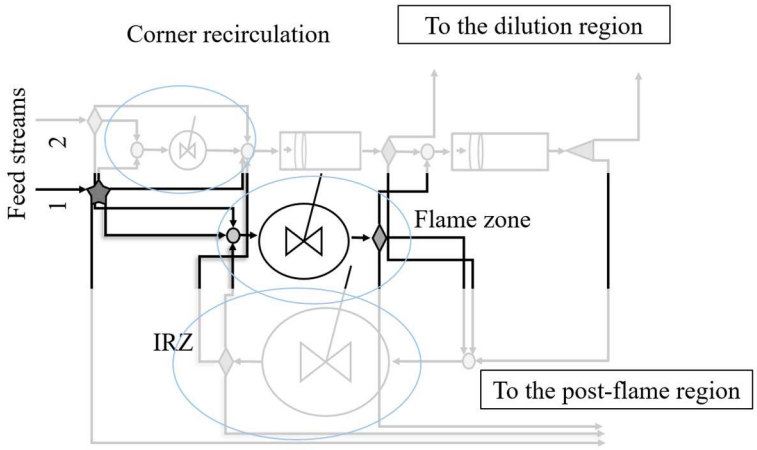

Figure 82: modification to the near-burner region (Figure 77) to take chemical reaction into account.

Indeed, par. 1.2, swirling flows encourage the stabilization of the flame in the shear layers delimiting recirculation zones. Given the existence of a zone yielding high temperatures and high species formation rate, it is incorrect to not take it into account while examining the reactive case. Therefore, a zone

referred to as “flame zone” is added to the CRN, in the near burner region. It is represented by a CSTR, due to the high turbulence levels and the mixing associated with the swirl motion. The rest of the CRN remains the same, and it is based on the flow features discussed in 4.2.1. An important characteristic of reactive swirling flows is the reduction of the size of the internal recirculation zone due to the higher flow momentum, with respect to non-reactive flow [116]. As the definition of the CRN volumes is crucial, as stated also in [62], Figure 83 aided the sizing of the zones for reactive conditions.

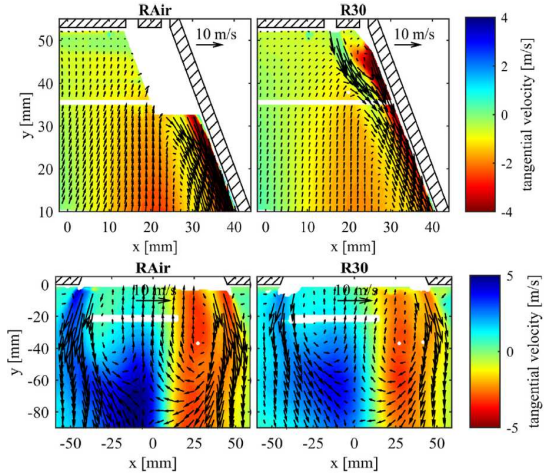

Figure 83: flow field of reactive operation points [111].

4.2.2.1 Experimental fit

Figure 84 shows the dynamic response of the CRN after the parameter estimation via the optimization routine. It is superimposed to the experimental curve, and the residuals between the experimental tracer response and the CRN optimized response are reported. The Inlet Pulse is shown for graphical comparison, though scaled to the maximum of the plots for graphical reasons.

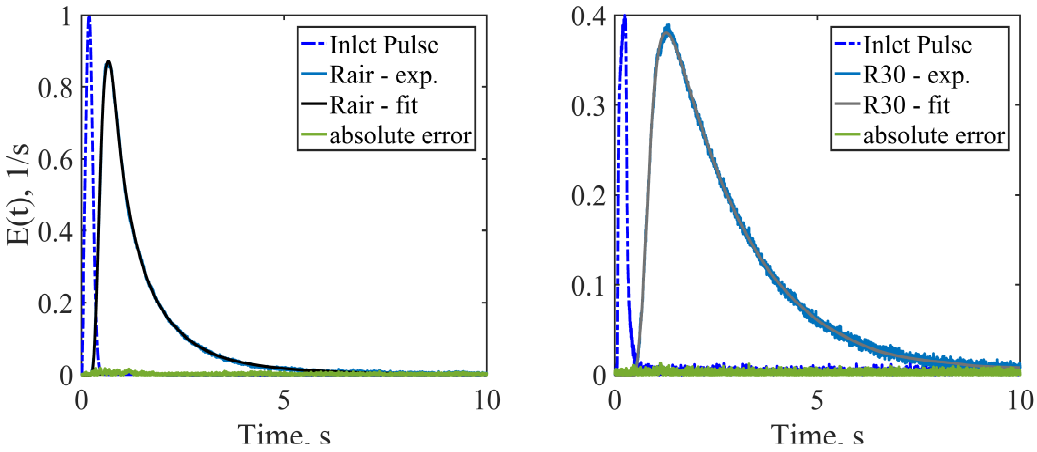

Figure 84: experimental RTD with superimposed CRN fit, Rair (left) and R30 (right).

Table 25 contains the uncertainties associated to selected fit-derived parameters. These parameters are chosen to carry out the comparison on the impact of the oxidizer on the flow and reacting field, 4.3.2.

Table 25: uncertainties associated with the CRN fit, Rair

	Rair – average fit	Mean values		Rair – average fit	Mean values
τ_1^m	1.5±0.2	1.6	τ_1^c	0.25±0.05	0.26
σ_1^2	1.7±0.5	1.6	$\tau_1^{0.95}$	4.1±0.5	4.0
S_1^3	2.8±0.2	2.8	$\tau_1^{0.99}$	7±1	7
$\frac{m_{main\rightarrow dilution}}{m_{total\_feed}}$	0.21±0.04	0.22	$\frac{m_{IRZ}}{m_{in\_quarl}}$	0.50±0.09	0.55
$\frac{m_{dilution\rightarrow main}}{m_{total\_feed}}$	0.54±0.09	0.62	τ_{IRZ}	0.026±0.004	0.022
$\frac{m_{dead}}{m_{tot}}$	0.8±0.1	0.8	$\frac{m_{flame}}{m_{in\_quarl}}$	0.4±0.1	0.3
$\frac{V_{dead}}{V^{tot}}$	0.31±0.05	0.31	τ_{flame}	0.002±0.002	0.003

As in the previous paragraph, 4.2.1, uncertainty was calculated fitting the network to ten single-injections measured distribution curves out of fifty. Rair was chosen to carry out the analysis. Figure 85 compares the fit of the average RTD (Figure 84) and the fits of the ten considered single injection curves. The standard deviation among the ten single-injection fits is also proposed.

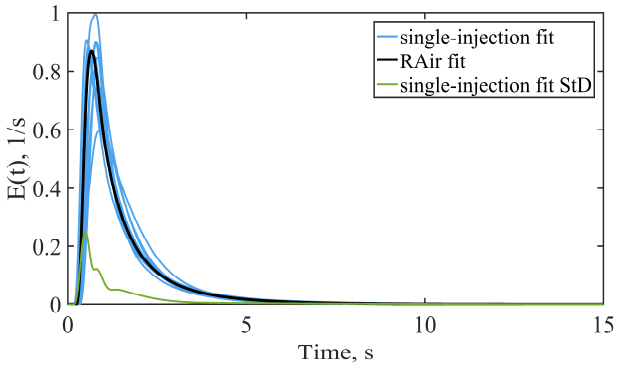

Figure 85: comparison among the fit of the average RTD and the fits of the single injection curves. The standard deviation among the ten single-injection fits is also proposed.

Table 26 shows the comparison between experimental data [129] and the species concentrations calculated from the CRN after optimization, 35 mm above the exit plane of the combustor. This measurement location is taken as comparison because it is easily recognized as belonging to a determined reactor-zone inside the combustor, namely the mixed exit zone. The GRI 3 kinetic mechanism was used to carry out this analysis because the complete C1C3 mechanism was not reaching convergence. The chance of this issue happening has been pointed out before, paragraph 3.3.2.3. Owing to the similar prediction shown in 3.3.2.3, the GRI 3 mechanism has been employed in the following to calculate species formation in the OFC.

Table 26: comparison between experimental data [129] *and CRN-predicted species concentration near the exit of the combustor.*

	CO, ppm		$CO_2, mole\ fraction$		$H_2O, mole\ fraction$		CH_4, ppm	
	CRN	Exp.	CRN	Exp.	CRN	Exp.	CRN	Exp.
Rair	1140	1300	1.90×10^{-2}	1.9×10^{-2}	4×10^{-2}	3.9×10^{-2}	559	570
R30	107	~ 40	71×10^{-1}	72.5×10^{-1}	6.2×10^{-2}	6.1×10^{-2}	61	< 60
	$O_2, mole\ fraction$							
Rair	16.5	16.6						
R30	22.9	22.4						

The agreement is good for Rair, for all the species considered. R30 shows an overall good agreement for all the species except CO. In this case, the model overestimates its value, and this overestimation is mirrored by the lower CO_2 mole fraction value. CO is one of the species with the highest sensitivity to the flow field characteristics. It is possible that the present model, even if properly calibrated, in order to catch all the main mixing features, slightly overestimates the mixing with the dilution region. This region has a low temperature compared with that of the main flow path, and, as shown in par. 4.3.2, its CO content is high because of the quenching of the reactions at low temperatures. If a higher share of reacting flow carrying CO is entrained in the cold side zone, a higher amount of CO will be quenched and available for mixing along the combustor coordinate. Despite this discrepancy, the overall suitability of the model to reproduce the RTD and the reactive features of the combustion chamber has been proven: there is indeed a higher CO prediction for R30, but the significant CO reduction compared to Rair is correctly reproduced. The model is employed in 4.3.2 to draw conclusion on the behaviour of the system while changing the oxidizer.

4.3 Results and discussion

In the following, the impact of the operating atmosphere on the behaviour of the OFC is retrieved. First, the effect on the cold flow is described, par. 4.3.1, followed by comments on the reactive flow as well, par. 4.3.2.

4.3.1 Non-reactive flow – effect of the oxidizer

The RTDs retrieved by means of the CRN fit are shown superimposed to each other in Figure 86, to describe the mixing behaviour of the combustor while operating under different atmospheres. The main three moments of the distributions are reported in Table 27. Selected flow parameters are reported as well, to aid the description of the results.

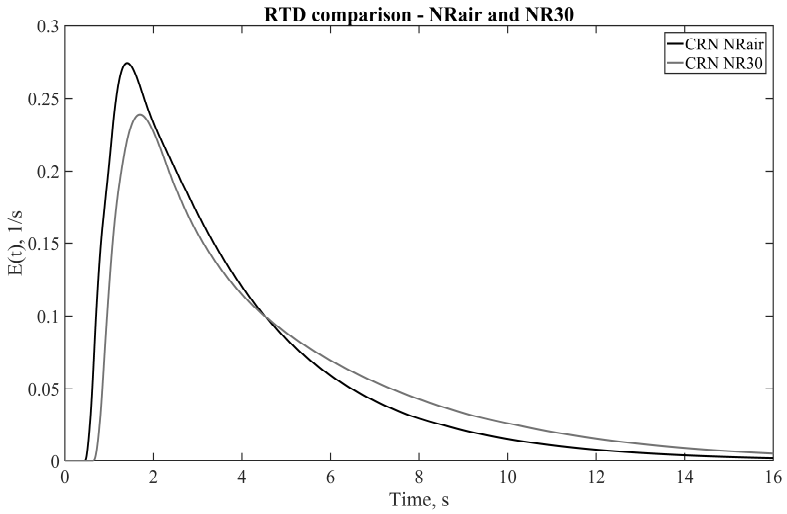

Figure 86: comparison between the CRN fit for NRair and NR30.

From Figure 86, the NR30 appears delayed with respect to NRair, and generates a broader distribution of residence times. Accordingly, a higher τ^m is calculated for oxyfuel atmospheres. These features agree with the lower mass flow rate fed to the system in this case, Table 22. Therefore, a lower bulk velocity is associated with NR30, justifying the delayed arrival of the tracer to the detection point. The lower velocity is also responsible for a greater share of the combustor volume associated to the IRZ, as evident from Figure 76.a. In this recirculation zone, more mass flow is entrained for the oxyfuel atmosphere with respect to the mass flow fed to the quarl zone, $\frac{m_{IRZ}}{m_{in\_quarl}}$. This effect is balanced by the larger IRZ volume, resulting in a higher value of the recirculation time in this zone, τ_{IRZ}. The amount of mass flow

exchanged between main flow path and the dilution zone with respect to the total mass flow fed to the combustor, $\frac{m_{main\rightarrow dilution}}{m_{total\_feed}}$, is approximately the same for both operating conditions, slightly higher for NRair. On the other hand, the amount of mass flow exchanged between the dilution zone and the main flow path, $\frac{m_{dilution\rightarrow main}}{m_{total\_feed}}$, is higher for oxyfuel atmospheres. This is likely an explanation for the longer oxyfuel distribution: the recirculation zones identified in the dilution region of the combustor (Figure 76.b) present the higher residence times in the system and are therefore regarded as dead volume zones. This is in agreement with observations from [63]. As these dead zones cause longer local residence times, the mass flow from these zones has experienced a high mixing time, and its tracer concentration is severely broadened. A higher percentage of this heavily mixed flow is then transported into the main flow for NR30, causing the stretch of the tail of the oxyfuel distribution. The ratio of the dead time, $\frac{\tau_{dead}}{\tau^m}$, to the mean residence time corroborates this hypothesis.

Table 27: global properties of the RTDs and CRN-fit parameters, NRair and NR30

	NRair	NR30		NRair	NR30
τ_1^m	3.8	4.7	τ_1^c	0.4	0.7
σ_1^2	8	12	$\tau_1^{0.95}$	9.6	11.9
S_1^3	1.75	1.48	$\tau_1^{0.99}$	14.1	16.5
$\frac{m_{main\rightarrow dilution}}{m_{total\_feed}}$	0.21	0.17	$\frac{m_{IRZ}}{m_{in\_quarl}}$	1.4	1.6
$\frac{m_{dilution\rightarrow main}}{m_{total\_feed}}$	0.79	0.85	τ_{IRZ}	0.077	0.084
$\frac{V_{dead}}{V_{tot}}$	0.33	0.30	$\frac{\tau_{dead}}{\tau^m}$	0.4	0.6

4.3.2 Reactive flow – effect of the diluent

The RTD-fits obtained after optimizing the parameters of the reactive CRN for both operating atmospheres are compared in Figure 87. Table 28 contains the value of the three principal moments of the RTDs and selected parameters chosen to aid the comparison between the two operating conditions. What clearly emerges is the huge difference between the spread of the two distributions, and the strong resemblance between R30 and *N*R30 (shown in Figure 86). Referring to Figure 86, the maximum value of the distribution corresponding to *N*R30 is around 0.25 s^{-1}; and the one corresponding to R30 is around 0.4 (Figure 87). Instead, the two maxima corresponding to *N*Rair (around 0.275) and Rair (around 0.9) are distant from each other, as expected when comparing a cold flow distribution to a reactive flow one (higher temperatures). The broadening of the R30 distribution is the cause of the higher τ_1^m and σ_1^2, Table 28. Both distributions are right skewed.

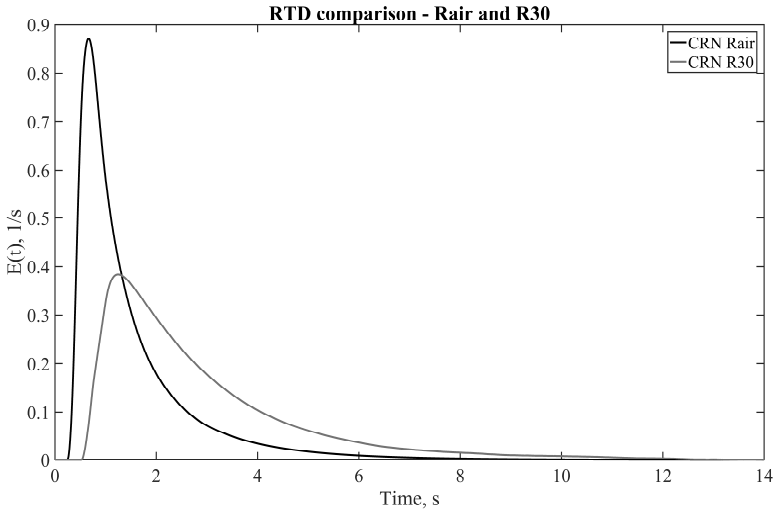

Figure 87: comparison between the CRN fit for Rair and R30.

The first cause for the broader distribution found for R30 is the lower mass flow introduced into the system in this case, compared to Rair. For this reason, higher residence times are associated with the oxyfuel atmosphere, despite the higher measured temperatures [129] that should translate to a faster flow [116] in virtue of the thermal expansion. In addition to the lower amount of mass fed to the system, a higher entrainment in recirculation zones has been calculated from the model for R30. The parameter $\frac{m_{IRZ}}{m_{in\_quarl}}$ is one order of magnitude higher when feeding the O_2/CO_2 as oxidizer, while the amount of mass flow entrained in the lateral recirculation zones, $\frac{m_{V_{dead}}}{m_{total\_feed}}$, is doubled. Therefore, a higher share of the flow experiences strong mixing inside the system, broadening the distribution. The parameters $\frac{m_{main\rightarrow dilution}}{m_{total\_feed}}$ and $\frac{m_{dilution\rightarrow main}}{m_{total\_feed}}$ present similar values in both cases, differently from the non-reactive case.

Table 28: global properties of the RTDs and CRN-fit parameters, Rair and R30

	Rair	R30		Rair	R30
τ_1^m	1.5	2.9	τ_1^c	0.25	0.52
σ_1^2	1.7	3.8	$\tau_1^{0.95}$	4.1	7.0
S_1^3	2.8	1.9	$\tau_1^{0.99}$	7	10
$\frac{m_{main\rightarrow dilution}}{m_{total\_feed}}$	0.21	0.23	$\frac{m_{IRZ}}{m_{in\_quarl}}$	0.50	1.38
$\frac{m_{dilution\rightarrow main}}{m_{total\_feed}}$	0.54	0.50	τ_{IRZ}	0.026	0.012
$\frac{V_{dead}}{V_{tot}}$	0.31	0.22	$\frac{m_{flame}}{m_{in\_quarl}}$	0.4	0.6
$\frac{m_{V_{dead}}}{m_{total\_feed}}$	0.8	1.4	τ_{flame}	0.002	0.002

The impact on the kinetic behaviour of the system is addressed in the following, Figure 89. The coordinates refer to the coordinate system introduced in Figure 75.b, and the selected profiles are clarified in Figure 88.

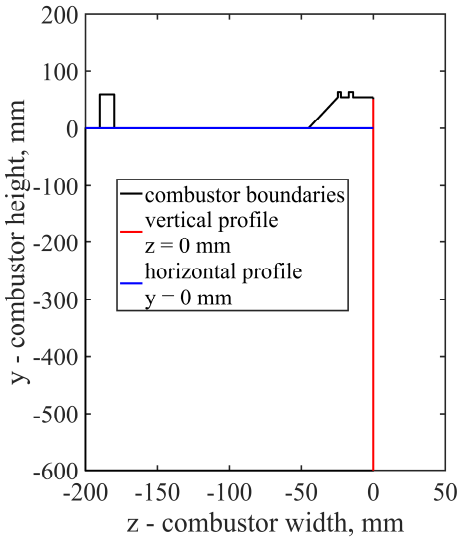

Figure 88: sketch of the lower half of the OFC. The horizontal (blue) and vertical (red) profiles used to show species formation under different operating conditions are highlighted.

The vertical profile in Figure 89 is taken along a central vertical line passing through the combustor starting from the inlet of the quarl until the exit plane (red line in Figure 88). The horizontal profile follows a line cutting the combustor horizontally just below the exit of the quarl (blue line in Figure 88). In Figure 89, the upper row shows the temperature along the vertical centreline of the combustor (right side) and the horizontal line at the dump plane of the quarl, the middle row presents the CO mole fraction, followed by the methane mole fraction in the third row and the oxygen mole fraction in the lower row. Starting the description from the vertical profile, the first, flat part of all shown quantities (temperature, CO mole fraction, CH_4 mass fraction O_2) corresponds to the IRZ. Follows the PFR post-flame region, and the last flat part representing the exit stirred region. The CRN fit temperatures Figure 89, vertical profile, upper row) do not significantly differ in the IRZ, and their value is around 1800 K for both atmospheres. The CO mole fraction in this region is higher for R30, but the intense mixing and reaction encouraged by the IRZ is clear: the values are below 500 ppm, and no methane is present in this zone. In the post-flame region, the behaviour is similar at the beginning, though yielding different concentration values, and then differs for the two examined cases. More in detail, for Rair the CO concentration experiences a sharp rise, due to the combined effect of direct transport of flow from the reaction regions and from the side dilution region (~ 50-200 mm part of the horizontal profiles). The amount of carbon monoxide decreases until the temperatures are high enough to promote the reactions (> 1000 K), and then increases again as the low temperatures freeze the reactions and the CO that is formed is no longer oxidized to CO_2. R30 exhibits a slightly different situation: the CO content experiences as well an increase due to transport from CO-rich zones, but the intensity of this peak is approximately one order of magnitude lower than the one calculated for Rair, despite the higher fuel to oxidizer ratio that characterizes R30 (Table 22). This behaviour is attributed to several factors. The first one is the higher $\frac{m_{flame}}{m_{in\_quarl}}$ found for the oxyfuel atmosphere, Table 28: a higher share of the inlet mass flow in entrained in the high temperature CSTR used to simulate the flame region, meaning that less is available to react at a later stage in the system. Also, the higher temperatures enhance CO consumption, encouraging its reaction in the near-burner region (horizontal profile, ~30-50 mm). Furthermore, the model predicts a lower fuel-slip amount for R30, in accordance with [129], where the conclusion was based on species measurements. Due to the lack of reactive species and the slightly higher temperatures, the content of carbon monoxide decreases along the post-flame PFR, and decreases further in the exit region CSTR, owing to further mixing with the dilution mixture as well. It is worth comment about the occurrence of fuel slip in the system. The model includes a flow split parameter that pushes flow from the quarl region to the post-flame region. This parameter is one order of magnitude lower for R30, meaning that the reaction consumes almost all the available reacting mixture. This is the explanation

behind the different behaviour of the CO profile in the different operating conditions. The oxygen concentration is also reported. According to the vertical profile, the mixing and reaction lower its concentration in the IRZ, but it increases again in the post-flame region because of the mixing of flow from the dilution region. From this point on, this concentration remains rather constant for Rair and exhibits a slight decrease for R30, mainly attributed to the mixing from the side region.
The horizontal profile has partially already been introduced, to complement the observation of the phenomena along the vertical one. Its right part shows, once again, the species content in the IRZ. Then, the plot coordinate passes the reaction zone and the bypass. In the latter zone, there is a clear difference between Rair and R30: the CO and CH_4 content is significantly higher for Rair, meaning that the reaction is proceeding slower with respect to R30, whose CO and CH_4 content is significantly lower, because the reaction has already proceeded towards CO_2 formation. The oxygen content for Rair is lower as well, compared to the O_2 concentration calculated for the oxyfuel atmosphere.

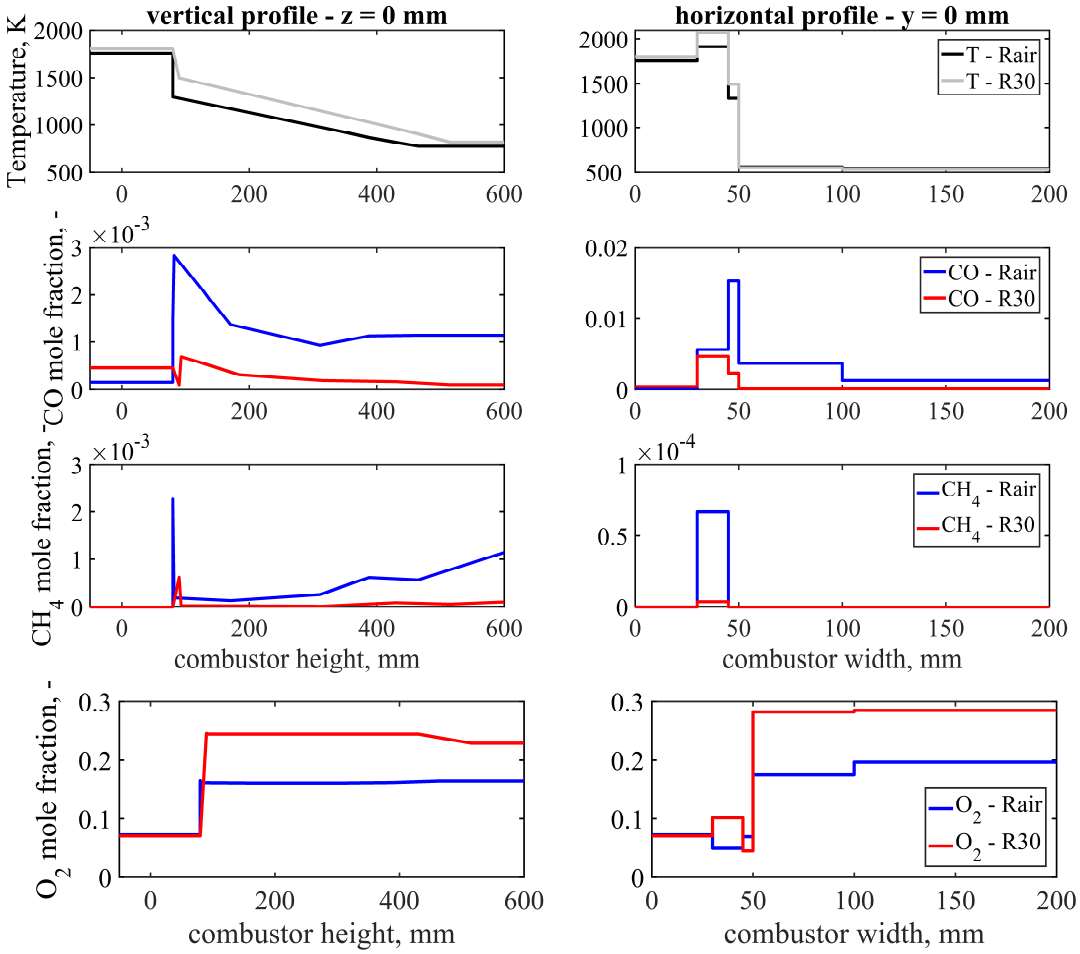

Figure 89: impact of the oxidizer on temperatures (CRN-fit) and species formation. Upper row: temperature along the vertical centreline of the combustor (right side) and the horizontal line at the dump plane of the quarl. Second row: CO mole fraction. Third row: CH_4 mole fraction. Fourth row: O_2 mole fraction.

4.4 Summary

In this chapter, CRN modeling calibrated against the RTD of the system has been applied to a close to reality configuration designed to operate gas, as well as gas-assisted coal flames, using air or oxyfuel mixtures as oxidizers. In this way, a better understanding of combustion under oxyfuel conditions is gained by comparing the results to those obtained in air. The modeling was applied to both non-reactive

and reactive flows, and two operating conditions were tested: one employing air and the other employing an oxyfuel mixture as oxidizer.
The RTD of the oxyfuel case is always broader with respect to the one measured in air. This is caused by the more intense entrainment in recirculation regions experienced by both $NR30$ and $R30$ with respect to the "air" counterparts. This different behaviour is attributed both to the different mass flow rate introduced in the system, and the different molecular weight of the oxyfuel mixture.
$R30$ yields as well the lowest CO production and CH_4 emission, meaning higher fuel burnout. This is due to the higher share of reactive mixture entrained in the zone used to exemplify the high temperature reaction zone and the higher temperatures, that ensure that most of the reactants are consumed in the near burner region.
In this chapter, a CRN - properly calibrated against the RTD of the system under different operating conditions - enabled the study of species formation along selected profile in a close-to-reality configuration while varying the oxidizer from air to a mixture composed by CO_2 and O_2. The significant role of these simple and flexible tools is stressed once again: the importance of CFD is increasing over the years, and a computational technique like LES is gaining more and more attention. Still, the huge computational effort needed and their complexity, makes these numerical model much more difficult to adapt in order to obtain a fast estimation of the crucial parameters that characterize a certain system [130].

5 Summary and Outlook

The aviation transportation and power generation sectors are experiencing an increasing demand. Combustion is the main source of energy for both sectors, and the push towards greater efficiencies and drastic reduction of pollutant emission is strong. Therefore, combustion-based devices should be continuously optimized and new concepts should be considered and tested.

At the beginning of this work, two combustion concepts were identified, that deserve further attention because they are able to achieve efficient processes while limiting pollutants emissions. According to the interest towards both aviation transportation and power generation, two concepts applicable to these cases were investigated. More in detail, lean combustion coupled with effusion cooling was considered for the improvement of aviation gas turbine combustors, and oxyfuel combustion was considered for the improvement of stationary power generation devices. The need for further investigation on these concepts in close to reality configurations was stressed. These configurations enable the study of practical combustion processes on a smaller scale. The application of simple and flexible tools to complement and extend the understanding gained through experiments is crucial.

Therefore, after a brief introduction about the basics of combustion phenomena, two modeling strategies were outlined, and one of them chosen: Chemical Reactors Network modeling was chosen based on the need to use a tool that is simple, and with the possibility to implement detailed kinetic mechanisms.

In the second chapter, Residence Time Distribution theory: among the several strategies to apply the Chemical Reactors Network strategy, Residence Time Distribution was found to be suitable to guide the design and calibration of the network. Furthermore, a reactors network obtained from the residence time promotes a strong synergy between experiments and modeling. The methodology followed in this work was introduced later in the chapter, together with the tools employed.

The third chapter was dedicated to an extensive investigation on a single sector gas turbine model combustor designed at Technische Universität Darmstadt. Experiments were carried out on this test rig to measure the residence time distribution inside the system. Then, a network was designed and calibrated against measurements results. The networks designed to reproduce the mixing and chemical reaction phenomena have been presented and explained, and several parameters chosen to carry out the comparison among the different operating conditions explored. After the calibration of the network against experimental results, detailed kinetics was applied in the reactive cases. The results of the network after a kinetic evaluation yielded a good overall agreement with available experimental data on CO concentration, along selected profiles inside the combustor. Therefore, the network of reactors was considered suitable to model the impact of the different operating conditions on pollutants formation.

After the experiments and the modelling on the gas turbine combustor, another experimental facility was taken into account: a scaled down version of a combustor for power generation suitable to burn coal as well as gaseous mixtures, using either air or oxyfuel as oxidizing atmospheres. Residence time distribution measurements were already available in this case and were exploited to achieve a network of interconnected reactors. As before, after a verification of the model performance in terms of species concentrations, the model was used to gain insight into the combustion process. The differences between oxyfuel-flames were commented exploiting the comparison with air flames.

To summarize this work, Chemical Reactors Network modeling based on the measured Residence Time Distribution of the flow has been applied in two close-to-reality configurations designed at TU Darmstadt. Experiments and subsequent modeling were carried out in a single sector gas turbine model combustor, and modeling of existing experimental data was applied to a scaled-version of an oxyfuel combustor. In both cases, the designed networks yielded a good agreement with available experimental data on species concentration. Therefore, the models developed in this work have been employed to assess the impact of the boundary conditions on the combustion process in terms of distribution of residence times and species concentration.

5.1 Scientific Contribution

Residence Time Distribution is an intrinsic flow quantity crucial to gain insight into the essential features of the flow dynamics. Residence Time Distribution data are also the starting point to design a network of properly interconnected ideal flow reactors to schematize the flow features in a complex configuration, like a practical combustion system. This coupled investigation strategy, promoting a strong synergy between experiments and modeling of the observed phenomena, has been applied in this work. Residence Time Distribution was measured in a gas turbine model combustor, that mimics the features of aviation gas turbine combustor, under realistic boundary conditions.

With respect to previous works, a larger variety of operating conditions was explored, considering both non-reactive and reactive flow fields.

Furthermore, despite the large usage of Residence Time Distribution as a valuable investigation tool, few attempts have been made to couple it with Chemical Reactors Network in order to apply detailed kinetics in the system under investigation [57], [58].

In the present work, an overall good agreement with experiments despite the use of macro-mixing zone/reactors has been achieved for both investigated configurations. Where the availability of experimental data allowed the comparison, the model results in terms of species concentration was found in good agreement with the experiments along selected profiles inside the system.

These results enabled the further exploitation of the developed networks to deepen the understanding of the impact of the boundary conditions on the combustion process.

5.2 Future research

In view of the insight that can be gained, coupling RTD studies with CRN models is a modeling strategy that should be further applied. A next step with respect to the present work is the inclusion of chemical kinetics in the optimization procedure, at the fitting stage of the CRN response to the experimental tracer response. To this aim, the necessary tools should be improved in terms of both efficiency and robustness. At the present stage, a coupled mixing-chemical reaction optimization was not possible in view of the calculation time required by the RNA code. Each kinetic calculation of the CRNs was taking, on average, few hours for the C_1C_4 mechanism, and few minutes for the GRI 3 mechanism. Both calculation times are far too long to be included in the optimization procedure. However, simplified kinetic mechanisms can be conceived and adapted for the RTD optimization and employed in the optimization phase, to guide the parameters evaluation.

Another point of interest concerns the possibility to carry out sensitivity studies without the need of configuration-specific tuning parameters. Usually, the common procedure designs a network on a given operating condition, and the network is then employed to carry out sensitivity analysis without tuning the model again. In this work, it has been shown that a different operating condition might yield a value of the parameters that is very different from the parameters calculated for the reference condition. Therefore, a comprehensive investigation of RTD in practical combustor under a large variety of operating conditions might be crucial to retrieve relationships to calculate the value of a certain parameter in a different situation.

Furthermore, an interesting suggestion about the exploitation of CRN comes from [106], [107], that suggests and shows the proof of concept for live monitoring of combustion using a CRN. The network is kept simple and it receives on-line information from the control program of the experimental test rig. This idea would fit well a modeling strategy based on the coupling of the RTD and the CRN. Once a robust model and optimization procedure has been established for a certain apparatus, online RTD-derived CRN could be generated via an optimization. This would link the original usage of the RTD, namely performance evaluation and troubleshooting of chemical reactors, to an online CRN fitting procedure to monitor the combustion process.

Appendix A

Example of Chemical Reactors Networks trials

The reactive network designed in 3.3.2 is the results of several tests carried out to properly describe the mixing features of the SSGT in the presence of combustion. Here, the CO prediction results of two tests are reported, as examples of this sensitivity analysis studies. Referring to Figure 90, the results of simulations with the RNA software and the C_1C_4 mechanism are reported. The CRN referred to as "network simple" is the same used to model the cold flow, see Figure 20 and Figure 21. Though the good quality of the with experimental RTD, the agreement with experiments in terms of CO is poor. It stems from the absence of a high temperature reaction zone, where high CO levels are produced. The CRN indicated as "network complex" is oriented toward a "flame modeling" approach [82], though on a simplified level. In this "network complex" the flame had been taken as a thin sheet between the jet region and the IRZ. Its value was estimated by OH LIF available data [18]. As obvious, this solution was not able to provide the desired agreement with the available experimental data. In this case, the CO amount is even lower, attributed to the high fuel and CO consumption in the speculated reaction zone prior the arrival in the IRZ.

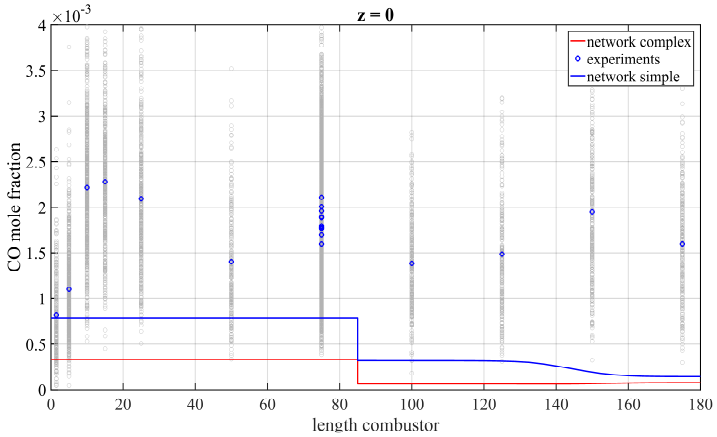

Figure 90: comparison between network prediction and experiments for other tested network models.

References

[1] World Energy Council, “World Energy Resources: 2013 survey,” 2013.

[2] “Intergovernmental Panel on Climate Change. Climate Change 2014: Synthesis Report. Contribution of Working Groups I, II and III to the Fifth Assessment Report of the Intergovernmental Panel on Climate Change. IPCC, Geneva, Switzerland 2014;2014:151 pp.”

[3] International Energy Agency, “Energy and Air Pollution,” 2016.

[4] F. Ommi and M. Azimi, “Most effective combustion technologies for reducing Nox emissions in aero gas turbines,” *Int. J. Multiphys.*, vol. 6, no. 4, pp. 417–424, 2012.

[5] D. Dunn-Rankin, Ed., *Lean combustion: technology and control.* Academic Press, 2001.

[6] A. Schulz, “j.1749-6632.2001.tb05848.x.pdf,” *Ann. N. Y. Acad. Sci.*, vol. 934, no. 1, p. 135.146, 2001.

[7] B. M. Abraham, J. G. Asbury, E. P. Lynch, and A. P. S. Teotia, “Coal-Oxygen Process Provides CO2 for Enhanced Recovery.,” *Oil Gas J.*, vol. 80, no. 11, 1982.

[8] “Intergovernmental Pannel on Climate Change. Carbon Capture and Storage. Technical report.,” 2005.

[9] R. B. Bird, W. E. Stewart, and C. Lightfoot, *Transport Phenomena*. New York: John Wiley, 1960.

[10] J. D. Busckmaster and G. S. Ludford, *Theory of Laminar Flames*. Cambridge University Press, 1982.

[11] D. E. Rosner, *Transport Processes in Chemically Reacting Flow Systems*. Boston: Butterworths, 1986.

[12] O. Reynolds, “An experimental investigation of the circumstances which determine whether the motion of water shall be direct or sinuous and the law of resistance in parallel channels.,” *Phil. Trans. R. Soc.*, no. 174, 1883.

[13] L. F. Richardson, “The supply of energy from and to Atmosheric Eddies,” *Proc. R. Soc. Math. Phys. Eng. Sci.*, vol. 97, no. 686, pp. 354–73, 1920.

[14] A. Kolmogorov, “The local structure of turbulence in incompressible viscous fluid for very large Reynolds Numbers.,” *Dokl. Acad. Nauk SSSR*, no. 30, pp. 301–305, 1941.

[15] J. F. Griffiths and J. A. Barnard, *Flame and Combustion. CRC Press, 1995.* 1995.

[16] N. Syred and J. M. Beér, “Combustion in Swirling Flows: A Review,” *Combust. Flame*, vol. 23, pp. 143–201, 1974.

[17] D. G. Lilley, “Swirl Flows in Combustion: A Review,” *AIAA J.*, vol. 15, no. 8, 1977.

[18] J. Hermann, M. Greifenstein, B. Boehm, and A. Dreizler, “Experimental Investigation of Global Combustion Characteristics in an Effusion Cooled Single Sector Model Gas Turbine Combustor,” *Flow, Turbul. Combust.*, 2019.

[19] R. C. Flagan and J. H. Seinfeld, *Fundamentals of air pollution engineering*. Courier Corporation, 2012.

[20] Y. B. Zeldovich, “The oxidation of nitrogen in combustion and explosions.,” *Acta Physicochim.*, vol. 21, no. 4, pp. 577–628, 1946.

[21] P. Glarborg *et al.*, “Interactions of CO , NO x and H 2 O Under Post-Flame Conditions,” vol. 2202, no. x, 2007.

[22] H. Wang, “Formation os nascent soot and other condensed-phase materials in flames.,” *Proc. Combust. Inst. 33*, vol. 33, pp. 41–67, 2011.

[23] V. Y. Basevich and S. M. Kogarko, “Kinetics of acatylene formation in combustion of methane-oxygen mixtures.,” *Combust. Explos. Shock Waves*, vol. 14, no. 1, pp. 35–40, 1978.

[24] Y. M. Al-Abdeli and A. R. Masri, “Review of laboratory swirl burners and experiments for modelvalidation.,” *Exp. Therm. Fluid Sci.*, vol. 69, pp. 178–196, 2015.

[25] T. Poinsot and D. Veynante, “Theoretical and Numerical Combustion,” *Combust. Flame*, p. 534, 2005.

[26] G. J. Sturgess and D. T. Shouse, “A hybrid model for calculating lean blowouts in practical combustors,” *AIAA, ASME, SAE, ASEE, Jt. Propuls. Conf. Exhib. 32nd, Lake Buena Vista, FL, July 1-3, 1996*, no. July, pp. 1–15, 1996.

[27] A. B. Lebedev, A. N. Secundov, A. M. Starik, N. S. Titova, and A. M. Schepin, “Modeling study of gas-turbine combustor emission,” *Proc. Combust. Inst.*, vol. 32 II, no. 2, pp. 2941–2947, 2009.

[28] R. Hackney, S. K. Sadasivuni, J. W. Rogerson, and G. Bulat, "PREDICTIVE EMISSIONS MONITORING SYSTEM FOR SMALL SIEMENS DRY LOW," in *Proceedings of ASME Turbo Expo 2016: Turbine Technical Conference and Exposition GT2016*, 2016, pp. 1–8.
[29] A. Colorado and V. McDonell, "Exploring Computational Methods for Predicting Pollutant Emissions and Stability Performance of Premixed Reactions Stabilized by a Low Swirl Injector," *Combust. Sci. Technol.*, vol. 189, no. 12, pp. 2115–2134, 2017.
[30] O. Levenspiel, *Chemical Reaction Engineering*. 2009.
[31] P. V. Danckwerts, "Continuous flow systems. Distribution of residence times," *Chem. Eng. Sci.*, vol. 2, no. 1, pp. 1–13, 1953.
[32] T. N. Zwietering, "The degree of mixing in continuous flow systems," *Chem. Eng. Sci.*, vol. 11, no. 1, pp. 1–15, 1959.
[33] O. Levenspiel, *Tracer Technology*, vol. 96. 2012.
[34] E. B. Nauman, "Residence time theory," *Ind. Eng. Chem. Res.*, vol. 47, no. 10, pp. 3752–3766, 2008.
[35] G. Stephanopoulos, *Chemical Process Control*. 1984.
[36] W. M. Deen, *Analysis of Transport Phenomena*. New York: Oxford University Press, 1998.
[37] A. C. Kokossis and C. A. Floudas, "Optimization of Complex Reactor Networks - I. Isothermal Operation," *Chem. Eng. Sci.*, vol. 45, no. 3, pp. 595–614, 1990.
[38] A. C. Kokossis and C. A. Floudas, "Optimization of complex reactor networks-II. Nonisothermal operation," *Chem. Eng. Sci.*, vol. 49, no. 7, pp. 1037–1051, 1994.
[39] D. Hildebrandt and L. T. Biegler, "Synthesis of Chemical Reactor Networks," *AIChE Symp. Ser.*, vol. 91, no. 1992, p. 52, 1995.
[40] M. Mensi, "Reactor network model of biomass combustion in fluidized beds.," Politecnico di Milano, 2018.
[41] R. P. Van Der Lans, P. Glarborg, K. Dam-Johansen, and P. S. Larsen, "Residence time distributions in a cold, confined swirl flow. Implications for chemical engineering combustion modelling," *Chem. Eng. Sci.*, vol. 52, no. 16, pp. 2743–2756, 1997.
[42] E. B. Nauman, "Residence Time Distributions," *Chem. React. Des. Optim. Scaleup*, vol. 29, no. 11, pp. 535–574, 2008.
[43] E. B. Nauman, "RESIDENCE TIME DISTRIBUTIONS AND MICROMIXING," vol. 6445, 2007.
[44] A. D. Martin, "Interpretation of residence time distribution data," vol. 55, no. November 1998, pp. 5907–5917, 2000.
[45] K. B. van Gelder and K. R. Westerterp, "Residence time distribution and hold□up in a cocurrent upflow packed bed reactor at elevated pressure," *Chem. Eng. Technol.*, vol. 13, no. 1, pp. 27–40, 1990.
[46] N. Othman and S. K. Kamarudin, "Radiotracer technology in mixing processes for industrial applications," *Sci. World J.*, vol. 2014, 2014.
[47] C. M. Planarization, A. Philipossian, and E. Mitchell, "A study of residence time distribution using radiotracer technique in the large scale plant facility A study of residence time distribution using radiotracer technique in the large scale plant facility," 2017.
[48] M. Sheoran, A. Chandra, H. Bhunia, P. K. Bajpai, and H. J. Pant, "Residence time distribution studies using radiotracers in chemical industry—A review," *Chem. Eng. Commun.*, vol. 205, no. 6, pp. 739–758, 2018.
[49] D. C. Hammond and A. M. Mellor, "Analytical Calculations for the Performance and Pollutant Emissions of Gas Turbine Combustors," *Combust. Sci. Technol.*, vol. 4, no. 1, pp. 101–112, 1971.
[50] T. Faravelli, L. Bua, A. Frassoldati, A. Antifora, L. Tognotti, and E. Ranzi, "A new procedure for predicting NOx emissions from furnaces," *Comput. Chem. Eng.*, vol. 25, no. 4–6, pp. 613–618, 2001.
[51] J. M. Beér and K. B. Lee, "The effect of the residence time distribution on the performance and efficiency of combustors," *Symp. Combust.*, vol. 10, no. 1, pp. 1187–1202, 1965.
[52] J. S. C. C R. Ewan, F. Boysan, "CLOSING THE GAP BETWEEN FINITE DIFFERENCE AND STIRRED REACTOR COMBUSTOR MODELLING PROCEDURES," in *Twentieth Symposium (International) on Combustion/The Combustion Institute*, 1984, pp. 541–547.

[53] J. E. C. Topps, “AN OPTICAL TECHNIQUE FOR THE INVESTIGATION GAS TURBINE COMBUSTORS,” in *Symposium (Interna- tional) on Combustion, The combustion Institute.*, 1978.

[54] M. RAVICHANDRAN and F. C. GOULDIN, “Residence Time Calculations Using the Numerical Simulation of Incinerator Flows,” *Combust. Sci. Technol.*, vol. 91, no. 4–6, pp. 257–269, 1993.

[55] V. NASSERZADEH, J. SWITHENBANK, C. SCHOFIELD, D. W. SCOTT, and A. LOADER, “Effects of High-Speed Jets and Internal Baffles on the Gas Residence Times in Large Municipal Incinerators,” *Environ. Prog.*, vol. 13, no. 2, pp. 124–133, 1994.

[56] L. S. Pedersen, P. Breithaupt, K. Dam-Johansen, and R. Weber, “Residence time distributions in confined swirling flames,” *Combust. Sci. Technol.*, vol. 127, no. 1–6, pp. 251–273, 1997.

[57] L. S. Pedersen, P. Glarborg, K. Dam-Johansen, P. W. Hepburn, and G. Hesselmann, “A chemical engineering model for predicting NO emissions and burnout from pulverised coal flames,” *Combust. Sci. Technol.*, vol. 132, no. 1–6, pp. 251–314, 1998.

[58] C. A. J. Bass, “Application of chemical kinetic modeling to improve design and performance criteria for a practical incineration system.,” New Jersey Institute of Technlogy, 2002.

[59] C. A. Bass, R. B. Barat, and P. M. Lemieux, “Identification of an ideal reactor model in a secondary combustion chamber,” *AIChE J.*, vol. 49, no. 10, pp. 2619–2630, 2003.

[60] L. Cheng and A. Spencer, “Residence time measurement of an isothermal combustor flow field,” *Exp. Fluids*, vol. 52, no. 3, pp. 647–661, 2012.

[61] K. Göckeler, S. Terhaar, A. Lacarelle, and C. O. Paschereit, “Residence Time Distribution in a Swirl-Stabilized Combustor at Cold Conditions,” *41st AIAA Fluid Dyn. Conf. Exhib. 27 - 30 June 2011, Honolulu, Hawaii*, no. June, pp. 1–13, 2011.

[62] K. Göckeler, S. Terhaar, and C. Oliver Paschereit, “Residence Time Distribution in a Swirling Flow at Nonreacting, Reacting, and Steam-Diluted Conditions,” *J. Eng. Gas Turbines Power*, vol. 136, no. 4, p. 041505, 2013.

[63] S. Bürkle, L. G. Becker, M. A. Agizza, A. Dreizler, V. Ebert, and S. Wagner, “In-situ measurement of residence time distributions in a turbulent oxy-fuel gas-flame combustor,” *Exp. Fluids*, vol. 58, no. 7, 2017.

[64] S. E. B. Ürkle, L. U. G. B. Ecker, M. A. A. A. Gizza, A. N. D. Reizler, and S. T. W. Agner, “Comparison of two measurement strategies to obtain the residence time distribution in combustion chambers using tunable diode laser absorption spectroscopy,” vol. 58, no. 10, pp. 36–46, 2019.

[65] D. C. HAMMOND and A. M. MELLOR, “A Preliminary Investigation of Gas Turbine Combustor Modelling,” *Combust. Sci. Technol.*, vol. 2, no. 2–3, pp. 67–80, Nov. 1970.

[66] A. M. Mellor, “Gas turbine engine pollution,” *Prog. Energy Combust. Sci.*, vol. 1, no. 2–3, pp. 111–133, 1976.

[67] J. Swithenbank, I. Poll, M. W. Vincent, and D. D. Wright, “Combustion design fundamentals,” *Symp. Combust.*, vol. 14, no. 1, pp. 627–638, 1973.

[68] H. C. Hottel, G. C. Williams, and A. H. Bonnell, “Application of well-stirred reactor theory to the prediction of combustor performance,” *Combust. Flame*, vol. 2, no. 1, pp. 13–34, 1958.

[69] G. J. Sturgess, S. P. Heneghan, M. D. Vangsness, D. R. Ballal, and A. L. Lesmerises, “Lean Blowout in a Research Combustor at Simulated Low Pressures,” in *Volume 3: Coal, Biomass and Alternative Fuels; Combustion and Fuels; Oil and Gas Applications; Cycle Innovations*, 1991, p. V003T06A029.

[70] B. Singh and W. E. Lear, “Flame blowout stability in vitated combustion,” *7th Int. Energy Convers. Eng. Conf.*, no. August, pp. 2–5, 2009.

[71] M. F. Karalus, K. B. Fackler, I. V. Novosselov, J. C. Kramlich, and P. C. Malte, “Characterizing the Mechanism of Lean Blowout for a Recirculation-Stabilized Premixed Hydrogen Flame,” *Vol. 2 Combust. Fuels Emiss. Parts A B*, p. 21, 2012.

[72] M. A. Soroudi, S. H. Bafekr, M. Timaji, and N. Rasooli, “A Priori Calculation of Lean Blowout Limit in an Industrial Gas Turbine Combustor,” no. January 2013, 2013.

[73] N. K. Rizk and H. C. Mongia, “Semianalytical Correlations for NOx, CO, and UHC Emissions,” *J. Eng. Gas Turbines Power*, vol. 115, no. 3, p. 612, 1993.

[74] A. Andreini and B. Facchini, “Gas Turbines Design and Off-Design Performance Analysis With

Emissions Evaluation," *J. Eng. Gas Turbines Power*, vol. 126, no. 1, p. 83, 2004.

[75] J. E. Broadwell and A. E. Lutz, "A turbulent jet chemical reaction model: NO(x) production in jet flames," *Combust. Flame*, vol. 114, no. 3–4, pp. 319–335, 1998.

[76] V. M. Zakharov *et al.*, "Development of reactor models of a diffusion combustion chamber for comparative analysis of detailed and reduced kinetic schemes of combustion of hydrocarbon fuels," *Combust. Explos. Shock Waves*, vol. 45, no. 2, pp. 126–133, 2009.

[77] A. M. Starik, A. B. Lebedev, A. M. Savel'ev, N. S. Titova, and P. Leyland, "Impact of Operating Regime on Aviation Engine Emissions: Modeling Study," *J. Propuls. Power*, vol. 29, no. 3, pp. 709–717, 2013.

[78] A. M. Starik, V. E. Kozlov, A. B. Lebedev, and N. S. Titova, "Application of reactor net models for the simulation of gas-turbine combustor emissions," *Int. J. Sustain. Aviat. J. Sustain. Aviat.*, vol. 1, no. 1, pp. 43–57, 2014.

[79] P. C. Malte, "THE IMPORTANCE OF THE NITROUS OXIDE PATHWAY TO NOx IN LEAN -PREMIXED COMBUSTION," 2015.

[80] T. Rutar, P. C. Malte, and J. C. Kramlich, "INVESTIGATION OF NO x AND CO FORMATION IN LEAN-PREMIXED , METHANE / AIR , HIGH-INTENSITY , CONFINED FLAMES AT ELEVATED PRESSURES," *Combustion*, vol. 28, no. x, pp. 2435–2441, 2000.

[81] D. G. Nicol, T. Rutar, S. M. Martin, P. C. Malte, and D. T. Pratt, "Chemical reactor modeling applied to the production of pollutant emission in LP combustors," *33rd Jt. Propuls. Conf. Exhib.*, no. July 1997, 1997.

[82] I. V. Novosselov, "Chemical Reactor Networks for Combustion Systems Modeling," 2006.

[83] I. V. Novosselov, P. C. Malte, S. Yuan, R. Srinivasan, and J. C. Y. Lee, "Chemical Reactor Network Application to Emissions Prediction for Industial DLE Gas Turbine," in *Proceedings of GT2006 ASME Turbo Expo 2006: Power for Land, Sea and Air*, 2006, vol. 2006, no. October, pp. 221–235.

[84] A. Frassoldati, S. Frigerio, E. Colombo, F. Inzoli, and T. Faravelli, "Determination of NOxemissions from strong swirling confined flames with an integrated CFD-based procedure," *Chem. Eng. Sci.*, vol. 60, no. 11, pp. 2851–2869, 2005.

[85] A. Cuoci, A. Frassoldati, G. Buzzi Ferraris, T. Faravelli, and E. Ranzi, "The ignition, combustion and flame structure of carbon monoxide/hydrogen mixtures. Note 2: Fluid dynamics and kinetic aspects of syngas combustion," *Int. J. Hydrogen Energy*, vol. 32, no. 15 SPEC. ISS., pp. 3486–3500, 2007.

[86] A. Stagni, A. Cuoci, A. Frassoldati, T. Faravelli, and E. Ranzi, "A fully coupled , parallel approach for the post-processing of CFD data through reactor network analysis," *Comput. Chem. Eng.*, vol. 60, pp. 197–212, 2014.

[87] A. Andreini, A. Ceccherini, B. Facchini, F. Turrini, and I. Vitale, "Assessment of a set of numerical tools fot the design of aero-engines combustors: study of a tubular test rig," in *Proceedings of ASME Turbo Expo 2009: Power for Land, Sea and Air GT2009*, 2009.

[88] A. Innocenti, A. Andreini, D. Bertini, B. Facchini, and M. Motta, "Turbulent fl ow- fi eld e ff ects in a hybrid CFD-CRN model for the prediction of NO x and CO emissions in aero-engine combustors," *Fuel*, vol. 215, no. November 2017, pp. 853–864, 2018.

[89] V. Fichet, M. Kanniche, P. Plion, and O. Gicquel, "A reactor network model for predicting NOx emissions in gas turbines," *Fuel*, vol. 89, no. 9, pp. 2202–2210, 2010.

[90] I. R. Sigfrid, R. Whiddon, R. Collin, and J. Klingmann, "Experimental and Reactor Network study of Nitrogen Dilution Effects on NOx Formation for Natural Gas and Syngas At Elevated Pressures," *Proc. ASME Turbo Expo 2013 Turbine Tech. Conf. Expo. GT2013*, no. X, pp. 1–12, 2013.

[91] A. Colorado and V. McDonell, "Exploring Computational Methods for Predicting Pollutant Emissions and Stability Performance of Premixed Reactions Stabilized by a Low Swirl Injector," *Combust. Sci. Technol.*, vol. 189, no. 12, pp. 2115–2134, 2017.

[92] T. H. Nguyen, S. Kim, J. Park, S. Jung, and S. Kim, "CFD-CRN validation study for NOx emission prediction in lean premixed gas turbine combustor," *J. Mech. Sci. Technol.*, vol. 31, no. 10, pp. 4933–4942, 2017.

[93] D. Lee, J. Park, J. Jin, and M. Lee, "A simulation for prediction of nitrogen oxide emissions in lean premixed combustor," *J. Mech. Sci. Technol.*, vol. 25, no. 7, pp. 1871–1878, 2011.

[94] J. Park, T. H. Nguyen, D. Joung, K. Y. Huh, and M. C. Lee, "Prediction of NO $_x$ and CO Emissions from an Industrial Lean-Premixed Gas Turbine Combustor Using a Chemical Reactor Network Model," *Energy & Fuels*, vol. 27, no. 3, pp. 1643–1651, 2013.

[95] R. Rezvani, R. Denny, and D. Mavris, "A Design-Oriented Semi-Analytical Emissions Prediction Method for Gas Turbine Combustors," *47th AIAA Aerosp. Sci. Meet. Incl. New Horizons Forum Aerosp. Expo.*, no. January, pp. 1–10, 2009.

[96] R. F. D. M. Sajjad Yousefian, Gilles Bourque, "REVIEW OF HYBRID EMISSIONS PREDICTION TOOLS AND UNCERTAINTY QUANTIFICATION METHODS FOR GAS TURBINE COMBUSTION SYSTEMS," in *Proceedings of ASME Turbo Expo 2017: Turbomachinery Technical Conference and Exposition GT2017*, 2017, pp. 294–300.

[97] D. Allaire, I. Waitz, and K. Willcox, "A Comparison of Two Methods for Predicting Emissions from Aircraft Gas Turbine Combustors Objective Emissions Modeling," 2007.

[98] E. M. Mendoza Orbegoso, C. D. Romeiro, S. B. Ferreira, and L. F. Figueira Da Silva, "Emissions and Thermodynamic Performance Simulation of an Industrial Gas Turbine," *J. Propuls. Power*, vol. 27, no. 1, pp. 78–93, 2011.

[99] E. Hataysal, "A coupled flow and chemical reactor network model for predicting gas turbine combustor performance," no. January, pp. 0–16, 2018.

[100] A. De Toni, T. Hayashi, and P. Schneider, "A reactor network model for predicting NOx emissions in an industrial natural gas burner," *J. Brazilian Soc. Mech. Sci. Eng.*, vol. 35, no. 3, pp. 199–206, 2013.

[101] P. J. Stuttaford and P. A. Rubini, "Preliminary Gas Turbine Combustor Design Using a Network Approach," *J. Eng. Gas Turbines Power*, vol. 119, no. 3, p. 546, 1997.

[102] C. C. Leong and L. J. Rye, "Gt2010- Reverse Engineering Gas Turbine Emission Performance : Applied To an Aircraft Auxiliary Power Unit Nomenclature," pp. 1–11, 2010.

[103] C. Leong and S. Blakey, "Genetic Algorithms Optimised Chemical Reactors Network Application: Hydrogen Emissions Performance of a V2527 engine," *USES Conf. Proc.*, vol. 01, no. x, pp. 3–4, 2015.

[104] S. Tietz and M. Schaefer, "Development and application of a reactor network approach for estimating NO," *ONERA-DLR Aerosp. Symp. 2013*, no. x, pp. 1–8, 2013.

[105] A. Kaluri, P. Malte, and I. Novosselov, "Real-time prediction of lean blowout using chemical reactor network," *Fuel*, vol. 234, no. August, pp. 797–808, 2018.

[106] P. Depape and I. Novosselov, "Model-based Approach for Combustion Monitoring using Real-Time Chemical Reactor Network," *J. Combust.*, no. September, 2018.

[107] S. Gupta, P. Malte, S. L. Brunton, and I. Novosselov, "Prevention of lean flame blowout using a predictive chemical reactor network control," *Fuel*, vol. 236, no. September 2018, pp. 583–588, 2019.

[108] M. G. J. Hermann and B. B. A. Dreizler, "Flame – cooling air interaction in an effusion □ cooled model gas turbine combustor at elevated pressure," *Exp. Fluids*, vol. 0, no. 0, p. 0, 2019.

[109] E. Schlosser, J. Wolfrum, L. Hildebrandt, H. Seifert, B. Oser, and V. Ebert, "Diode laser based in situ detection of alkali atoms: Development of a new method for determination of residence-time distribution in combustion plants," *Appl. Phys. B Lasers Opt.*, vol. 75, no. 2–3, pp. 237–247, 2002.

[110] I. Roehle, R. Schodl, P. Voigt, and C. Willert, "Recent developments and applications of quantitative laser light sheet measuring techniques in turbomachinery components," *Meas. Sci. Technol.*, vol. 11, pp. 1023–1035, 2000.

[111] L. G. Becker *et al.*, "Experimental investigation of flame stabilization inside the quarl of an oxyfuel swirl burner," *Fuel*, vol. 201, pp. 124–135, 2017.

[112] L. G. Becker, T. Von Langenthal, S. Pielsticker, B. Böhm, R. Kneer, and A. Dreizler, "Experimental investigation of particle-laden fl ows in an oxy-coal combustion chamber for non-reacting conditions," *Fuel*, vol. 235, no. August 2018, pp. 753–762, 2019.

[113] M. P. B. Musculus and L. M. Pickett, "Diagnostic considerations for optical laser-extinction measurements of soot in high-pressure transient combustion environments," vol. 141, pp. 371–391, 2005.

[114] R. Di Sante, "Laser extinction technique for measurements of carbon particles concentration during combustion," *Opt. Lasers Eng.*, vol. 51, no. 6, pp. 783–789, 2013.

[115] "MATLAB and Global Optimization Toolbox, The MathWorks Inc." Natick, Massachusetts, United States.
[116] R. Weber and J. Dugué, "Combustion accelerated swirling flows in high confinements," *Prog. Energy Combust. Sci.*, vol. 18, no. 4, pp. 349–367, 1992.
[117] "ANSYS® Academic Research Mechanical, Release 18.1." .
[118] G. P. Smith *et al.*, "GRI-MECH 3.0." [Online]. Available: http://www.me.berkeley.edu/gri_mech/.
[119] T. Faravelli, A. Frassoldati, and E. Ranzi, "Kinetic modeling of the interactions between NO and hydrocarbons in the oxidation of hydrocarbons at low temperatures.," *Combust. Flame*, vol. 132, no. 1–2, pp. 188–207, 2003.
[120] A. Frassoldati, T. Faravelli, and E. Ranzi, "Kinetic modeling of the interactions between NO and hydrocarbons at high temperature.," *Combust. Flame*, vol. 135, pp. 97–112, 2003.
[121] A. Cuoci, A. Frassoldati, T. Faravelli, and E. Ranzi, "Formation of soot and nitrogen oxides in unsteady counterflow diffusion flames.," *Combust. Flame*, vol. 156, no. 10, pp. 2010–2022, 2009.
[122] E. Ranzi *et al.*, "Hierarchical and comparative kinetic modeling of laminar flame speeds of hydrocarbon and oxygenated fuels.," *Prog. Energy Combust. Sci.*, vol. 38, no. 4, pp. 468–501, 2012.
[123] W. K. Metcalfe, S. M. Burke, S. S. Ahmed, and H. J. Curran, "A hierarchical and comparative kinetic modeling study of C1–C2 hydrocarbon and oxygenated fuels.," *Int. J. Chem. Kinet.*, vol. 45, no. 10, pp. 638–675, 2013.
[124] Z. Mansouri, M. Aouissi, and T. Boushaki, "A Numerical Study of Swirl Effects on the Flow and Flame Dynamics in a Lean Premixed Combustor," *Int. J. heat Technol.*, vol. 34, no. 2, pp. 227–235, 2016.
[125] R. S. Gabruk and L. A. Roet, "Velocity Characteristics of Reacting and Nonreacting Flows in a Dump Combustor," vol. 10, no. 2, pp. 148–154, 1994.
[126] M. D. Barringer, K. A. Thole, and M. D. Polanka, "Effects of Combustor Exit Profiles on High Pressure Turbine Vane Aerodynamics and Heat Transfer," in *Proceedings of GT2006 ASME Turbo Expo 2006: Power for Land, Sea and Air*, 2016, pp. 1–11.
[127] Z. Qingjun, W. Huishe, Z. Xiaolu, and X. Jianzhong, "Numerical Investigation on the Influence of Hot Streak Temperature Ratio in a High-Pressure Stage of Vaneless Counter-Rotating Turbine.," vol. 2007, 2007.
[128] O. S. Motsamai, J. A. Snyman, and J. P. Meyer, "Optimization of gas turbine combustor mixing for improved exit temperature profile.," *Heat Transf. Eng.*, vol. 31, no. 5, pp. 402–418, 2010.
[129] S. Bürkle, L. G. Becker, A. Dreizler, and S. Wagner, "Experimental investigation of the fl ue gas thermochemical composition of an oxy-fuel swirl burner," *Fuel*, vol. 231, no. March, pp. 61–72, 2018.
[130] A. S. Doost *et al.*, "Residence time calculations for complex swirling flow in a combustion chamber using large-eddy simulations," *Chem. Eng. Sci.*, vol. 156, pp. 97–114, 2016.
[131] R. Knappstein *et al.*, "Large Eddy Simulation of a Novel Gas-Assisted Coal Combustion Chamber," *Flow, Turbul. Combust.*, 2018.